December 2021

Analyzing Weathering Patterns in Modern and Paleolake Deposits of Tecopa, California: Implications for the Detection of Paleolakes on Mars

Jason Benjamin Carman
University of Wisconsin-Milwaukee

ANALYZING WEATHERING PATTERNS IN MODERN AND PALEOLAKE DEPOSITS OF TECOPA, CALIFORNIA: IMPLICATIONS FOR THE DETECTION OF PALEOLAKES ON MARS

by

Jason Benjamin Carman

A Thesis Submitted in

Partial Fulfillment of the

Requirements for the Degree of

Master of Science

in Geosciences

at

The University of Wisconsin-Milwaukee

December 2021

ABSTRACT

ANALYZING WEATHERING PATTERNS IN MODERN AND PALEOLAKE DEPOSITS OF TECOPA, CALIFORNIA: IMPLICATIONS FOR THE DETECTION OF PALEOLAKES ON MARS

by

Jason Benjamin Carman

The University of Wisconsin-Milwaukee, 2021
Under the Supervision of Professor Lindsay J. McHenry

This study focuses on two stratigraphic sections from the Tecopa paleolake and samples from the modern Tecopa and Amargosa River basins as a terrestrial analogue to Martian paleolakes. Previous work shows that the later stages of Pleistocene Lake Tecopa were highly alkaline and saline due to evaporation, which led to the formation of authigenic lacustrine minerals such as zeolites, clays, and precipitates that are potentially similar to Martian paleolakes. Paleolakes can provide information on past aqueous processes, such as the changes in the hydrologic cycle that a particular area experienced over the lifespan of a lake on Earth or Mars. While morphological evidence for paleolakes on Mars is widespread, direct orbital spectroscopic evidence for lacustrine minerals is sparse. Whether this is due to the lack of such deposits, or to limitations in our ability to detect them, is unclear.

This study used the overall grain sizes, mineral assemblages, spectral features, and the major oxides of SiO_2, Al_2O_3, K_2O, Fe_2O_3, CaO, Na_2O, MgO, TiO_2, P_2O_5 (weight %) and trace elements Zr, Sr, and Ba (ppm) to determine if the surface crusts that developed on the paleolake deposits can mask the true remote sensing signal of the underlying strata. A total of 48 samples, including pairs of samples (surface and subsurface) from two stratigraphic columns, were

collected for laboratory X-Ray Fluorescence (XRF), X-Ray Diffraction (XRD), Visible and Near-Infrared Reflectance (VNIR) spectroscopy, and grain size analysis. Major and trace element concentrations using XRF were used for chemical weathering calculations and examined for geochemical differences between the paired samples. XRD data were used to qualitatively identify differences in mineral assemblages between the surface crust and underlying strata. VNIR spectra of surface samples, together with the XRD data, were used to determine which minerals might be identifiable using VNIR remote sensing. The VNIR spectra for the surface was compared to underlying strata to determine changes in the signal and the possible effect it might have on the interpretation. Section 1, located near Greenwater Valley, has smectite, calcite, analcime, K-feldspar, searlesite, and illite. K-feldspar and analcime typically form under more saline-alkaline conditions, closer to the lake basin. Section 1 is dominated by mudstone, siltstone, and white colored volcanic ash beds. Section 2, located near Tecopa Peak, is dominated by mudstone, siltstone, sandstone, and white to green colored volcanic ash beds. Section 2 has phillipsite and clinoptilolite, which is consistent with intermediate saline-alkaline conditions.

Some individual sample pairs had significantly different mineral assemblages and elemental abundances compared to each other, including the presence or absence of carbonate minerals, or differences in Al_2O_3, TiO_2, and Zr concentrations, potentially indicating different source lithologies. Such differences could be attributed to sheet flow. Differences in mineral assemblage between surface and underlying strata can change the VNIR signal, especially if these include typical paleolake minerals such as zeolites, clay minerals, and carbonates. This is especially important when using remote sensing to map geomorphic features and minerals on Mars to better understand its geological and climatic history. Ground truthing orbital data with in-situ rover data is thus critical from current and future missions.

To my wife, Nancy, for all the cups of coffee and caffeinated teas to get through the many lengthy nights of writing this thesis.

TABLE OF CONTENTS

LIST OF FIGURES

LIST OF TABLES

LIST OF ABBREVIATIONS

CIA	Chemical Index of Alteration
CIW	Chemical Index of Weathering
CPA	Chemical Proxy of Alteration
CRISM	Compact Reconnaissance Imaging Spectrometer for Mars
ICV	Index of Compositional Variability
MRO	Mars Reconnaissance Orbiter
PIA	Plagioclase Index of Alteration
VNIR	Visible and Near-Infrared Reflectance (350–2500 nm)
WIP	Weathering Index of Parker
XRD	X-Ray Diffraction
XRF	X-Ray Fluorescence

ACKNOWLEDGEMENTS

I would like to foremost thank my advisor Dr. Lindsay McHenry for her support and dedication to our Tecopa project. Her efforts in getting the grants to fund this project and continuous edits of my thesis to be in top shape for my fall defense are greatly appreciated. I would also like to thank my colleague and friend, Gayantha Kodikara, for his advice on VNIR and endless talks on philosophy and science. Without his expertise on VNIR, part of my analysis would have not been done. I would also like to thank my undergraduate field assistants, Mark Eskritt and Kaitlin Krause for helping me collect my soil and water samples in Tecopa.

I want to thank my committee members Dr. Barry Cameron and Dr. John Isbell for the necessary corrections, advice and for being part of my committee. I would also want to thank Dr Elisabeth Hausrath and Ngoc Luu from the Soil Science lab at UNLV, for providing us with an acid solution for our field work. In addition to that, I would like to thank Dr. Christopher Adcock from the Soil Science lab at UNLV, for his advice on how to tackle VNIR for my area of interest.

In addition, I would love to thank my parents (Sharon and Gary Carman) for their support, love, and extra push for me to finish my masters. I would also love to thank my in-laws, Pedro, Maria Elena, and Jerry Duque for their endless love, support and cheering me on until the finish line. Finally, I would love to thank my loving and caring wife, Nancy Carman, for all the help and endless support during my timespan as a graduate student at UW-Milwaukee. I also want to thank the Wisconsin Space Grant Consortium for the Research Infrastructure Program grant, which provided the necessary funding for this research.

“Take a good, long, honest, positive look at what good can come out of every situation you’re in. Wherever you are, that’s where you are. You’re there with it. This is your history you’re living right now. So do what you can to make the most of what comes along. And please, don’t try to do everything on your own. There are a lot of people out there in the universe who wish you well and want to be your friend. Let them help you. You don’t have to carry it all on your own.”

--Dr. Buzz Aldrin,
“Life lessons from legendary Astronaut Buzz Aldrin”

1. Introduction

1.1 Objective

When geologists collect samples from paleolake deposits, they typically dig into the exposure to collect a fresher specimen, or even rely on drill cores. Both approaches avoid surface samples, which are more likely to be contaminated by sheetwash, dust, or duricrust materials, masking the composition of the underlying deposit. Unfortunately, this is not possible for studies conducted by remote sensing, where only the problematic surface is available for study. This study aims to show how detrital material from sheet flow may significantly obstruct the remote sensing geochemical and mineralogical signal of the strata of paleolake Tecopa and the modern Tecopa basin. Also, it is hypothesized that weathering at Tecopa is controlled by mechanical weathering with limited chemical weathering due to the arid environment, though a small amount of silcrete or calcrete duricrust is expected to form on the soil surface by capillary action because of the rapid evaporation rate.

In this study, we used two stratigraphic sections in the paleolake Tecopa because work from Larsen (2008) and Larsen and Olson (2019) indicated a highly alkaline and saline environment that led to the formation of authigenic lacustrine minerals (i.e., smectites & carbonates), similar to the minerals found on Mars (Bristow and Milliken, 2011). Authigenic lacustrine minerals can give us information about the chemical conditions that a lake basin experienced over time. Authigenic minerals often exhibit lateral zonation, based on difference in the chemical environment. When water moves into the basin, the salinity and pH will change, leading to the precipitation of different minerals (Bristow and Milliken, 2011). This lateral zonation is also observed in element abundances, as the centers of closed lake basins are enriched in Mg^{2+} and

depleted in Al^{3+} relative to the lake margins. Larsen (2008) noted this lateral zonation of authigenic minerals in the Lake Tecopa beds, which is another reason why we chose Tecopa as our Martian analog.

1.2 Terrestrial surface weathering

Exposed material is vulnerable to a variety of weathering processes and the nature of the weathering is strongly controlled by regional climate. Minerals have different resistances to weathering, based on their composition, grain size, and crystal structure. The regional climate along with the minerals present can affect alteration rates, the mechanical breakdown of particles, removal of weathering products, and the type of biological processes that can occur (Warke, 2013).

Physical, chemical, and biological weathering processes are thought to be limited in arid regions and produce weathering features with little transport of loosened or altered material. Physical processes are assumed to be dominant, but these are less effective due to a lack of moisture (Warke, 2013). Hydrolysis of minerals and dissolution of soluble primary minerals are limited while mass-wasting processes (e.g., creep, loess and mudflow), and intermediate sheet flooding are prominent (Verheye, 2006; Han and Singer, 2007). Rain drops or atmospheric dew can interact with desert soils and form a surface crust with some accompanying chemical alteration, oxidation, and hydration of anhydrous minerals, but this is unlikely to have a significant effect because of high evaporation rates. Temperature differences within the clasts should be small, therefore physical weathering by thermal stresses from solar insolation should be insignificant compared to other surface weathering processes that can act more quickly to disintegrate clasts (Twidale, 1973; McFadden et al., 2005).

Wind can affect the soil surface by deflation, abrasion, erosion, and transport (Verheye, 2006). Deflation removes clay and silt sized grains, leaving a sheet-like surface of rock fragments with a slightly hardened salt horizon below the surface (de Haas et al., 2014). Abrasion of the rock through wind or water can lead to the deposition of illite and possibly some interlayered montmorillonite on the surface of rocks (Potter and Rossman, 1977). It can also disintegrate rock layers and form ventifact features. Wind can transport foreign material that intermixes with and chemically alters the original composition of the materials (Han and Singer, 2007). Windblown dust can deposit carbonate on soil surfaces and through the process of calcification, create a carbonate-rich zone near the surface, or migrate downwards to enrich soils at depth (Gile et al., 1981; Reheis et al., 1995; Schaetzl and Anderson, 2005; Reheis and Urban, 2011). Calcification commonly occurs in subhumid to hyperarid climates with soil classified as aridisols (Ritter et al., 2011).

Besides surface weathering processes, chemical precipitates can form a duricrust near or at the surface by capillary action because the rapid evaporation exceeds precipitation rates (Bachman and Machette, 1977). Duricrust can be subclassified by its dominant mineralogy, for example ferricrete is iron-rich, while calcrete is carbonate-rich. Silcrete (quartz-rich), calcrete (carbonate-rich), and gypcrete (gypsum-rich) can all form in arid climates. Hyperarid climates may not allow for the accumulation of carbonates to form calcrete because there must be sufficient precipitation for carbonate-rich solutions to infiltrate the soil horizons, and too much precipitation will leach out the carbonates (Bachman and Machette, 1977). The formation of duricrusts is not limited to Earth, as the Martian surface has dusty regions with a duricrust overlain by surficial dust (Golombek et al., 2020).

1.3 Tecopa Paleolake as a Martian Analog Candidate

A paleolake is a lake that existed in the past but no longer remains due to the different climate and hydrological conditions occurring today. Paleolakes can provide information on past aqueous processes and the geomorphological history of a lake whether on Earth, Mars, or some other planetary body. There is orbital evidence of paleolakes in Gale and Jezero craters on Mars (Grotzinger et al., 2015; Goudge et al., 2015a), which is further supported by rover-based analyses of Martian sediment deposits that contain clays and precipitate minerals that resemble those in paleolakes on Earth (Gellert et al., 2004; Clark et al., 2005; Morris et al., 2010; Goudge et al., 2015b; Grotzinger et al., 2015). In this study we chose the Tecopa paleolake basin and the modern Amargosa river basin because previous work suggests that the later stages of Lake Tecopa were highly alkaline and saline due to evaporation. This led to the formation of authigenic lacustrine minerals such as clays and precipitates that have also been found on Mars. Paleolakes on Earth, such as Tecopa, are commonly used as comparisons to past processes on Mars. These paleolakes on Earth serve as ground truth to the orbital data for Mars, which is important for selecting and validating landing sites for future missions (Wiens et al., 2021).

2. Geologic Background

2.1 Lake Tecopa

The Tecopa valley is a well-exposed sedimentary basin in Inyo County, California. Bedrock surrounding the basin includes: Paleozoic carbonate rocks in the Resting Spring Range, Cenozoic sedimentary rocks in the Ibex Hills and mixed with intrusions in the Sperry Hills, and Cambrian siliciclastic and Cenozoic volcanic rocks in Dublin Hills, see Figure 1.

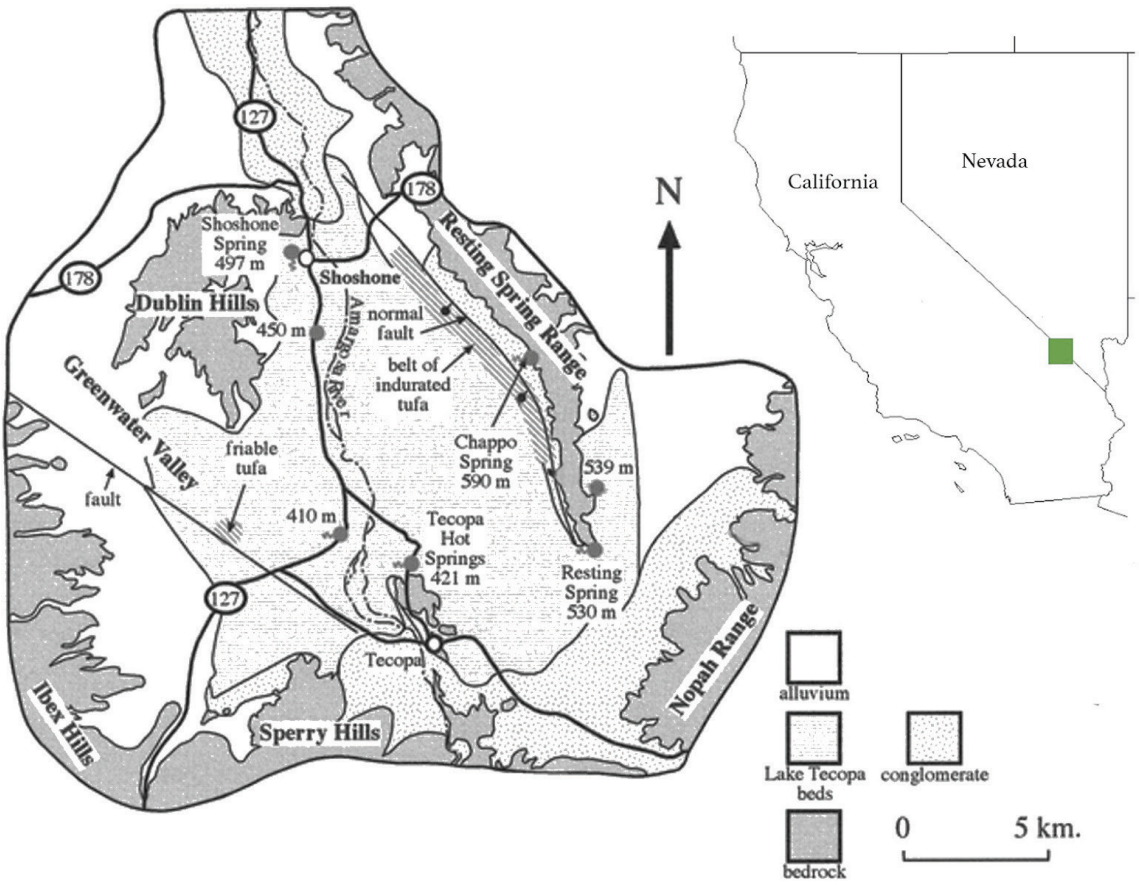

Figure 1: A simplified geologic map for the Tecopa basin area (modified from Nelson et al., 2001, which is simplified after Hillhouse, 1987).

Deposits associated with Lake Tecopa consist of lacustrine mudstones, siltstones, sandstones, conglomerates, and ash beds (Larsen, 2008). The Pleistocene Tecopa Basin is interpreted as a shallow endorheic (closed, with no outlet) saline lake surrounded by ponds located near groundwater seeps and fluvial inlets (Gibert et al., 2011). Lake Tecopa underwent dramatic changes in salinity and water level (Larsen, 2008). Sediments accumulated during dry periods from local low-alkalinity groundwater discharge or runoff (Reheis et al., 2019).

During the Miocene to the Pliocene, silicic to mafic rocks were exposed in the northern headwater of the Amargosa River (Morrison, 1999; Menges, 2008). A mixture of sediment sources came from the Amargosa River, groundwater discharge (bicarbonate springs and seeps), and clastic detrital material from nearby sources (Morrison, 1999; Belcher et al., 2019; Reheis et al., 2019). Intermittent local water sources created fluctuating shallow saline lakes in the Tecopa basin during early Pleistocene interglacial periods. About 1 Ma, the Amargosa River integrated with Lake Tecopa, which was followed by six periods of drier conditions, leading to the deposition of shallow lacustrine layers in the basin (Reheis et al., 2019; Larsen and Olson, 2019). Three major tuff marker beds are found in the valley; the 2.02 Ma Huckleberry Ridge, 0.760 Ma Bishop from the Long Valley Caldera, and 0.655 Ma Lava Creek B from the Yellowstone Caldera eruption (Bogaard and Schirnick, 1995; Gansecki et al., 1998; Larsen, 2008). The Island Park Caldera eruption deposited the Huckleberry Ridge tuff (2.02 Ma) onto the shallow lacustrine deposits. Sedimentation rates then decreased due to drier conditions, creating ephemeral lakes and mudflats (Larsen, 2008).

The lacustrine sediments and tuff in the central part of the basin were diagenetically altered to clay and zeolites (Sheppard and Gude, 1968; Starkey and Blackmon, 1979; Larsen, 2008; Larsen and Olson, 2019). Later, these sediments were exhumed by the Amargosa River.

Exorheic waters from the Greenwater Valley brought alluvial sediments into the western side of the basin (Gibert et al., 2011). Modern processes include the transport of fine dust and salt particles that form during wet months from wet playas, which produce efflorescent salts that are blown around the basin (Reheis et al., 1995; Reheis, 2006; Reheis and Urban, 2011). These particles can physically cover the surface of the exposed Tecopa lake beds, forming a crust and contributing to the alteration of the original material on the surface.

2.2 Geology of Mars

2.2.1 Martian History

Mars is smaller than Earth, with a diameter of 6,780 km. Mars is less dense than Earth and has a thin carbon dioxide (CO_2) atmosphere. More of the rich and complex early geological history of Mars is preserved, compared to Earth, which has active plate tectonics and a longer history of aqueous processes. For Mars, impact craters are less abundant in the lowland plains of the northern hemisphere, while the highlands of the southern hemisphere have more impact craters and basins, indicating their greater age (Rossi and Van Gasselt, 2010). Impact cratering, volcanism, fluvial, glacial and aeolian resurfacing processes played an important role in developing the morphologies that we see today. These morphological features were the result of three major time periods that encompass most of the geological record of Mars (Figure 2), the Noachian (4.65 to 3.7 Gyr), Hesperian (3.7 to 3.0 Gyr), and Amazonian (3.0 Gyr to present).

The Noachian is associated with frequent and large impacts in the highlands, large scale volcanism, and extensive valley formations indicative of fluvial channels and a warmer and wetter early Mars (Ramirez and Craddock, 2018). Volcanic activity was most prominent in the Tharsis region. The high erosion rates observed during valley formations may have been due to

surface runoff, which reflects a warmer and wetter early Mars (Craddock and Maxwell, 1993; Craddock and Howard, 2002).

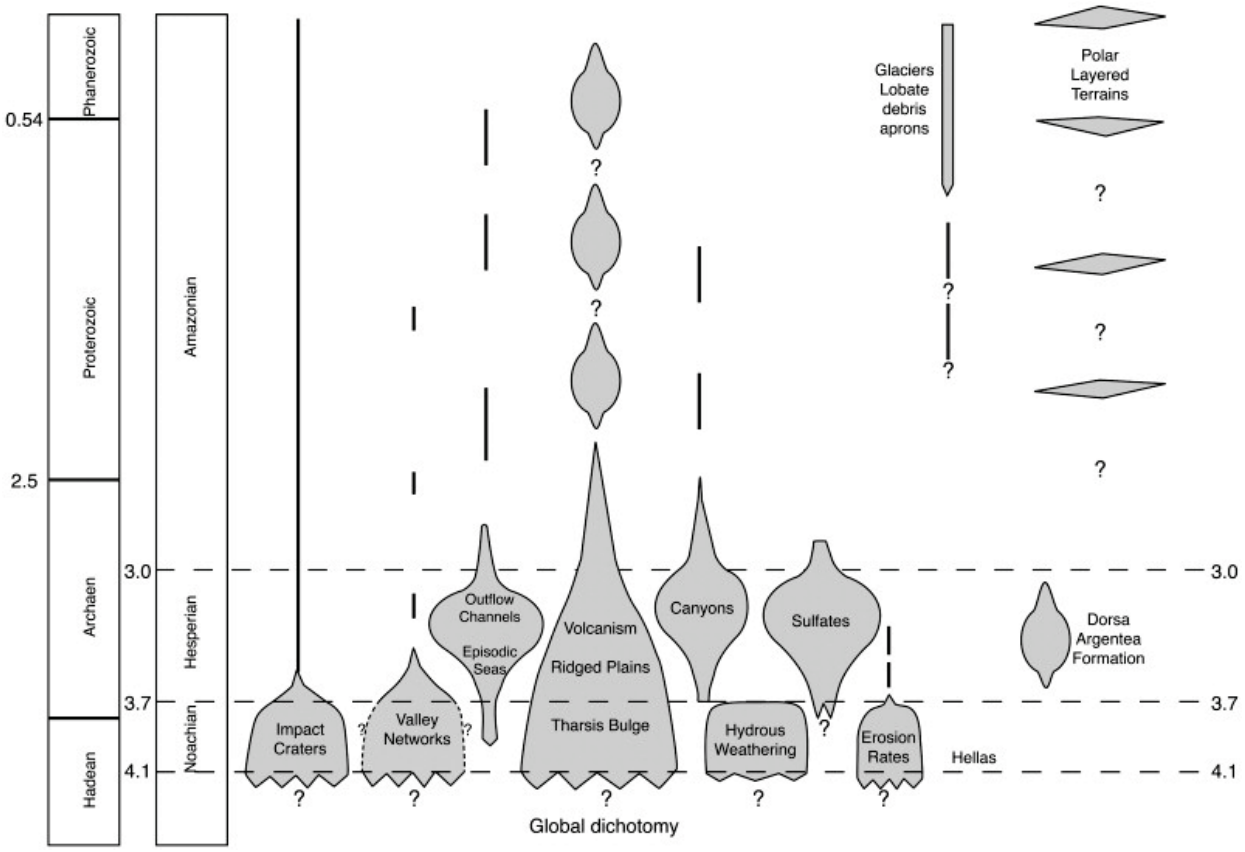

Figure 2: Geological processes on Mars from the Noachian to Amazonian (Carr and Head, 2010).

Deltas are observed in some impact craters imaged by orbiters and have been or are being investigated by rovers at Jezero and Gale craters (Figure 3), and finely layered sediments were likely deposited at the bottom of a lake in Gale crater (Carr and Head, 2010). Phyllosilicate minerals are identified in Noachian and early Hesperian deposits, and these minerals likely formed in a neutral to alkaline water-rich environment. The Hesperian is marked by extensive volcanism and deposits formed by the catastrophic release of water, which led to the formation

of outflow channels. These outflow channels are in Chryse, the eastern Hellas Planitia regions, and the Valles Marineris (Tanaka, 1986; Tanaka et al., 2003). All the large shield volcanoes such as Olympus Mons formed during this period (Head and Wilson, 2011). The outgassing of sulfur dioxide (SO_2) and hydrogen sulfide (H_2S) was a catalyst in transitioning from an alkaline environment to an acidic environment. Weathering products changed from dominantly phyllosilicate minerals to more sulfate minerals (Head and Wilson, 2011). This transitioned into the Amazonian period, which is the youngest and is marked by fewer impact craters, glacial activity, fewer lava flows, and minimal, if any, aqueous activity.

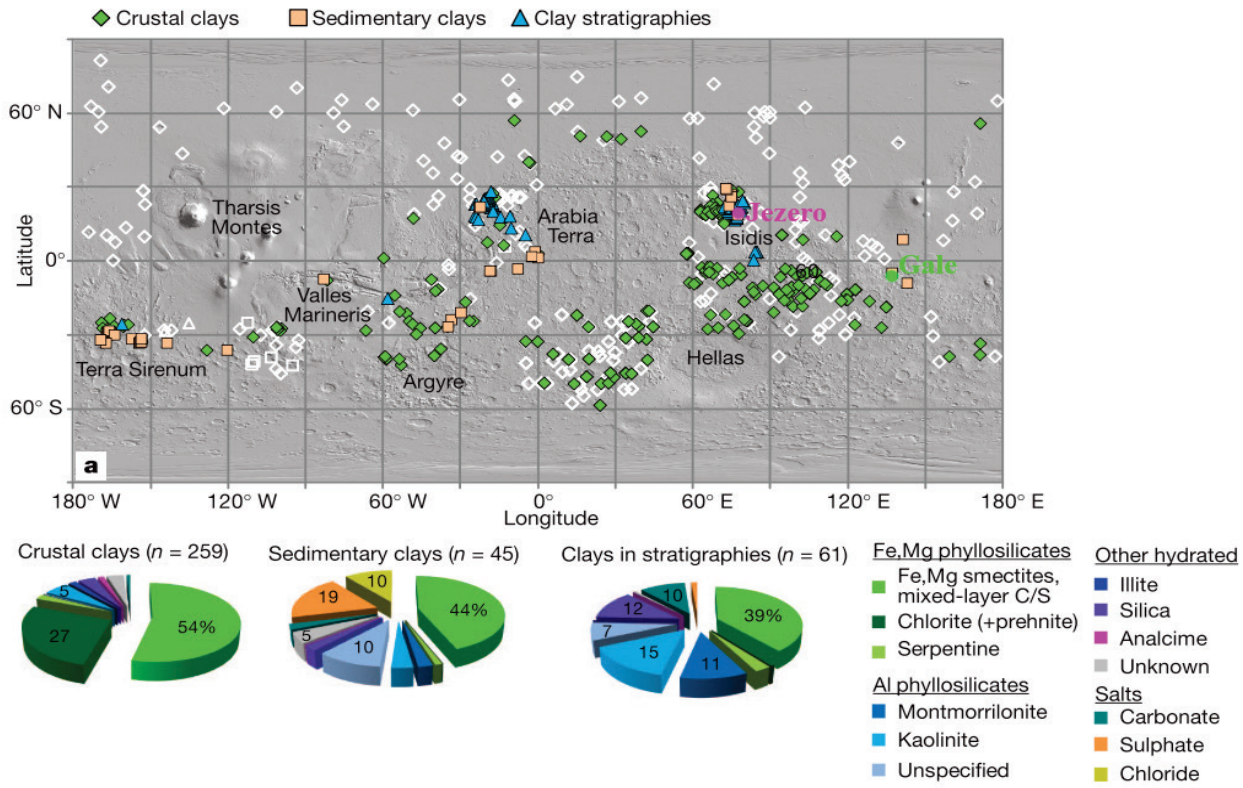

Figure 3: Martian clay mineral distribution, with the location of Jezero (marked in pink) and Gale craters (marked in light green). Note that Fe and Mg smectites are the largest component of the Martian clays. Modified from Ehlmann et al. (2011).

2.2.2 Martian Exploration: Orbiters and Rover Missions

The earliest studies of Martian geology were conducted using images from early planetary missions of the 60's and 70's. The Mariner flyby missions in the 60's gave us the first photographs and we learned that Mars has a cratered surface. The Mariner 9 orbiter provided evidence of dry flow channels and volcanism on Mars. The twin Viking missions of the 70's provided more comprehensive imagery that covered the entire surface, and thus most global-scale geological and stratigraphic interpretations were originally made using Viking imagery (Tanaka, 1986). The twin Viking missions also included landers, which conducted three astrobiological experiments to look for evidence of life by analyzing soil samples. The Viking missions helped us better understand that Mars is cold with a dry carbon dioxide atmosphere and provided evidence of ancient river channels and flooding.

Mars exploration was on hiatus in the 80's and early 90's, until the arrival of the first rover (Sojourner) as part of the Pathfinder mission in 1997. Sojourner analyzed the geology, composition of rocks, soil, and atmosphere, and it was the interpretation of the data from this mission that first highlighted the potential effects of surface weathering and dust coatings on our ability to identify Martian rocks. The first compositional data for the rock "Barnacle Bill" (A-3) indicated that it had a similar chemical composition to andesites on Earth, while the chemical composition of the nearby "Yogi" rock (A-7), appeared to have a lower weight percent of SiO_2, and was initially interpreted as basaltic. However, the "Yogi" rock was noted to have a possible dust coating from the Martian soil (McSween et al., 1999). The geochemical contribution from the Martian soil was roughly estimated and subtracted from the "Yogi" rock. After the correction, the "Yogi" rock was found to have a similar chemical composition to "Barnacle Bill" and reclassified as a basaltic andesite (Bridges et al., 2001). To avoid this kind of issue, the later

Mars Exploration Rovers (MER) Spirit and Opportunity each had a Rock Abrasion Tool (RAT) that would aid in exposing fresh rock surfaces to help the scientific instruments obtain more accurate measurements (Gorevan et al., 2003).

The reinterpretation of the chemical analyses at the Pathfinder site gives us a look at changes in interpretation over time (McSween et al., 1999; Wänke et al., 2001; Bridges et al., 2001; Foley et al., 2003). The Martian surface is complex and is worked by windblown dust that can often interfere with the results and lead to misinterpretation (Bridges et al., 2001). This windblown dust is rich in oxidized iron and sulfate. This leads us to one of the basic questions geologists ask, is the rock igneous, sedimentary, or metamorphic. For the Pathfinder rocks, if they were igneous then their bulk chemistry would need to be analyzed anhydrously. The water from these rocks (e.g., Yogi: 1.3 +/- 1.4 wt % to 7.1 +/- 1.4 wt %) is higher than unaltered terrestrial igneous rocks (< 2 wt %) (Foley et al., 2003). Thus, the presence of high weight percent water indicates the possibility of a non-igneous origin (i.e., sedimentary or metamorphic) for the Pathfinder rocks (Wänke et al., 2001). The texture from these rocks resembles those of volcanic vesicles but these vesicles may also form through chemical etching as observed for some rocks in Antarctica (Campbell and Claridge, 1987; Foley et al., 2003). It is also possible that the Pathfinder rocks may have been altered by the process of palagonitization, which would explain the increased water content with minimal change in bulk chemistry (Wyatt and McSween, 2002; Foley et al., 2003). The result of these interpretations over time should be a guide for future missions to various locations on Mars on what to expect and the best sampling strategies to determine the rock types.

2.2.3 Martian Paleolakes

A. Open-basin lakes versus Closed-basin lakes

The important geomorphic processes that have shaped the surface of Mars include fluvial, impact cratering, aeolian, and mass wasting processes (Fassett and Head, 2008). For several decades since the retrieval of Viking data, paleolakes have been identified in some impact craters (Goudge et al., 2015a). New analysis and surveys were undertaken using data from the more recent Mars Global Surveyor, Mars Odyssey, Mars Express, and Mars Reconnaissance Orbiter missions to recognize good paleolake candidates. Martian paleolakes are classified as either open-basin (exorheic) or closed-basin (endorheic) lakes. An open-basin lake has an outlet valley that drains the basin, in contrast, a closed-basin lake is where water has pooled in the basin through groundwater or an inlet valley with alluvial fans, but which lacks an outlet (Goudge et al., 2012b, 2015b). Gale crater is interpreted to be a closed-basin paleolake while Jezero crater is an open-basin paleolake. Studying the lacustrine activity within these basins is important (Goudge et al., 2012b, 2012a, 2015b; Grotzinger et al., 2014), since paleolakes can provide information on past aqueous processes, such as changes in the hydrologic cycle that a particular area experienced over the lifespan of a lake whether on Mars or on Earth.

B. Gale crater

Gale crater is currently under study by the Curiosity rover. Curiosity landed close to an alluvial fan, which shows clear evidence for past flowing water. The goals of the Curiosity rover are to characterize the possibility for ancient life in Gale crater, how water played a role in its current mineral assemblages, and to determine the climate and radiation environment of the surface to help prepare for future human missions (Grotzinger et al., 2014, 2015; Vaniman et al.,

2014). The rover has a suite of instruments that has helped carry out the scientific goals since 2012. The Mastcam takes color pictures and short videos of the Martian landscape. The Chemistry and Camera (CheCam) instrument has a laser, camera, and spectrograph that helps identify the mineral composition of rocks and soils. The Chemistry and Mineralogy (CheMin) instrument conducts X-ray Diffraction analysis on powdered rock samples to identify the different types of minerals. Finally, the Alpha Particle X-Ray Spectrometer (APXS) instrument measures the abundance of chemical elements in rocks and soils. The rover's suite of instruments is used together to better understand the geology, atmosphere, environmental conditions, and the potential for biosignatures on Mars.

One of the Curiosity rover's principal goals was to study the aqueous geochemistry of Aeolis Mons. Based on the visible-near infrared spectroscopic imagery of MRO's Compact Reconnaissance Imaging Spectrometer for Mars (CRISM), analysis of the sedimentary layers at the base of Aeolis Mons suggested clay minerals near the base transitioning into sulfate salts further up (Vaniman et al., 2014). The Curiosity rover first studied the environment near its landing site, and observed both clays and sulfate salts in the upper Sheepbed unit of Yellowknife Bay Formation before moving on to its primary targets on Aeolis Mons, as seen in Figure 4 and Figure 5 (Grotzinger et al., 2014; Vaniman et al., 2014). CheMin revealed bassanite and anhydrite but not gypsum, likely due to the lower vapor pressure of water on Mars, as seen in Figure 6 and Figure 7. Bassanite can form in various ways such as alteration of calcium carbonates by sulfuric acid, direct precipitation in fumaroles and a desiccation product of gypsum in hyperarid environments (Gunatilaka et al., 1985; Worku and Parker, 1992; Vaniman and Chipera, 2006; Rapin et al., 2016). Anhydrite converts directly to gypsum in humid environments and is evidence of an environment with a nearly neutral pH (Worku and Parker,

1992; Douglas and Yang, 2002; Mees and De Dapper, 2005; Vaniman et al., 2014). McLennan et al. (2014) used ternary diagrams to illustrate the geochemical relationships between the samples and provided constraints on diagenetic history, as shown in Figure 8.

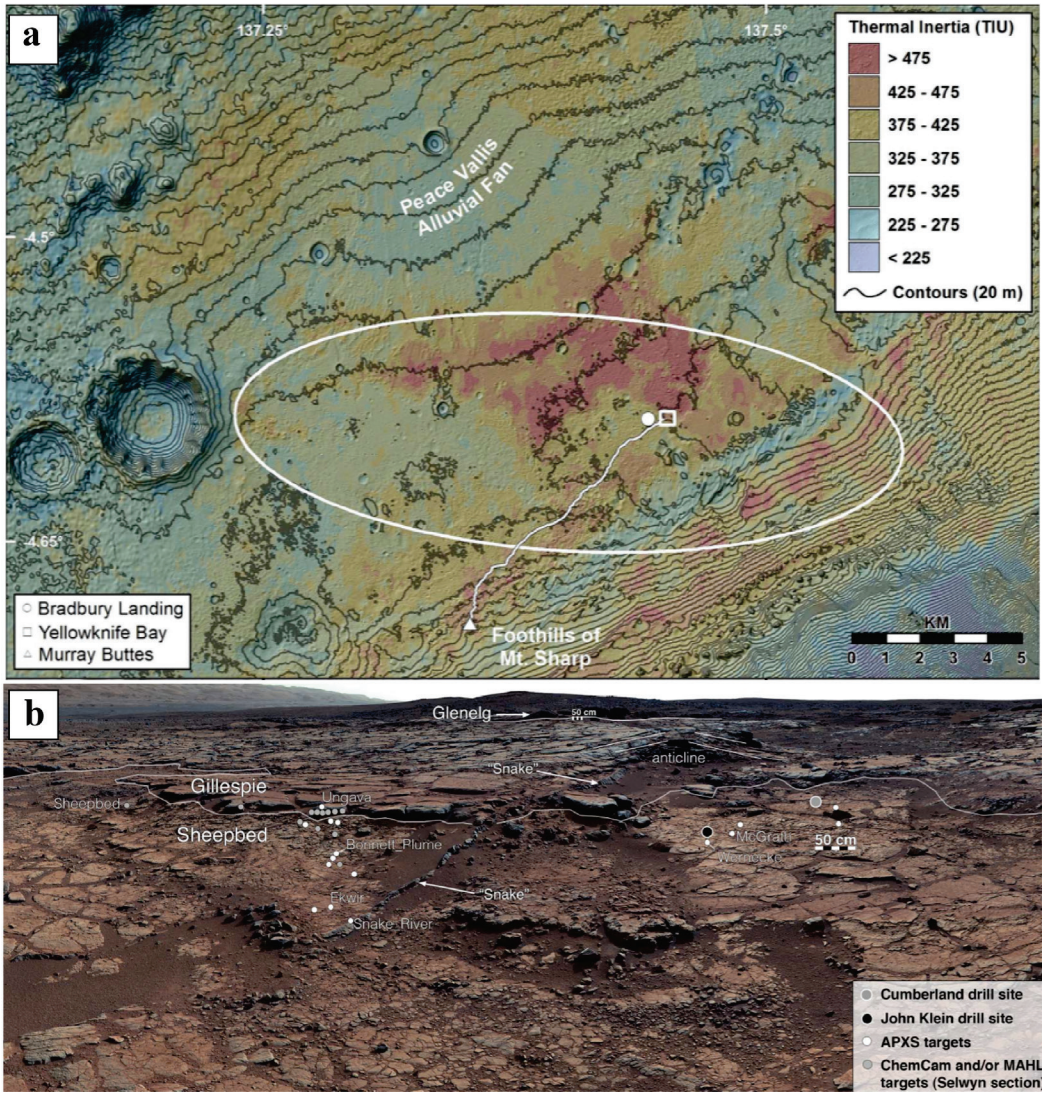

Figure 4: (a) Thermal Inertia regional context map of the valley between Gale crater's rim and the foothills of Aeolis Mons, informally known as Mt. Sharp, (b) Mastcam image of the Yellowknife Bay formation. Adapted from Grotzinger et al. (2014).

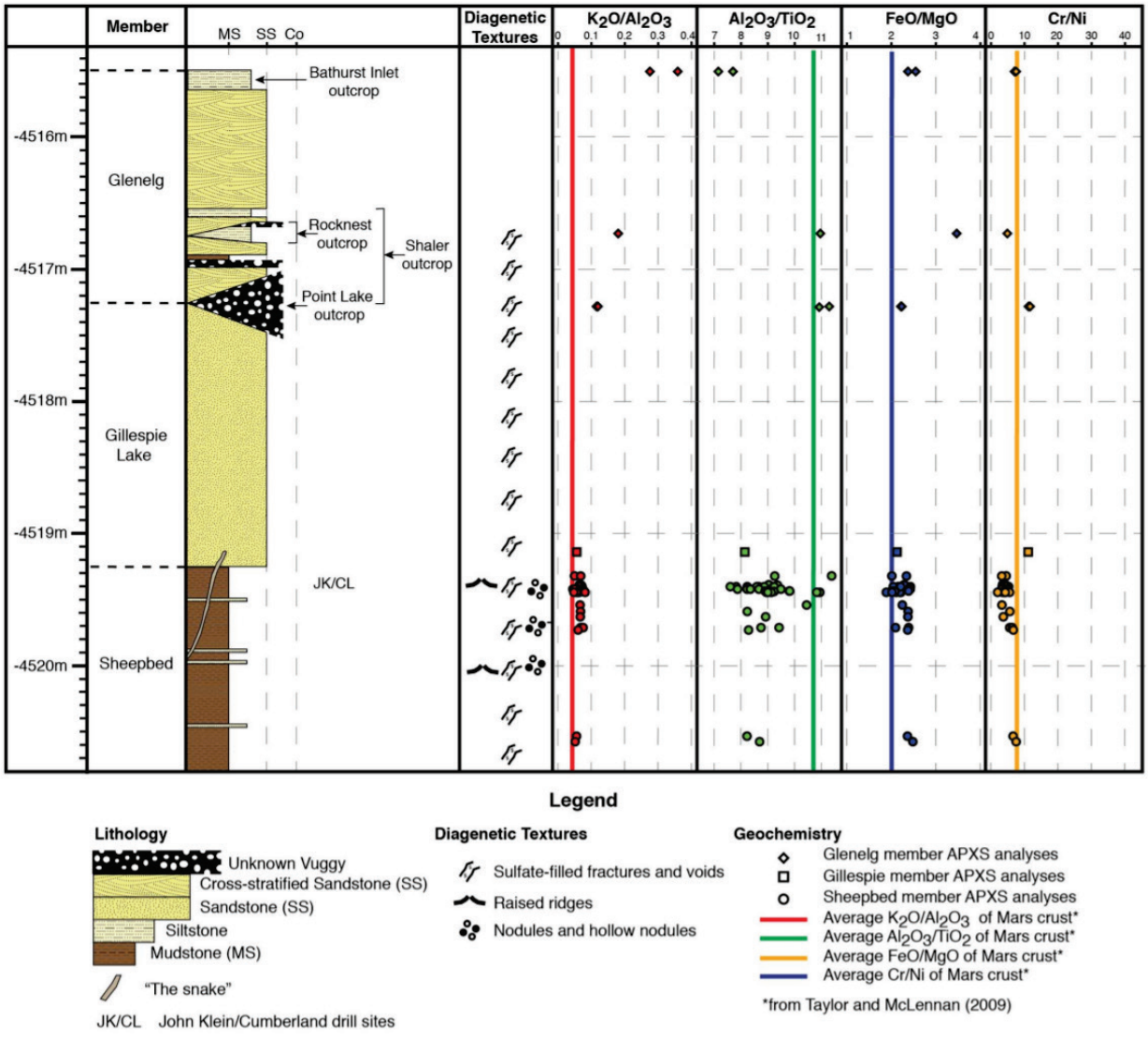

Figure 5: Yellowknife Bay Formation stratigraphic column with diagenetic textures and elemental and oxide ratios measured by Curiority's AXPS instrument (Grotzinger et al., 2014).

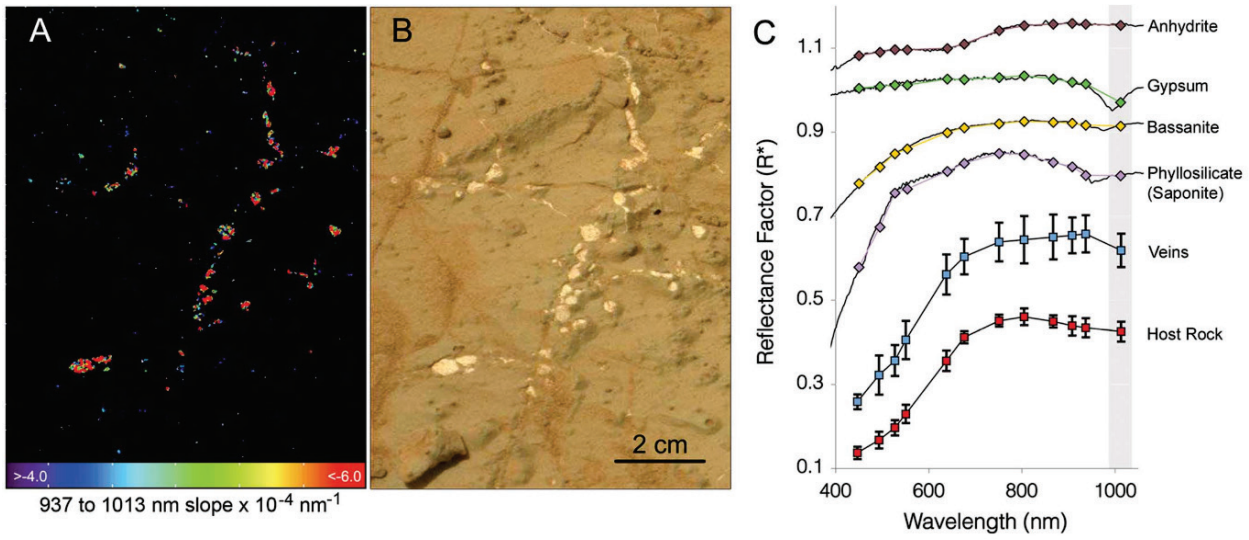

Figure 6: (a) Mastcam spectra, showing possible hydrated minerals, (b) Mastcam color image of (a), (c) Comparison of Mastcam reflectance with laboratory reflectance spectra (Vaniman et al., 2014).

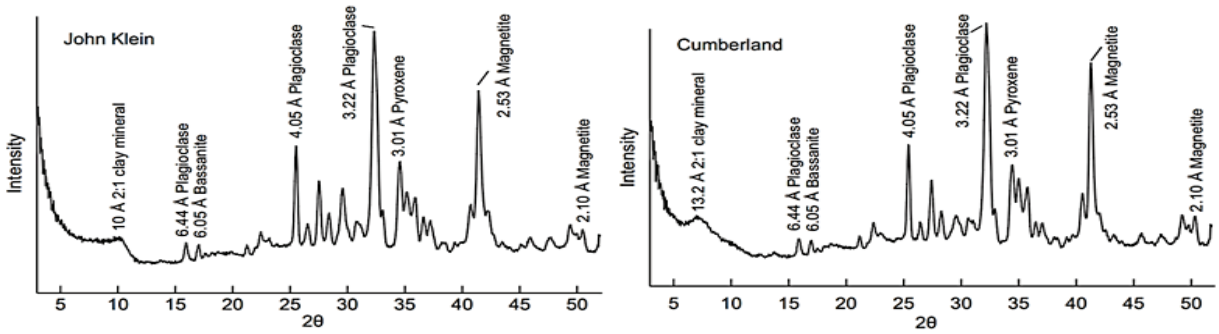

Figure 7: XRD patterns from the Sheepbed mudstone samples of John Klein and Cumberland (adapted from Grotzinger et al., 2014)**.**

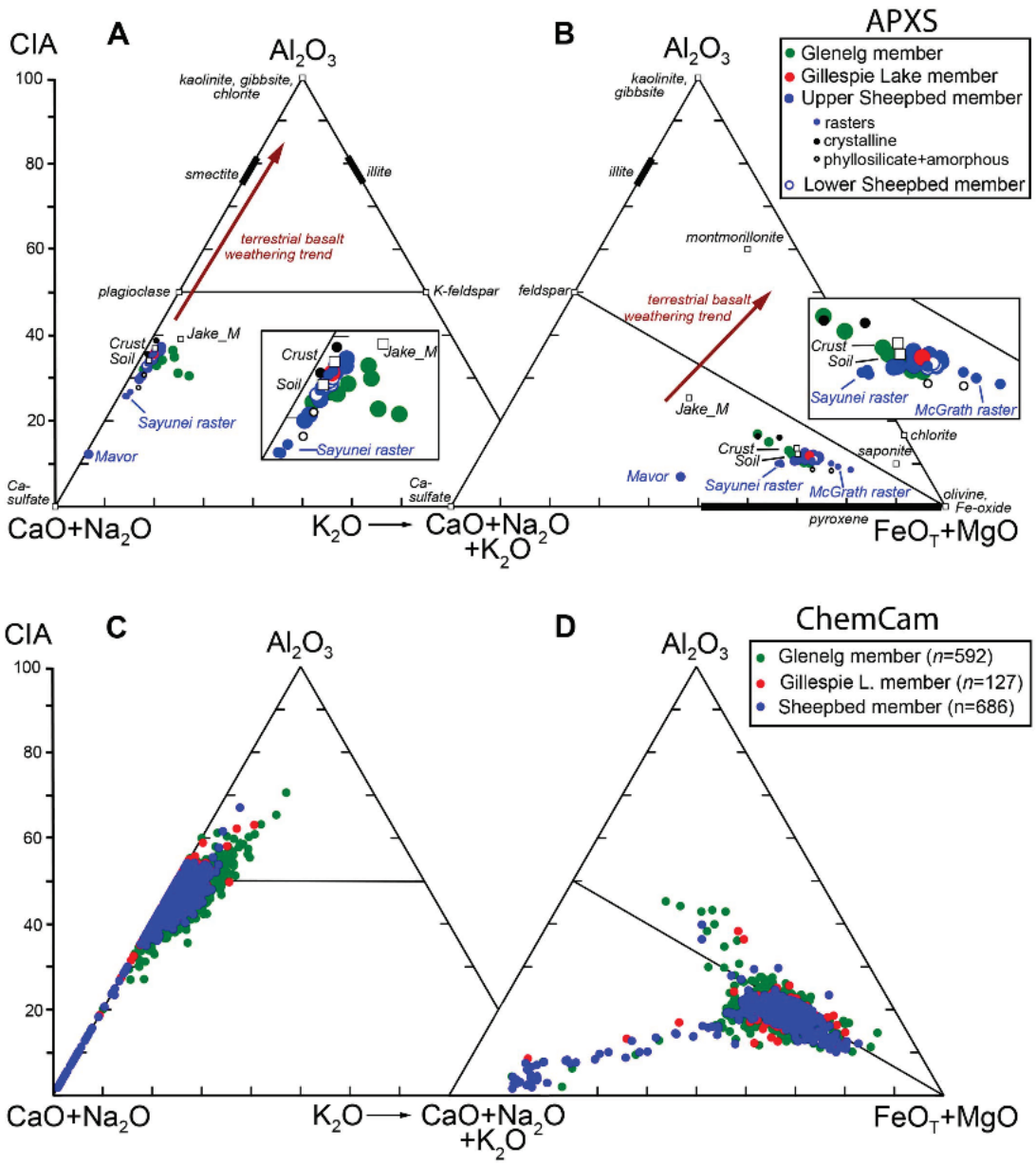

Figure 8: CIA ternary diagrams of Upper Sheepbed, Lower Sheepbed, Glenelg Member, and Gillespie Member revealing chemical weathering upsection in the Yellowknife Bay Formation. (A and B) Using the APXS instrument, the data shows that the Lower Sheepbed and Gillespie Lake rock samples are slightly more mafic than the average Martian crust, while the Upper Sheepbed and Glenelg Members plot more towards the Ca-sulfate endmember. (C and D) Using ChemCam instrument data, this shows an overall linear trend towards the Ca-sulfate end member for the Sheepbed, Gillespie, and Glenelg members. The Glenelg member has less FeO_T (total iron) + MgO and higher K_2O (McLennan et al., 2014).

The chemical weathering history of sediments can be quantitatively evaluated using weathering indices and possibly used as a proxy for paleoclimate. A commonly used weathering index is the Chemical Index of Alteration (CIA), proposed by Nesbitt and Young (1982). The CIA measures the degree of chemical weathering from feldspars to clays. Since this is based on feldspar alteration, it is calculated using the following relationship: $[Al_2O_3/ (Al_2O_3 + K_2O + Na_2O + CaO)] * 100$ (Siebach and McLennan, 2018). The CIA analysis shows the geochemical trends within the Yellowknife Bay Formation at Gale crater on Mars. The low CIA values indicate that the mudstones of Sheepbed and Gillespie Lake Members were likely derived from a slightly more mafic source than the average Martian crust. High-K alkaline igneous rocks of the Glenelg Member seem to be more common on Mars than previously thought, as similar rocks are also observed in Gusev crater (McLennan et al., 2014). Low CIA (30 to 37) values suggest only limited chemical weathering before deposition (Siebach and McLennan, 2018). Milliken et al. (2010) suggest that the transition from clays to the stratigraphically higher sulfates in Gale crater was due to the Noachian-Hesperian climate change.

Using Tecopa as a potential analog for ancient Martian paleolakes, such as at Gale crater, provides the opportunity to understand the transition from a wet to a dry environment. This wet-dry transition in Tecopa can help us observe how climatic change affects the mineralogy, geochemistry, and lacustrine history of a closed basin lake. This paleolake has the authigenic silicates (zeolites and feldspar), phyllosilicates, sulfates, carbonates, and other salts expected in paleolakes and playas, but which are difficult to detect using remote sensing. The lack of evidence for some of these minerals on Mars could be due to their low abundance, spectral masking, or the low spatial resolution of CRISM (Clark, 1999; Bibring et al., 2006; Murchie et al., 2009). This study can help interpret VNIR spectra for paleolakes on Mars by testing how

spectral masking can affect the true signal of certain mineral assemblages. Kodikara et al. (2012) noted similar remote sensing difficulties in mapping evaporite minerals from Lake Magadi, Kenya. Thus, further work is needed for terrestrial analogs to apply VNIR analysis to paleolake sediments and evaporites to help ground truth the orbital and rover data (Milliken et al., 2010).

C. Jezero crater

The geomorphology of Jezero crater was analyzed using the Context Camera (CTX) and High-Resolution Imaging Science Experiment (HiRISE) instruments on the MRO. CRISM was used to study the mineralogy of the two alluvial fans using their visible to near infrared spectral signatures. The deposits in the alluvial fans show aqueous alteration mineral spectral signatures, but these minerals were likely transported into the basin and thus not formed in situ (Goudge et al., 2015b). This paleolake candidate was chosen for the Perseverance rover and the Ingenuity helicopter mission. The goal of the Perseverance rover is to find evidence for possible ancient life and collect rock and soil samples for a future Mars sample return mission. Tecopa is relevant to Jezero crater because it also exposes paleolake deposits. CRISM orbital data revealed carbonates and clay minerals that resemble those of terrestrial playas. The basin samples from Tecopa can serve as a playa analog and serve as ground truth for orbital data and future in situ analysis from the Perseverance rover on Mars.

2.3 Laboratory Instruments

2.3.1 Visible and Near-Infrared Reflectance (VNIR) Spectroscopy

Visible and Near-Infrared Reflectance (VNIR, 350-2500 nm) spectroscopy is the study of light at 350-2500 nm from reflected material being emitted, reflected, or scattered from a solid,

liquid, or gas. In the remote sensing literature, however, VNIR typically refers to the portion of the electromagnetic spectrum that lies between 350-1000nm (Figure 9; Clark, 1999). Our eyes are equipped to see the visible spectrum, where we see these wavelengths as color, however modern spectroscopy observes details over a broader wavelength range, including the infrared (Fang et al., 2018).

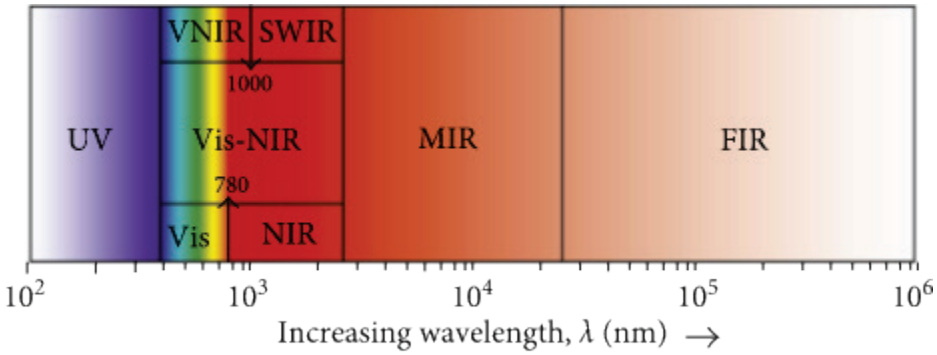

Figure 9: Electromagnetic spectrum between Ultraviolet (UV) to Far-infrared (FIR) (Fang et al., 2018).

Photons can either be reflected, scattered, or emitted, which can be detected and measured by a spectrometer. Several general physical processes generate the absorption pattern in the spectra of minerals: electronic and vibrational transitions. Electronic transitions occur because of the high energy and mobility of ions and atoms. These are caused by crystalline structure effects and the mineralogic composition of the material (Burns and Fisher, 1993; Fang et al., 2018). These variations in crystalline structure and mineralogic composition can cause shifts in the position and shape of absorption bands (Fang et al., 2018). Vibrational transitions occur because of the vibrations in the bonds of crystal lattices or molecules. It is these spring-like vibrations that produce unique features in the VNIR region from the stretching and bending of

molecular bonds like O-H, C-H, C-C, and N-H, such as from phyllosilicates and carbonate minerals (Clark et al., 1990).

This technique has been widely used since it is quick, cost-efficient, nondestructive, and can be used for remote sensing. This same technique is used by MRO, which has studied the Martian atmosphere, along with its surface from orbit since 2006. It is equipped with the CRISM instrument which has been searching for clues of secondary minerals that may have formed in the presence of water.

2.3.2 Laser diffraction in grain sizes

The Malvern Mastersizer 2000 is a laser diffraction particle size analyzer that measures particle sizes in the 0.02 to 2000 micron range. The instrument uses a blue LED and red (633.8-micron wavelength) He-Ne laser and single-lens detection system. The light is diffracted by a sample in solution that circulates through the cell and is measured by 52 sensors. The Malvern Mastersizer 2000 software uses the Mie diffraction theory for the compiled light scattering data. This theory uses the refractive index and adsorption of the dispersed sample material, and the refractive index of the dispersant liquid. Some assumptions to note are that: (1) the particle is mineralogically homogeneous, (2) particles are perfect spheres, (3) the optical properties of the sample and liquid are known, and (4) the dilution in suspension guarantees the measurement of light scattering of one particle before being re-scattered by other particles (Storti and Balsamo, 2010).

3. Methods

3.1 Field Work

I conducted two field expeditions to southeastern California from October 12th to October 20th, 2018 and October 17th to October 25th, 2019 to collect paleolake and modern deposits in the Tecopa valley with research team members, Gayantha Kodikara (PhD Candidate at UW-Milwaukee), Dr Lindsay McHenry, and two undergraduate assistants (Figure 10).

This project sampled two sections of Lake Tecopa beds, exposed Lake Tecopa deposits and a mix of modern surface samples. Section 1 (noted in green) is close to the LT-7 of Larsen (2008) and section 2 (noted in blue) (Figure 11) is close to the LT-9C section of Larsen and Olson (2019). We used these two stratigraphic sections in paleolake Tecopa because the later stages of Lake Tecopa were highly alkaline and saline due to the evaporation which led to the formation of authigenic lacustrine minerals (clays, carbonates and salts), similar minerals that are found on Mars. The tuff beds can be correlated laterally across the central Tecopa basin. Larsen and Olson (2019) correlated the 2.02 Ma Huckleberry Ridge tuff bed and the 1.25 Ma tuff are into the lake basin-center. While the 0.760 Ma Bishop tuff bed is exposed near the lake margins.

A total of 44 surface samples were collected in 2018 (T1 to T44). Samples T13 to T22 were collected from Section 1, which was resampled for paired surface and interior samples in 2019 (T103T to T118B). Samples IDs for the 2019 samples started at T50. For this study, a surface crust sample (sample ID suffix T) was collected, along with a fresh subsurface sample (sample ID suffix B) from the base of a hole dug to a depth of approximately 6 to 8 cm using a trowel (Figure 12). Collected samples were placed into plastic sample bags. Each sample and location were logged in a field notebook and GPS coordinates (EPSG:4326/WGS84) were determined using a Garmin GPSMap 64S.

In 2019, 28 samples (T78(T) to T88(B) and T103T to T118B) were collected from two stratigraphic sections (Sections 2 and 1), based on differences in color, grain size, lithology, and weathering features (Figure 13). Section 1 2019 samples were collected after section 2. An additional 20 samples (T65(T) to T68(B), T73(T), T74(B), T76(T), T77(B), T89(T), T90(B), T93(T), T94(B), T98(T) to T102(B), T119(B), T120(T), T121(B)) were collected for this study from flatter areas across the basin surface, with clay, silt or evaporite surface crusts (see Figure 10). See Appendix A Table 4 for sample collection locations, used for this study.

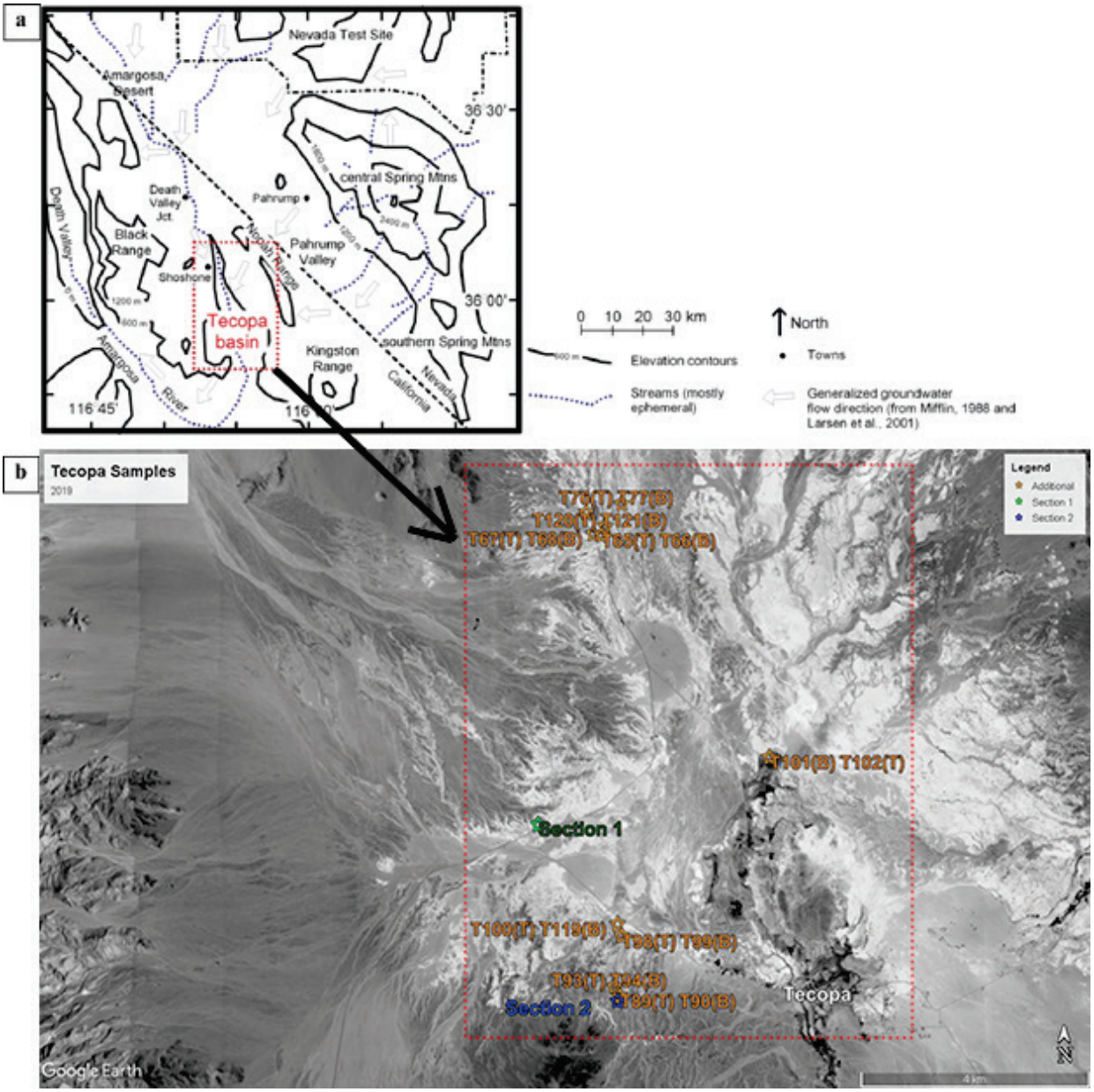

Figure 10: (a) Modified map of the Tecopa basin in California and surrounding regions from Larsen (2008), (b) Google Earth map of samples from section 1, section 2, and additional samples.

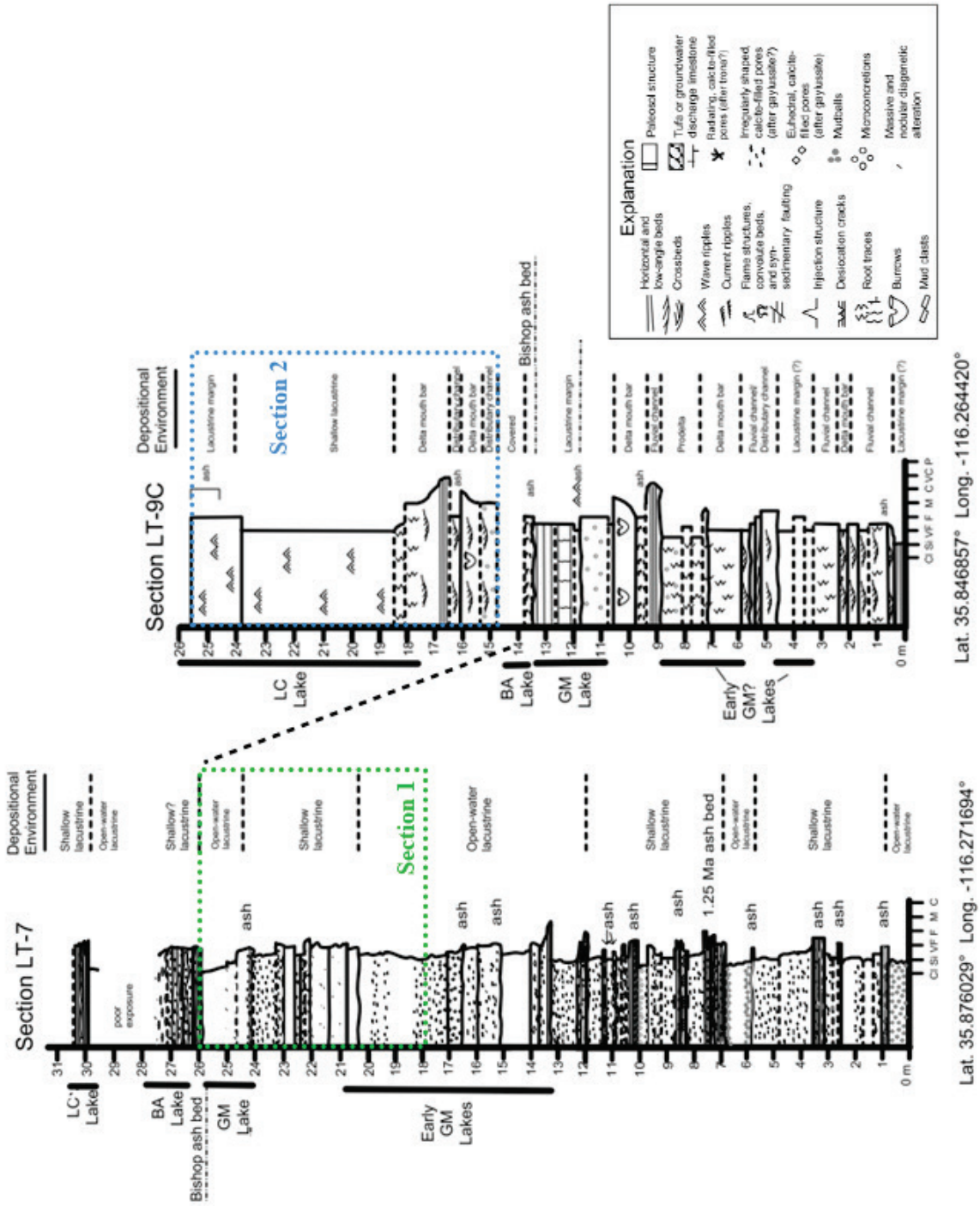

Figure 11: Stratigraphic column for sections 1 and 2 from Lake Tecopa. Modified from Larsen and Olson (2019). The green and blue rectangles represent the intervals that were sampled within these stratigraphic columns. Section 1 represents open-water to shallow lacustrine and Section 2 is the lake margin. The Bishop ash bed caps Section 1 in this study, while it is below Section 2.

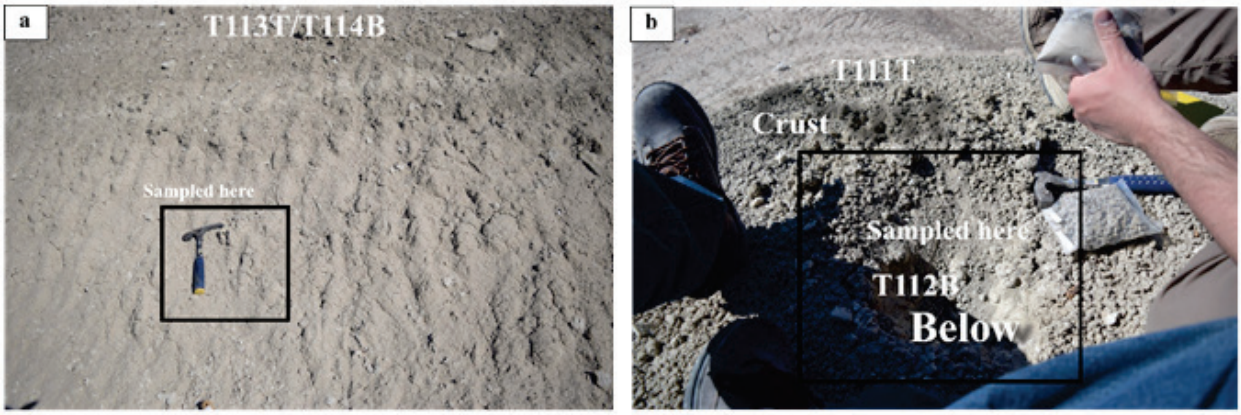

Figure 12: (a) Close-up view of T113T (crust) and T114B (subsurface) samples from the middle of section 1, (b) close-up view of T111T (crust) and T112B (subsurface) from the middle of section 1. Hammer is 32 cm long.

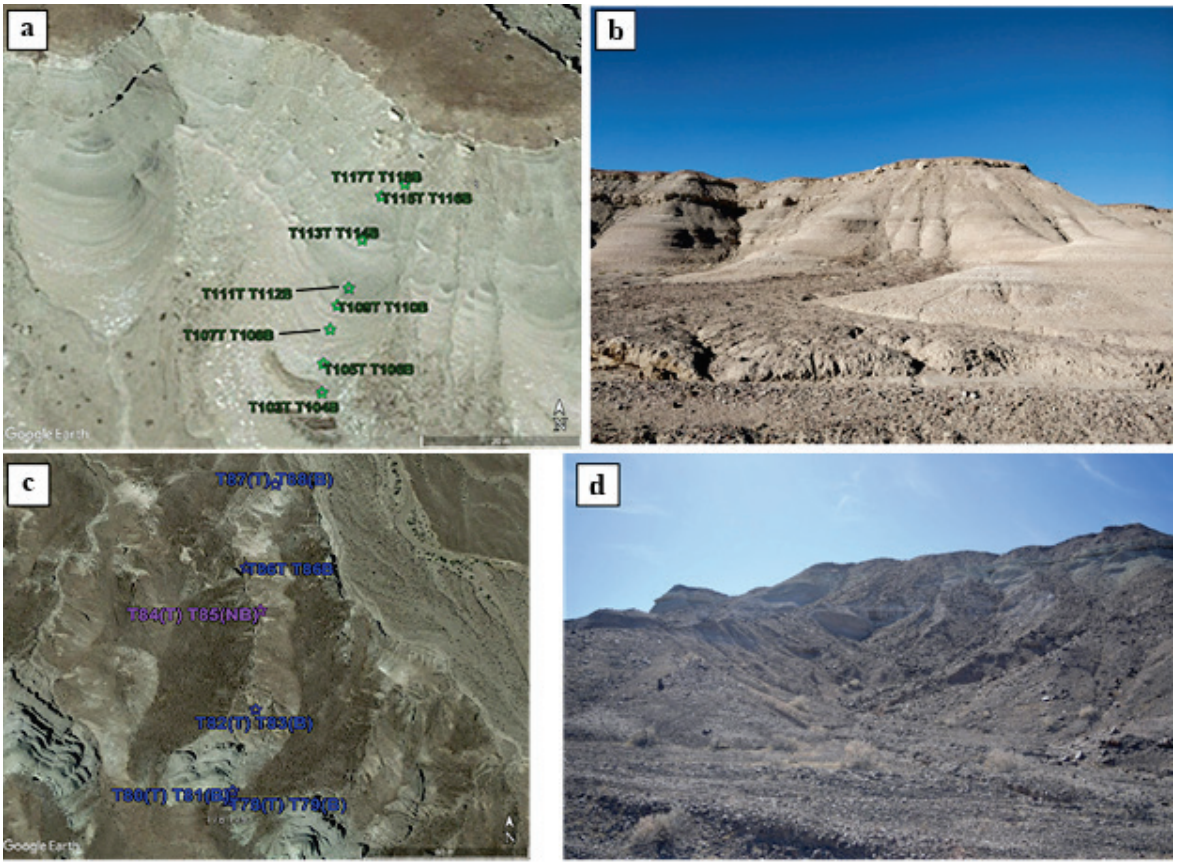

Figure 13: (a) Google Earth map of section 1 samples, (b) sideview photo of section 1, (c) Google Earth map of section 2 samples, and (c) sideview photo of section 2.

3.2 X-Ray Methods

3.2.1 X-Ray Diffraction (XRD) Analysis

Mineralogical analyses were conducted by X-Ray Powder Diffraction (XRD) using a Bruker D8 Focus instrument at the Department of Geosciences at the University of Wisconsin-Milwaukee. All samples were hand crushed into a fine powder using an agate pestle and mortar. Approximately 1 gram of each sample was placed into a plastic cavity mount sample holder and leveled with a razor blade. Samples were analyzed by XRD for a 2-theta range of 2° to 60° with a step size of 0.02° and a one second count time, a scintillation detector, a divergence slit of 0.6 mm, and a total of 2900 steps. The copper tube was set to 40kV and 40mA for all samples. Minerals in each sample were determined by comparing the diffraction patterns against the International Centre for Diffraction Data PDF-2 2006 database. Relative abundances were estimated visually. Pattern matches were informed by previous mineral assemblage studies of the Tecopa beds, nearby playas, and mineral occurrences in other arid regions. Raw smooth scans of surface and subsurface samples from the bottom, middle, and top of each section were converted to xy files using Profex 4.3 and imported into OriginLab OriginPro 2021b for graphing.

3.2.2 X-Ray Fluorescence (XRF) Analysis

Bulk geochemical analysis was conducted by X-Ray Fluorescence (XRF) using a Bruker S4 Pioneer instrument at the Department of Geosciences at the University of Wisconsin-Milwaukee. All samples were hand crushed into a fine powder using an agate pestle and mortar and transferred to glass vials. Each vial was dried overnight in a 105°C oven to remove moisture. Loss on Ignition was determined for each sample by weighing ~1 g of each sample into a pre-

ignited and weighed crucible, igniting it in a muffle furnace at 1050°C for 15 minutes, then cooling in a desiccator for 5 minutes before weighing and calculating the amount lost.

Approximately 1 gram of Ammonium Nitrate, 11 grams (+/- 0.003 g) of Claisse 50:50 LiT:LiM flux with an integrated LiBr non-wetting agent and 1.1 grams (+/- 0.003 g) of powdered sample were combined and transferred to a platinum crucible. The mixtures were fused at ~1050° C using a ~20-minute routine in a Claisse M4 fluxer (methods of Byers et al., 2016). Each disk was analyzed for major, minor and trace elements using a Bruker S4 Pioneer WD-XRF spectrometer. Concentrations were calculated using a calibration based on eleven USGS igneous and sedimentary rock standards (McHenry, 2009; Byers et al., 2016). Only elements for which the calculated concentrations exceeded twice the lower limit of detection (LLD) and with analytical errors of less than 2% (for major elements) or 12% (for trace elements) are reported for each sample, otherwise it is noted as "Not Detected (ND)." In this study, the major oxides of SiO_2, Al_2O_3, K_2O, Fe_2O_3, CaO, Na_2O, MgO, TiO_2, P_2O_5 (weight %) and trace elements Zr, Sr, and Ba (ppm) were used for examining bulk geochemical differences between soil crust and subsurface samples and relevant weathering calculations. TiO_2 (weight %) versus Al_2O_3 (weight %) and Zr (ppm) versus TiO_2 (weight %) were plotted in OriginLab OriginPro 2021b. The possible parent rock type based on TiO_2 (weight %) versus Al_2O_3 (weight %) was interpreted using the methods of Xu et al. (2020), which was adapted from Girty et al. (1996), while Zr (ppm) versus TiO_2 (weight %) was interpreted using Hayashi et al. (1997).

3.3 Weathering Calculations

Weathering indices were used for the XRF data to interpret weathering trends as a paleoenvironment proxy as discussed in (Sheldon and Tabor, 2009). The Chemical Index of Alteration (CIA), Plagioclase Index of Alteration (PIA), Weathering Index of Parker (WIP), Index of Compositional Variability (ICV), Chemical Proxy of Alteration (CPA), and weathering ratios were used to group the sediment samples, see Table 1. These calculations can be used to determine weathering rates and characterize the chemical and physical weathering of soils (Cox et al., 1995; Ohta and Arai, 2007; Sheldon and Tabor, 2009; Buggle et al., 2011; Le Blond et al., 2015; Perri, 2020). Weathering ratios and indices provide information about possible pedogenic processes and quantify, the amount of chemical weathering, if any (Yousefifard et al., 2012).

The base loss ratio was calculated using [$(CaO + MgO + K_2O + Na_2O)/TiO$], where the abundance of the titanium is divided by the abundance of the bases. A high value indicates a greater amount of leaching of bases relative to aluminum. Clayeyness (C) was calculated using Al_2O_3/SiO_2, a higher value indicates clay formation because clay minerals have an elevated abundance of aluminum (Retallack, 2008). Hydrolysis (H) was determined using [$Al_2O_3/(CaO + MgO + K_2O + Na_2O)$], which is based on the idea that bases are lost during chemical weathering compared to Al, resulting in the formation of clay (Sheldon and Tabor, 2009). BasesAl (1/H) is the reciprocal of Hydrolysis (H). Salinization was determined using [$(Na_2O + K_2O)/Al_2O_3$], where higher values indicate that alkali elements are accumulating as soluble salts (Sheldon and Tabor, 2009). Calcification was calculated using [$(CaO + MgO)/Al_2O_3$], where a greater value indicates a higher concentration of carbonate minerals. Leaching (L) was calculated using the ratio of [Ba/Sr], where hydrolysis or leaching is strong when the ratio is greater than 10. Ba and Sr have similar atomic radii but Sr is more soluble than Ba (Vinogradov, 1959).

Weathering Indices and Ratios	Formula	Pedogenesis and Notes
Major elements		
Chemical Index of Alteration (CIA)	$[Al_2O_3/(Al_2O_3 + K_2O + Na_2O + CaO^*)] \times 100$	< 50 is fresh Ig Rx, 100 is fully weathered
Chemical Index of Weathering (CIW/CIA-K)	$[Al_2O_3/(Al_2O_3 + Na_2O + CaO^*)] \times 100$	Like CIA but has an enrichment problem.
Plagioclase Index of Alteration (PIA)	$[(Al_2O_3 - K_2O)/(Al_2O_3 + CaO^* + Na_2O - K_2O)] \times 100$	100 is completely altered materials
Weathering Index of Parker (WIP)	$[CaO^*/0.72 + 2\times Na_2O/0.35 + 2\times K_2O/0.25 + MgO/0.9] \times 100$	Low values reflect intense weathering conditions
Index of Compositional Variability (ICV)	$[(Fe_2O_3^* + K_2O + Na_2O + CaO^* + MgO + MnO + TiO_2)/Al_2O_3]$	> 1 are compositionally immature (first cycle of sediments deposited)
Chemical Proxy of Alteration (CPA)	$[Al_2O_3/(Al_2O_3 + Na_2O)] \times 100$	Measures the rate of weathering for silicates in a soil profile, like CIA with a check for approx. CaO*
Base Loss	$[(CaO + MgO + K_2O + Na_2O)/TiO]$	Leaching, greater with smaller base values
Clayeyness (C)	$[Al_2O_3/SiO_2]$	Hydrolysis, <0.1 normal, >0.3 strong
Hydrolysis (H)	$[Al_2O_3/(CaO + MgO + K_2O + Na_2O)]$	Higher values reflect intense weathering conditions
BasesAl (1/H)	$[(CaO + MgO + K_2O + Na_2O)/Al_2O_3]$	Lower values reflect intense weathering conditions
Calcification	$[(CaO + MgO)/Al_2O_3]$	Calcification (Ca, Mg into the subsurface), <1 normal, >10 strong
Salinization (S)	$[(Na_2O + K_2O)/Al_2O_3]$	Salinization (Ca, Mg into the subsurface), <2 normal, >1 strong
Trace elements		
Leaching (L) Ba/Sr	[Ba/Sr] ratio	Hydrolysis or Leaching, >10 strong

Table 1: Weathering Indices, the corresponding formula and possible pedogenesis, based on Fedo et al. (1995), Retallack (2008), Sheldon & Tabor (2009), Buggle et al. (2011), Baiyegunhi et al. (2017) and Perri (2020). CaO* represents the CaO content that is contained only in the silicate fraction. ICV was modified to use CaO*, as Cox et al. (1995) used samples with less than 5 wt% CaO. Fe_2O_3* is total iron, reported as Fe_2O_3.

The mole fraction was calculated using the molecular proportion of the elemental oxides which were obtained by dividing the weight percentage (XRF data) of each major oxide by the average molecular weight of the oxide. Trace elements were converted from raw abundances into moles by dividing ppm by the molecular mass (Sheldon and Tabor, 2009). Major elements were normalized with respect to Al and Ti and analyzed for gain or loss in the concentration of these major elements, when compared the subsurface sample to the surface sample.

The Index of Compositional Variability (ICV) was modified to use CaO*, since the Cox et al. (1995) study included only samples with less than 5 wt% CaO while the current study has more carbonate-rich samples. The Chemical Index of Alteration, Chemical Index of Weathering, Plagioclase Index of Alteration, and Weathering Index of Parker also use CaO*. CaO* represents the CaO content contained only in the silicate fraction, and it is necessary to make a correction to the measured CaO content to account for the presence of Ca in carbonates (cc = calcite and dol = dolomite) and phosphates (ap = apatite) using equation 1.

Eq 1. $CaO^* = \text{mol CaO} - \text{mol } CO_2(cc) - (0.5 \times \text{mol } CO_2)(dol) - 10/3 \text{ mol } P_2O_5(ap)$ (Fedo et al., 1995)

Since $[CO_2]$ from each carbonate is unknown, an approximate CaO* correction can be made by assuming reasonable Ca/Na ratios (less than 1) in silicate material as described by McLennan (1993) and using equation 2 to adjust for phosphates.

Eq 2. $CaO^* = \text{mol CaO} - 10/3 \text{ mol } P_2O_5(ap)$ (McLennan, 1993)

If CaO* is greater than mol Na_2O, after the phosphate calculation above and the sample does not contain halite (checked using XRD), then the approximate CaO* from equation 2 is discarded and equation 3 is used (McLennan, 1993).

Eq 3. CaO* = mol Na_2O

Since CaO* is uncertain, this study also uses the Chemical Proxy of Alteration (CPA) index which is a CaO*-free version of the Chemical Index of Weathering (CIW). This was used to check that the apparent weathering rates given by the other indices (since calcite and halite are easily dissolved or precipitated, which can skew the results, see Figure 14) are representing the true silicate weathering rate and provide a measurement for the degree of degradation of the feldspars (Buggle et al., 2011).

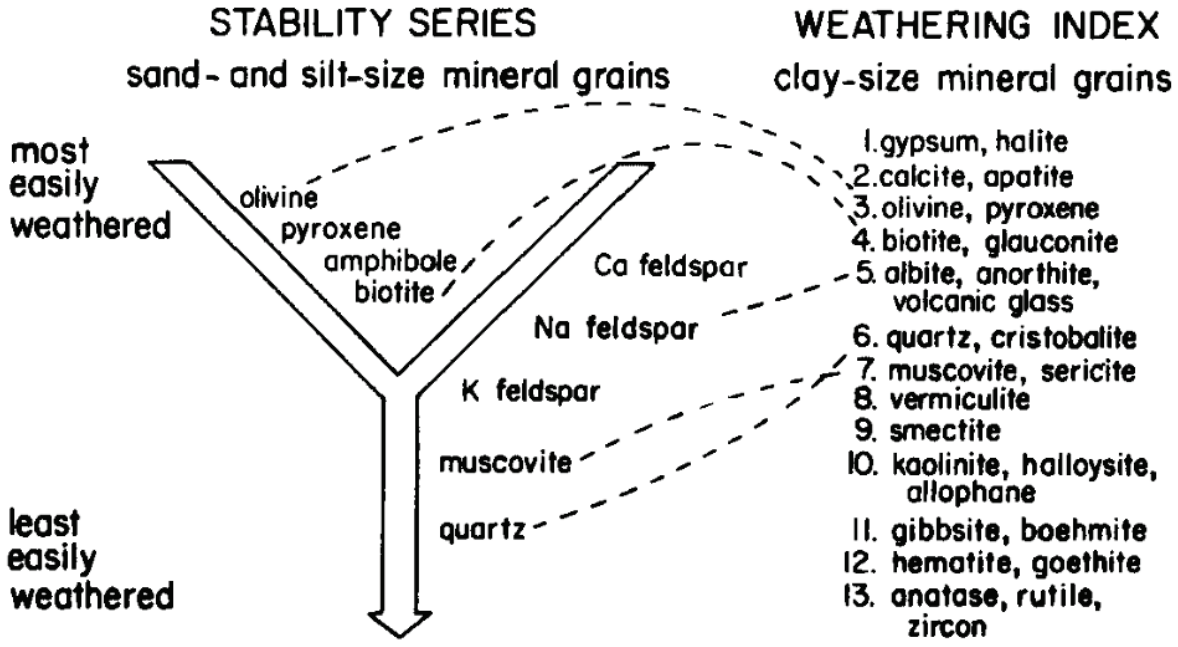

Figure 14: Relative stability of mineral grains upon weathering conditions (Retallack, 2008).

Ternary diagrams showing the molecular proportions of A-CN-K and A-CNK-FM were created using OriginLab OriginPro 2021b. These diagrams were used to interpret CIA and compare the results to the Yellowknife Bay Formation and possible weathering trends (Nesbitt and Young, 1982).

3.4 Visible and Near-Infrared Reflectance (VNIR) Spectroscopy Analysis

In this study, 45 powdered samples were analyzed by laboratory VNIR spectroscopy at the University of Colorado Boulder in the laboratory of Dr. Thomas McCollom using a high-resolution reflectance TerraSpec HALO spectrometer from Analytical Spectral Devices (ASD), Inc. All samples were sieved with a #100 mesh sieve and any larger grains were hand crushed using an agate pestle and mortar to less than 150 microns (Vane and Goetz, 1988). Each powdered sample was spread out on a piece of filter paper and the ASD instrument was placed a few millimeters above the powder. ASD HaloManager software version 2.4 was used to acquire the Visible and Near-Infrared Reflectance (VNIR) spectra from each sample, which was analyzed 3 times and averaged. Using the mineral assemblages present in the XRD results for the Tecopa samples, select reference mineral spectra from the USGS Spectral Library Version 7 were convolved to ASD (Analytical Spectral Devices) standard resolution and full range (see Appendix K). Reference mineral spectra were selected based on the reference sample description, spectral purity, and XRD and XRF results.

The reference and Tecopa spectra were imported into OriginLab OriginPro 2021b. The Tecopa mineral spectra were treated to eliminate unwanted noise and the signal-to-noise ratio was enhanced using a Savitzky-Golay (SG) smoothing algorithm (Stenberg et al., 2010; Fang et

al., 2018), set with the parameters of a 4th polynomial order and 67 points of window as recommend by Chen et al. (2013). The results were compared to the raw spectra and the signal integrity was verified. A 2nd derivative was performed on the reflectance to find hidden signals. The Peak Analyzer was used to find peaks, using a baseline of y=0, a peak finding setting of method of local maximum, positive direction, 2 local points and peak filtering by height percent method and a threshold height of 3 percent.

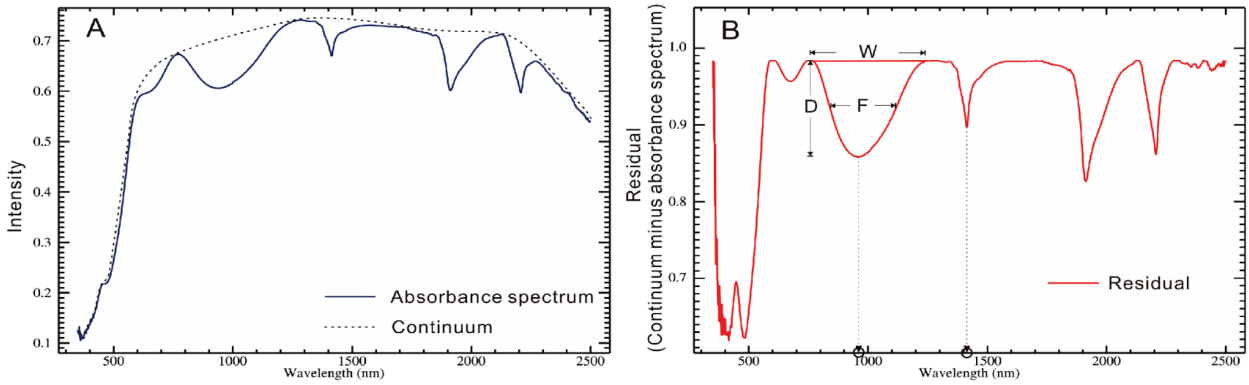

Figure 15: (A) Example of reflectance VNIR spectrum and corresponding continuum; (B) the residual spectrum from A and spectral parameters of Depth (D), full width at half maximum (F), and width (W), modified from Zhao et al. (2020).

The baseline tool in the Peak Analyzer was used on the smoothed data to fit a continuum line over the spectrum. The absorption band depth (continuum-removed spectrum) was calculated by dividing the original spectrum by the continuum line. Figure 15 (A) is an example of a continuum line and residual spectrum after the continuum is removed. Both the Tecopa and reference mineral spectra were processed to remove the continuum (CR), leaving the normalized residual.

Local features were examined for Depth (D), full width at half maximum absorption (F), and width (W), see Figure 15 (B). The Peak Analyzer was used to find and analyze absorption peaks, with a baseline of Y=1, a peak finding setting of method of local maximum, negative direction, 2 local points and peak filtering by height percent method and a threshold height of 1 percent. The absorption band depth of Tecopa spectra was compared between samples and the reference mineral spectra.

3.5 Grain Size Analysis

Grain size analysis was conducted using a Malvern Mastersizer 2000 and Hydro 2000MU wet sample dispersion unit. A 2 gram specimen was randomly selected from each sample and sieved through a #10 2 mm sieve. None of the specimen had 2 mm or greater sized material. 50 grams of Sodium Metaphosphate was slowly added to 1000 mL of deionized water in a beaker and stirred for 4 hours with a magnetic mixer.

The Wentworth grain size class system was used in this study to differentiate between the various grain sizes of the Tecopa samples (Figure 16). A small scoop of each sample was placed onto a sheet of paper and examined. If it felt smooth, sticky, and powdery, then it was determined to be clay sized. If it felt gritty, then it was determined to be silt sized. If it felt coarse and gritty, then the sample would be fine-grained sand. Approximately 0.1 grams of sample for clay size particles, 0.25 grams of sample for silt size particles and 0.5 grams of sample for fine sand size particles was placed in a 125 mL beaker with 20 mL of Sodium Metaphosphate solution for 24 hours.

The Hydro 2000MU was set with a pump speed of 1400 and the Malvern Mastersizer 2000 was calibrated using deionized water. The mixture was placed into a beaker with 600 mL

of deionized (DI) water. Great care was taken to reduce bubbles from being introduced and biasing the results. The Hydro 2000MU was switched off briefly to allow trapped air to escape the system. The diluted mixture was mixed using the Hydro 2000MU's ultrasonic for 60 seconds. The diluted mixture was measured three times using the Malvern Mastersizer 2000. The laser obscuration must be between 2 to 20 percent and ideally with a 15 percent or greater obscuration. The Malvern is rinsed three times with DI water between each run. Grain size was used to determine how physical weathering or other processes are affecting the surface crust.

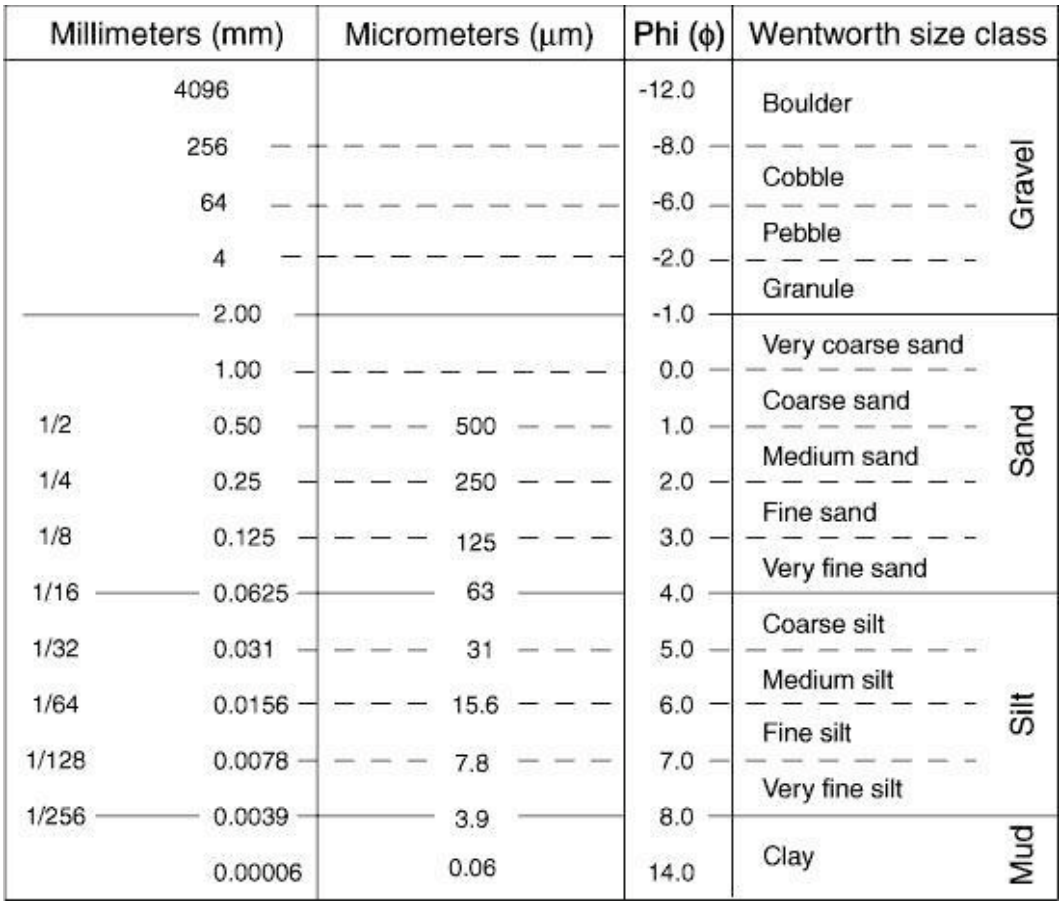

Figure 16: The Wentworth sediment grain size classification system (Wentworth, 1922).

4. Results

4.1 Field observations

The deposits from the two stratigraphic sections of the Pliocene-Pleistocene Lake Tecopa beds include a variety of mudstone, siltstone, sandstone, and volcanic ash. Most of the samples are located along the central to southwestern parts of Tecopa and Tecopa Hot Springs (Figure 10). Section 1 is dominated by mudstone, siltstone, and white colored altered volcanic ash beds. Desiccation cracks were observed on top of the mudstones, which suggests drying. The presence of calcareous crusts on these deposits is consistent with leaching from saline-alkaline paleolake beds under semi-arid conditions. Section 2 is dominated by mudstone, sandstone, siltstone, and white to green colored altered volcanic ash beds. In this section, calcareous crusts were observed in the middle of the section with desiccation cracks in the lower section. At the bottom of section 1, layers of yellow, white, brown, and gray silty mudstones to fine siltstones alternate, along with a carbonate cement (Appendix C Figure 49). At the middle of section 1, alternating yellow-white fine-grained silt to mud samples were collected. Towards the top of section 1, a brown-grey ash along with dark white to white silty samples were collected. At the bottom of section 2, a well-sorted and fine-grained sediment with a popcorn weathering texture at the surface was sampled (Appendix C Figure 50). Around the middle of section 2, grain size increases from silt to very fine sand. At the top of section 2, a white to green tuff on the surface (T78(T)) along with a distinct brown color subsurface soil (T79(B)) were sampled. The additional samples from the modern basin include materials with orange colored mudcracks, popcorn weathering textures, and evaporite crusts at the surface (Figure 17). Most of the subsurface samples from the modern basin are silty to very fine-grained sand.

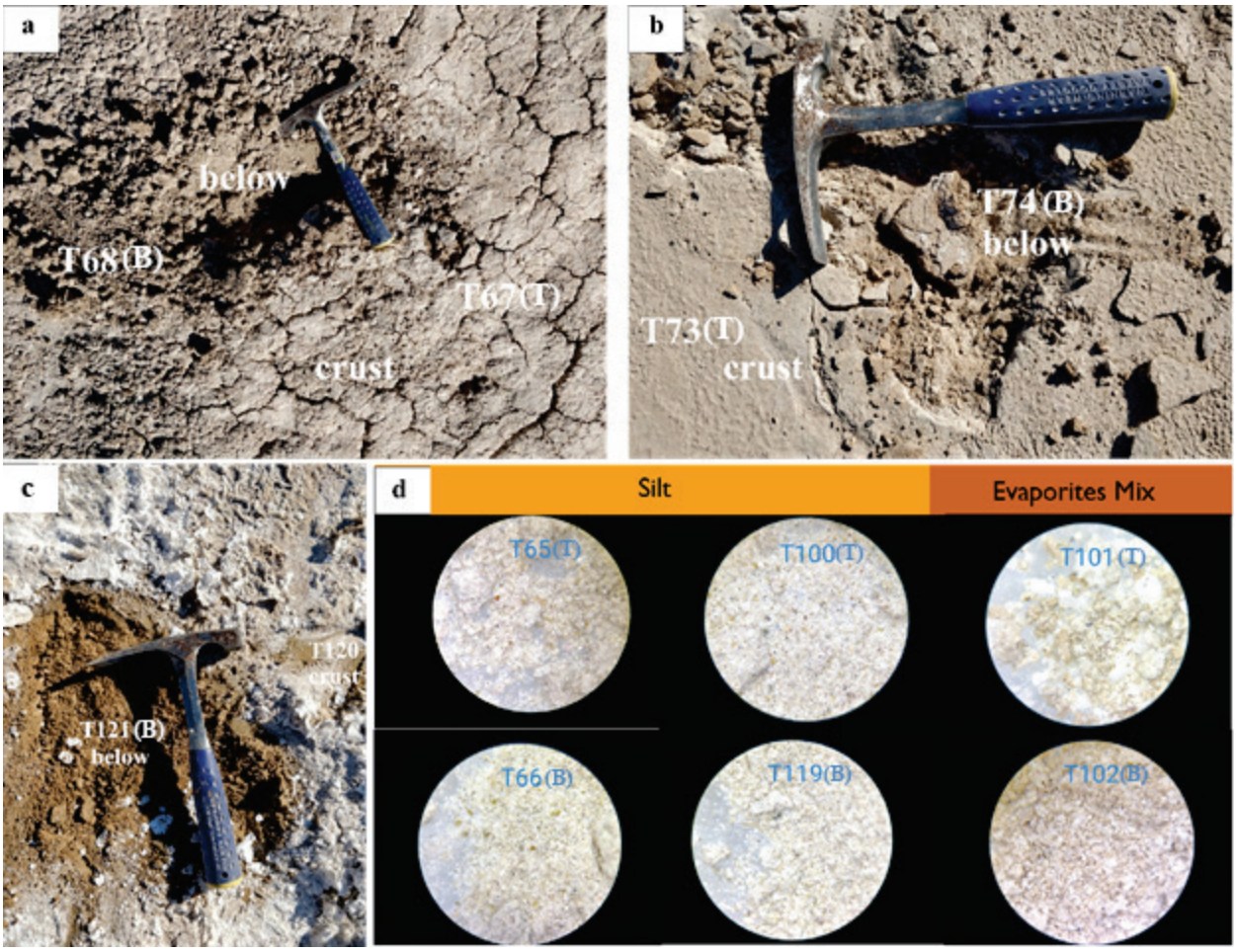

Figure 17: (a) View of T67(T) (crust) and T68(B) (subsurface) samples from an additional Tecopa paleolake bed, (b) view of T73(T) (crust) and T74(B) (subsurface) samples from the modern basin, (c) view of T120(T) (crust) and T121(B) (subsurface) samples from the modern basin. Hammer is 32 cm long. (d) 10X stereoscopic microscope view of select samples from the modern basin

4.2 X-Ray Methods Results

4.2.1 X-Ray Diffraction (XRD)

The mineral assemblages of the forty-eight samples from Tecopa are summarized in Appendix G Table 12 to Table 14. The tables were divided by mineral group: carbonates, tectosilicates, phyllosilicates, inosilicates, halides, and oxides. Each sample site was paired with a top (surface/crust) sample and bottom (subsurface) sample (except T84(T) and T85(NB)) to

denote any differences in minerals within the section. T84(T) was a single surface sample and T85(NB) was the calcareous nodules without the matrix from the subsurface. Select paired samples from each section were compared in more detail to identify mineralogical differences, see Figure 18 and Appendix I Figure 54 to Figure 57.

The mineral assemblage of the first stratigraphic section (Appendix G Table 12) is dominated by calcite, K-feldspar, albite (but with no albite at the bottom of the section), and illite, while smectite is present in lower amounts in T117T, T118B, T109T, T110B, T105T and trace levels in T103T and T104B. Trace amounts of quartz, amphibole, and searlesite were observed in some XRD patterns (Appendix J Figure 58 to Figure 73). The white-sandy powder samples (T105T, T106B, and T104B) contain halite towards the bottom of the section, which is not seen in the middle or top of the section.

Surface sample T115T and the corresponding subsurface sample T116B near the top of Section 1 are mineralogically distinct, likely because of sheet flow. The surface sample has a higher relative abundance of dolomite compared to the subsurface sample. The subsurface sample contains the zeolite mineral analcime, while the surface sample does not. Samples T115T and T116B have similar relative abundances of smectite, illite, searlesite, K-feldspar, and albite (Appendix I Figure 54). Near the middle of Section 1, paired samples T109T and T110B had only minor mineral abundance differences. Surface sample T109T has a higher relative abundance of amphibole compared to subsurface sample T110B. Samples T115T and T116B have similar relative abundance of montmorillonite, illite, searlesite, K-feldspar, and albite (Figure 19). At the bottom of the section, paired samples T105T and T106B have mineralogical differences like the top of Section 1, likely caused by sheet flow. Samples T105T and T106B

have similar relative abundances of illite, K-feldspar and halite. Surface sample T105T contains smectite and amphibole, which subsurface sample T106B lacks (Appendix I Figure 55).

The mineral assemblages obtained from the twelve samples from section 2 are summarized in Appendix G Table 13. The mineral assemblage of the second stratigraphic section is dominated by calcite, quartz, K-feldspar, and albite. Trace amounts of zeolites (analcime, clinoptilolite, and/or phillipsite) along with amphibole are also observed. Illite and smectite are mainly present in lower amounts as well (Appendix J Figure 74 to Figure 85). Significantly different relative mineral abundances are observed between surface and subsurface samples. It is likely that the surface of the whole section has been overprinted by a mixture of sheet flow, caliche (duricrust) from carbonate accumulation on the surface, and wind transport. Near the top of section 2, surface sample T78(T) lacks amphibole, albite, and hematite compared to subsurface sample T79(B). T78(T) and T79(B) have similar relative abundances of illite, calcite, and clinoptilolite.

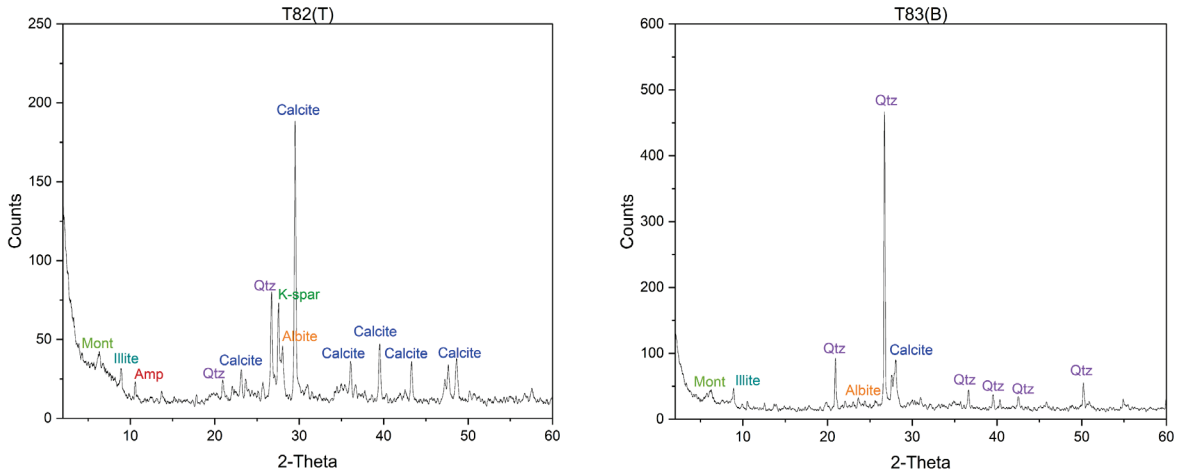

Figure 18: XRD patterns for samples T82(T) and T83(B), showing a higher abundance of calcite (dark blue) on the surface, compared to the subsurface, which has a higher abundance of quartz (purple).

Surface sample T78(T) has a lower relative abundance of quartz compared to subsurface sample T79(B) (Figure 20). Near the middle of section 2, subsurface sample T83(B) lacks calcite, K-feldspar, and amphibole, compared to surface sample T82(T). Both samples contain similar relative abundance of illite, smectite, and albite. Surface sample T82(T) has a lower relative abundance of quartz compared to subsurface sample T83(B). Near the bottom of Section 2, surface sample T86T lacks the zeolite minerals clinoptilolite and phillipsite compared to subsurface sample T86B. Both samples contain similar relative abundances of the zeolite mineral analcime, smectite, quartz, calcite, and albite. Surface sample T86T has a higher relative abundance of illite compared to subsurface sample T86B (Appendix I Figure 57).

Additional samples from the modern basin and Tecopa paleolake beds are summarized in Appendix G Table 14. Their mineral assemblages are also dominated by calcite, quartz, K-feldspar, and albite. The following minerals are present in lower amounts: dolomite, illite, and smectite. Trace amounts of zeolites minerals (analcime, clinoptilolite, and phillipsite) along with amphibole are observed (Appendix J Figure 86 to Figure 105).

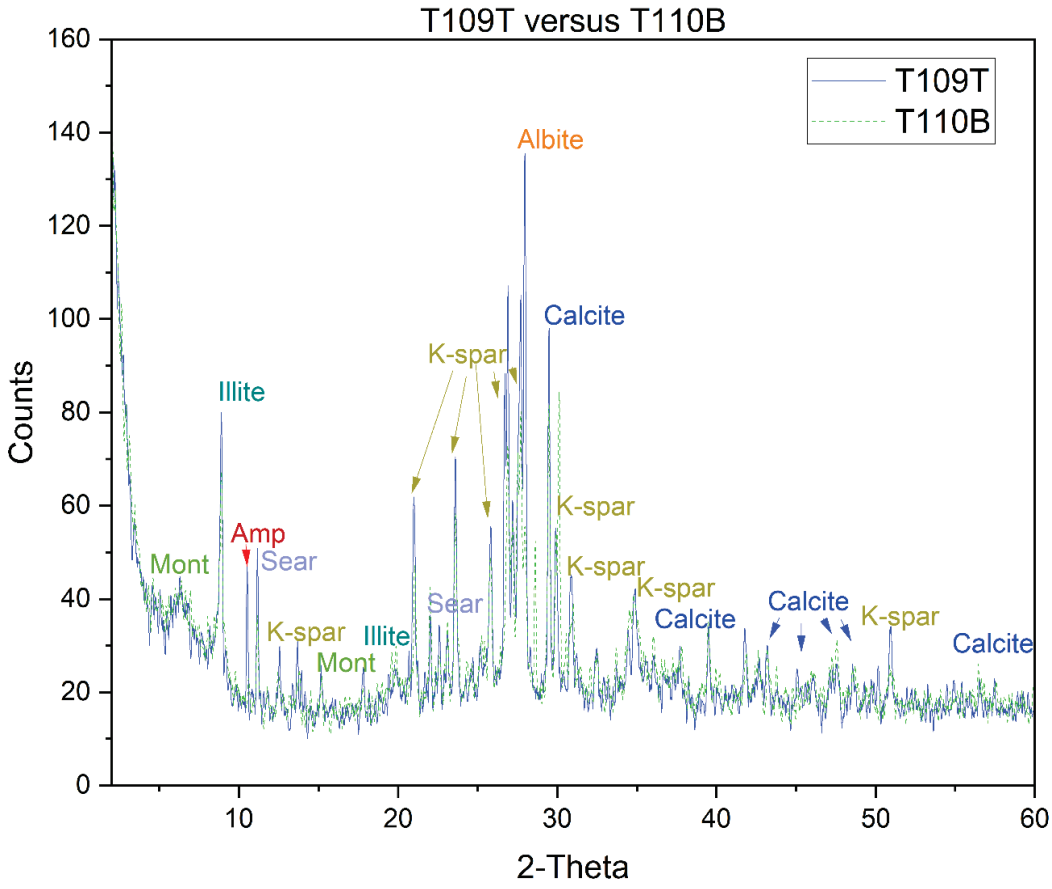

Figure 19: XRD patterns for surface sample T109T (shown as a solid blue line) and subsurface sample T110B (shown as a dotted green line), near the middle of Section 1. Surface sample T109T has a higher relative abundance of amphibole (Amp, red) compared to subsurface sample T110B. Both samples have similar relative abundances of smectite (Mont, yellow green), illite (turquoise), searlesite (Sear, lavender), K-feldspar (K-spar, yellow), and albite (orange).

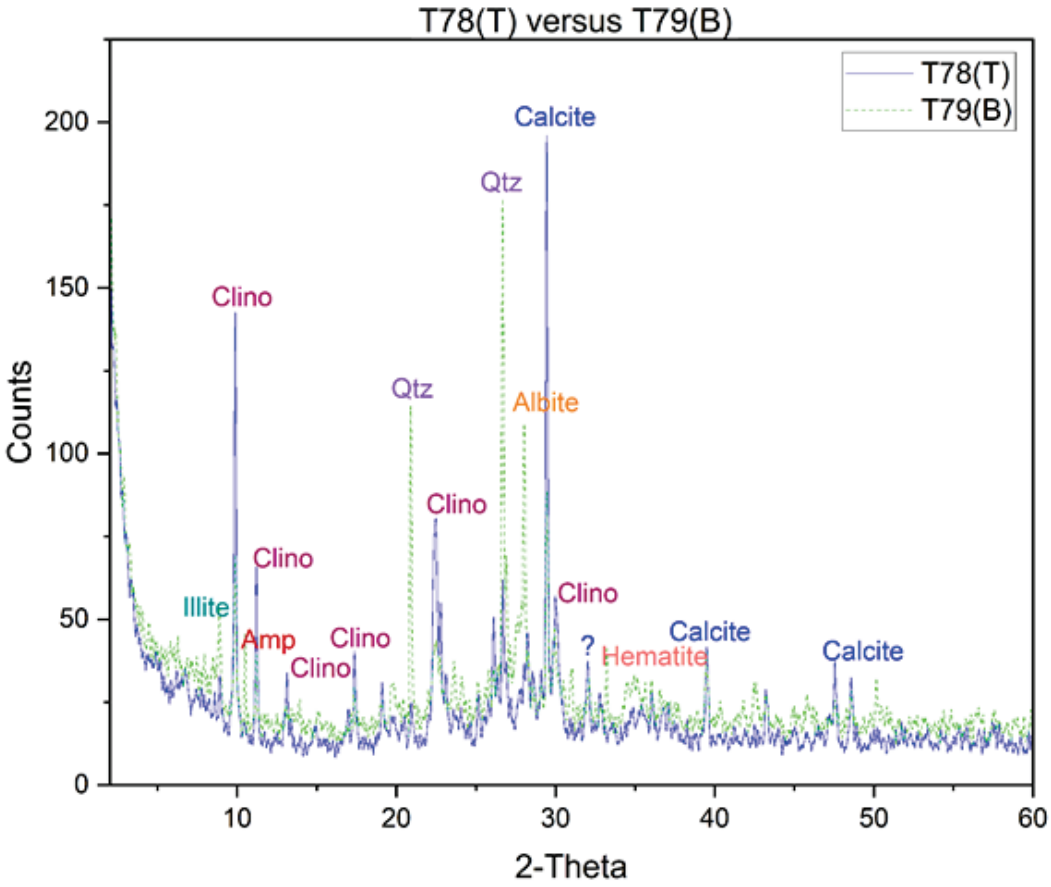

Figure 20: XRD patterns for surface sample T78(T) (shown as a solid blue line) and subsurface sample T79(B) (shown as a dotted green line), near the top of Section 2. Surface sample T78(T) lacks amphibole (Amp, dark red), albite (orange) and hematite (dark orange) compared to subsurface sample T79(B). Both samples have similar relative abundances of illite (turquoise), calcite (blue), and clinoptilolite (Clino, dark red). Surface sample T78(T) has a lower relative abundance of quartz (Qtz, purple) compared to subsurface sample T79(B). It is likely that the whole section has been overprinted by a mixture of sheet flow, caliche from carbonate accumulation on the surface, and/or wind transport.

4.2.2 X-Ray Fluorescence (XRF)

The major oxides and trace elements SiO_2, Al_2O_3, K_2O, Fe_2O_3, CaO, Na_2O, MgO, MnO, TiO_2, P_2O_5 and Zr, Sr, and Ba measured by XRF were used for the weathering calculations presented in section 4.4. The XRF results for section 1, section 2, and the modern basin are presented in Appendix E Table 7 to Table 9. The parent rock type for both sections is likely felsic, based on ratios of Al_2O_3 (weight %) versus TiO_2 (weight %), and Zr (ppm) versus TiO_2 (weight %), see Figure 21 and Figure 22. All samples in Section 1 generally grouped together for both methods, except T117T and T118B. The surface samples were enriched in TiO_2 and Zr compared to the corresponding subsurface samples. The compositions of samples from Section 2 (T78(T), T80(T), T81(B), T82(T)) were more scattered compared to Section 1, for Al_2O_3 (weight %) versus TiO_2 (weight %). Section 2 were generally grouped together for Zr (ppm) and TiO_2 (weight %). The surface samples from Section 2 are generally depleted in TiO_2 and enriched in Zr, compared to the corresponding subsurface samples. It is likely that the dominant processes are different for each section.

In section 1, the compositions of the surface deposits from the stratigraphic section vary slightly and are very similar in weight percent of SiO_2 (48.52-53.50 weight %). The subsurface deposits vary more in SiO_2 from the bottom to the top of the section, but do not follow an overall trend (44.62-54.90 weight %). Generally, the subsurface samples have a lower weight percent of SiO_2 than the surface samples, see Figure 23. For example, sample T115T (surface) is 48.52 weight % SiO_2 while sample T116B (subsurface) is 46.19 weight % SiO_2. The weight percent of Al_2O_3, K_2O, Fe_2O_3, CaO, and Na_2O also vary from the bottom to the top and between surface and subsurface samples for the first stratigraphic section, see Figure 23. The surface samples have a similar K_2O/Al_2O_3 and Al_2O_3/TiO_2 ratios to the subsurface (Figure 24).

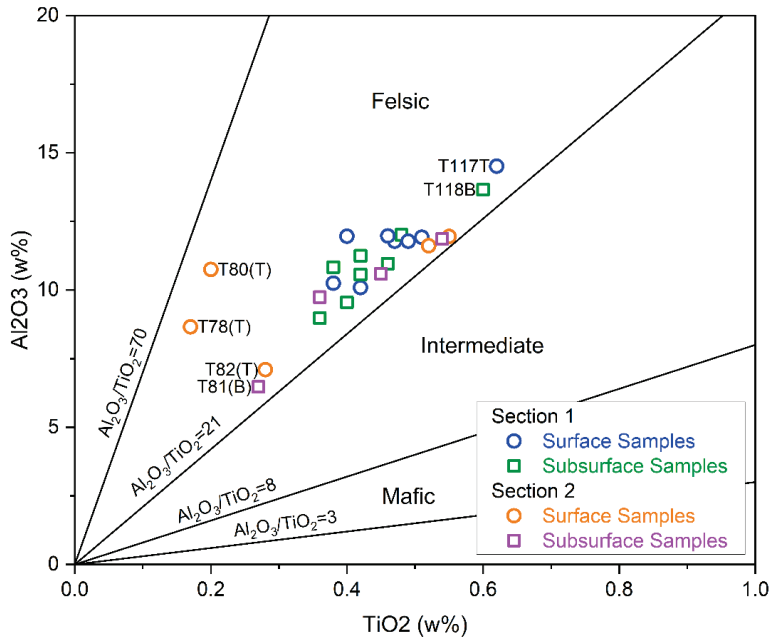

Figure 21: Possible source rock type, based on weight percent of Al_2O_3 and TiO_2, based on Xu et al. (2020), which is adapted from Girty et al. (1996). Samples T78(T), T80(T), T81(B), T82(T), T117T and T118B are labeled, since these samples did not group with the main population. All samples are likely felsic. The ratios for the black lines are in weight percent.

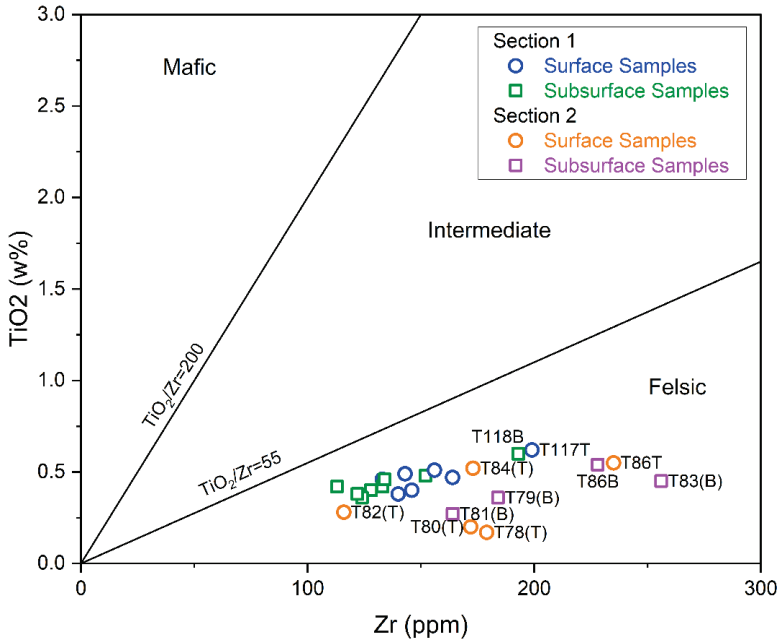

Figure 22: Possible source rock type, based on ppm of Zr and weight percent of TiO_2, following Hayashi et al. (1997). Samples T78(T), T79(B), T80(T), T81(B), T82(T), T83(B), T84(T), T86T, T86B, T117T and T118B are labeled. All samples are likely felsic. All samples are likely felsic. The ratios for the black lines are in weight percent.

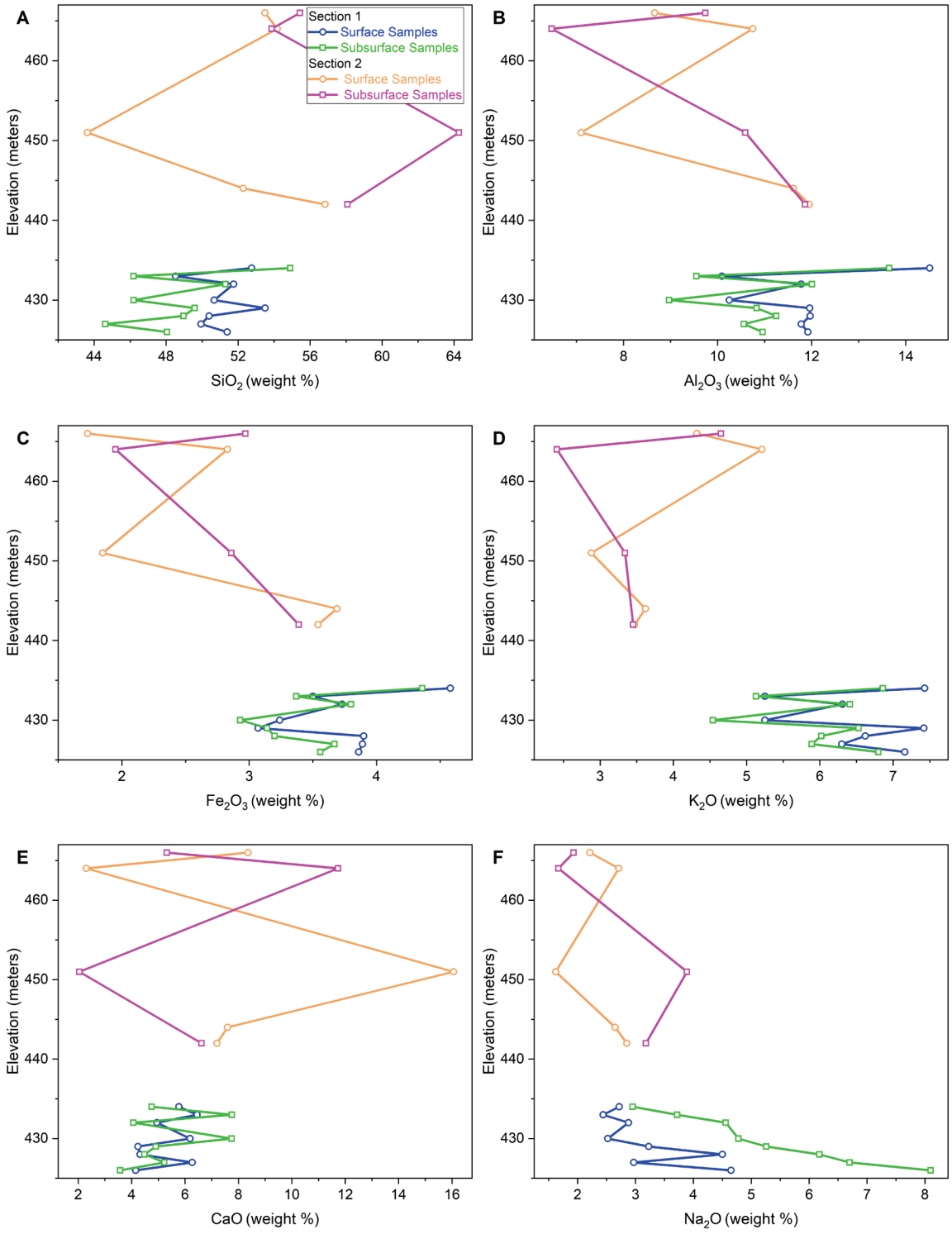

Figure 23: Oxides versus elevation for Sections 1 and 2. Generally, the surface samples follow a similar pattern as the subsurface for Section 1, while Section 2 the surface samples are an inverse of the subsurface samples.

In section 2, the composition of the surface samples down the stratigraphic section are similar in weight percent SiO_2 (53.49-56.83 weight %), except for T82 (43.62 weight %). The subsurface deposits vary more in SiO_2 down the section, but do not follow an overall trend (53.87-64.28 weight %), see Figure 23. Generally, the subsurface has a slightly higher weight percent of SiO_2 than the surface. For example, sample T78(T) (surface) has 53.49 weight % SiO_2 while sample T79(B) (subsurface) has 55.44 weight % SiO_2. The weight percent of Al_2O_3, K_2O, Fe_2O_3, CaO, and Na_2O vary, but have an increasing tread within the second stratigraphic section, see Figure 23. The surface samples have a higher K_2O/Al_2O_3 and Al_2O_3/TiO_2 ratios than the subsurface, but both have a decreasing trend (Figure 24). The higher silica in section 2 is due to abundant quartz and other silicate minerals observed in these samples. The samples from the modern basin have similar compositions to sections 1 and 2. However, the mineral assemblages are slightly different between sections 1 and 2 with regards to the presence of K-feldspar and dolomite. An evaluation of the type of weathering that the area has experienced is needed to further elucidate any geochemical trends.

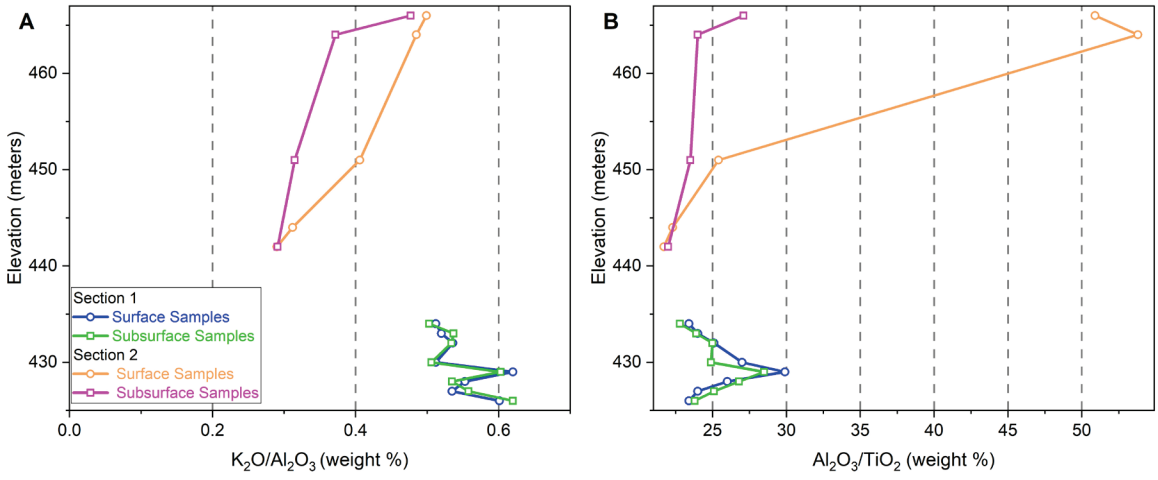

Figure 24: K_2O/Al_2O_3 and Al_2O_3/TiO_2 ratios versus elevation for Sections 1 and 2. Generally, the surface samples follow a similar pattern as the subsurface for Section 1, while Section 2 the surface samples are dissimilar to the subsurface samples.

4.3 Weathering Calculations

The XRF data was used to estimate the degree of weathering for the two stratigraphic sections of the 2019 Tecopa samples. The CIA values varied between 30.29 and 46.06 (37.62 mean) with a trend towards higher values from the bottom to the top of section 1 (Figure 25). CIA values for section 2 have a smaller range of 42.02 to 47.88 (45.16 mean) (Appendix F Table 11). The CIA values for both sections are below 50 (see the plagioclase-K-feldspar line in Figure 26), which suggests that little chemical weathering has occurred for either section. The samples have higher concentrations of CaO and Na_2O compared to Al_2O_3 than would be expected if they formed from the weathering of felsic materials (commonly feldspar-rich), and this is likely tied to the formation of zeolites, salts, and other authigenic minerals in contact with alkaline waters.

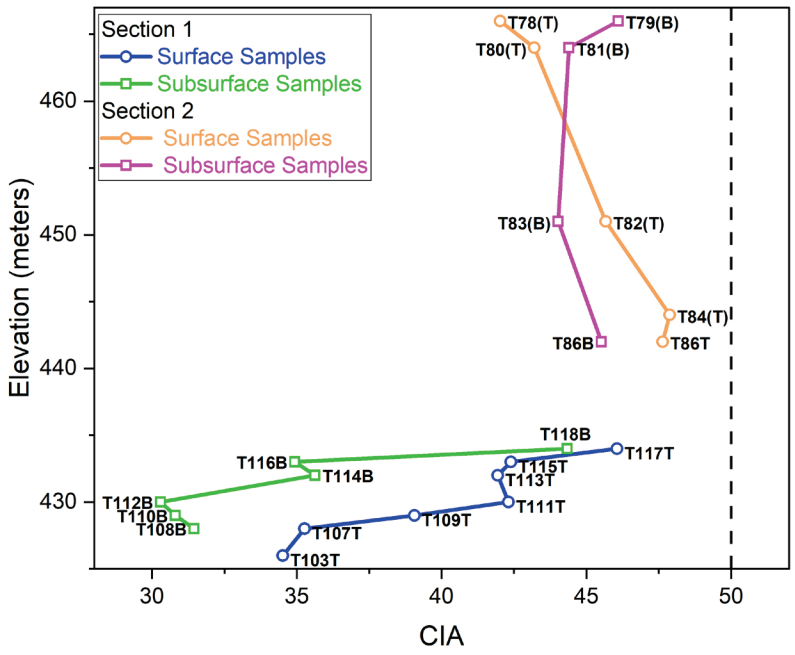

Figure 25: CIA versus elevation for Sections 1 and 2. The dashed line at CIA 50 denotes the plagioclase-K-feldspar line (weathered-unweathered igneous rock boundary). Samples T105T, T106B, and T104B were omitted since they were not corrected for the sodium contribution from halite.

The CPA values for section 1 vary between 45.13 and 76.43 (62.80 mean), with an overall increase up section, and the CPA values for section 2 vary between 62.33 to 75.42 (70.63 mean), and these low values are evidence for weak chemical weathering. The PIA values vary between 17.89 and 41.95 (28.37 mean) in section 1 and in section 2 they vary between 35.40 and 46.87 (42.03 mean), and the low values for both sections suggest little altered materials. The WIP values vary between 97.23 and 131.93 (113.10 mean) in section 1 and in section 2 they vary between 56.84 and 83.58 (72.14 mean), and these high values suggest that little to no chemical weathering has occurred. The CIW values in section 1 vary between 36.22 to 61.85 (48.54 mean) and in section 2 they vary between 56.84 and 83.58 (55.56 mean). These values are higher than expected based on the other proxies and this could be misleading, because of the uncorrected total aluminum derived from K-feldspar in both sections. The ICV values in section 1 vary between 1.96 and 5.24 (3.35 mean) while in section 2 they vary between 2.11 and 4.02 (2.71 mean). Both sections have ICV values greater than 1, therefore both sections are considered compositionally immature. The high WIP and the low CIA and PIA values indicate weak chemical alteration, consistent with arid conditions.

The next set of weathering indices, including base loss, Clayeyness (C), hydrolysis (H), basesAl (1/H), calcification, salinization (S), and leaching (L), provide more information on specific weathering processes. The base loss values vary between 37.11 and 110.53 (67.96 mean) in section 1 and between 35.73 and 150.06 (83.43 mean) for section 2. Higher base loss values are interpreted to indicate a greater amount of leaching for a sample. The Clayeyness values vary between 0.11 and 0.16 (0.13 mean) in section 1 and 0.07 and 0.13 (0.11 mean) in section 2, which indicates that section 1 has a greater amount of clay minerals forming due to the greater

A

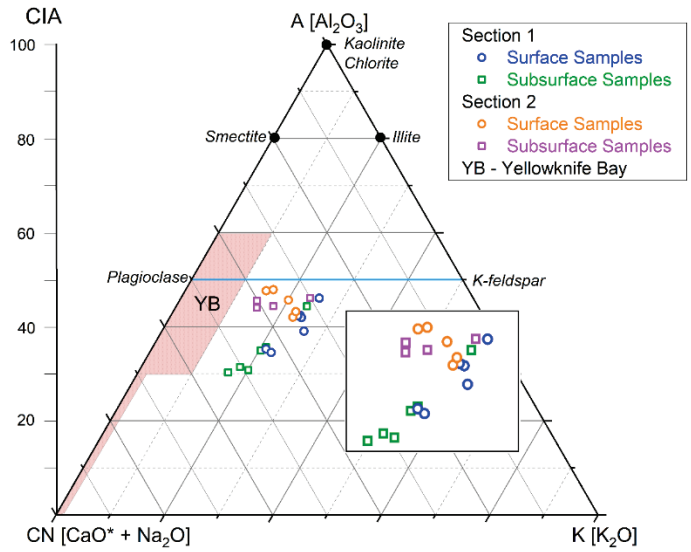

B

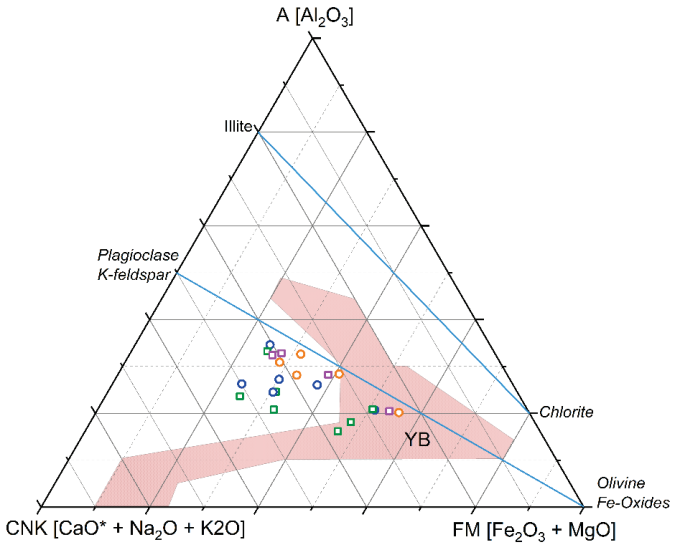

Figure 26: (a) The A-CN-K ternary diagram shows the overall chemical weathering (CIA) of sections 1 and 2. The blue line is the 50 percent plagioclase-K-feldspar line that is the boundary between some evidence of chemical weathering to strong evidence of chemical weathering. The red area denotes the Yellowknife Bay Formation Mars samples from McLennan et al. (2014). (b) The A-CNK-FM ternary diagram shows sedimentary weathering considering mafic components. Half of the subsurface samples (which have a higher amount of FM) in Section 1, plot within the Yellowknife Formation Mars samples (red area). Section 1 is likely felsic with the addition of Mg.

abundance of aluminum. The calcification values for section 1 vary between 1.13 and 4.24 (2.21 mean) and for section 2 from 0.99 to 6.71 (2.84 mean). Higher calcification values indicate a higher concentration of Ca^{2+}, reflecting an abundant of carbonate minerals. These values are generally higher for the surface samples, likely due to a duricrust. The salinization values for section 1 vary from 0.86 to 1.89 (1.23 mean) in section 1 and in section 2, samples vary from 0.71 to 0.96 (0.83). This suggests that section 1 has higher amounts of alkali elements and associated anionic complexes that accumulate as soluble salts (such as Ca^{2+}, Mg^{2+}, Na^{+}, Cl^{-}, SO_4^{2-}, and HCO_3^{-}).

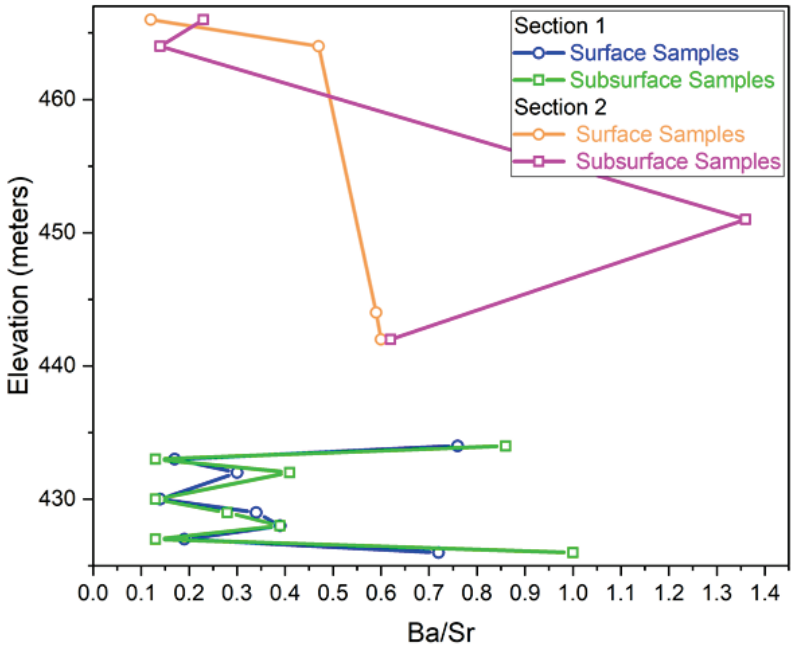

Figure 27: Ba/Sr ratio versus elevation for Sections 1 and 2. Sample T82(T) was omitted as the Ba concentration was below the LLD.

The Ba/Sr (L) values vary between 0.13 and 1.00 in section 1 and 0.12 to 1.36 in section 2. In Section 1, the highest Ba/Sr ratios are in the top (0.76 for T117T and 0.80 for T118B, with a 5.1% difference between the surface and subsurface sample) and bottom (0.72 for T103T and

1.00 for T104B, with a 32.6% difference between the surface and subsurface sample) of the section, see Figure 27. The largest differences in the Ba/Sr ratio for subsurface and surface samples for Section 1 is for T106B (0.13) and T105T (0.19)**,** a 37.5% difference. There is a 0% difference between subsurface T108B and surface T107T samples (both are 0.39). In Section 2, subsurface sample T81(B) has 0.14 and surface sample T80(T) has 0.47, a 108.2% difference, while the subsurface sample T86(B) has 0.60 and the surface sample T86(T) has 0.62, a 3.2% difference. Overall, the Ba/Sr (L) values for both sections were well below 10 (well-leached paleosol), therefore leaching and hydrolysis are weak weathering processes in Tecopa (Retallack, 2001; Sheldon and Tabor, 2009; Mitchell and Sheldon, 2010).

Examining the amount of and differences in mobile cations such as Ca^{2+} and Mg^{2+} (alkaline earth elements) and Na^{+} and K^{+} (alkali elements) with respect to relatively immobile Ti^{4+} (Table 2) and Al^{3+} (Table 3) during chemical weathering provides the degree and pattern of element mobility in the subsurface and surface of the soils (Sheldon and Tabor, 2009). Aluminum (Al^{3+}) is commonly used for sediment normalization, since it represents aluminosilicates that are generally found in fine sediment fractions and corrects for both grain size (likely negligible for lab prepared samples) and the compositional variability between samples (Daskalakis and O'Connor, 1995; Covelli and Fontolan, 1997).

Al^{3+} is thought to be relatively more immobile than Ti^{4+}, therefore the surface Al/Ti ratio should be higher than the subsurface, indicating an apparent increase in the concentration of Al^{3+} relative to Ti^{4+}. The Al/Ti ratio values for section 1 vary between 17.82 and 23.42, and in section 2, they vary from 17.02 and 42.10, see Figure 28 A. The upper half of Section 1 has higher concentrations of Al^{3+} relative to Ti^{4+} on the surface compared to the corresponding subsurface

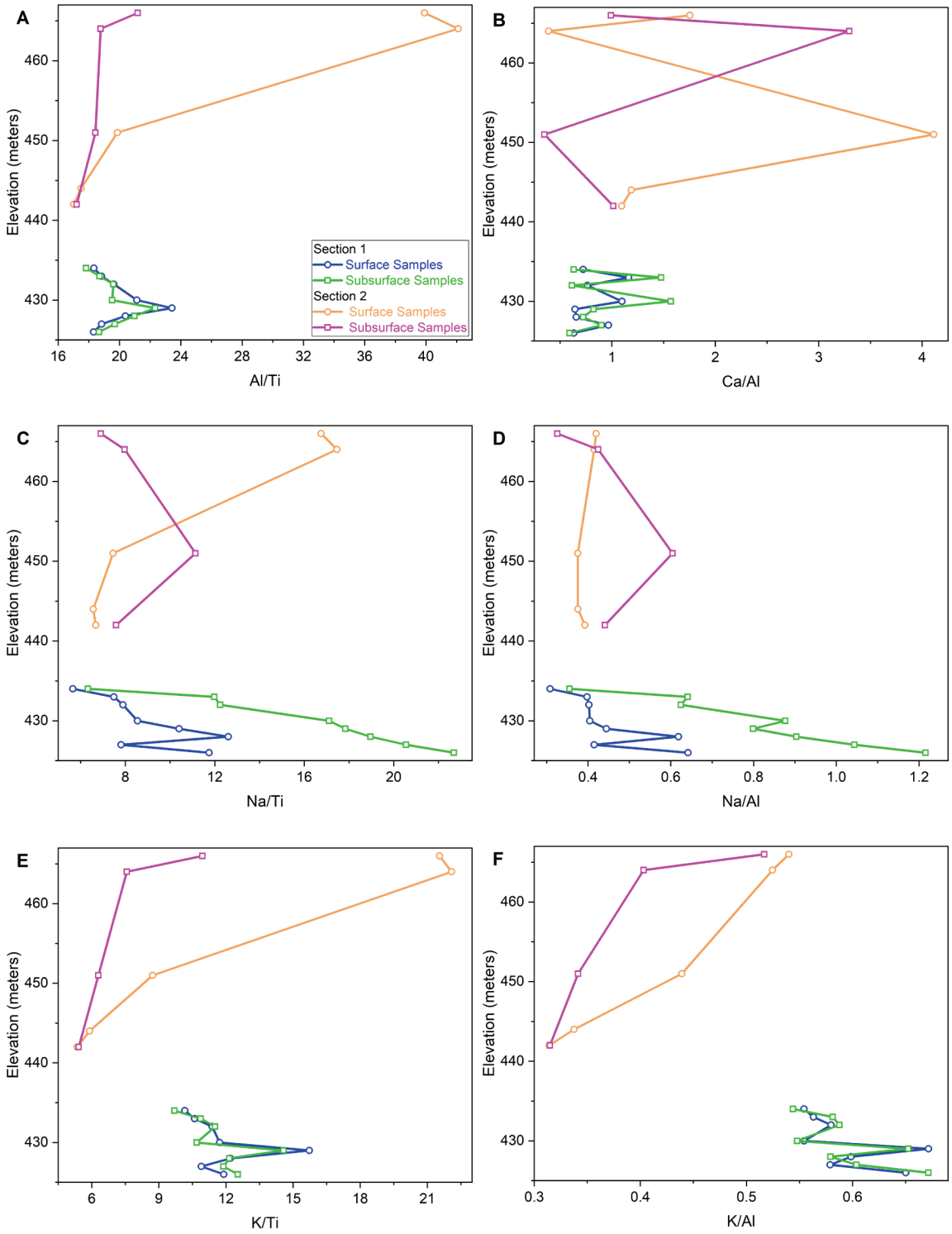

Figure 28: Select oxides normalized to Ti^{4+} or Al^{3+} versus elevation for Sections 1 and 2. For section 1, K+ in the surface and subsurface samples follow a similar pattern and dissimilar pattern for Na+, while for Section 2, K^{+} and Na^{+} in the surface samples are dissimilar to the subsurface samples.

Sample	Si/Ti	Al/Ti	Fe/Ti	Mg/Ti	Mn/Ti	Ca/Ti	Na/Ti	K/Ti	P/Ti
T117T	113.09	18.33	3.69	9.49	0.20	13.25	5.65	10.16	0.15
T118B	121.62	17.82	3.63	9.81	0.19	11.27	6.34	9.69	0.14
T115T	153.56	18.82	4.17	42.23	0.21	21.87	7.49	10.60	0.13
T116B	153.49	18.70	4.21	45.23	0.25	27.63	11.98	10.87	0.15
T113T	146.36	19.63	3.97	24.54	0.24	15.00	7.90	11.38	0.12
T114B	142.06	19.60	3.96	20.72	0.21	12.08	12.24	11.52	0.13
T111T	177.24	21.13	4.26	46.98	0.24	23.20	8.55	11.71	0.15
T112B	170.55	19.52	4.07	52.07	0.25	30.66	17.11	10.69	0.19
T109T	177.78	23.42	3.84	22.14	0.23	15.10	10.41	15.73	0.14
T110B	173.46	22.32	4.13	30.71	0.30	18.40	17.84	14.57	0.19
T107T	145.61	20.38	4.24	21.11	0.22	13.38	12.61	12.20	0.12
T108B	154.98	20.98	3.81	18.21	0.19	15.19	18.96	12.15	0.17
T105T	135.47	18.83	3.97	26.49	0.25	18.22	7.81	10.90	0.13
T106B	141.21	19.69	4.37	30.81	0.29	17.73	20.56	11.89	0.15
T103T	133.94	18.31	3.79	12.82	0.22	11.59	11.75	11.90	0.15
T104B	138.85	18.66	3.87	9.99	0.22	11.05	22.69	12.53	0.21

Sample	Si/Ti	Al/Ti	Fe/Ti	Mg/Ti	Mn/Ti	Ca/Ti	Na/Ti	K/Ti	P/Ti
T78(T)	418.24	39.90	5.09	41.73	0.33	70.04	16.75	21.55	0.23
T79(B)	204.70	21.19	4.13	24.99	0.22	21.05	6.91	10.95	0.16
T80(T)	360.09	42.10	7.08	31.80	0.28	16.38	17.46	22.09	0.17
T81(B)	265.21	18.77	3.61	45.87	0.17	61.87	7.97	7.57	0.21
T82(T)	207.07	19.86	3.30	51.66	0.16	81.69	7.46	8.72	0.22
T83(B)	189.87	18.43	3.18	11.85	0.10	6.46	11.14	6.29	0.14
T84(T)	133.66	17.49	3.55	21.53	0.15	20.79	6.57	5.90	0.13
T86T	137.35	17.02	3.22	13.22	0.14	18.64	6.68	5.35	0.16
T86B	142.97	17.20	3.14	11.49	0.15	17.46	7.59	5.42	0.16

Table 2: Major elements normalized to Ti^{4+} for 2019 Tecopa samples from sections 1 and 2. Samples T104B, T105T, and T106B contain halite and thus have anomalously high Na concentrations.

Sample	Si/Al	Ti/Al	Fe/Al	Mg/Al	Mn/Al	Ca/Al	Na/Al	K/Al	P/Al
T117T	6.17	0.05	0.20	0.52	0.01	0.72	0.31	0.55	0.01
T118B	6.83	0.06	0.20	0.55	0.01	0.63	0.36	0.54	0.01
T115T	8.16	0.05	0.22	2.24	0.01	1.16	0.40	0.56	0.01
T116B	8.21	0.05	0.23	2.42	0.01	1.48	0.64	0.58	0.01
T113T	7.45	0.05	0.20	1.25	0.01	0.76	0.40	0.58	0.01
T114B	7.25	0.05	0.20	1.06	0.01	0.62	0.62	0.59	0.01
T111T	8.39	0.05	0.20	2.22	0.01	1.10	0.40	0.55	0.01
T112B	8.74	0.05	0.21	2.67	0.01	1.57	0.88	0.55	0.01
T109T	7.59	0.04	0.16	0.95	0.01	0.64	0.44	0.67	0.01
T110B	7.77	0.04	0.19	1.38	0.01	0.82	0.80	0.65	0.01
T107T	7.14	0.05	0.21	1.04	0.01	0.66	0.62	0.60	0.01
T108B	7.39	0.05	0.18	0.87	0.01	0.72	0.90	0.58	0.01
T105T	7.19	0.05	0.21	1.41	0.01	0.97	0.41	0.58	0.01
T106B	7.17	0.05	0.22	1.56	0.01	0.90	1.04	0.60	0.01
T103T	7.32	0.05	0.21	0.70	0.01	0.63	0.64	0.65	0.01
T104B	7.44	0.05	0.21	0.54	0.01	0.59	1.22	0.67	0.01

Sample	Si/Al	Ti/Al	Fe/Al	Mg/Al	Mn/Al	Ca/Al	Na/Al	K/Al	P/Al
T78(T)	10.48	0.03	0.13	1.05	0.01	1.76	0.42	0.54	0.01
T79(B)	9.66	0.05	0.19	1.18	0.01	0.99	0.33	0.52	0.01
T80(T)	8.55	0.02	0.17	0.76	0.01	0.39	0.41	0.52	0.00
T81(B)	14.13	0.05	0.19	2.44	0.01	3.30	0.42	0.40	0.01
T82(T)	10.43	0.05	0.17	2.60	0.01	4.11	0.38	0.44	0.01
T83(B)	10.30	0.05	0.17	0.64	0.01	0.35	0.60	0.34	0.01
T84(T)	7.64	0.06	0.20	1.23	0.01	1.19	0.38	0.34	0.01
T86T	8.07	0.06	0.19	0.78	0.01	1.10	0.39	0.31	0.01
T86B	8.31	0.06	0.18	0.67	0.01	1.01	0.44	0.31	0.01

Table 3: Major elements normalized with Al^{3+} for 2019 Tecopa samples from sections 1 and 2. Samples T104B, T105T, and T106B contain halite and thus have anomalously high Na concentrations.

samples. The Al/Ti ratio for subsurface sample T110B is 22.32 compared to the surface T109T, which is 23.42 (a 4.8% difference). Samples from the lower half of Section 1 have lower concentrations of Al^{3+} relative to Ti^{4+} on the surface compared to the corresponding subsurface samples. The Al/Ti ratio for subsurface sample T108B is 20.98 is similar to that of surface sample T107T, which is 20.38. Section 2 may have a similar pattern, but this trend is difficult to confirm because of the small number of samples. The Ti/Al ratio did not show an overall increasing or decreasing pattern for Section 1, but the surface samples have similar values to corresponding subsurface samples (except TT117(T)), while Section 2, surface samples T78(T) and T80(T) were lower compared to subsurface samples T79(B) and T81(B). The Ti/Al ratio values for section 1 vary between 0.04 and 0.06, and in section 2, they vary from 0.02 and 0.06. Both ratios can be affected by alkalinity in the weathering profile (Mohanty and Nanda, 2016). The Na/Ti and Na/Al element ratios are sensitive to chemical weathering and can be used as a paleoclimate proxy. Na is mobile compared to Al and Ti during chemical weathering and the ratio is higher for arid conditions. The Na/Ti ratio values for section 1 vary between 5.65 and 22.69, and for section 2 they range from 6.57 to 17.46. The Na/Al ratio values for section 1 vary between 0.31 and 1.22 and in section 2, they vary from 0.33 to 0.60. The Na/Al ratio for subsurface sample T104B is 1.22 compared to surface sample T103T, which is 0.64 (a 62.4% difference). The Na/Al ratio for subsurface sample T83(B) is 0.60 compared to surface sample T82(T), which is 0.38 (a 44.9% difference). Na/Ti and Na/Al ratios are lower for subsurface samples compared to surface samples for Section 1. For Section 2, the Na/Al ratio is lower (except T78(T)) for the subsurface samples relative to the surface samples, while Na/Ti is higher for the top of the section and lower for the others, see Figure 28 C and D. Comparing the Na/Ti and Na/Al ratios to Na_2O (w %), Na_2O (w %) follows the same pattern for Section 1, but for

Section 2 it follows the pattern of Na/Ti and diverges from the Na/Al pattern (specifically for T80(T) and T81(B)). Sodium can be found in chlorides (e.g. halite), hanksite, smectites and Na-rich plagioclase (e.g. albite), and it can migrate to the crust and precipitate as a salt, potentially explaining its elevated concentration in some surface samples.

K/Al is another element ratio that is sensitive to chemical weathering and can be used as a paleoclimate proxy. K is water soluble as it is released from the breakdown of K-feldspar, thus the ratio decreases as weathering occurs and K is removed from the system (Sinha et al., 2005; Wei et al., 2006). The K/Al ratio values for section 1 vary between 0.54 and 0.67, and in section 2 they vary from 0.31 and 0.54. The K/Ti ratio values for section 1 vary between 9.69 and 15.73, and in section 2, they vary from 5.35 and 22.09. Subsurface sample T110B is 14.57 compared to surface sample T109T, which is 15.73 (a 7.7% difference). K/Ti and K/Al follow a similar pattern alternating between higher and lower values for Section 1, while for Section 2, both ratios are higher (except for T86B and T86T) for the subsurface samples compared to the surface samples, see Figure 28 E and F. Comparing the K/Ti and K/Al ratios to K_2O (wt. %), the K_2O (wt. %) pattern is different from the K/Ti and K/Al pattern for both sections. For Section 1, surface samples T115T, T105T, and T103T have a higher K_2O (wt. %) and thus a higher concentration of K^+ than the subsurface samples, while the normalized K^+ to Al^{3+} and Ti^{4+} values show a lower concentration of K^+ for the surface samples compared to the subsurface samples. The opposite is observed for Section 2, where the surface samples T78(T) and T82(T) have a lower K_2O (w %) concentration, and thus a lower concentration of K^+ than the subsurface samples, while the normalized K^+ to Al^{3+} and Ti^{4+} values show a higher concentration of K^+ than the subsurface samples. It likely that the Al^{3+} or Ti^{4+} normalized data shows the most representative pattern of the surface and subsurface samples. K^+ is likely derived from potassium

feldspars and saline-alkaline fluids and usually accumulates in the upper soil horizon along with weathering-resistant minerals.

The Ca/Al ratio values for section 1 vary between 0.59 and 1.57, and in section 2 they vary from 0.35 and 4.11. The Ca/Al ratio for subsurface sample T112B is 1.57 compared to surface sample T111T, which is 1.10 (a 35.2% difference), see Figure 28 B. The Ca/Ti ratio values for section 1 vary between 11.05 and 30.66, and in section 2, they vary from 6.46 and 81.69. Ca/Ti, Ca/Al, and Ca (wt %) lack a clear pattern in both sections. Calcium can come from carbonate and smectite minerals, and like sodium it can migrate to the crust and precipitate as a salt.

4.4 Visible and Near-Infrared Reflectance

A total of 45 samples were prepared and sent to be analyzed by VNIR. These samples represented diverse mineral assemblages from outcrops around a paleolake that could be analogous to previously analyzed in-situ samples from Gale crater and orbital data of Jezero crater (Holm-Alwmark et al., 2021). The VNIR plots compiled in this study were compared to USGS v.7 Spectral Plots, convolved to Analytical Spectral Devices (ASD) standard resolution and full range characteristics (Figure 29).

The sample pairs for section 1 selected for VNIR analysis were T117T and T118B, T115T and T116B, T111T and T112B, T107T and T108B, and T103T and T104B. Most of the first stratigraphic section samples had similar bands between 300-2500 nm, as seen in Figure 30. Minor differences in the spectra were observed in samples T117T, T115T, T116B, T111T, and T112B, between 2100-2400 nm. Samples T117T and T118B have similar spectral patterns, however T117T has a higher reflectance than T118B. Samples T115T and T116B have similar

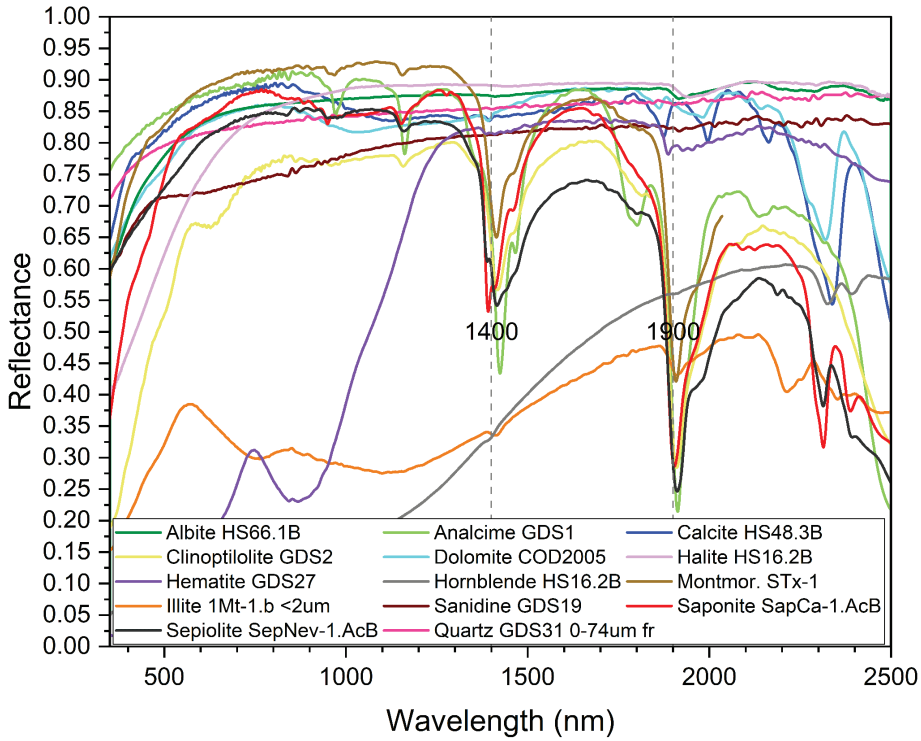

Figure 29: Composite USGS VNIR plot of the mineral assemblages present in the Tecopa samples. Dashed line at 1400 and 1900 nm represent the OH and H_2O absorption bands.

patterns, with a higher reflectance in T116B. From the middle of the section, sample T112B has a higher reflectance than T111T. A similar trend in higher reflectance is observed for samples T108B and T104B compared to T107T and T103T. Reflectance depends on the adsorptions of the different cations or anions of a mineral along with its grain size (Clark et al., 1990), which will be discussed further in section 5.3.

These differences in spectral bands are likely due to the vibrations in the bonds of crystal lattices or molecules such as from phyllosilicates and carbonate minerals. The spectra shown in Figure 30 are a mixture of clays and other minerals, which could make it difficult to identify which minerals contributed to the OH, H_2O, and CO_3 bands. Absorption bands due to OH, H_2O, and CO_3 are usually observed in the 900 nm to 2500 nm range. Generally, the presence of the 1410 nm band indicates OH and the 1910 nm band indicates molecular water (Figure 31 to

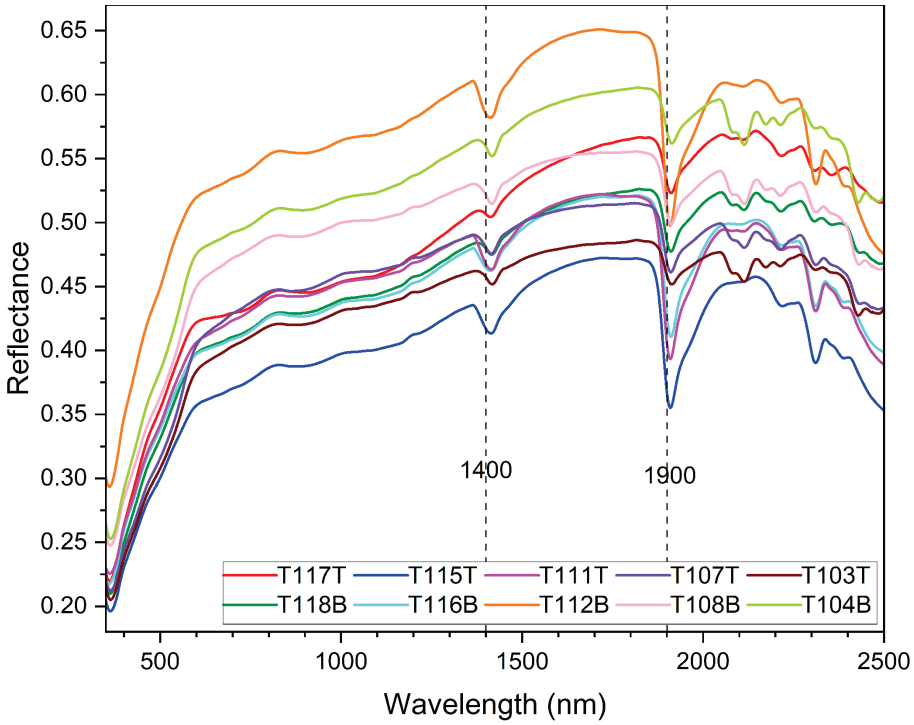

Figure 30: Composite VNIR plot of selected section 1 spectra. Dashed line at 1400 and 1900 nm represent the OH and H_2O absorption bands.

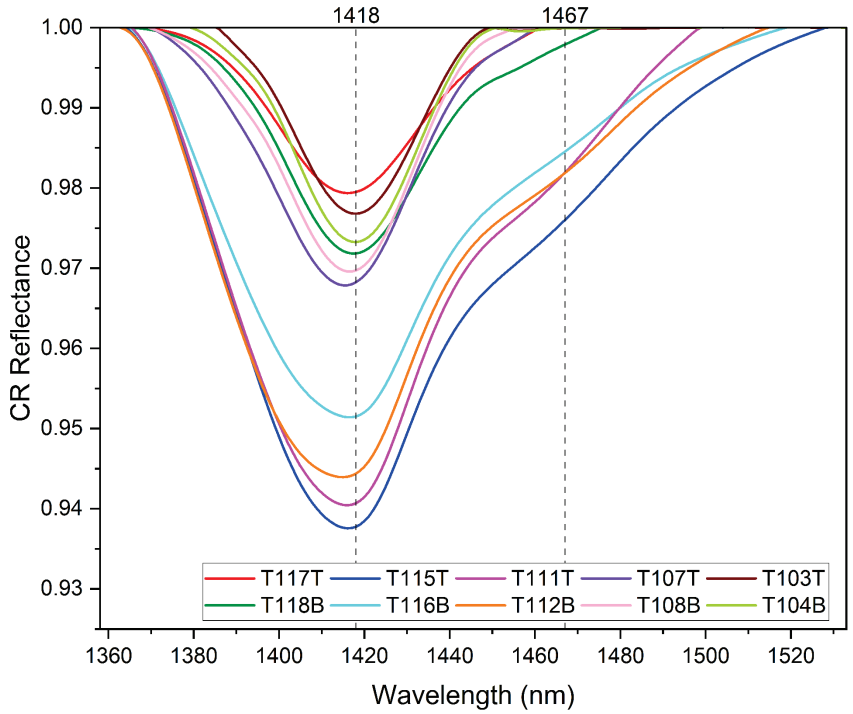

Figure 31: Continuum-removed (CR) Reflectance plot of Section 1 for the wavelengths 1360 to 1530nm. Dashed line at 1418 and 1467 nm represent the OH and H_2O absorption bands.

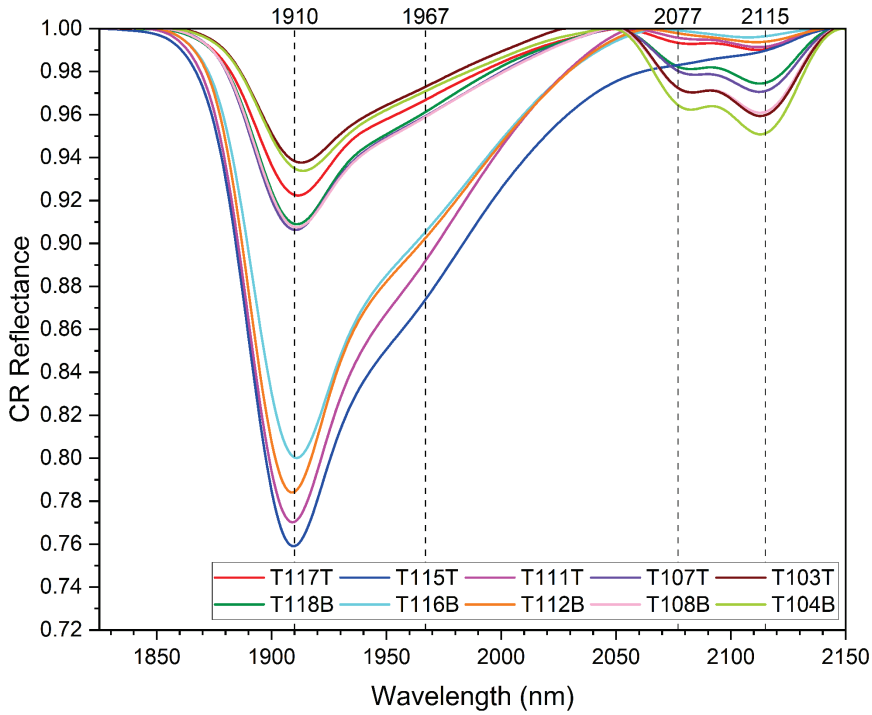

Figure 32: Continuum-removed (CR) Reflectance plot of Section 1 for the wavelengths 1830 to 2150nm.

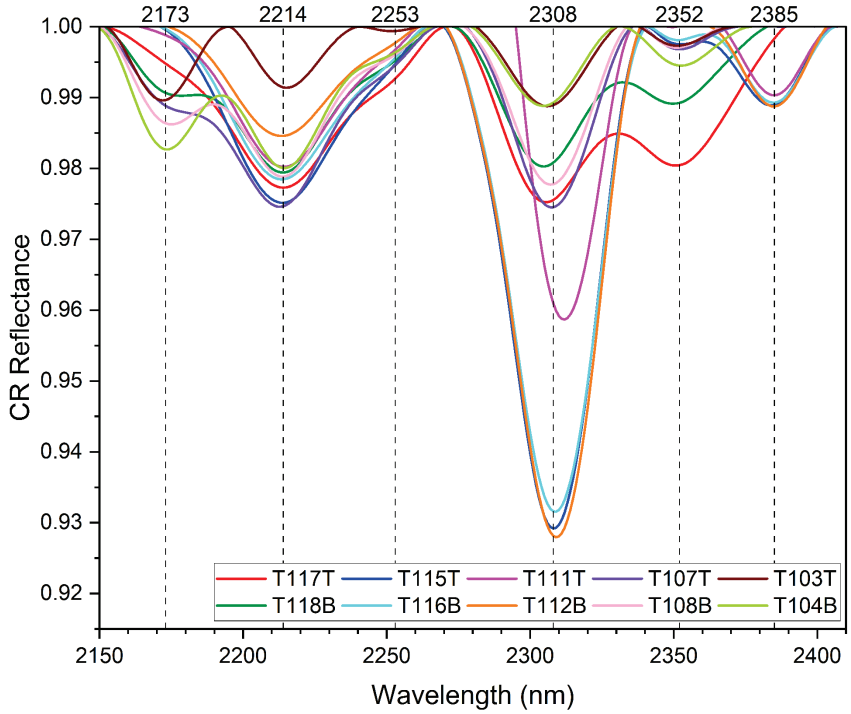

Figure 33: Continuum-removed (CR) Reflectance plot of Section 1 for the wavelengths 2150 to 2500nm.

Figure 33). The presence of these bands is consistent with the XRD results, which show clay minerals such as illite and smectite that have the OH and H_2O bonds in their molecular structures. Illite has spectral bands near 1410 nm, 1910 nm, 2350 nm, and 2440 nm, which may shift depending on the octahedral cation present (Bishop et al., 2017). In these samples, spectral bands are identified at 1418 nm and 1910 nm (Figure 31 and Figure 32). Another candidate phase is the Al-bearing smectite, montmorillonite, which has spectral bands near 1410 nm and 1910 nm, and an OH combination band near 2077-2115 nm, shown as a doublet (two peaks, Figure 32). Based on the XRD mineralogy, minor calcite and minor to trace dolomite would be expected in the spectra. Two strong CO_3 absorption bands at 2300 to 2350 nm and 2500 to 2550 nm and three weaker CO_3 bands at 1850 to 1870 nm, 1970-2000 nm, and 2120 to 2160 nm would be expected. In section 1, we observe the 2300 to 2350 nm band in the spectra for all samples except T117T, T115T, T116B, T111T, and T112B. Analcime is a zeolite mineral identified by XRD in samples T118B and T116B, with an absorption near 2350 nm. The absorption bands of these minerals are due to water molecules trapped in the crystal lattice (Clark et al., 1990).

The sample pairs for section 2 analyzed by VNIR analysis are T78(T) and T79(B), T82(T) and T83(B), T86T and T86B, and T87(T) and T88(B). The 500 to 2200 nm spectral signals for the second stratigraphic section have similar patterns (Figure 34). High reflectance is observed for samples T83(B) and T88(B) relative to their paired surface samples T82(T) and T87T. Another high reflectance sample is T86T, which has a similar reflectance to the samples from the base of the stratigraphic section. The samples at the top of the stratigraphic section (T78(T) and T79(B)) are similar, with a slightly higher reflectance for T79(B) at around 1400 nm (Figure 35). The 600 nm absorption band is only observed for T78(T) and T79(B) and could indicate the zeolite mineral clinoptilolite, which was detected in small abundances by XRD. The

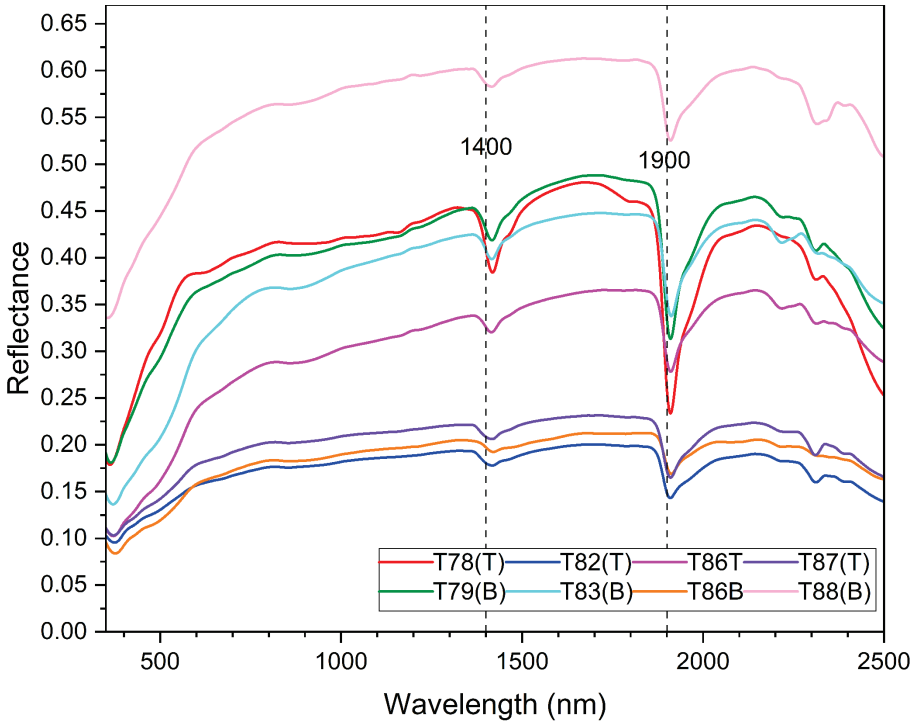

Figure 34: Composite VNIR plot of selected section 2 spectra. Dashed line at 1400 and 1900 nm represent the OH and H_2O absorption bands.

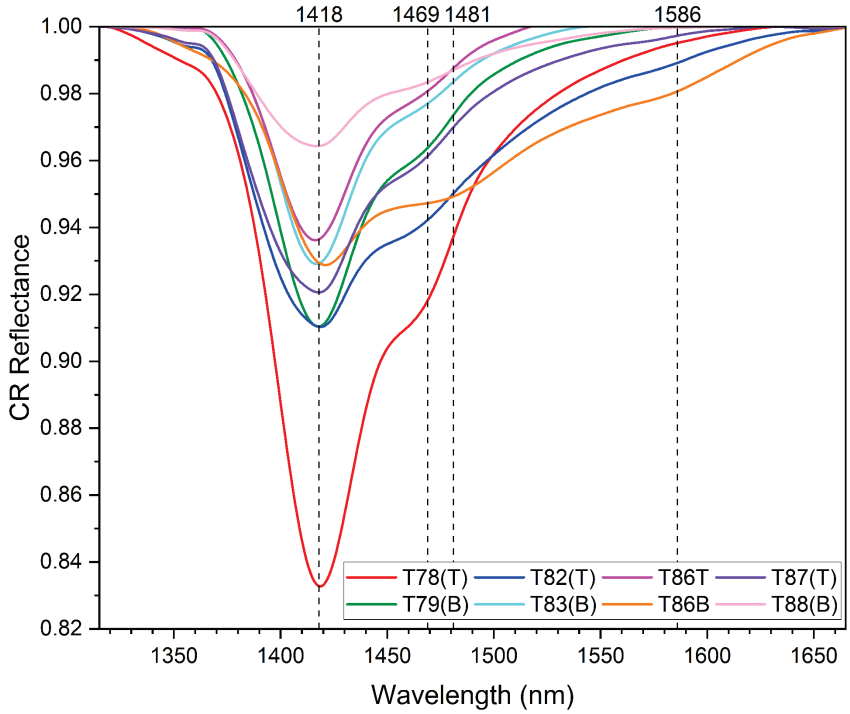

Figure 35: Continuum-removed (CR) Reflectance plot of Section 2 for the wavelengths 1320 to 1650nm.

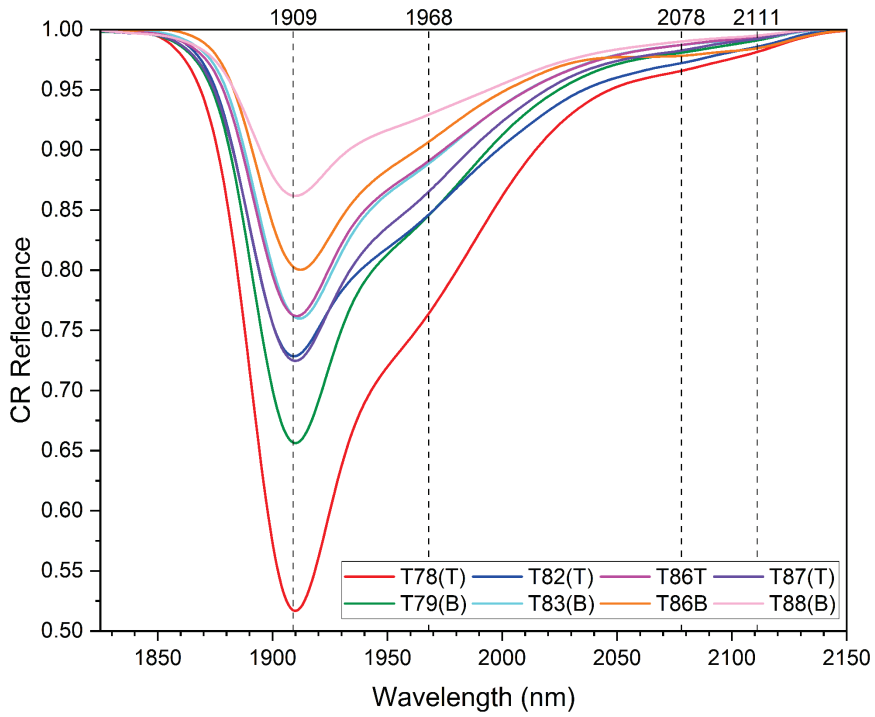

Figure 36: Continuum-removed (CR) Reflectance plot of Section 2 for the wavelengths 1830 to 2150nm.

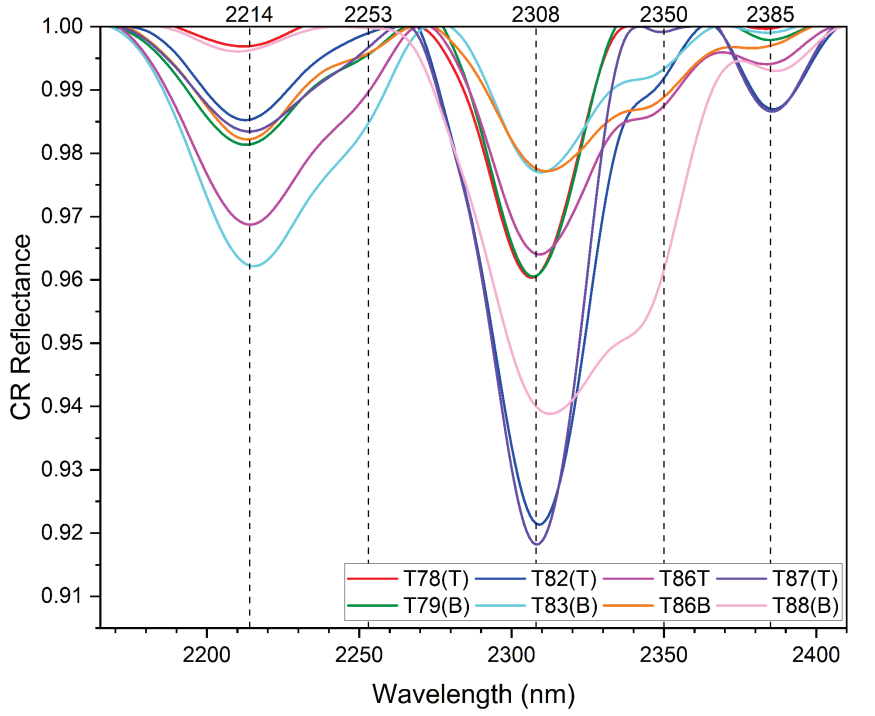

Figure 37: Continuum-removed (CR) Reflectance plot of Section 2 for the wavelengths 2170 to 2500nm.

1400 and 1900 nm absorptions are also observed in samples from the second section, again indicating OH and H_2O bands, likely associated with clay minerals such as illite and montmorillonite (Figure 36). It is difficult to distinguish between illite and montmorillonite using 1400 and 1900 nm absorptions since they're similar. The XRD data showed minor amounts of a smectite mineral, yet the expected montmorillonite spectral bands at 2077-2115 nm were not observed (Figure 36). Other potential clay minerals that could contribute to the observed absorption bands are saponite and sepiolite, which have been identified as widespread in Tecopa deposits by previous researchers (Sheppard and Gude, 1968; Starkey and Blackmon, 1979, 1984). Starkey and Blackmon (1979) noted sepiolite within one meter of the tuff layers, and we observed a potential sepiolite-related feature near 1900 to 2100 nm in section 2, while there is a saponite absorption feature near 2100 nm in section 1. Saponite-Mg has a diagnostic doublet near the 2300 nm and 2400 nm (Léveillé et al., 2013), which is found in both sections.

From the XRD mineral assemblage, calcite is present, but dolomite is absent in the second stratigraphic section. The 2300 to 2350 nm band is present in all samples (Figure 37). Albite, K-feldspar, and quartz do not have notable absorptions in the VNIR wavelength range (Figure 29 and Clark, 1999). The sample pairs for the modern basin analyzed by VNIR were T73(T) and T74(B), T76(T) and T77(B), T89(T) and T90(B), T100(T) and T119(B), and T101(T) and T102(B). Most modern basin samples had similar bands between 300 to 2500 nm, as seen in Figure 38. Samples T73(T) and T74(B) have similar spectral patterns, however T74(B) has a higher reflectance than T73(T). Samples T76(T) and T77(B) also have similar patterns, though sample T76(T) has a higher reflectance than T77(B) and sample T90(B) has a higher reflectance than T89(T). The spectral signals for T100(T) and T119(B) are similar but show minor differences between 300 – 1150 nm. Sample T101(T) has a higher reflectance than

T102(B). The illite spectral bands at 1418 nm and 1910 nm are observed in all samples (Figure 39 and Figure 40). The XRD data showed trace amounts of a smectite mineral, however, the expected spectral band at 2077 to 2115 nm for montmorillonite was not observed. From the XRD mineral assemblage, we expect calcite and trace amounts of dolomite in samples T65(T) and T66(B), T89(T) and T90(B), and T99(T), and the 2300 to 2350 nm band is observed in all these samples (Figure 41). As previously mentioned, K-feldspar, albite, and quartz do not have notable absorption bands in the VNIR range, therefore, none were observed.

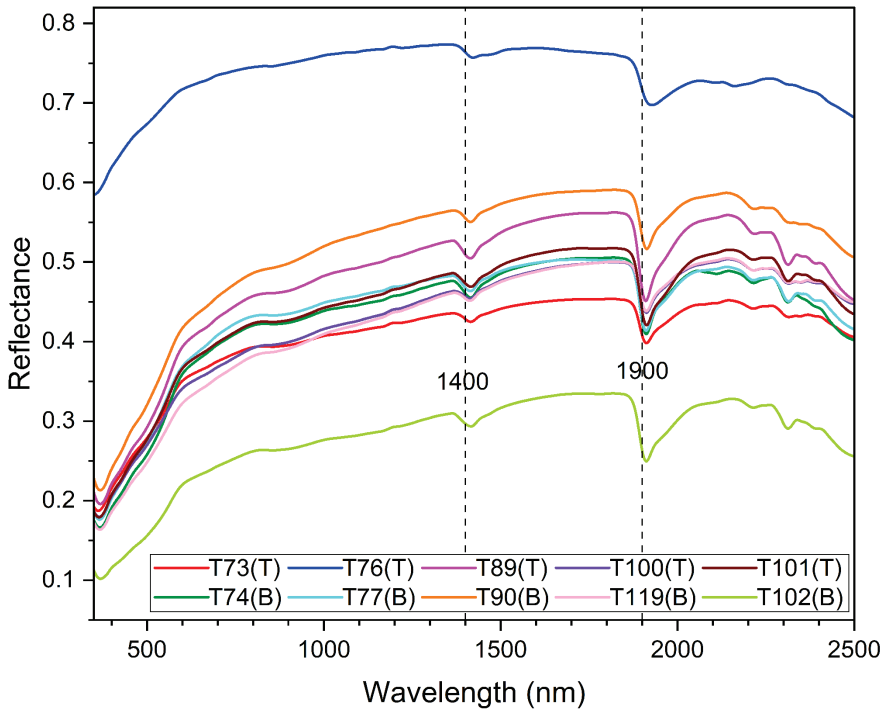

Figure 38: Composite VNIR plot of select additional samples from the Tecopa basin. Dashed line at 1400 and 1900 nm represent the OH and H_2O absorption bands.

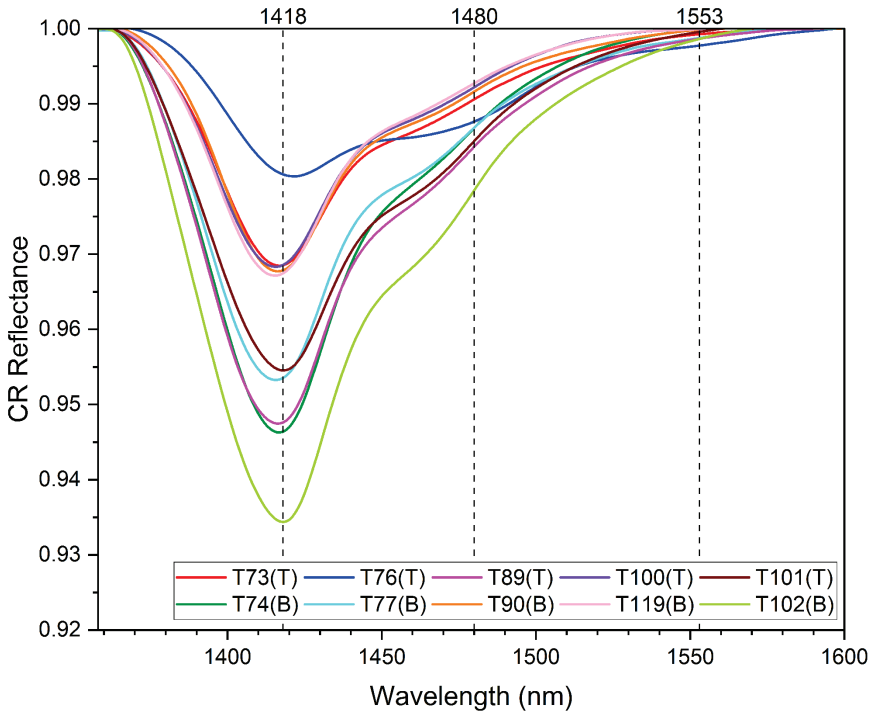

Figure 39: Continuum-removed (CR) Reflectance plot of the additional samples for the wavelengths 1360 to 1600nm.

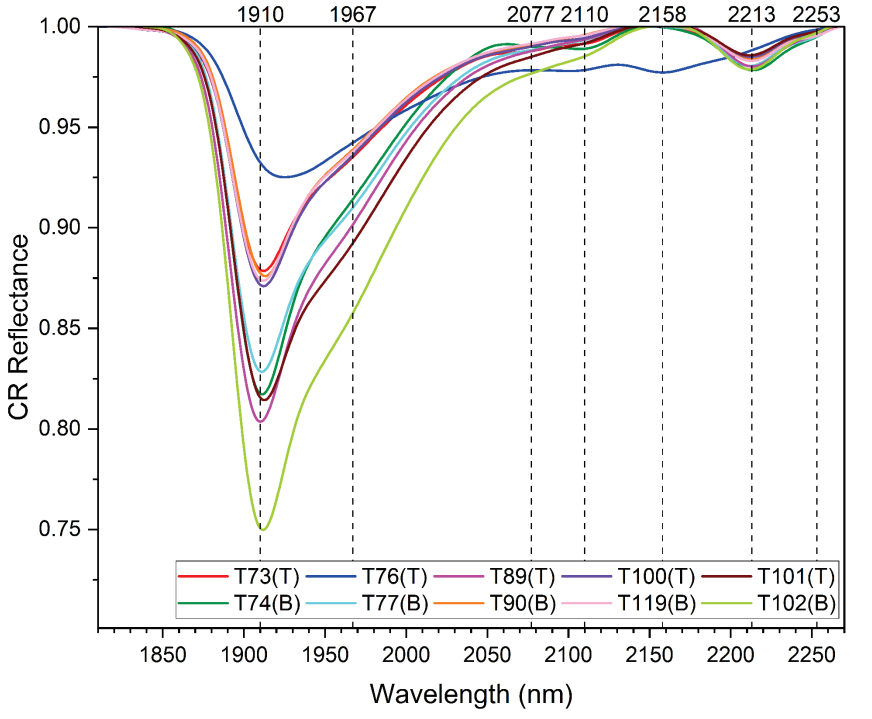

Figure 40: Continuum-removed (CR) Reflectance plot of the additional samples for the wavelengths 1810 to 2260nm.

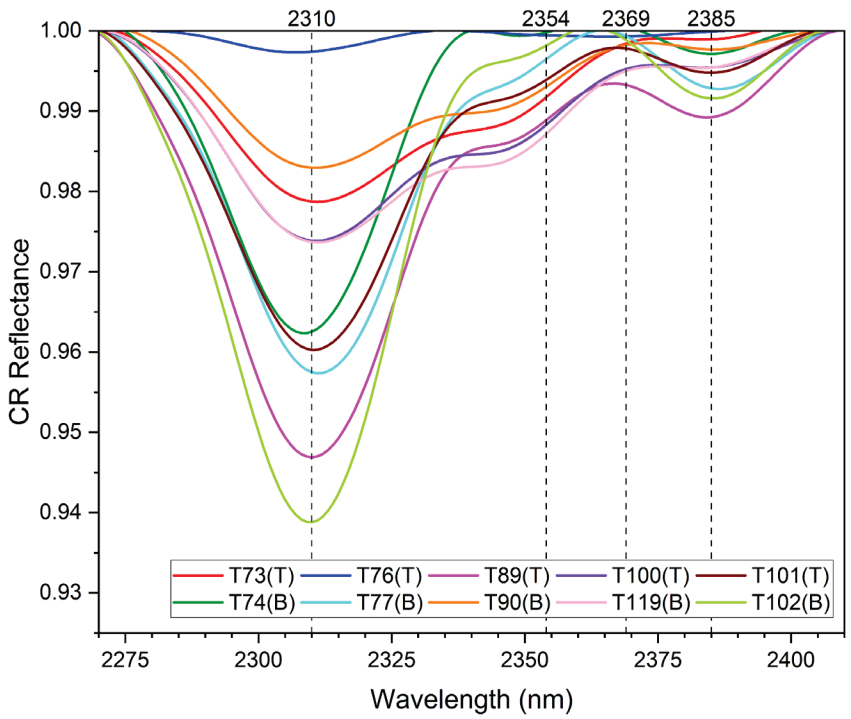

Figure 41: Continuum-removed (CR) Reflectance plot of the additional samples for the wavelengths 2275 to 2500nm.

4.5 Grain Size

The grain size results for sections 1 and 2 are presented in Appendix D Table 5 and Table 6. The distribution of the grain sizes for Section 1 and 2, are plotted in Appendix H. The distribution of grain sizes for paired samples, generally follow two patterns. In the first pattern, the pairs are very similar with only minor differences in the shape of the distribution or peak, as seen in Figure 42 B. In the second pattern, a sample is more spread out with peak differences, compared to its paired sample (Figure 42 A). Also, the soil texture of the paired samples is compared using a clay-silt-sand ternary diagram. The grain sizes for the first section lie in the silt, silty clay loam, and silty clay side of the clay-silt-sand ternary diagram (Figure 43). Most samples from the first section have a volume of 52.07% to 84.61% of grains that are silt size, followed by a volume of 12.35% to 41.68% that are clay size, and a volume of 3.05% to 17.88%

that are sand size. The silt grain sizes of the first pair at the top of section 1 are similar but this varies down section. The same percent range of silt is observed for the bottom of section 1. There is no obvious trend for the clay and sand sized grains, but T105T and T106B have a much higher clay percent than the rest of the samples.

The grain sizes for the second section lie in the sandy loam and silty loam side of the clay-silt-sand ternary diagram (Figure 43). The samples from the second section have a volume of 34.79% to 74.49% of grains that are silt size, followed by a volume of 11.04% to 62.16% that are sand size, and a volume of 2.84% to 24.28% that are clay size. The silt grain sizes for the pair at the top of section 2 (T78(T) and T79 (B)) differ by about 17%, and the silt proportion varies down section. The silt percentage is highest in the middle of section 2. There is no general trend for the sand sized grains, but T78(T) and T79(B) have a much higher sand percent than the rest of the samples. The clay percentage for T87(T), T88(B), and T82(T) is larger compared to the rest of the samples in section 2.

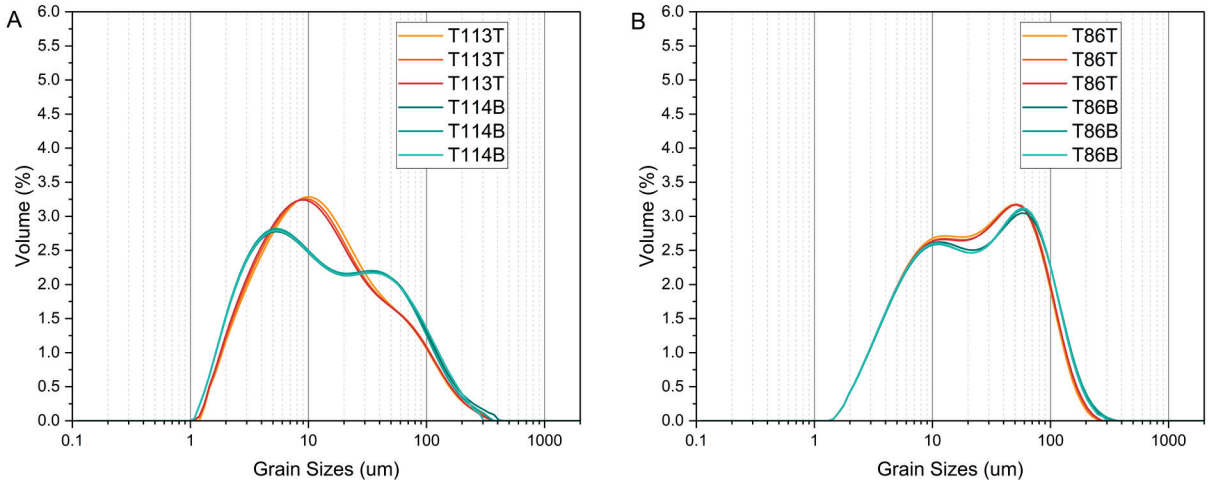

Figure 42: (A) An example of paired samples with differences in the distribution of grain sizes. The bulk of the surface (T113T) is 9.5 um, while the subsurface (T114B), has peaks at 5.25 and 34.5 um. (B) An example of paired samples with very similar distribution of grain sizes (surface T86T and subsurface T86B).

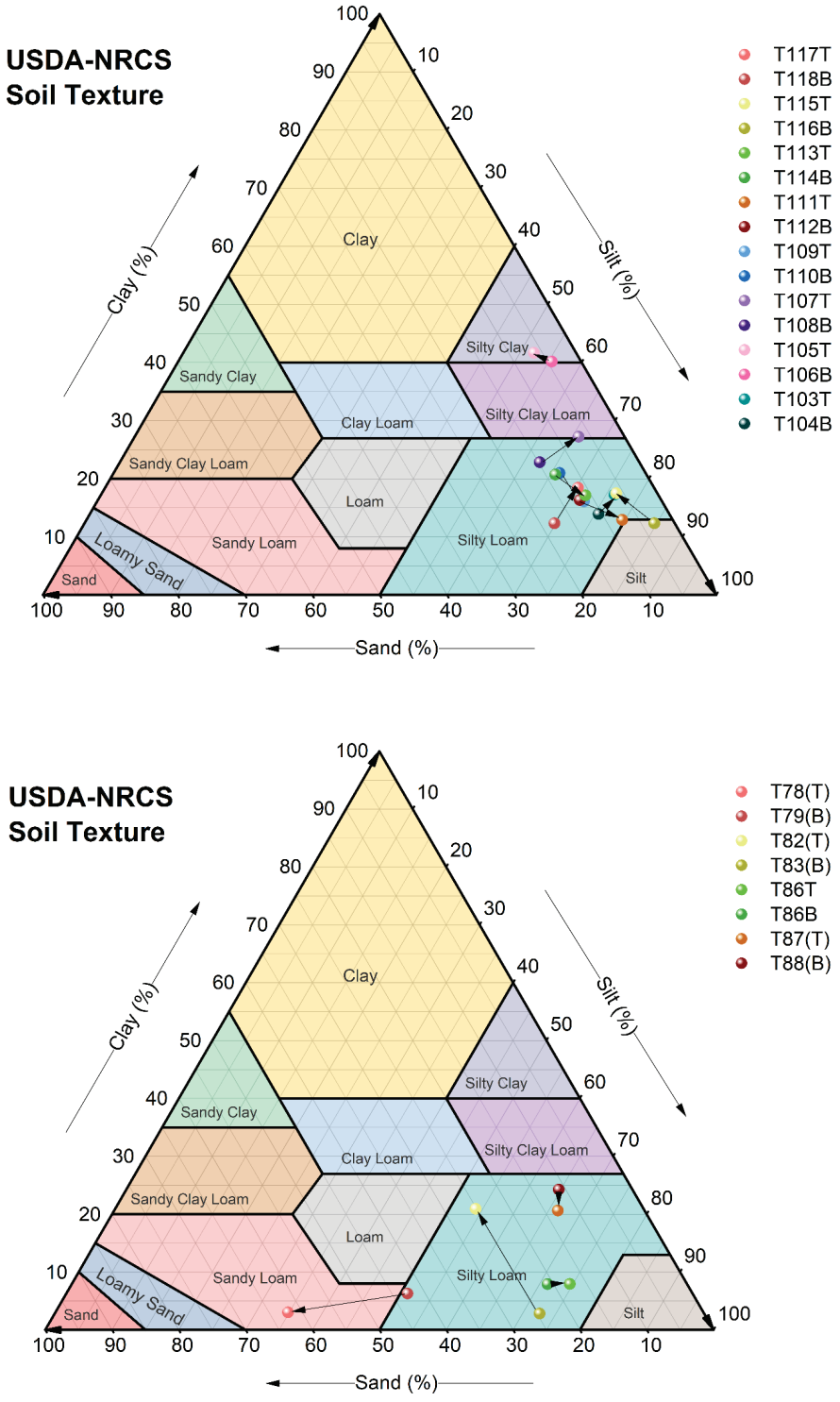

Figure 43: (Top) Soil texture ternary diagram for samples in section 1. (Bottom) Soil texture ternary diagram for samples in section 2. Arrows join surface samples to paired subsurface sample.

5. Discussion

5.1 Interpretation of XRD and major element data

Mineralogical assemblages of the Tecopa samples identified using XRD have similar abundant minerals across both stratigraphic sections and the modern basin deposits. However, there were slight differences in the abundances of dolomite, K-feldspar, clay minerals, amphibole, and zeolite minerals. The Tecopa basin sediment beds are interpreted to derive from the ancestral Amargosa River, local sediments, aeolian silt and sand, and volcanic ash (Larsen, 2008). The reworked local sediments were deposited as debris flows on alluvial fans and mudflats that also contributed to the lacustrine margin. The aeolian silt and sand are mainly found in the subaerial and lacustrine margin deposits (Larsen, 2008). Finally, the volcanic ash originated from various eruptions from western North America. The volcanic ash was washed and blown to the lake basin where it settled from suspension. These processes could lead to differences in the original mineralogy, sediment source, and grain size during the Pliocene and Pleistocene. Other factors that could play a role in these differences are spatial variations in water chemistry, since Tecopa is a closed-basin system. The pH, temperature, chemical solutions, and the original mineralogy can help drive the different mineral assemblages observed at Lake Tecopa. If this is the case, then the variations in lake level through the Pliocene and Pleistocene would have provided a distribution of minerals based on water chemistry (Larsen, 2008).

Field observations of section 1 showed a range of silty mudstones to fine grained siltstones, along with calcareous crusts, indicating interbedded shallow lacustrine, lacustrine margin, and mudflat deposits up section (Larsen and Olson, 2019). Comparing these observations to the XRD data we identify calcite + K-feldspar + illite +/- albite +/- amphibole +/-

smectite +/- analcime +/- halite +/- searlesite +/- quartz for the whole section. The presence of authigenic silicate minerals such as K-feldspar, illite, smectite, albite, analcime, and searlesite is consistent with saline-alkaline waters during deposition (Larsen, 2008). Authigenic albite likely formed as analcime reacted with silica-bearing waters during desiccation (Larsen, 2008). Searlesite is associated with altered volcanic ash and occurs with boron-bearing evaporite deposits along with the authigenic silicates such as analcime, clinoptilolite, phillipsite, clay minerals, and K-feldspar. Smectite minerals are found in or very close to the tuffs, and form by the alteration of volcanic ash when magnesium is present (Starkey and Blackmon, 1979). The presence of halite at the base of section 1 likely reflects modern processes, as halite would not have survived dissolution during weathering over time.

Section 1 shows evidence for overprinting, likely from sheet flow, as seen in the mineralogical differences between the paired surface and subsurface samples. Subsurface samples T118B and T116B contain analcime, which is absent in their paired surface samples. Surface sample T115T has a higher relative abundance of dolomite compared to subsurface sample T116B. Generally, the relative abundance of clay minerals, searlesite, K-feldspar, and albite is similar between paired surface and subsurface samples. Surface sample T107T is the only sample that contains albite that is completely missing from the corresponding subsurface sample. Subsurface samples T114B and T104B have amphibole, which is absent in the XRD patterns for their corresponding surface samples, T113T and T103T. Surface sample T109T has a higher relative abundance of amphibole than its corresponding subsurface sample, T110B. Also, T109T has detrital quartz, which is missing from T110B.

Section 2 consisted mostly of mudstones to sandstones. Towards the bottom of the section, surface samples had a popcorn weathering texture, consistent with smectite clays. Near

the top of the section was a white to green colored ash deposit, the first sample (T78(T)) was collected slightly lower in the section, along with the underlying red-brown soil (T79(B)), the red-brown color is likely from the hematite. Comparing these observations to the XRD data, we identify calcite + quartz (except T80(T)) + albite (except T78(T)) +/- illite +/- smectite +/- K-feldspar +/- clinoptilolite +/- amphibole +/- phillipsite +/- analcime +/- hematite.

Some differences between the second section and the first section include the abundance of quartz and the presence of clinoptilolite, phillipsite, and hematite. In the field section 2 was observed to be coarser grained than Section 1, and contained alternating mudstone, siltstone, and sandstone. This quartz is detrital, and differences in its abundance likely indicate differences in sediment source and/or volume of incoming sediments to the basin. Grain size differences are further discussed in discussion section 5.3.

Significant mineralogical differences are found between surface and subsurface samples in Section 2. These differences are more apparent in this section than in Section 1. Section 2 exhibits major differences in mineral assemblages and abundances. For example, for samples T82(T) and T82(B), calcite, K-feldspar, and minor quartz and amphibole are observed at the surface but none in the subsurface. The surface of Section 2 has been overprinted by rills (more commonly found in sandy soils) or sheet flow, forming a caliche (duricrust) crust from carbonate accumulation, and/or aeolian processes.

The samples from the modern basin include mudcracks, popcorn weathering textures, and evaporite crusts at the surface. Most of the modern basin samples are silty to very fine-grained sand. Comparing these observations to the XRD data, we identify calcite + quartz + albite + K-feldspar + illite + smectite +/- halite +/- dolomite +/- amphibole +/- phillipsite +/- clinoptilolite +/- analcime +/- cristobalite +/- burkeite ($Na_6(CO_3)(SO_4)_2$ +/- hanksite ($Na_{22}K(SO_4)_9(CO_3)_2Cl$)

+/- thenardite (Na_2SO_4) +/- tridymite. The modern basin deposits represent a mudflat environment with evidence for desiccation and dry conditions as indicated by the presence of the evaporite minerals hanksite, halite, burkeite, and thenardite.

In arid environments, ions from the leaching of sediments are unlikely to be carried away by moisture and can precipitate calcite and other minerals beneath the surface or calcrete (calcium-rich duricrust) and salts on the surface (Bachman and Machette, 1977; Gile et al., 1981; Thomas et al., 2005). Feldspars and micas can react with slightly acidic waters (hydrolysis) and form clay minerals and soluble salts. Alkaline environment can prevent hydrolysis and hinder the migration of elements in ionic form (Kalinin et al., 2021). Clay and salt minerals can migrate in the soil profile by water and can be removed from the surface by deflation (Kalinin et al., 2021). Clay and salt minerals can migrate in the soil profile by water or removed from the surface by deflation (Reheis, 2006; Kalinin et al., 2021). The XRF data was used to quantify the degree of weathering based on the mobility of elements during alteration and can also be used to track the paleoclimate changes. The weathering indices CIA, PIA, WIP, ICV, CPA, and weathering ratios were used to assess any weathering trends in the Tecopa samples. The CIA values for both sections were below 50, which indicates that the samples have limited evidence for chemical weathering. This is possibly an erroneous conclusion. Given the saline-alkaline water-rock interactions of the Tecopa basin during the Pliocene and Pleistocene, cations such as Ca^{2+}, Na^{+}, and K^{+} would not be removed from the system and could instead be concentrated and incorporated into secondary minerals such as zeolites, clays, calcite, and halite.

The CIA is usually used for marine shales, poorly altered silicate rocks, or in areas with greater precipitation where dilute fluids remove cations and residually concentrate aluminum. The CIA weathering index is not typically applied to semi-arid to arid locations where zeolites or

evaporites are abundant (Kalinin et al., 2021). The presence of zeolites and evaporites could drive up the Mg, Ca, Na and K concentrations in the samples (as seen in Figure 26), which is problematic for chemical weathering indices, which are based on the removal of mobile cations from clastic sediments. This shows that these indices need to be interpreted and applied carefully (Kalinin et al., 2021).

5.2 Interpretation of VNIR

The VNIR results are consistent with the XRD and XRF data with some minor differences. The identification of authigenic illite in all samples from section 1 indicates the presence K and Al-rich rocks under alkaline conditions, because illite typically forms through the alteration of feldspars by alkaline waters, through hydrolysis. It is difficult to distinguish between illite and montmorillonite, however, the absorption bands for montmorillonite are not present at 2077-2115 nm for the VNIR. XRD does detect some form of smectite for section 1, section 2, and the modern basin Tecopa samples. Starkey and Blackmon (1979) reported that saponite was the most common smectite mineral found around the Tecopa basin while sepiolite was found near tuff beds and likely formed during saline water-rock interactions. The montmorillonite signal may be masked by the other clays and minerals present, so a careful interpretation is needed when looking at VNIR data for a particular field site. It is also possible that the smectite clay observed in XRD is not montmorillonite. A striking observation is the high concentration of MgO in the XRF data, but a lack of Mg-bearing minerals identified by XRD for most samples. This could also indicate that the smectite mineral present could be an Mg-rich variety, rather than montmorillonite. Saponite (section 1) and sepiolite (section 2) are likely candidates and may be consistent with the VNIR plots. The Amargosa River drainage areas

could have supplied significant Mg, as they contain abundant dolomite, high magnesium smectite, and saponite. Saponite typically forms in three settings, which are (1) alkaline, evaporative lakes, (2) weathering or low-grade metamorphism of mafic and ultramafic rocks, and (3) hydrothermal alteration of volcanic rocks (Meunier, 2005). The most likely formation of saponite in Tecopa is (1), and this could be responsible for the doublet in the 2100 nm absorption band (while sepiolite is flat around that absorption band).

Sepiolite has four possible sources: (1) clastic deposition, (2) diagenesis from the volcanic ash, (3) the alteration of a smectite clay to sepiolite, and (4) direct precipitation at high pH within the basin (Meunier, 2005). Clastic deposition was ruled out since we would expect a uniform distribution of sepiolite within the beds and this hydrated magnesium silicate is concentrated near the ash beds and margins of the lake basin. Diagenesis from volcanic ash is also unlikely because the reactive alumina released by the dissolution of volcanic ash would have favored zeolite formation within the tuff beds (Starkey and Blackmon, 1984). The pH 9 to 10 is more suitable for forming zeolites or other aluminosilicates rather than precipitating sepiolite.

The alteration of a Mg-rich clay such as saponite to sepiolite is possible and is not ruled out, as it could provide the silica and magnesium under high pH conditions to authigenically form sepiolite. However, the most likely formation mechanism would have been the precipitation of sepiolite directly from solution. The mudstones, siltstones, and volcanic ash may have been deposited in waters with a pH of 9 or greater. Under these pH conditions and without high aluminum (required for zeolites), silica from the volcanic ash may have been supersaturated in solution and could have combined with magnesium to precipitate sepiolite (Starkey and Blackmon, 1984). This is because silica has a greater affinity for magnesium, which would form

a hydrated magnesium silicate. As this deposit was desiccated, water would have been removed, leaving behind sepiolite.

Unlike XRD and XRF analysis, VNIR can be used in remote sensing. Satellite and drone-mounted spectrometers can provide spectra for the ground surface, assuming that appropriate atmospheric corrections can be made. Hyperion hyperspectral (VNIR-SWIR) satellite data can be used to identify some minerals exposed on the Earth's surface (Kruse et al., 2003; Bishop et al., 2017). For Mars, the CRISM and OMEGA instruments onboard the MRO and Mars Express spacecraft have revealed a rich mineralogical record of past aqueous alteration (Ehlmann et al., 2009, 2011; Carter et al., 2015; Bishop et al., 2017). As a result, these instruments have been used to identify large swaths of sulfate and phyllosilicate-rich deposits, adding support for an early wet and warm Mars (Liu et al., 2021). However, using remote hyperspectral imaging without other supporting techniques requires careful interpretation of the data, as it is limited by spatial sampling, spatial resolution, and environmental conditions. Satellite-based remote sensing of the Earth's surface (e.g. Hyperion hyperspectral imaging) typically has a pixel size of ~10m^2 and it can thus be difficult to distinguish between bedrock, soil, vegetation, and water if they are present in a single pixel. The smaller the pixel size, the better control for what part of the sample is being measured, thus minimizing the spatial sampling effect (Bishop et al., 2017).

It is also challenging to use VNIR for remote sensing on Earth, due to the interference of atmospheric factors such as water vapor, gases, aerosols, and dust. There are windows in the VNIR bands and model techniques to subtract the atmospheric factors from the VNIR data to get around these challenges. These atmospheric factors are less likely to be an issue for spectral observations using OMEGA and CRISM on Mars, since the Martian atmosphere is much thinner and drier. Another consideration for VNIR is the depth of penetration. VNIR spectrometers can

only measure the top 1 to 100 microns of the material being examined. As a result, a thin layer of contaminants can obscure the dominant mineralogy of a rock. Even clay minerals can be masked by coatings such as dust, preventing their detection using remote sensing (Bishop et al., 2017). Therefore, remote sensing studies are often paired with another analytical technique such as XRD or XRF to provide some "ground truth" to help identify the different mineral assemblages or chemical composition of the samples from the field site, something that is much more easily accomplished on Earth than on Mars. A final consideration when using VNIR is the environmental conditions in the field compared to a laboratory setting, since the Tecopa samples were prepared and analyzed in a laboratory setting rather than in the field. The absorptions and scattering from different grain sizes (crushed), gases (vacuum chamber), moisture (dried) and aerosols (mixed into sample) are factors that can be reduced in the laboratory (Bishop et al., 2017), minimizing the signal to noise ratio. However, the absorptions and scattering that result from the grain size, gases, moisture, aerosols, and dust are a problem for remote sensing in the field, making it difficult to discern the true spectral signal. This makes it difficult to use terrestrial remote sensing, especially since two prominent atmospheric absorptions at 1400 and 1900 nm, tied to H_2O, overlap with absorption features related to the O-H molecular bond in clay minerals and other water-bearing minerals.

5.3 Interpretation of Grain Sizes

There are two main factors that affect the behavior of element mobility in soils, which are parent material and climate. The parent material of a given region gives us information about the different grain sizes and mineral distribution. The climate of a region gives us information about which elements migrate with salts, and the intensity of the soil weathering and biogenic

mobilization (Kalinin et al., 2021). Silt-sized grains are the main carriers of clay minerals, sand-sized grains are the main carriers of quartz. Incorporating grain size into this study is important because it affects the distribution of minerals and the chemical composition of the sediments (Kalinin et al., 2021). The grain size distribution in the Tecopa basin provides information about the way the chemical elements are distributed in this arid environment. Most of the grain size distributions in the first section are more silt and clay rich compared to the silt and sand in the second section. Incorporating grain size in this study is important because it can complicate the VNIR absorption bands. A decrease in grain size tends to increase reflectance and decrease the absorption band strengths. When the grain size increases, more light is absorbed and thus the reflectance decreases, since larger grains have a longer internal path where the photons can be absorbed based on Beers Law (Clark, 1999). The samples were sieved and crushed to enhance the signal-to-noise ratio, reduce grain size differences between samples and thus to reduce the contribution of grain size to the VNIR signal. Aa handheld VNIR spectrometer deployed in the field would have been susceptible to these grain size differences and any dust or increased clay content on the topmost surface.

5.4 The Importance of Multiple Techniques

It is important to use multiple techniques because this provides cross-validation from different kinds of data. However, it is also important to know the limitations of each technique and any complexities each may bring to the interpretation of the results. In this study, we used XRD to provide a qualitative view of the mineral assemblages of the Tecopa paleolake and modern basin samples. Using the bulk XRD data from this study, we could not identify specific smectite minerals, though previous studies in the area revealed saponite. The high concentrations

of MgO measured by XRF, and the lack of any MgO-bearing phases in the XRD data, also support the likely presence of saponite. The VNIR data also supports the presence of a Mg-rich smectite, with saponite being a likely candidate.

XRD measurements provided the mineral assemblages of the Tecopa paleolake and modern Amargosa river basin samples. In section 1, XRD data revealed calcite, smectite, K-feldspar, albite, illite, analcime, amphibole, halite, searlesite, and small amounts of quartz. Section two has calcite, quartz, albite, illite, smectite, K-feldspar, clinoptilolite, phillipsite, analcime, amphibole, and trace amounts of hematite. The pH, temperature, cationic ratios, and the original mineralogy all contribute to the different mineral assemblages observed in Lake Tecopa. Bulk geochemical analysis of the two stratigraphic sections allowed for the determination of elemental changes that can indicate chemical weathering or leaching of ions. Tecopa samples may have undergone some chemical weathering, but the CIA values are all less than 50. Secondary minerals including zeolites, clays, calcite, and halite are present, indicating saline-alkaline water-rock interactions may account for the lower CIA values by concentrating alkali and alkali earth elements relative to aluminum.

Since samples were powdered prior to VNIR analysis, any dust on the surface of the surface samples would have been mixed in, which could result in a different VNIR pattern than what would be observed by a field or remote sensing instrument. Comparing the pattern obtained from a field VNIR instrument against the laboratory pattern could help determine if dust is obstructing the surface. Using grain size analysis in tandem with XRD, XRF, and VNIR provides insight into mineral distribution and which elements are mobile in each environment. In Tecopa, the grain sizes for the first section lie in the silt, silty clay loam, and silty clay side of the clay-

silt-sand ternary diagram, while the grain sizes for the second section lie in the sandy loam and silty loam side. The grain sizes can also reveal the environment in which they were deposited.

5.5 Development of the Tecopa Basin

The two stratigraphic sections in this study are fundamentally different in mineral assemblage and grain size distribution. Sections 1 and 2 represent slightly different environments in the lake. Since lake levels are sensitive to climatic and hydrologic conditions, these can be reconstructed through the lake deposits. Comparing the two stratigraphic sections reveals that one is silty to finer-grained (section 1), which indicates an open-water, shallow lacustrine, and mudflat environment. Section 1 is dominated by mudstone, siltstone, and white colored altered volcanic ash beds. Desiccation cracks were observed on top of the mudstones, which suggests modern drying cycles (Larsen, 2008). Saline-alkaline paleolake deposits typically have concentric rings with fresher mineral signatures (i.e., phillipsite and clinoptilolite) at the lake margins. More saline-alkaline mineral assemblages, including minerals such as analcime and authigenic K-feldspar, form closer to the basin center. The second section is more silt to sand rich, which is more indicative of a lake margin environment. Section 2 is dominated by mudstone, siltstone, sandstone, and white to green colored altered volcanic ash beds. Phillipsite and clinoptilolite are observed in the mineral assemblage of this section, consistent with less saline-alkaline conditions closer to the margins.

5.6 The Tecopa Basin and Implications for Mars

We can use the physical and hydrological conditions that ultimately control the sedimentation and therefore the mineralogy of the area to observe the formation of clays for both planets (Bristow and Milliken, 2011). From orbital data of Mars, we observe primarily phyllosilicate minerals in the Noachian which are indicative of a neutral to alkaline water-rich environment. The dominant clays on Mars are Fe/Mg-smectites and they can form in different environments such as, (1) bodies of standing water, (2) alteration of volcanic rocks, and (3) impact-induced hydrothermal sites (Bristow and Milliken, 2011). Comparing that to mineral deposits on Earth such as in the Tecopa paleolake, Mg-smectites (i.e., saponite) form authigenically in a standing body of water under alkaline or saline conditions. This is due to the water evaporation in a closed basin where the bicarbonate (HCO_3^-) concentration is greater than the Ca^{2+}, resulting in precipitation of calcium carbonate ($CaCO_3$). As a result, the high-pH and Mg-rich waters favored the formation of Mg-rich clay minerals (Bristow and Milliken, 2011).

In Gale crater, we can observe how climatic change affects the mineralogy, geochemistry, and lacustrine history of a closed basin lake. This paleolake has phyllosilicates, sulfates, carbonates, and other salts expected in paleolakes but which are difficult to detect using remote sensing. Thus, the Tecopa paleolake basin and the modern Amargosa river basin can serve as a potential analog to the paleolake in Gale crater. The bulk elemental composition, including Al_2O_3 (wt %) vs TiO_2 (wt %) and Zr (ppm) vs TiO_2 (wt %) ratios of the Tecopa paleolake and modern basin samples, can be used to determine the likely parent rock type. Based on the ratios of the above oxides, the parent rock type for both sections is likely felsic. Since the parent material is likely felsic and the CIA weathering index yielded values below 50 for both sections, little chemical weathering has occurred. CIA values less than 50 (Figure 25 and Figure

26) suggest that the samples have higher concentrations of CaO and Na_2O compared to Al_2O_3 than would be expected if they formed from the weathering of felsic materials (commonly feldspar-rich), and this can likely be tied to the formation of zeolites, salts, and other authigenic minerals in contact with alkaline waters. The mudstones of the Sheepbed and Gillespie Lake Members of the Yellowknife Bay Formation also have CIA values below 50 (Figure 8), but this could relate to different starting lithologies compared to Lake Tecopa (e.g. felsic vs. mafic; (McLennan et al., 2014). However, CIA values must be intepreted with caution as corrections need to be done to account for the calcium sulfate, which tends to lower the CIA values in the Yellowknife Bay Formation. Additionally, the presence of amorphous minerals can skew the CIA values to be much lower than they should be because there could be more elements present that are not bound to crystalline silicates or salt minerals (Siebach and McLennan, 2018). In the Murray Members, above the Yellowknife Bay Formation, Thorpe et al. (2021) suggested the uncorrected CIA values are not consistent, likely reflecting significant and variable addition of secondary salts which lower the CIA values. McLennan et al. (2014) looked at the oxide ratios such as K_2O/Al_2O_3 and TiO_2/Al_2O_3 using the AXPS data and see if they come to the same interpretation as the CIA. The Glenelg Member has higher K_2O/Al_2O_3 ratio with variable TiO_2/Al_2O_3 compared to the Sheepbed and Gillespie Members. McLennan et al. (2014) interpretated that up section, the sediments are derived from a more alkali-rich basalts, but it is possible that salts, zeolites or amorphous minerals could be responsible for the lower CIA values.

As mentioned earlier in this study, Jezero crater is interpreted to be an open-basin paleolake with two inflow and one outflow channels (Goudge et al., 2012b, 2015b). These channels could be part of the valley networks observed since the Mariner 9 and the Viking missions in the 1970s. This also suggests an early Mars warmer and wetter climate that could

have supported a hydrological cycle in the late Noachian or early Hesperian, but it is uncertain for how long the lake persisted (Schon et al., 2012; Goudge et al., 2015b). Through CRISM orbital data of Jezero crater (Horgan et al., 2020) observed Fe/Mg-phyllosilicates along with Mg-carbonates that resemble those of playas on Earth. Thus, the Tecopa paleolake can serve as a potential analog of Jezero crater to study clay minerals and carbonates from paleolakes.

6. Conclusions

Using paired surface and subsurface samples collected from two stratigraphic sections and the modern land surface at paleolake Tecopa, this study employed multiple analytical techniques to determine if the soil crust can obstruct the remote sensing signal of the strata of paleolake Tecopa beds and the modern basin. This study additionally identified differences in the mineralogical, geochemical, spectral, and grain size patterns of the strata of paleolake Tecopa beds and the modern basin. Based on the results from this study, we can conclude that:

I. Our XRD, XRF, VNIR, and grain size data for two paleolake Tecopa sections (1 and 2) support the sedimentological reconstructions of Larsen (2008) and Larsen and Olson (2019) for this area. Section 1 has smectite, calcite, analcime, K-feldspar, searlesite, and illite. Authigenic K-feldspar and analcime, which typically form under more saline-alkaline conditions, closer to the center of the lake basin. Section 2 has phillipsite and clinoptilolite, which is associated with less saline-alkaline conditions closer to the lake margins.

II. High MgO concentrations for many samples that lack obvious Mg-bearing minerals in XRD are likely explained by Mg-rich clay minerals. Smectites have clearly identifiable bands in the VNIR spectra and Mg-rich smectite (i.e., saponite) was likely detected in Section 1. Sepiolite was likely detected in the VNIR patterns for samples from Section 2.

III. Surface samples for both sections generally show some evidence for sheetwash deposition. The paired surface and subsurface samples show differences in grain size distribution, mineral assemblages, and/or relative mineral abundances. These

mineralogical and grain size differences are more apparent in Section 2 and less apparent for Section 1.

IV. Albite, K-feldspar, and quartz, which are more abundant in Section 1, do not have notable absorptions in the VNIR range. Zeolites (e.g., analcime and clinoptilolite), smectites, and carbonate minerals do have absorptions in this range (largely due to their O-H and carbonate components), and changes in their relative abundances can thus change or shift the overall absorption patterns. These changes are more apparent in Section 2, where these minerals are more abundant. Therefore, the surface VNIR signal better represents the subsurface in the center of the lake basin (Section 1) than at the margin (Section 2).

V. Given the saline-alkaline water-rock interactions of the Tecopa basin during the Pliocene and Pleistocene, cations such as Ca^{2+}, Na^{+}, and K^{+} would not have been leached out of the system and would have instead been concentrated and incorporated into secondary minerals such as zeolites, clays, calcite, and halite. The presence of zeolites and evaporites could drive up the MgO, CaO, Na_2O, and K_2O concentrations in the samples which is problematic for chemical weathering indices (e.g., CIA), which are based on the removal of mobile cations from clastic sediments.

The Tecopa paleolake basin and the modern Amargosa river basin were chosen because the later stages of Lake Tecopa were highly alkaline and saline due to evaporation. The Tecopa paleolake basin can serve as a potential analog of Gale and Jezero crater to study clay minerals and salt surfaces from playas. Evaluating the surface characteristics of paleolakes on Earth can

serve as ground truth for the orbital data and in-situ data on Mars and is essential for selecting validating landing sites for current and future missions.

7. References

Bachman, G.O., and Machette, M.N., 1977, Calcretes in the southwestern United States: Washington, DC, United States Department of the Interior Geological Survey, 163 p., doi:10.3133/OFR77794.

Baiyegunhi, C., Liu, K., and Gwavava, O., 2017, Geochemistry of sandstones and shales from the Ecca Group, Karoo Supergroup, in the Eastern Cape Province of South Africa: Implications for provenance, weathering and tectonic setting: Open Geosciences, v. 9, doi:10.1515/geo-2017-0028.

Belcher, W.R., Sweetkind, D.S., Hopkins, C.B., and Poff, M.E., 2019, Hydrogeology of Lower Amargosa Valley and groundwater discharge to the Amargosa Wild and Scenic River, Inyo and San Bernardino Counties, California, and adjacent areas in Nye and Clark Counties, Nevada: U.S. Geological Survey Scientific Investigations Report 2018–5151, p. 131, doi:10.3133/SIR20185151.

Bibring, J.-P. et al., 2006, Global Mineralogical and Aqueous Mars History Derived from OMEGA/Mars Express Data: Science, v. 312, p. 400–404, doi:10.1126/science.1122659.

Bishop, J.L., Michalski, J.R., and Carter, J., 2017, Remote Detection of Clay Minerals: Developments in clay science, v. 8, p. 482, doi:10.1016/B978-0-08-100355-8.00014-X.

Le Blond, J.S., Cuadros, J., Molla, Y.B., Berhanu, T., Umer, M., Baxter, P.J., and Davey, G., 2015, Weathering of the Ethiopian volcanic province: A new weathering index to characterize and compare soils: American Mineralogist, v. 100, p. 2518–2532, doi:10.2138/am-2015-5168ccby.

Bogaard, P. van den, and Schirnick, C., 1995, 40Ar/39Ar laser probe ages of Bishop Tuff quartz phenocrysts substantiate long-lived silicic magma chamber at Long Valley, United States:

Geology, v. 23, p. 759–762, doi:10.1130/0091-7613(1995)023<0759:aalpao>2.3.co;2.

Bridges, N.T., Crisp, J.A., and Bell, J.F., 2001, Characteristics of the Pathfinder APXS sites: Implications for the composition of Martian rocks and soils: Journal of Geophysical Research E: Planets, v. 106, p. 14621–14665, doi:10.1029/2000JE001393/FORMAT/PDF.

Bristow, T.F., and Milliken, R.E., 2011, Terrestrial perspective on authigenic clay mineral production in ancient Martian lakes: Clays and Clay Minerals, v. 59, p. 339–358, doi:10.1346/CCMN.2011.0590401.

Buggle, B., Glaser, B., Hambach, U., Gerasimenko, N., and Marković, S., 2011, An evaluation of geochemical weathering indices in loess-paleosol studies: Quaternary International, v. 240, p. 12–21, doi:10.1016/J.QUAINT.2010.07.019.

Burns, R.G., and Fisher, D.S., 1993, Rates of oxidative weathering on the surface of Mars: Journal of Geophysical Research: Planets, v. 98, p. 3365–3372, doi:10.1029/92JE02055.

Byers, H.L., McHenry, L.J., and Grundl, T.J., 2016, Forty-Nine Major and Trace Element Concentrations Measured in Soil Reference Materials NIST SRM 2586, 2587, 2709a, 2710a and 2711a Using ICP-MS and Wavelength Dispersive-XRF: Geostandards and Geoanalytical Research, v. 40, p. 433–445, doi:10.1111/j.1751-908X.2016.00376.x.

Campbell, I.B., and Claridge, G.G.C., 1987, Antarctica : soils, weathering processes, and environment: v. 16, p. 368.

Carr, M.H., and Head, J.W., 2010, Geologic history of Mars: Earth and Planetary Science Letters, v. 294, p. 185–203, doi:10.1016/j.epsl.2009.06.042.

Carter, J., Loizeau, D., Mangold, N., Poulet, F., and Bibring, J.P., 2015, Widespread surface weathering on early Mars: A case for a warmer and wetter climate: Icarus, v. 248, p. 373–382, doi:10.1016/j.icarus.2014.11.011.

Chen, H., Song, Q., Tang, G., Feng, Q., and Lin, L., 2013, The Combined Optimization of Savitzky-Golay Smoothing and Multiplicative Scatter Correction for FT-NIR PLS Models: ISRN Spectroscopy, v. 2013, p. 1–9, doi:10.1155/2013/642190.

Clark, B.C. et al., 2005, Chemistry and mineralogy of outcrops at Meridiani Planum: Earth and Planetary Science Letters, v. 240, p. 73–94, doi:10.1016/j.epsl.2005.09.040.

Clark, R.N., 1999, Spectroscopy of Rocks and Minerals, and Principles of Spectroscopy, in Manual of Remote Sensing (A. N. Rencz, Ed.): Remote Sens. Earth Sci., v. 3, 3–58 p.

Clark, R.N., King, T. V., Klejwa, M., Swayze, G.A., and Vergo, N., 1990, High spectral resolution reflectance spectroscopy of minerals: Journal of Geophysical Research, v. 95, doi:10.1029/JB095IB08P12653.

Covelli, S., and Fontolan, G., 1997, Application of a normalization procedure in determining regional geochemical baselines: Environmental Geology 1997 30:1, v. 30, p. 34–45, doi:10.1007/S002540050130.

Cox, R., Lowe, D.R., and Cullers, R.L., 1995, The influence of sediment recycling and basement composition on evolution of mudrock chemistry in the southwestern United States: Geochimica et Cosmochimica Acta, v. 59, p. 2919–2940, doi:10.1016/0016-7037(95)00185-9.

Craddock, R.A., and Howard, A.D., 2002, The case for rainfall on a warm, wet early Mars: Journal of Geophysical Research E: Planets, v. 107, p. 21-1-21–36, doi:10.1029/2001JE001505.

Craddock, R.A., and Maxwell, T.A., 1993, Geomorphic evolution of the Martian highlands through ancient fluvial processes: Journal of Geophysical Research, v. 98, p. 3453–3468, doi:10.1029/92JE02508.

Daskalakis, K.D., and O'Connor, T.P., 1995, Normalization and elemental sediment contamination in the coastal United States.: Environmental science & technology, v. 29, p. 470–477, doi:10.1021/es00002a024.

Douglas, S., and Yang, H., 2002, Mineral biosignatures in evaporites: Presence of rosickyite in an endoevaporitic microbial community from Death Valley, California: Geology, v. 30, p. 1075, doi:10.1130/0091-7613(2002)030<1075:MBIEPO>2.0.CO;2.

Ehlmann, B.L. et al., 2009, Identification of hydrated silicate minerals on Mars using MRO-CRISM: Geologic context near Nili Fossae and implications for aqueous alteration: Journal of Geophysical Research: Planets, v. 114, p. 0–08, doi:10.1029/2009JE003339.

Ehlmann, B.L., Mustard, J.F., Murchie, S.L., Bibring, J.-P.P., Meunier, A., Fraeman, A.A., and Langevin, Y., 2011, Subsurface water and clay mineral formation during the early history of Mars: Nature, v. 479, p. 53–60, doi:10.1038/nature10582.

Fang, Q., Hong, H., Zhao, L., Kukolich, S., Yin, K., and Wang, C., 2018, Visible and Near-Infrared Reflectance Spectroscopy for Investigating Soil Mineralogy: A Review: Journal of Spectroscopy, v. 2018, p. 1–14, doi:10.1155/2018/3168974.

Fassett, C.I., and Head, J.W., 2008, Valley network-fed, open-basin lakes on Mars: Distribution and implications for Noachian surface and subsurface hydrology: Icarus, v. 198, p. 37–56, doi:10.1016/j.icarus.2008.06.016.

Fedo, C.M., Nesbitt, H.W., and Young, G.M., 1995, Unravelling the effects of potassium metasomatism in sedimentary rocks and paleosols, with implications for paleoweathering conditions and provenance: Geology, v. 23, p. 921–924, doi:10.1130/0091-7613(1995)023<0921:UTEOPM>2.3.CO.

Foley, C.N., Economou, T., and Clayton, R.N., 2003, Final chemical results from the Mars

Pathfinder alpha proton X-ray spectrometer: Journal of Geophysical Research E: Planets, v. 108, doi:10.1029/2002JE002019/FORMAT/PDF.

Gansecki, C.A., Mahood, G.A., and McWilliams, M., 1998, New ages for the climactic eruptions at Yellowstone: Single-crystal 40Ar/39Ar dating identifies contamination: Geology, v. 26, p. 343–346, doi:10.1130/0091-7613(1998)026<0343:naftce>2.3.co;2.

Gellert, R. et al., 2004, Chemistry of rocks and soils in Gusev crater from the alpha particle x-ray spectrometer: Science, v. 305, p. 829–832, doi:10.1126/science.1099913.

Gibert, L., Alfaro, P., García-Tortosa, F.J., and Scott, G., 2011, Superposed deformed beds produced by single earthquakes (Tecopa Basin, California): Insights into paleoseismology: Sedimentary Geology, v. 235, p. 148–159, doi:10.1016/j.sedgeo.2010.08.003.

Gile, L.H., Hawley, J.W., and Grossman, R.B., 1981, Soils and geomorphology in the Basin and Range area of southern New Mexico: New Mexico Bureau of Mines & Mineral Resources, Memoir (New Mexico. Bureau of Mines and Mineral Resources), v. Memoir 39, 222 p. p.

Girty, G.H., Ridge, D.L., Knaack, C., Johnson, D., and Al-Riyami, R.K., 1996, Provenance and depositional setting of Paleozoic chert and argillite, Sierra Nevada, California: Journal of Sedimentary Research, v. 66, p. 107–118, doi:10.1306/D42682CA-2B26-11D7-8648000102C1865D.

Golombek, M. et al., 2020, Geology of the InSight landing site on Mars: Nature Communications, v. 11, p. 1–11, doi:10.1038/s41467-020-14679-1.

Gorevan, S.P. et al., 2003, Rock Abrasion Tool: Mars exploration rover mission: Journal of Geophysical Research E: Planets, v. 108, doi:10.1029/2003je002061.

Goudge, T.A., Aureli, K.L., Head, J.W., Fassett, C.I., and Mustard, J.F., 2015a, Classification and analysis of candidate impact crater-hosted closed-basin lakes on Mars: Icarus, v. 260, p.

346–367, doi:10.1016/j.icarus.2015.07.026.

Goudge, T.A., Head, J.W., Mustard, J.F., and Fassett, C.I., 2012a, An analysis of open-basin lake deposits on Mars: Evidence for the nature of associated lacustrine deposits and post-lacustrine modification processes: Icarus, v. 219, p. 211–229, doi:10.1016/j.icarus.2012.02.027.

Goudge, T.A., Mustard, J.F., Head, J.W., and Fassett, C.I., 2012b, Constraints on the history of open-basin lakes on Mars from the composition and timing of volcanic resurfacing: Journal of Geophysical Research E: Planets, v. 117, doi:10.1029/2012JE004115.

Goudge, T.A., Mustard, J.F., Head, J.W., Fassett, C.I., and Wiseman, S.M., 2015b, Assessing the mineralogy of the watershed and fan deposits of the Jezero crater paleolake system, Mars: Journal of Geophysical Research: Planets, v. 120, p. 775–808, doi:10.1002/2014JE004782.

Grotzinger, J.P. et al., 2014, A Habitable Fluvio-Lacustrine Environment at Yellowknife Bay, Gale Crater, Mars: Science, v. 343, p. 1242777–1242777, doi:10.1126/science.1242777.

Grotzinger, J.P. et al., 2015, Deposition, exhumation, and paleoclimate of an ancient lake deposit, Gale crater, Mars: Science, v. 350, p. aac7575, doi:10.1126/science.aac7575.

Gunatilaka, A., Al-Temeemi, A., Saleh, A., and Nassar, N., 1985, A new occurrence of bassanite in recent evaporitic environments, Kuwait, Arabian Gulf: Journal of the University of Kuwait (Science), v. 12, p. 157–166.

de Haas, T., Ventra, D., Carbonneau, P.E., and Kleinhans, M.G., 2014, Debris-flow dominance of alluvial fans masked by runoff reworking and weathering: Geomorphology, v. 217, p. 165–181, doi:10.1016/j.geomorph.2014.04.028.

Han, F.X., and Singer, A., 2007, Solution Chemistry Of Trace Elements In Arid Zone Soils, *in* Biogeochemistry of Trace Elements in Arid Environments, Springer Netherlands, p. 69–

105, doi:10.1007/978-1-4020-6024-3_3.

Hayashi, K.I., Fujisawa, H., Holland, H.D., and Ohmoto, H., 1997, Geochemistry of approximately 1.9 Ga sedimentary rocks from northeastern Labrador, Canada: Geochimica et cosmochimica acta, v. 61, p. 4115–4137, doi:10.1016/S0016-7037(97)00214-7.

Head, J.W., and Wilson, L., 2011, The Noachian-Hesperian Transition on Mars: Geological Evidence for a Punctuated Phase of Global Volcanism as a Key Driver in Climate and Atmospheric Evolution, *in* Lunar and Planetary Science Conference, Lunar and Planetary Science Conference, p. 1214.

Hillhouse, J.W., 1987, Late Tertiary and Quaternary geology of the Tecopa basin, southeastern California:, doi:10.2172/60181.

Holm-Alwmark, S. et al., 2021, Stratigraphic Relationships in Jezero Crater, Mars: Constraints on the Timing of Fluvial-Lacustrine Activity From Orbital Observations: Journal of Geophysical Research: Planets, v. 126, doi:10.1029/2021JE006840.

Horgan, B.H.N., Anderson, R.B., Dromart, G., Amador, E.S., and Rice, M.S., 2020, The mineral diversity of Jezero crater: Evidence for possible lacustrine carbonates on Mars: Icarus, v. 339, p. 113526, doi:10.1016/j.icarus.2019.113526.

Hunt, G.R., and Salisbury, J.W., 1970, Visible and near infrared spectra of minerals and rocks. I. Silicate minerals: Modern Geology, v. 1, p. 283–300.

Hunt, G.R., and Salisbury, J.W., 1971, Visible and near infrared spectra of minerals and rocks. II. Carbonates: Modern Geology, v. 2, p. 23–30.

Hunt, G.R., Salisbury, J.W., and Lenhoff, C.J., 1972, Visible and near infrared spectra of minerals and rocks. V. Halides, phosphates, arsenates, vanadates and borates: Modern Geology, v. 3, p. 121–132.

Hunt, G.R., Salisbury, J.W., and Lenhoff, C.J., 1973, Visible and near infrared spectra of minerals and rocks. VI. Additional silicates: Modern Geology, v. 4, p. 85–106.

Kalinin, P.I., Kudrevatykh, I.Y., Malyshev, V. V., Pilguy, L.S., Buhonov, A. V., Mitenko, G. V., and Alekseev, A.O., 2021, Chemical weathering in semi-arid soils of the Russian plain: CATENA, v. 206, p. 105554, doi:10.1016/J.CATENA.2021.105554.

Kodikara, G.R.L., Woldai, T., van Ruitenbeek, F.J.A., Kuria, Z., van der Meer, F., Shepherd, K.D., and van Hummel, G.J., 2012, Hyperspectral remote sensing of evaporate minerals and associated sediments in Lake Magadi area, Kenya: International Journal of Applied Earth Observation and Geoinformation, v. 14, p. 22–32, doi:10.1016/J.JAG.2011.08.009.

Kokaly, R.F. et al., 2017, USGS Spectral Library Version 7: Data Series, doi:10.3133/DS1035.

Kruse, F.A., and P.L.H., 1992, The IGCP-264 Spectral Properties Database: IUGS/UNESCO, p. 211.

Kruse, F.A., Boardman, J.W., and Huntington, J.F., 2003, Comparison of airborne hyperspectral data and EO-1 Hyperion for mineral mapping: IEEE Transactions on Geoscience and Remote Sensing, v. 41, p. 1388–1400, doi:10.1109/TGRS.2003.812908.

Larsen, D., 2008, Revisiting silicate authigenesis in the Pliocene-Pleistocene Lake Tecopa beds, southeastern California: Depositional and hydrological controls: Geosphere, v. 4, p. 612–639, doi:10.1130/GES00152.1.

Larsen, D., and Olson, K., 2019, Evolution of the Pleistocene Lake Tecopa beds, southeastern California: A stratigraphic and sedimentologic perspective, *in* Starratt, S.W. and Rosen, M.R. eds., From Saline to Freshwater: The Diversity of Western Lakes in Space and Time, Geological Society of America, v. 536, p. 0, doi:10.1130/2019.2536(17).

Léveillé, R.J., Cloutis, E., Mann, P., Sobrón, P., Lefebvre, C., and Koujelev, A., 2013, Spectral

Reflectance and Chemical Properties of Magnesium-Rich Phyllosilicates, *in* Lunar and Planetary Science Conference,.

Liu, J., Michalski, J.R., Tan, W., He, H., Ye, B., and Xiao, L., 2021, Anoxic chemical weathering under a reducing greenhouse on early Mars: Nature Astronomy 2021 5:5, v. 5, p. 503–509, doi:10.1038/s41550-021-01303-5.

McFadden, L.D., Eppes, M.C., Gillespie, A.R., and Hallet, B., 2005, Physical weathering in arid landscapes due to diurnal variation in the direction of solar heating: Bulletin of the Geological Society of America, v. 117, p. 161–173, doi:10.1130/B25508.1.

McHenry, L.J., 2009, Element mobility during zeolitic and argillic alteration of volcanic ash in a closed-basin lacustrine environment: Case study Olduvai Gorge, Tanzania: Chemical Geology, v. 265, p. 540–552, doi:10.1016/j.chemgeo.2009.05.019.

McLennan, S.M. et al., 2014, Elemental Geochemistry of Sedimentary Rocks at Yellowknife Bay, Gale Crater, Mars: Science, v. 343, p. 1244734, doi:10.1126/science.1244734.

McLennan, S.M., 1993, Weathering and Global Denudation: The Journal of Geology, v. 101, p. 295–303.

McSween, H.Y. et al., 1999, Chemical, multispectral, and textural constraints on the composition and origin of rocks at the Mars Pathfinder landing site: Journal of Geophysical Research E: Planets, v. 104, p. 8679–8715, doi:10.1029/98JE02551/FORMAT/PDF.

Mees, F., and De Dapper, M., 2005, Vertical variations in bassanite distribution patterns in near-surface sediments, southern Egypt: Sedimentary Geology, v. 181, p. 225–229, doi:10.1016/j.sedgeo.2005.09.002.

Menges, C.M., 2008, Multistage late Cenozoic evolution of the Amargosa River drainage, southwestern Nevada and eastern California, *in* Special Paper 439: Late Cenozoic Drainage

History of the Southwestern Great Basin and Lower Colorado River Region: Geologic and Biotic Perspectives, Geological Society of America, p. 39–90, doi:10.1130/2008.2439(03).

Meunier, A., 2005, Clays: Berlin/Heidelberg, Springer-Verlag, 472 p., doi:10.1007/b138672.

Milliken, R.E., Grotzinger, J.P., and Thomson, B.J., 2010, Paleoclimate of mars as captured by the stratigraphic record in gale crater: Geophysical Research Letters, v. 37, doi:10.1029/2009GL041870.

Mitchell, R.L., and Sheldon, N.D., 2010, The ~1100 Ma Sturgeon Falls paleosol revisited: Implications for Mesoproterozoic weathering environments and atmospheric CO2 levels: Precambrian Research, v. 183, p. 738–748, doi:10.1016/J.PRECAMRES.2010.09.003.

Mohanty, S.P., and Nanda, S., 2016, Geochemistry of a paleosol horizon at the base of the Sausar Group, central India: Implications on atmospheric conditions at the Archean–Paleoproterozoic boundary: Geoscience Frontiers, v. 7, p. 759–773, doi:10.1016/J.GSF.2015.10.002.

Morris, R. V. et al., 2010, Identification of carbonate-rich outcrops on Mars by the spirit rover: Science, v. 329, p. 421–424, doi:10.1126/science.1189667.

Morrison, R.B., 1999, Lake Tecopa: Quaternary geology of Tecopa Valley, California, a multimillion-year record and its relevance to the proposed nuclear-waste repository at Yucca Mountain, Nevada: Special Paper of the Geological Society of America, v. 333, p. 301–344, doi:10.1130/0-8137-2333-7.301.

Murchie, S.L. et al., 2009, Compact Reconnaissance Imaging Spectrometer for Mars investigation and data set from the Mars Reconnaissance Orbiter's primary science phase: Journal of Geophysical Research: Planets, v. 114, p. 0–07, doi:10.1029/2009JE003344.

Nelson, S.T., Karlsson, H.R., Paces, J.B., Tingey, D.G., Ward, S., and Peters, M.T., 2001,

Paleohydrologic record of spring deposits in and around Pleistocene pluvial Lake Tecopa, southeastern California: Bulletin of the Geological Society of America, v. 113, p. 659–670, doi:10.1130/0016-7606(2001)113<0659:PROSDI>2.0.CO;2.

Nesbitt, H.W., and Young, G.M., 1982, Early Proterozoic climates and plate motions inferred from major element chemistry of lutites: Nature 1982 299:5885, v. 299, p. 715–717, doi:10.1038/299715a0.

Ohta, T., and Arai, H., 2007, Statistical empirical index of chemical weathering in igneous rocks: A new tool for evaluating the degree of weathering: Chemical Geology, v. 240, p. 280–297, doi:10.1016/j.chemgeo.2007.02.017.

Perri, F., 2020, Chemical weathering of crystalline rocks in contrasting climatic conditions using geochemical proxies: An overview: Palaeogeography, Palaeoclimatology, Palaeoecology, v. 556, p. 109873, doi:10.1016/j.palaeo.2020.109873.

Potter, R.M., and Rossman, G.R., 1977, Desert varnish: The importance of clay minerals: Science, v. 196, p. 1446–1448, doi:10.1126/science.196.4297.1446.

Ramirez, R.M., and Craddock, R.A., 2018, The geological and climatological case for a warmer and wetter early Mars: Nature Publishing Group, v. 11, p. 230–237, doi:10.1038/s41561-018-0093-9.

Rapin, W. et al., 2016, Hydration state of calcium sulfates in Gale crater, Mars: Identification of bassanite veins: Earth and Planetary Science Letters, v. 452, p. 197–205, doi:10.1016/J.EPSL.2016.07.045.

Reheis, M.C., 2006, A 16-year record of eolian dust in Southern Nevada and California, USA: Controls on dust generation and accumulation: Journal of Arid Environments, v. 67, p. 487–520, doi:10.1016/j.jaridenv.2006.03.006.

Reheis, M.C., Caskey, J., Bright, J., Paces, J.B., Mahan, S., and Wan, E., 2019, Pleistocene lakes and paleohydrologic environments of the Tecopa basin, California: Constraints on the drainage integration of the Amargosa River: GSA Bulletin, doi:10.1130/b35282.1.

Reheis, M.C., Goodmacher, J.C., Harden, J.W., McFadden, L.D., Rockwell, T.K., Shroba, R.R., Sowers, J.M., and Taylor, E.M., 1995, Quaternary soils and dust deposition in southern Nevada and California: Geological Society of America Bulletin, v. 107, p. 1003–1022, doi:10.1130/0016-7606(1995)107<1003:QSADDI>2.3.CO;2.

Reheis, M.C., and Urban, F.E., 2011, Regional and climatic controls on seasonal dust deposition in the southwestern U.S.: Aeolian Research, v. 3, p. 3–21, doi:10.1016/j.aeolia.2011.03.008.

Retallack, G.J., 2008, Soil-Forming Processes, *in* Soils of the Past, Oxford, UK, Blackwell Science Ltd, p. 37–62, doi:10.1002/9780470698716.ch4.

Retallack, G.J., 2001, Soils of the Past: An Introduction to Paleopedology: Oxford, UK, Blackwell Science Ltd., 404 p.

Ritter, D.F., Kochel, R.C., and Miller, J.R., 2011, Process Geomorphology: Long Grove, Ill., Waveland Press, 652 p.

Rossi, A.P., and Van Gasselt, S., 2010, Geology of Mars after the first 40 years of exploration: Research in Astronomy and Astrophysics, v. 10, p. 621–652, doi:10.1088/1674-4527/10/7/003.

Salisbury, J.W., and Walter, L.S., 1987, Mid-infrared (2.1-25 um) spectra of minerals: First edition: USGS Open-File Report, p. 390, doi:10.3133/OFR87263.

Schaetzl, R.J., and Anderson, S., 2005, Soils: Cambridge University Press, doi:10.1017/CBO9780511815560.

Schon, S.C., Head, J.W., and Fassett, C.I., 2012, An overfilled lacustrine system and

progradational delta in Jezero crater, Mars: Implications for Noachian climate: Planetary and Space Science, v. 67, p. 28–45, doi:10.1016/J.PSS.2012.02.003.

Sheldon, N.D., and Tabor, N.J., 2009, Quantitative paleoenvironmental and paleoclimatic reconstruction using paleosols: Earth-Science Reviews, v. 95, p. 1–52, doi:10.1016/j.earscirev.2009.03.004.

Sheppard, R.A., and Gude, A., 1968, Distribution and genesis of authigenic silicate minerals in tuffs of Pleistocene Lake Tecopa, Inyo County: U.S. Geological Survey Professional Paper, v. 597, p. 1–4.

Siebach, K.L., and McLennan, S.M., 2018, Re-Evaluating the CIA Paleoclimate Proxy on Mars at Curiosity's Drill Sites, *in* Lunar and Planetary Science Conference, p. 2694.

Starkey, H.C., and Blackmon, P.D., 1979, Clay mineralogy of Pleistocene Lake Tecopa, Inyo County, California.: U.S.Geological Survey Professional Paper, v. 1061, p. 34, doi:10.3133/pp1061.

Starkey, H.C., and Blackmon, P.D., 1984, Sepiolite in Pleistocene Lake Tecopa, Inyo County, California: Developments in Sedimentology, v. 37, p. 137–147, doi:10.1016/S0070-4571(08)70033-5.

Stenberg, B., Viscarra Rossel, R.A., Mouazen, A.M., and Wetterlind, J., 2010, Visible and Near Infrared Spectroscopy in Soil Science, *in* Donald L. Sparks ed., Advances in Agronomy, Vol. 107, Burlington, Academic Press, p. 163–215, doi:10.1016/S0065-2113(10)07005-7.

Storti, F., and Balsamo, F., 2010, Particle size distributions by laser diffraction: sensitivity of granular matter strength to analytical operating procedures.:

Tanaka, K.L., 1986, The stratigraphy of Mars: Journal of Geophysical Research, v. 91, p. E139, doi:10.1029/jb091ib13p0e139.

Tanaka, K.L., Skinner, J.A., Hare, T.M., Joyal, T., and Wenker, A., 2003, Resurfacing history of the northern plains of Mars based on geologic mapping of Mars Global Surveyor data: Journal of Geophysical Research E: Planets, v. 108, doi:10.1029/2002je001908.

Thomas, M., Clarke, J., Pain, C., A Clarke, J.D., and Pain, C.F., 2005, Weathering, erosion and landscape processes on Mars identified from recent rover imagery, and possible Earth analogues: Australian Journal of Earth Sciences, v. 52, p. 365–378, doi:10.1080/08120090500134597.

Thorpe, M.T., Hurowitz, J.A., and Siebach, K.L., 2021, Source-to-Sink Terrestrial Analogs for the Paleoenvironment of Gale Crater, Mars: Journal of Geophysical Research: Planets, v. 126, doi:10.1029/2020JE006530.

Twidale, C.R., 1973, Geomorphology, with special reference to Australia: Melbourne, Thomas Nelson (Australia), (Nelson's Australasian paperbacks), 406 p.

Vane, G., and Goetz, A.F.H., 1988, Terrestrial imaging spectroscopy: Remote Sensing of Environment, v. 24, p. 1–29, doi:10.1016/0034-4257(88)90003-X.

Vaniman, D.T. et al., 2014, Mineralogy of a Mudstone at Yellowknife Bay, Gale Crater, Mars: Science, v. 343, p. 1243480–1243480, doi:10.1126/science.1243480.

Vaniman, D.T., and Chipera, S.J., 2006, Transformations of Mg- and Ca-sulfate hydrates in Mars regolith: The American mineralogist, v. 91, p. 1628–1642.

Verheye, W., 2006, Soils of arid and semi-arid areas, *in* Verheye, W.H. ed., Land use, land cover and soil science, Oxford, UK, UNESCO-EOLSS Publishers.

Vinogradov, A.P., 1959, The geochemistry of rare and dispersed chemical elements in soils.: , p. 65–70.

Wänke, H., Brückner, J., Dreibus, G., Rieder, R., and Ryabchikov, I., 2001, Chemical

composition of rocks and soils at the pathfinder site: Space Science Reviews, v. 96, p. 317–330, doi:10.1023/A:1011961725645.

Warke, P., 2013, Weathering in Arid Regions: Treatise on Geomorphology, v. 4, p. 197–227, doi:10.1016/B978-0-12-374739-6.00060-9.

Wentworth, C.K., 1922, A Scale of Grade and Class Terms for Clastic Sediments: The Journal of Geology, v. 30, p. 377–392, doi:10.1086/622910.

Wiens, R.C. et al., 2021, The SuperCam Instrument Suite on the NASA Mars 2020 Rover: Body Unit and Combined System Tests: Space Science Reviews, v. 217, p. 4, doi:10.1007/s11214-020-00777-5.

Worku, T., and Parker, A., 1992, Occurrence of bassanite in Lower Lias rocks of the Lyme Regis area, England: Mineralogical Magazine, v. 56, p. 258–260, doi:10.1180/minmag.1992.056.383.15.

Wyatt, M.B., and McSween, H.Y., 2002, Spectral evidence for weathered basalt as an alternative to andesite in the northern lowlands of Mars: Nature 2002 417:6886, v. 417, p. 263–266, doi:10.1038/417263a.

Xu, X.T., Shao, L.Y., Lan, B., Wang, S., Hilton, J., Qin, J.Y., Hou, H.H., and Zhao, J., 2020, Continental chemical weathering during the Early Cretaceous Oceanic Anoxic Event (OAE1b): a case study from the Fuxin fluvio-lacustrine basin, Liaoning Province, NE China: Journal of Palaeogeography, v. 9, doi:10.1186/s42501-020-00056-y.

Yousefifard, M., Ayoubi, S., Jalalian, A., Khademi, H., and Makkizadeh, M.A., 2012, Mass balance of major elements in relation to weathering in soils developed on igneous rocks in a semiarid region, northwestern Iran: Journal of Mountain Science, v. 9, p. 41–58, doi:10.1007/s11629-012-2208-x.

Zhao, L., Hong, H., Fang, Q., Algeo, T.J., Wang, C., Li, M., and Yin, K., 2020, Potential of VNIR spectroscopy for prediction of clay mineralogy and magnetic properties, and its paleoclimatic application to two contrasting Quaternary soil deposits: Catena, v. 184, doi:10.1016/J.CATENA.2019.104239.

8. Appendices

Appendix A: Table of Collected Soil Samples

Sample	*Soil Crust/Subsurface*	*Tecopa Lake Section/ Bed or Modern Basin*	*Location EPSG:4326*
T117T	Soil Crust	Top of Section 1	35.874637 -116.280075
T118B	Subsurface of T117T		
T115T	Soil Crust	Section 1	35.874621 -116.280110
T116B	Subsurface of T115T		
T113T	Soil Crust	Section 1	35.874565 -116.280139
T114B	Subsurface of T113T		
T111T	Soil Crust	Section 1	35.874503 -116.280159
T112B	Subsurface of T111T		
T109T	Soil Crust	Section 1	35.874481 -116.280176
T110B	Subsurface of T109T		
T107T	Soil Crust	Section 1	35.874450 -116.280187
T108B	Subsurface of T107T		
T105T	Soil Crust	Section 1	35.874406 -116.280197
T106B	Subsurface of T105T		
T103T	Soil Crust	Bottom of Section 1	35.874369 -116.280199
T104B	Subsurface of T103T		
T78(T)	Soil Crust	Top of Section 2	35.845987 -116.264879
T79(B)	Subsurface of T78		
T80(T)	Soil Crust	Section 2	35.846024 -116.264861
T81(B)	Subsurface of T80		

Sample	*Soil Crust/Subsurface*	*Tecopa Lake Section/ Bed or Modern Basin*	*Location EPSG:4326*
T82(T)	Soil Crust	Section 2	35.846342 -116.264764
T83(B)	Subsurface of T82		
T84(T)	Soil Crust	Section 2	35.846729 -116.264744
T85(NB)	Nodules found below T84		
T86T	Soil Crust	Section 2	35.846897 -116.264804
T86B	Subsurface of T86T		
T87(T)	Soil Crust	Bottom of Section 2	35.847221 -116.264680
T88(B)	Subsurface of T87		
T65(T)	Soil Crust	Basin (playa)	35.920149 -116.267679
T66(B)	Subsurface of T65		
T67(T)	Soil Crust	Tecopa Paleolake Bed	35.920331 -116.269300
T68(B)	Subsurface of T67		
T73(T)	Soil Crust	Modern Basin	35.923718 -116.270629
T74(B)	Subsurface of T73		
T76(T)	Soil Crust	Basin (Amargosa River deposit)	35.92513 -116.2637030
T77(B)	Subsurface of T76		
T89(T)	Soil Crust	Basin (alluvial)	35.848016 -116.264194
T90(B)	Subsurface of T89		
T93(T)	Soil Crust	Basin (floodplain?)	35.849499 -116.265244
T94(B)	Subsurface of T93		

Sample	*Soil Crust/Subsurface*	*Tecopa Lake Section/ Bed or Modern Basin*	*Location EPSG:4326*
T98(T)	Soil Crust	Basin (alluvial)	35.857335 -116.263842
T99(B)	Subsurface of T98		
T100(T)	Soil Crust	Basin (playa)	35.859172 -116.264640
T119(B)	Subsurface of T100		
T101(T)	Soil Crust	Tecopa Paleolake Bed	35.885157 -116.234896
T102(B)	Subsurface of T101		
T120(T)	Soil Crust	Basin (Amargosa River deposit)	35.921533 -116.266972
T121(B)	Subsurface of T120		

Table 4: Sample collection locations and designated each sample as Tecopa Lake section/lakebed (bed) or modern basin.

Appendix B: Photos of Collected Soil Samples

Section 1

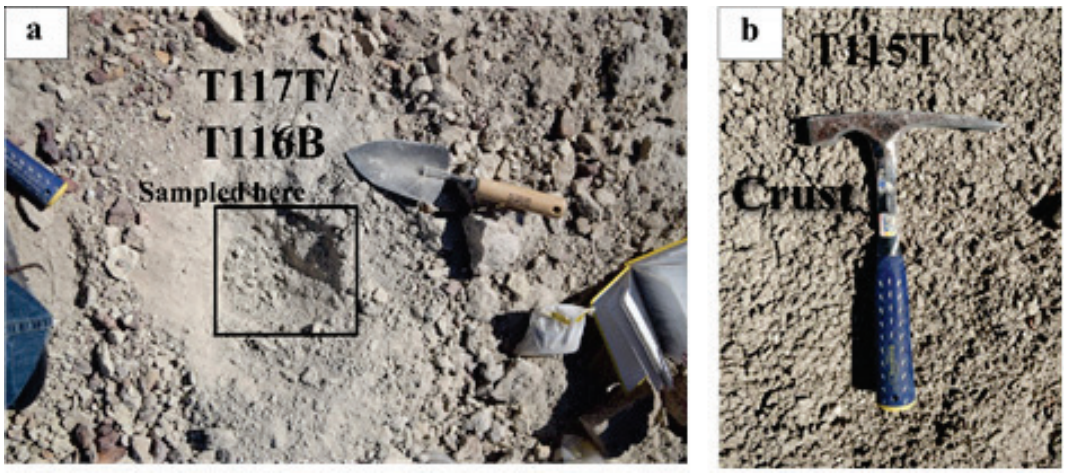

Figure 44: (a) Close-up view of T117T and T118B samples from the top of section 1, (b) close-up view of T115T (crust) from the top of section 1. Hammer is 32 cm long.

Figure 45: Close-up view of T103T (crust) and T104B (subsurface) samples from the bottom of section 1. Hammer is 32 cm long.

Section 2

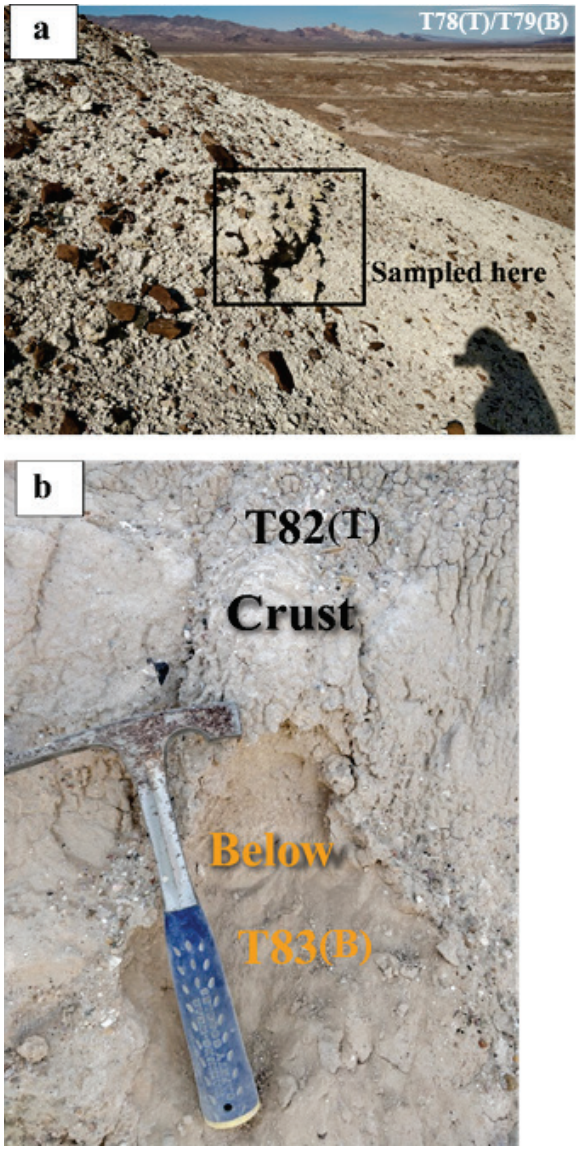

Figure 46: (a) View of T78(T) and T79(B) samples from the top of section 2, (b) Close-up view of T82(T) (crust) and T83(B) (subsurface) from the middle of section 2. Hammer is 32 cm long.

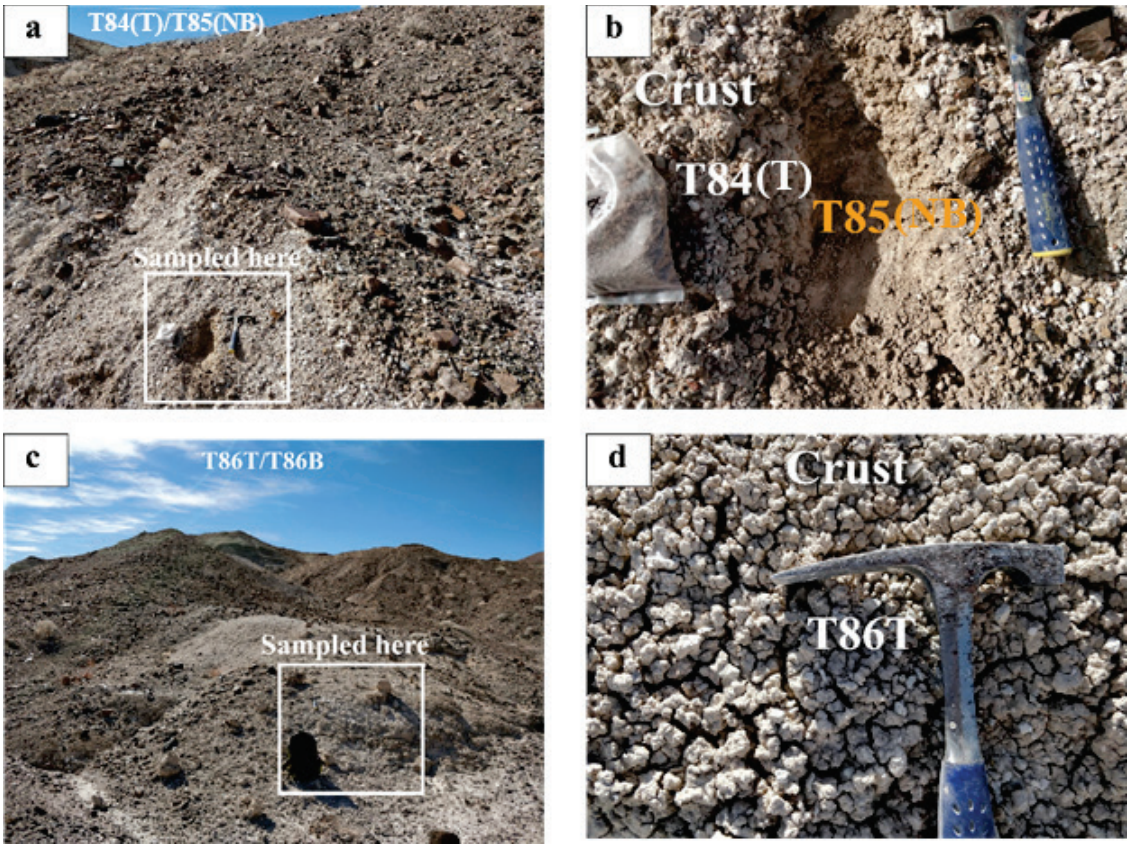

Figure 47: (a) View of T84(T) and T85(NB) (calcareous nodules) samples from the bottom of section 2, (b) Close-up view of T84(T) and T85(NB) (calcareous nodules) samples from the bottom of section 2 with a 32 cm hammer for scale, (c) View of T86T and T86B samples from the bottom of section 2, (d) close-up view of T86T (crust) sample from bottom of section. Hammer is 32 cm long.

Additional Samples

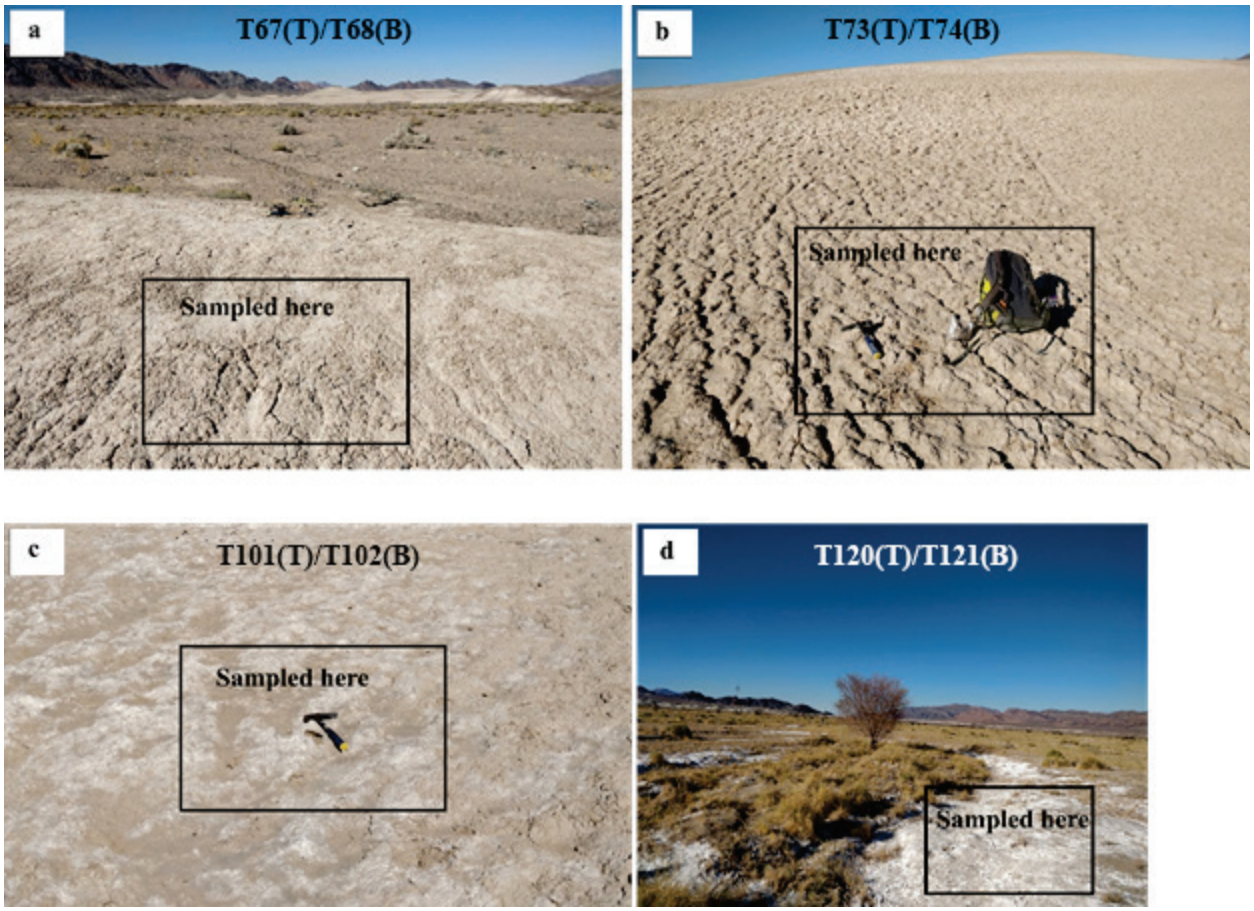

Figure 48: (a) View of T67(T) and T68(B) samples from an additional Tecopa Paleolake Bed, (b) view of T73(T) and T74(B) samples from the modern basin with a 32 cm hammer for scale, (c) view of T101(T) and T102(B) samples from the modern basin with a 32 cm hammer for scale (d) view of T120(T) and T121(B) samples from the modern basin.

Appendix C: 10X Stereoscopic Microscope View of Select Samples

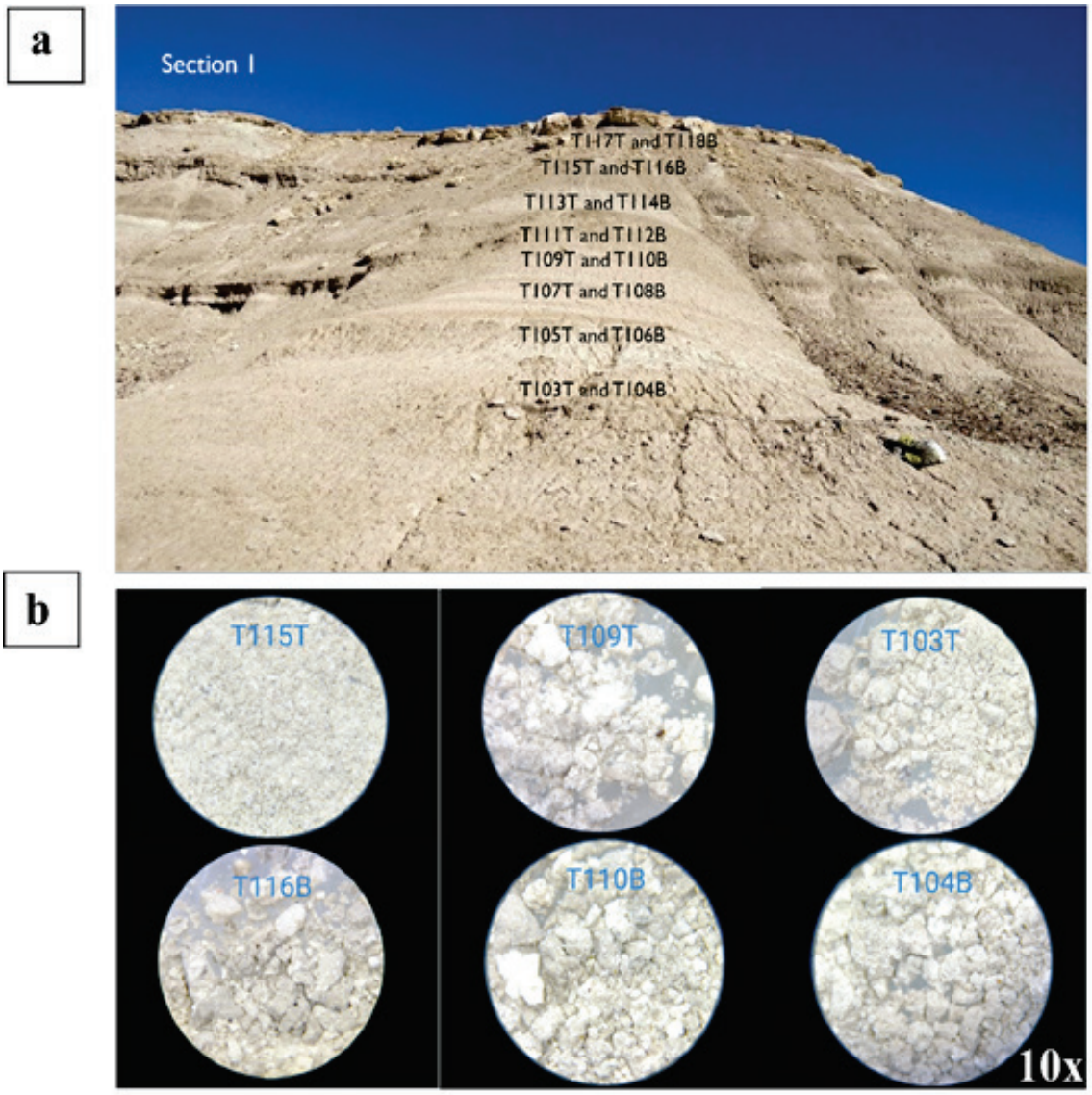

Figure 49: (a) View of Section 1, and (b) 10X stereoscopic microscope view of select samples from Section 1.

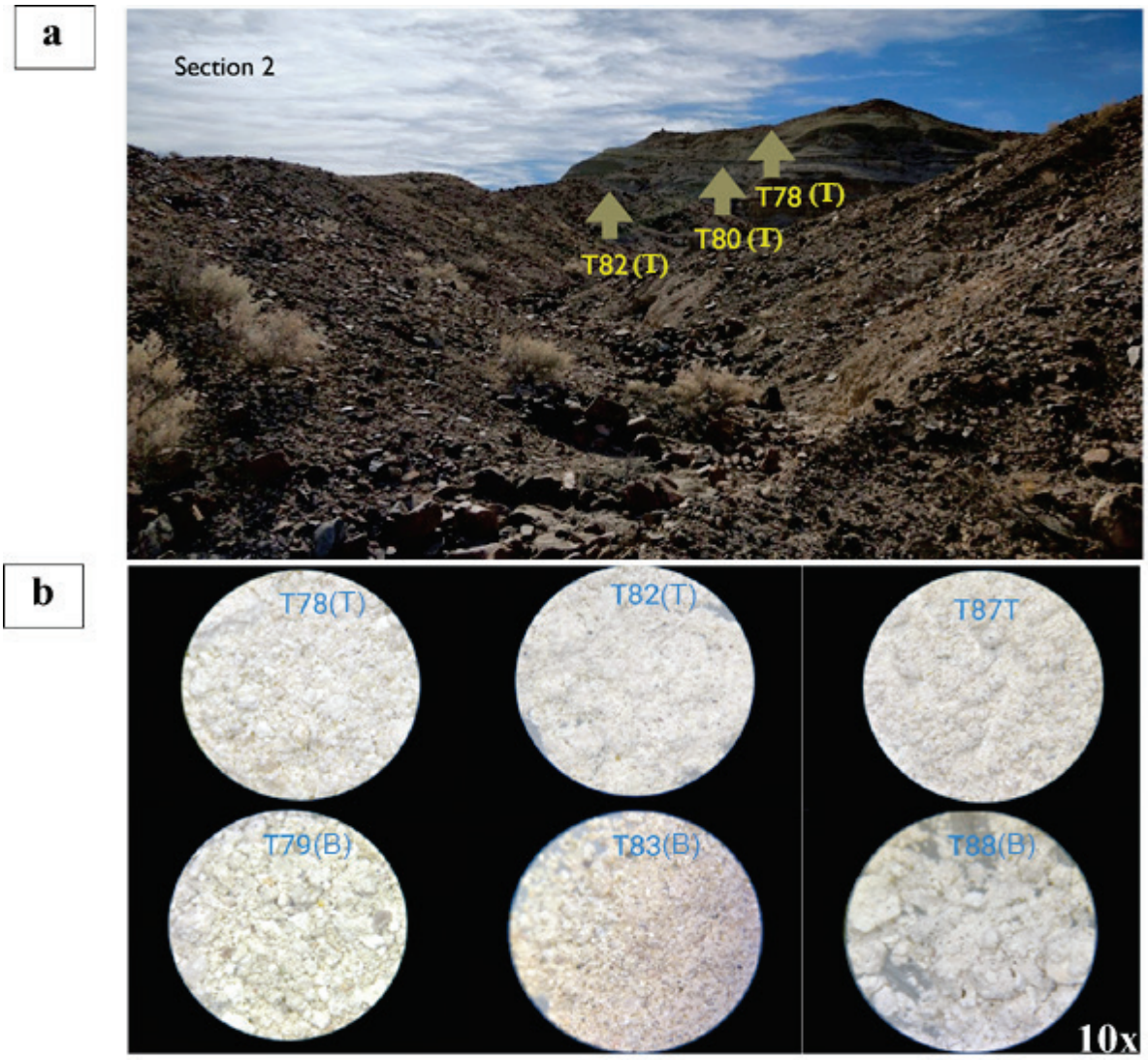

Figure 50: (a) View of Section 2, (b) side profile of Section 2, and (b) 10X stereoscopic microscope view of select samples from Section 2.

Appendix D: Grain Size Tables

See next page.

Sample Name (Ave)	Obscuration (%)	Amount used	Mode (um)	clay (vol%)	vf silt (v %)	f silt (v %)	m silt (v %)	c silt (v %)	vf sand (v %)	f sand (v %)	m sand (v %)	c sand (v %)	vc sand (vol %)
T117T	15.70	0.10g	7.27	18.48	19.70	19.38	16.23	14.89	9.60	1.72	0.00	0.00	0.00
T118B	12.58	0.10g	44.69	12.35	15.65	17.45	17.43	19.24	12.79	3.31	1.24	0.52	0.02
T115T	18.94	0.25g	8.59	17.51	26.39	27.98	16.44	5.57	2.70	1.41	0.91	1.00	0.09
T116B	17.94	0.25g	9.51	12.35	27.56	33.41	18.77	4.87	1.49	0.78	0.53	0.24	0.00
T113T	13.71	0.10g	9.00	17.15	20.66	22.11	16.90	12.31	8.00	2.64	0.23	0.00	0.00
T114B	12.52	0.10g	5.09	20.74	19.24	16.67	14.96	14.85	9.86	3.34	0.34	0.00	0.00
T111T	16.33	0.10g	11.98	12.94	20.23	25.75	21.52	12.05	5.00	1.88	0.55	0.08	0.00
T112B	12.70	0.10g	8.67	16.36	23.36	24.96	15.36	7.86	6.42	4.13	1.52	0.03	0.00
T109T	13.93	0.10g	9.32	16.12	20.52	22.39	17.50	11.88	7.03	3.37	1.19	0.00	0.00
T110B	13.34	0.10g	6.14	21	23.79	20.71	13.00	8.72	6.78	4.22	1.68	0.10	0.00
T107T	15.95	0.10g	5.67	27.25	28.66	22.24	10.15	4.86	3.22	2.70	0.92	0.00	0.00
T108B	13.96	0.10g	4.97	22.87	21.99	17.23	12.11	10.99	8.86	4.81	1.14	0.00	0.00
T105T	15.23	0.10g	4.50	41.68	20.99	15.69	9.13	6.26	4.59	1.57	0.09	0.00	0.00
T106B	16.82	0.10g	5.07	40.2	21.62	17.10	10.35	6.38	3.13	1.06	0.16	0.00	0.00
T103T	18.56	0.25g	11.17	17.27	20.83	24.62	20.27	10.50	3.15	2.17	0.75	0.38	0.06
T104B	19.58	0.25g	12.22	13.95	17.99	21.68	20.03	15.84	7.50	1.08	0.79	1.06	0.08

Table 5: Grain size table of 2019 Tecopa samples from section 1. The grain-size fractionation is clay (0.1-3.9 um), very fine silt (3.9-7.8 um), fine silt (7.8-15.6 um), medium silt (15.6-31 um), coarse silt (31-63 um), very fine sand (63-125 um), fine sand (125-250 um), medium sand (250-500 um), coarse sand (500-1000 um), very coarse sand (1000-2000 um).

Sample Name (Ave)	Obscuration (%)	Amount used	Mode (um)	clay (vol %)	vf silt (v %)	f silt (v %)	m silt (v %)	c silt (v %)	vf sand (v %)	f sand (v %)	m sand (v %)	c sand (v %)	vc sand (vol %)
T78T	14.48	0.50g	673.2	3.05	4.81	7.52	10.07	12.39	12.57	9.14	14.72	23.48	2.26
T79B	18.71	0.50g	646.8	6.30	9.56	13.27	14.62	13.60	10.94	6.70	9.60	14.16	1.25
T82T	15.76	0.50g	4.80	20.95	20.81	14.82	8.90	9.40	9.62	4.42	3.58	6.80	0.70
T83B	19.08	0.50g	16.09	2.84	10.12	21.28	22.42	18.73	17.08	7.23	0.31	0.00	0.00
T86T	9.52	0.10g	48.49	7.95	15.06	18.58	18.96	21.89	14.99	2.57	0.00	0.00	0.00
T86B	7.80	0.10g	55.73	7.92	14.89	18.03	17.46	20.80	16.70	4.09	0.11	0.00	0.00
T87T	18.74	0.50g	6.04	20.63	24.19	20.46	11.96	9.76	9.06	3.37	0.38	0.17	0.01
T88B	18.11	0.50g	5.28	24.28	33.31	20.33	6.09	4.95	4.89	1.99	1.15	2.72	0.3

Table 6: Grain size table of 2019 Tecopa samples from section 2. The grain-size fractionation is clay (0.1-3.9 um), very fine silt (3.9-7.8 um), fine silt (7.8-15.6 um), medium silt (15.6-31 um), coarse silt (31-63 um), very fine sand (63-125 um), fine sand (125-250 um), medium sand (250-500 um), coarse sand (500-1000 um), very coarse sand (1000-2000 um).

Appendix E: X-Ray Fluorescence Tables

See next page.

Sample	SiO_2	Al_2O_3	K_2O	Fe_2O_3	CaO	Na_2O	MgO	MnO	TiO_2	P_2O_5	Zr (ppm)	Sr (ppm)	Ba (ppm)	LOI	Total
T117T	52.75	14.51	7.43	4.58	5.77	2.72	2.97	0.11	0.62	0.17	199	630	751	6.95	98.77
T118B	54.90	13.65	6.86	4.36	4.75	2.95	2.97	0.10	0.60	0.15	193	510	690	6.63	98.11
T115T	48.52	10.09	5.25	3.50	6.45	2.44	8.95	0.08	0.42	0.10	133	1752	473	9.66	95.72
T116B	46.19	9.55	5.13	3.37	7.76	3.72	9.13	0.09	0.40	0.11	128	1913	396	11.6	97.30
T113T	51.75	11.78	6.31	3.73	4.95	2.88	5.82	0.10	0.47	0.10	164	1078	507	7.49	95.59
T114B	51.30	12.01	6.41	3.80	4.07	4.56	5.02	0.09	0.48	0.11	152	831	536	7.42	95.58
T111T	50.67	10.25	5.25	3.24	6.19	2.52	9.01	0.08	0.38	0.10	140	1861	416	9.43	97.39
T112B	46.19	8.97	4.54	2.93	7.75	4.78	9.46	0.08	0.36	0.12	124	2074	407	11.1	96.57
T109T	53.50	11.96	7.42	3.07	4.24	3.23	4.47	0.08	0.40	0.10	146	852	459	6.86	95.51
T110B	49.59	10.83	6.53	3.14	4.91	5.26	5.89	0.10	0.38	0.13	122	1274	559	9.32	96.29
T107T	50.39	11.97	6.62	3.90	4.32	4.50	4.90	0.09	0.46	0.10	133	941	571	7.88	95.32
T108B	48.97	11.25	6.02	3.20	4.48	6.18	3.86	0.07	0.42	0.13	133	806	491	8.91	93.67
T105T	49.94	11.78	6.30	3.89	6.27	2.97	6.55	0.11	0.49	0.11	143	1769	519	9.34	98.01
T106B	44.62	10.56	5.89	3.67	5.23	6.70	6.53	0.11	0.42	0.11	113	1769	331	12.2	96.26
T103T	51.39	11.92	7.16	3.86	4.15	4.65	3.30	0.10	0.51	0.14	156	574	649	7.77	95.1
T104B	48.05	10.96	6.80	3.56	3.57	8.10	2.32	0.09	0.46	0.17	134	330	517	8.90	93.1

Table 7: XRF table of 2019 Tecopa samples from section 1.

Sample	SiO_2	Al_2O_3	K_2O	Fe_2O_3	CaO	Na_2O	MgO	MnO	TiO_2	P_2O_5	Zr (ppm)	Sr (ppm)	Ba (ppm)	LOI	Total
T78(T)	53.49	8.66	4.32	1.73	8.36	2.21	3.58	0.05	0.17	0.07	179	1287	233	16.6	99.42
T79(B)	55.44	9.74	4.65	2.97	5.32	1.93	4.54	0.07	0.36	0.10	184	754	274	11.5	96.79
T80(T)	54.18	10.75	5.21	2.83	2.30	2.71	3.21	0.05	0.20	0.06	172	492	364	14.7	96.35
T81(B)	53.87	6.47	2.41	1.95	11.73	1.67	6.25	0.04	0.27	0.10	164	1560	350	14.5	99.50
T82(T)	43.62	7.10	2.88	1.85	16.06	1.62	7.30	0.04	0.28	0.11	116	1042	ND	18.3	95.35
T83(B)	64.28	10.59	3.34	2.86	2.04	3.89	2.69	0.04	0.45	0.11	256	256	547	6.92	97.35
T84(T)	52.29	11.61	3.62	3.69	7.59	2.65	5.65	0.07	0.52	0.12	173	559	515	11.1	99.04
T86T	56.83	11.95	3.47	3.54	7.20	2.85	3.67	0.07	0.55	0.16	235	612	577	8.92	99.36
T86B	58.08	11.86	3.45	3.39	6.62	3.18	3.13	0.07	0.54	0.15	228	615	599	8.49	99.12

Table 8: XRF table of 2019 Tecopa samples from section 2. Samples T85(NB), T87(T) and T88(B) are omitted, these samples contained significant carbonate minerals, and would have produced erroneous results. T84(T) does not have a below sample, and it has been highlighted in green. ND = not detected, the result was below the LLD.

Sample	SiO_2	Al_2O_3	K_2O	Fe_2O_3	CaO	Na_2O	MgO	MnO	TiO_2	P_2O_5	Zr (ppm)	Sr (ppm)	Ba (ppm)	LOI	Total
T65(T)	54.70	11.50	3.41	2.65	8.98	2.65	3.87	0.06	0.51	0.14	249	1030	659	10.1	98.82
T66(B)	56.72	12.29	3.56	2.93	8.44	2.87	3.36	0.07	0.56	0.16	289	886	717	8.58	99.77
T73(T)	43.22	9.13	3.52	2.14	19.54	2.08	2.75	0.05	0.39	0.10	192	1117	559	14.2	97.31
T74(B)	52.27	11.44	5.03	3.23	5.17	3.67	5.04	0.08	0.42	0.09	155	1008	526	9.35	95.98
T89(T)	45.93	10.53	3.55	3.49	11.94	1.64	4.97	0.09	0.48	0.15	165	864	605	16.7	99.63
T90(B)	54.63	11.13	3.42	3.26	8.24	1.89	3.77	0.08	0.51	0.15	227	701	654	12.5	99.76
T93(T)	53.11	10.14	3.24	2.50	5.95	3.99	6.24	0.06	0.38	0.09	165	535	654	12.1	97.96
T94(B)	52.36	9.56	3.20	2.46	4.82	5.08	6.92	0.06	0.37	0.10	156	511	451	12.7	97.71
T98(T)	53.25	9.55	3.66	2.56	6.59	2.31	6.30	0.06	0.38	0.10	165	828	512	10	94.94
T99(B)	48.86	9.18	3.83	2.81	7.85	2.62	8.02	0.07	0.37	0.10	125	898	462	13.2	97.11
T100(T)	54.80	11.79	4.16	3.40	7.93	2.26	3.31	0.08	0.64	0.18	264	1055	776	9.42	98.22
T119(B)	56.57	12.32	4.02	3.21	7.38	2.52	2.88	0.08	0.61	0.18	236	962	745	8.91	98.91

Table 9*:* XRF table of 2019 Tecopa samples of additional Tecopa paleolake beds, the playa and modern basin.

Appendix F: Weathering Indices Tables

Sample	CIA	CPA	PIA	CIW	WIP	ICV	Base Loss	Clay.	Hydro.	Bases Al	Calc.	Salin.	Ba/Sr
T117T	46.06	76.43	41.95	61.85	102.46	1.96	38.56	0.16	0.48	2.10	1.24	0.86	0.76
T118B	44.34	73.77	39.07	58.44	100.26	2.08	37.11	0.15	0.48	2.08	1.18	0.90	0.86
T115T	42.39	71.54	35.44	55.69	97.23	3.89	82.18	0.12	0.23	4.37	3.41	0.96	0.17
T116B	34.93	60.95	24.62	43.83	111.37	4.57	95.72	0.12	0.20	5.12	3.90	1.22	0.13
T113T	41.94	71.32	34.31	55.42	102.64	2.90	58.82	0.13	0.33	3.00	2.01	0.98	0.30
T114B	35.63	61.55	25.28	45.07	120.98	3.13	56.56	0.14	0.35	2.89	1.67	1.21	0.41
T111T	42.31	71.20	35.52	55.28	98.31	3.85	90.44	0.12	0.23	4.28	3.32	0.96	0.14
T112B	30.29	53.29	20.50	36.32	119.42	5.24	110.53	0.11	0.18	5.66	4.24	1.42	0.13
T109T	39.06	69.24	26.99	52.95	112.36	2.72	63.37	0.13	0.37	2.71	1.59	1.12	0.34
T110B	30.80	55.59	17.89	38.54	131.93	3.87	81.52	0.13	0.27	3.65	2.20	1.45	0.28
T107T	35.27	61.79	24.50	44.70	121.30	3.14	59.29	0.14	0.34	2.91	1.69	1.22	0.39
T108B	31.45	52.53	20.82	38.46	129.42	3.29	64.52	0.14	0.33	3.07	1.59	1.48	0.39
T105T	NR	70.68	NR	NR	NR	NR	63.42	0.14	0.30	3.37	2.37	0.99	0.19
T106B	NR	48.93	NR	NR	NR	NR	80.99	0.14	0.24	4.11	2.46	1.65	0.13
T103T	34.52	60.91	21.91	44.51	122.60	2.87	48.06	0.14	0.38	2.63	1.33	1.29	0.72
T104B	NR	45.13	NR	NR	NR	NR	56.27	0.13	0.33	3.02	1.13	1.89	1.00

Table 10: Weathering Indices for the 2019 Tecopa samples from section 1. Clay = Clayeyness, Calc = Calcification, and Salin = Salinization. NR= not reported, halite is in the sample and the Ca* could be not corrected for the sodium contribution.

Sample	CIA	CPA	PIA	CIW	WIP	ICV	Base Loss	Clay.	Hydro.	Bases Al	Calc.	Salin.	Ba/Sr
T78(T)	42.02	70.43	35.40	54.36	71.89	2.59	150.06	0.10	0.27	3.76	2.80	0.96	0.12
T79(B)	46.11	75.42	42.57	60.53	74.13	2.60	63.90	0.10	0.33	3.02	2.17	0.84	0.23
T80(T)	43.20	70.69	37.56	55.85	83.58	2.27	87.73	0.12	0.48	2.08	1.14	0.94	0.47
T81(B)	44.40	70.19	41.27	54.08	56.84	3.95	123.28	0.07	0.15	6.57	5.74	0.83	0.14
T82(T)	45.67	72.71	42.77	57.12	63.15	4.02	149.53	0.10	0.13	7.53	6.71	0.81	NR
T83(B)	44.03	62.33	41.47	51.82	76.34	2.15	35.73	0.10	0.52	1.94	0.99	0.95	1.36
T84(T)	47.88	72.70	46.87	57.11	76.69	2.59	54.79	0.13	0.32	3.13	2.42	0.71	0.59
T86T	47.64	71.82	46.63	56.03	72.25	2.13	43.89	0.12	0.39	2.58	1.87	0.71	0.60
T86B	45.52	69.39	43.71	53.13	74.37	2.11	41.95	0.12	0.41	2.44	1.68	0.76	0.62

Table 11: Weathering Indices for the 2019 Tecopa samples from section 2. Clay = Clayeyness, Calc = Calcification, and Salin = Salinization. Samples T85(NB), T87(T) and T88(B) are omitted, these samples contained significant carbonate minerals, and would have produced erroneous results. NR= not reported, the Ba value of the sample was below the LLD.

Appendix G: X-Ray Diffraction Tables

TOP of SECTION 1

Sample	CARBS		SPARS		ZEOLITES				CLAYS			EVAPS	
	Calcite	Dolomite	Albite	K-feldspar	Analcime	Clinoptilolite	Phillipsite	Quartz	Illite	Montmorillonite	Amphiboles	Halite	Searlesite
T117T	XX	-	XX	XX	-	-	-	+	XX	X	+	-	+
T118B	XX	-	XX	XX	X	-	-	+	XX	X	+	-	+
T115T	XX	X	XX	XX	-	-	-	+	XX	-	-	-	+
T116B	XX	+	XX	XX	X	-	-	+	XX	-	-	-	+
T113T	XX	-	XX	XX	-	-	-	X	XX	-	-	-	+
T114B	XX	-	XX	XX	-	-	-	+	XX	-	+	-	+
T111T	XX	-	XX	XX	-	-	-	-	XX	-	-	-	-
T112B	XX	-	XX	XX	-	-	-	-	XX	-	-	-	-
T109T	XX	-	XX	XX	-	-	-	+	XX	X	XX	-	+
T110B	XX	-	XX	XX	-	-	-	-	XX	X	X	-	+
T107T	XX	-	XX	XX	-	-	-	+	XX	-	-	-	+
T108B	XX	-	-	XX	-	-	-	X	XX	-	-	-	+
T105T	XX	-	-	XX	-	-	-	-	XX	X	+	X	+
T106B	XX	-	-	XX	-	-	-	-	XX	-	-	X	-
T103T	XX	-	-	XX	-	-	-	-	XX	+	-	-	X
T104B	XX	-	-	XX	-	-	-	-	XX	+	X	X	X

BOTTOM of SECTION 1

Table 12: XRD table of 2019 Tecopa samples from section 1. XX represents common minerals, X represents minerals that are present in lower amounts, + represents trace and – means absent. Carbs = carbonates, Spars = feldspars, and Evaps = evaporites minerals.

TOP of SECTION 2

Sample	Calcite	SPARS		ZEOLITES			Quartz	CLAYS		Amphiboles	Hematite
		Albite	K-feldspar	Analcime	Clinoptilolite	Phillipsite		Illite	Montmorillonite		
T78(T)	XX	-	-	-	X	-	X	X	-	-	-
T79(B)	XX	X	-	-	X	-	XX	X	-	X	+
T80(T)	XX	X	X	-	XX	X	-	-	-	-	-
T81(B)	XX	X	X	-	-	-	XX	+	X	-	-
T82(T)	XX	X	X	-	-	-	X	X	X	X	-
T83(B)	-	X	-	-	-	-	XX	X	X	-	-
T84(T)	X	X	-	X	-	-	XX	X	-	X	-
T85(NB)	XX	+	-	-	-	-	+	-	X	-	-
T86T	XX	X	-	+	-	-	XX	XX	X	-	-
T86B	XX	X	-	+	+	+	XX	X	X	-	-
T87(T)	XX	X	-	-	-	+	XX	X	-	-	-
T88(B)	XX	X	-	-	-	-	X	XX	X	-	-

BOTTOM of SECTION 2

Table 13: XRD table of 2019 Tecopa samples from section 2. XX represents common minerals, X represents minerals that are present in lower amounts, + represents trace and – means absent. Carbs = carbonates, Spars = feldspars, and Evaps = evaporites minerals.

Additional

Sample	CARBS		SPARS		ZEOLITES			SILICATES			CLAYS			EVAPS			
	Calcite	Dolomite	Albite	K-feldspar	Analcime	Clinoptilolite	Phillipsite	Quartz	Cristobalite	Tridymite	Illite	Montmorillonite	Amphiboles	Burkeite	Halite	Hanksite	Thenardite
T65(T)	XX	X	X	X	-	-	+	XX	-	-	+	+	+	-	-	-	-
T66(B)	XX	X	X	X	-	-	+	XX	-	-	+	+	X	-	+	-	-
T73(T)	XX	-	X	X	-	-	-	XX	-	-	+	+	-	-	-	-	-
T74(B)	XX	-	X	X	-	-	-	XX	-	-	X	+	-	-	-	-	-
T76(T)	-	-	X	-	-	-	-	+	-	-	-	X	-	X	XX	-	X
T77(B)	X	-	XX	-	-	-	-	XX	-	-	X	X	X	-	X	-	-
T89(T)	XX	X	X	XX	+	-	+	XX	-	-	X	+	+	-	-	-	-
T90(B)	XX	X	X	XX	-	+	+	XX	-	-	X	+	+	-	-	-	-
T93(T)	XX	-	X	X	+	+	+	XX	-	-	X	X	+	-	-	-	-
T94(B)	XX	-	X	X	+	+	+	XX	-	-	X	X	+	-	+	-	-
T98(T)	XX	-	X	X	-	-	-	XX	-	-	X	X	+	-	-	-	-
T99(B)	XX	X	X	X	-	-	-	XX	-	-	X	X	-	-	-	-	-
T100(T)	XX	-	X	X	-	-	+	XX	-	-	X	X	+	-	-	X	-
T119(B)	XX	-	X	X	-	-	-	XX	-	-	X	+	-	-	-	-	-
T101(T)	X	-	XX	X	-	-	-	X	-	-	-	X	X	-	XX	-	-
T102(B)	X	X	XX	X	-	-	-	X	-	-	X	X	-	-	XX	-	-
T120(T)	X	-	XX	-	-	+	-	X	XX	X	-	-	-	X	X	-	-
T121(B)	XX	-	XX	XX	-	+	-	XX	-	-	X	X	-	-	+	-	-

Table 14: XRD table of 2019 Tecopa samples of additional Tecopa paleolake beds, the playa and modern basin. XX represents common minerals, X represents minerals that are present in lower amounts, + represents trace and – means absent. Carbs = carbonates, Spars = feldspars, and Evaps = evaporites minerals.

Appendix H: Grain Size Plots
Section 1

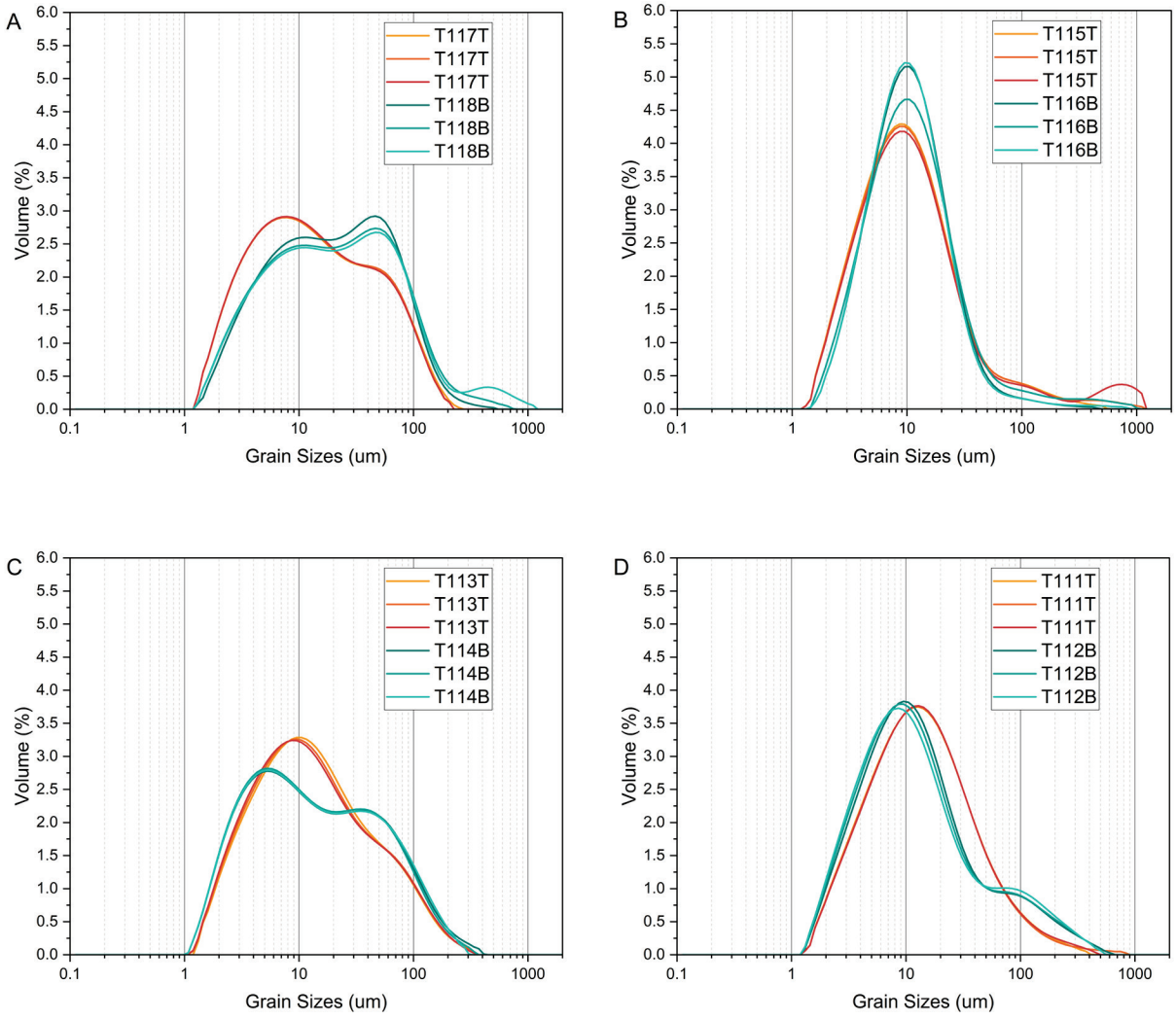

Figure 51: Grain size patterns of T117T to T112B, showing representative grain sizes (um) vs volume (%).

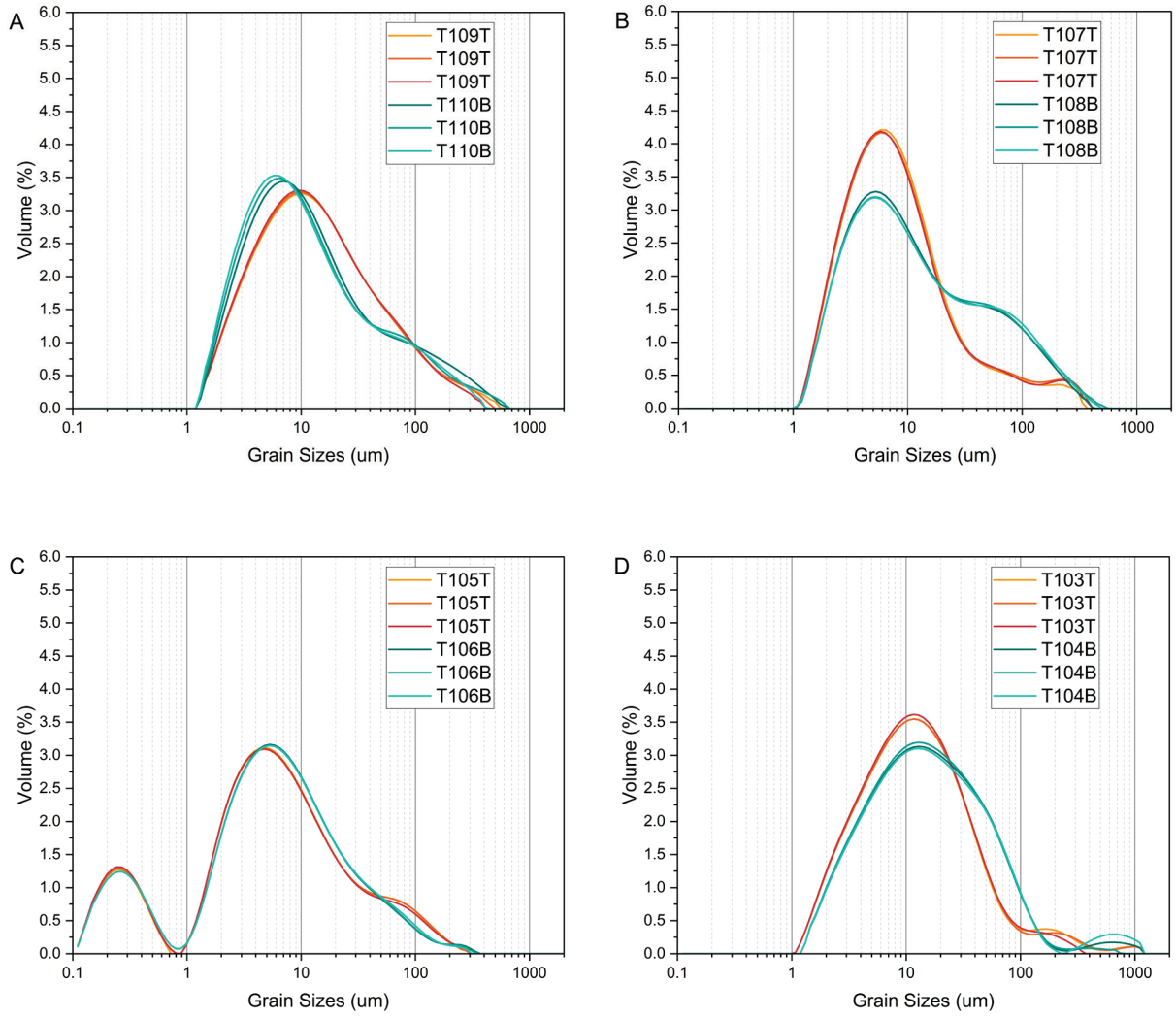

Figure 52: Grain size patterns of T109T to T104B, showing representative grain sizes (um) vs volume (%).

Section 2

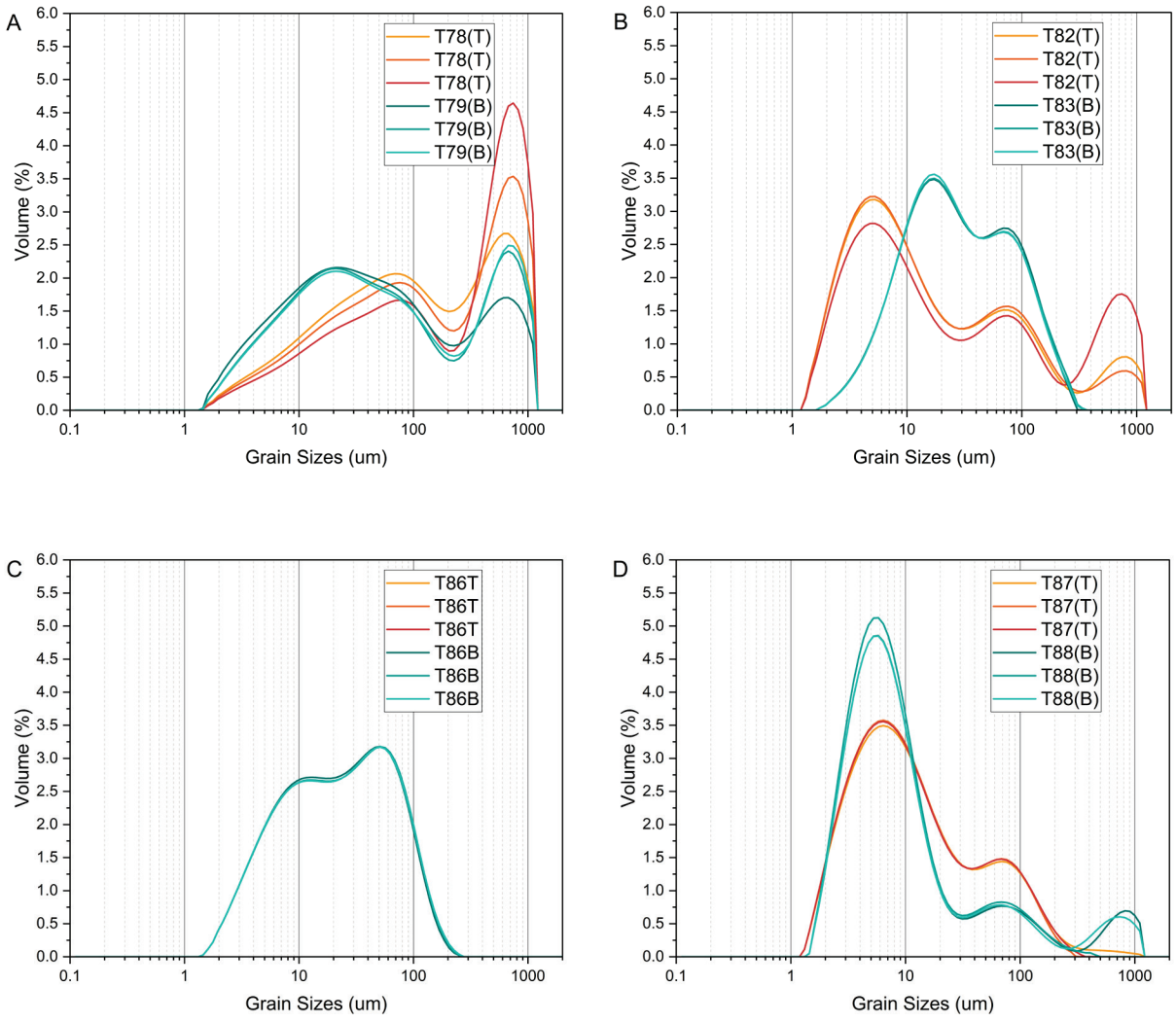

Figure 53: Grain size patterns of T78(T) to T88(B), showing representative grain sizes (um) vs volume (%).

Appendix I: Surface and Subsurface XRD Comparison Plots

Section 1

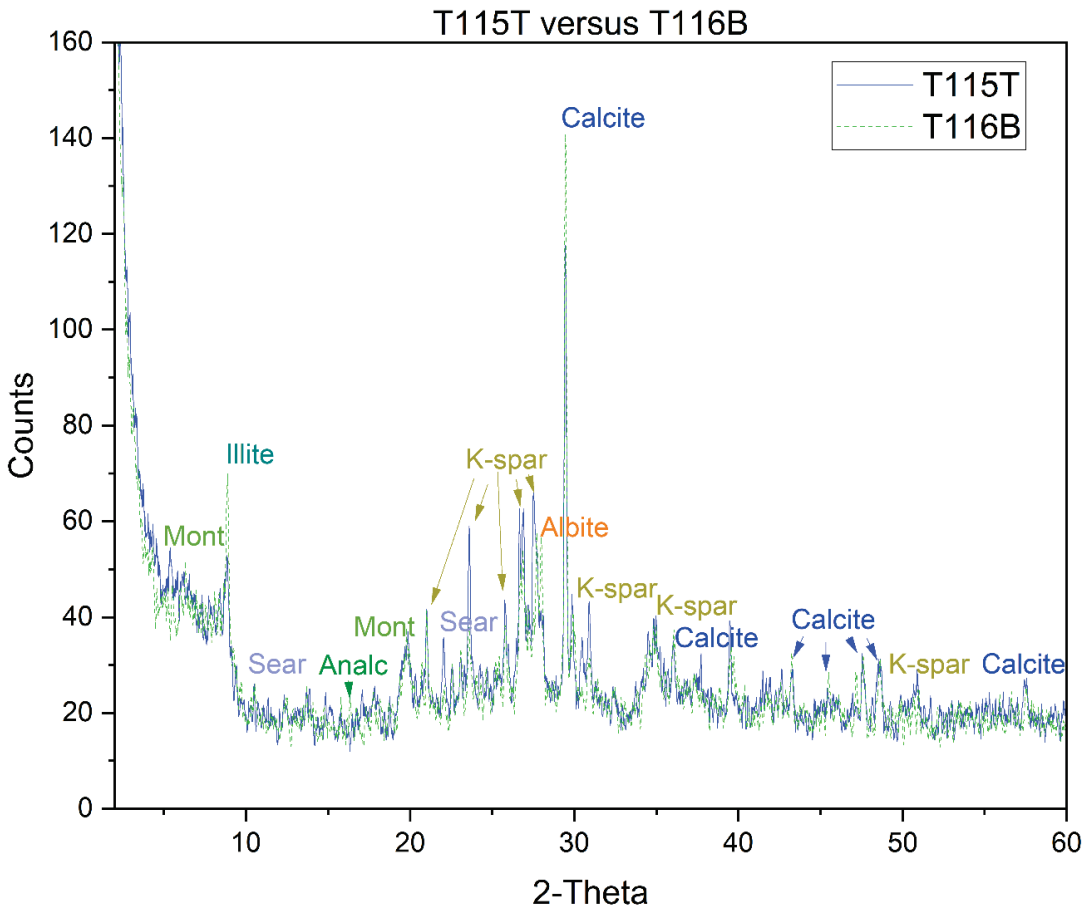

Figure 54: XRD patterns for the surface sample T115T (shown as a solid blue line) and subsurface sample T116B (shown as a dotted green line), near the top of Section 1. The surface sample T115T lower relative abundance of calcite (dark blue) compared to the subsurface sample T116B. The subsurface samples contains the zeolite mineral, analcime (Analc, dark green), while the surface lacks the mineral. Also, both samples contain similar relative abundance of smectite (Mont, yellow green), illite (turquoise), searlesite (Sear, lavender), K-feldspar (K-spar, yellow), and albite (orange).

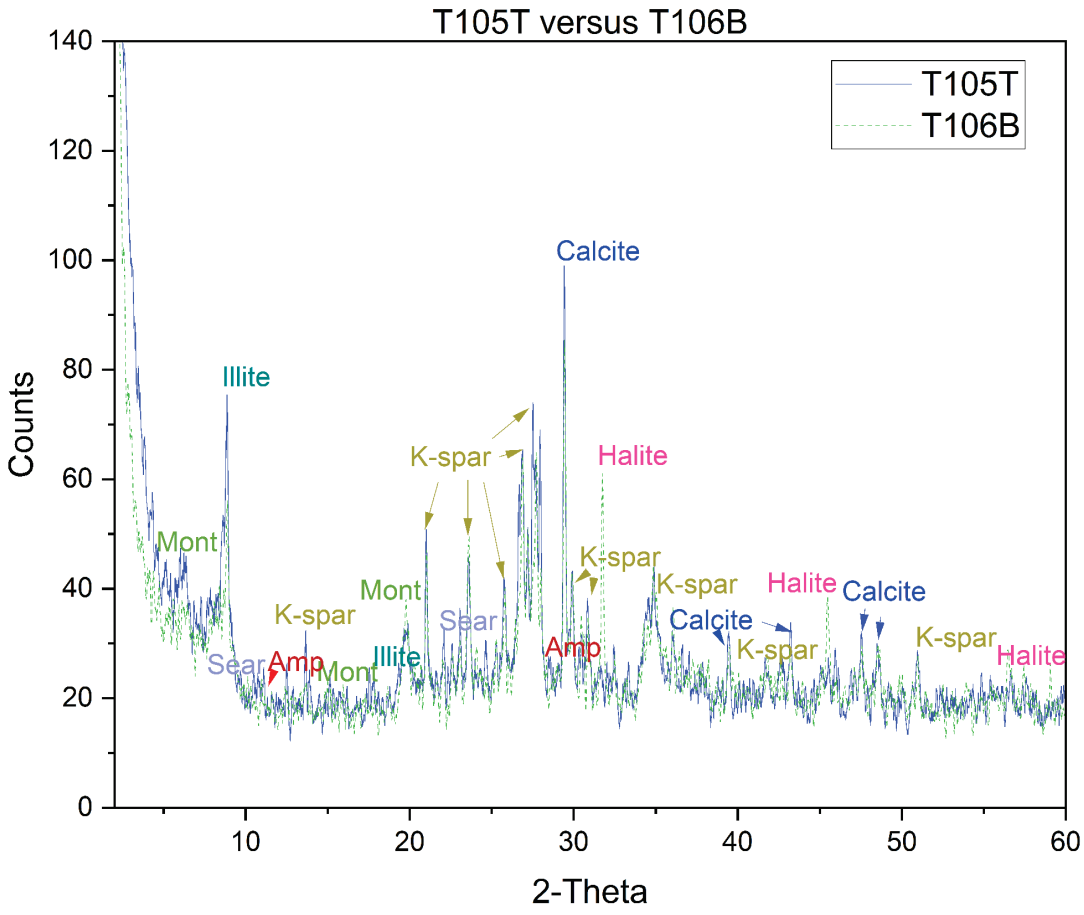

Figure 55: XRD patterns for the surface sample T105T (shown as a solid blue line) and subsurface sample T106B (shown as a dotted green line), near the bottom of Section 1. Both samples contain a similar relative abundance of illite (turquoise), K-feldspar (K-spar, yellow) and halite (pink). The surface sample T105T contains smectite (Mont, yellow green), amphibole (Amp, red), and searlesite (Sear, lavender) which the surface sample T106B lacks. It is likely that the bottom of Section 1 has been overprinted by sheet erosion.

Section 2

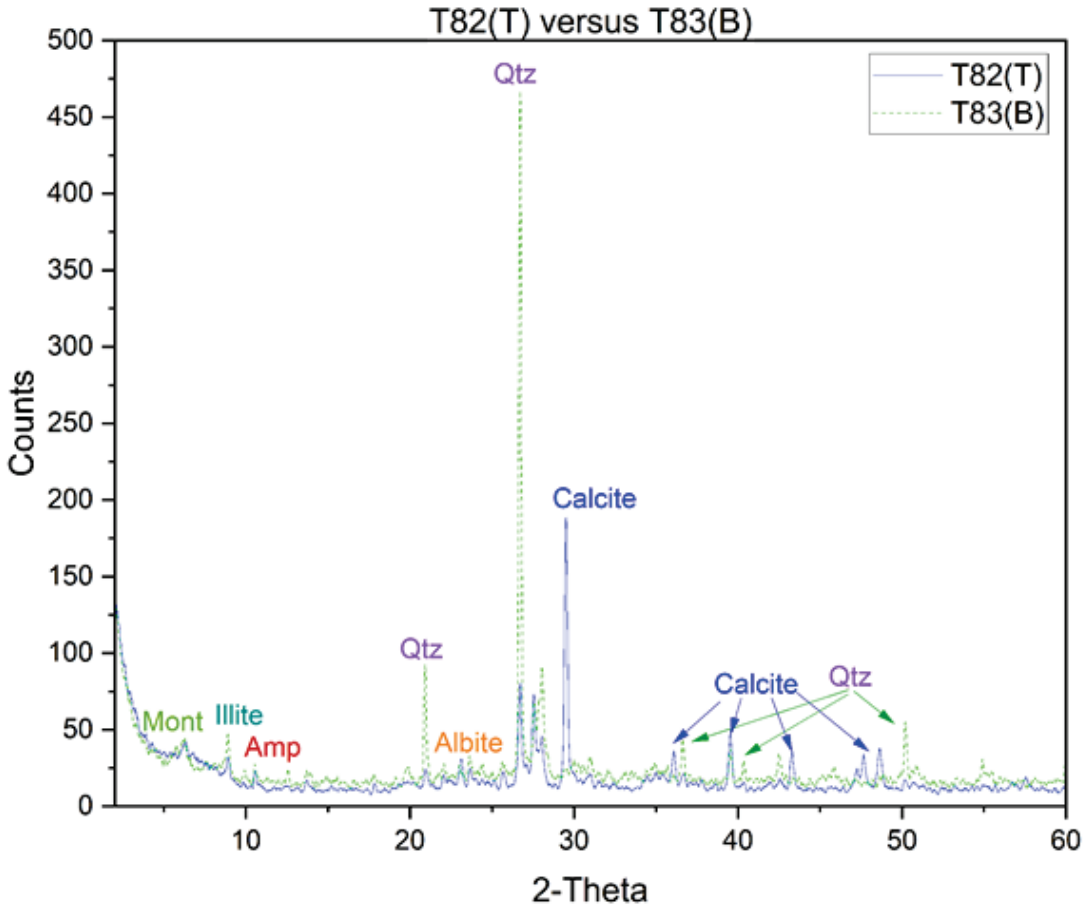

Figure 56: XRD patterns for the surface sample T82(T) (shown as a solid blue line) and subsurface sample T83(B) (shown as a dotted green line), near the middle of Section 2. The subsurface sample T83(B) lacks calcite (blue), K-feldspar (the small peaks are not labeled), and amphibole (Amp, red) compared to the surface sample T82(T). Both samples contain similar relative abundance of illite (turquoise), smectite (Mont, yellow green), and albite (orange). The surface sample T82(T) has a lower relative abundance of quartz (Qtz, purple) compared to the subsurface sample T83(B). It is likely that the whole section been overprinted by a mixture of sheet erosion, caliche from carbonate accumulation on the surface, and/or wind transport.

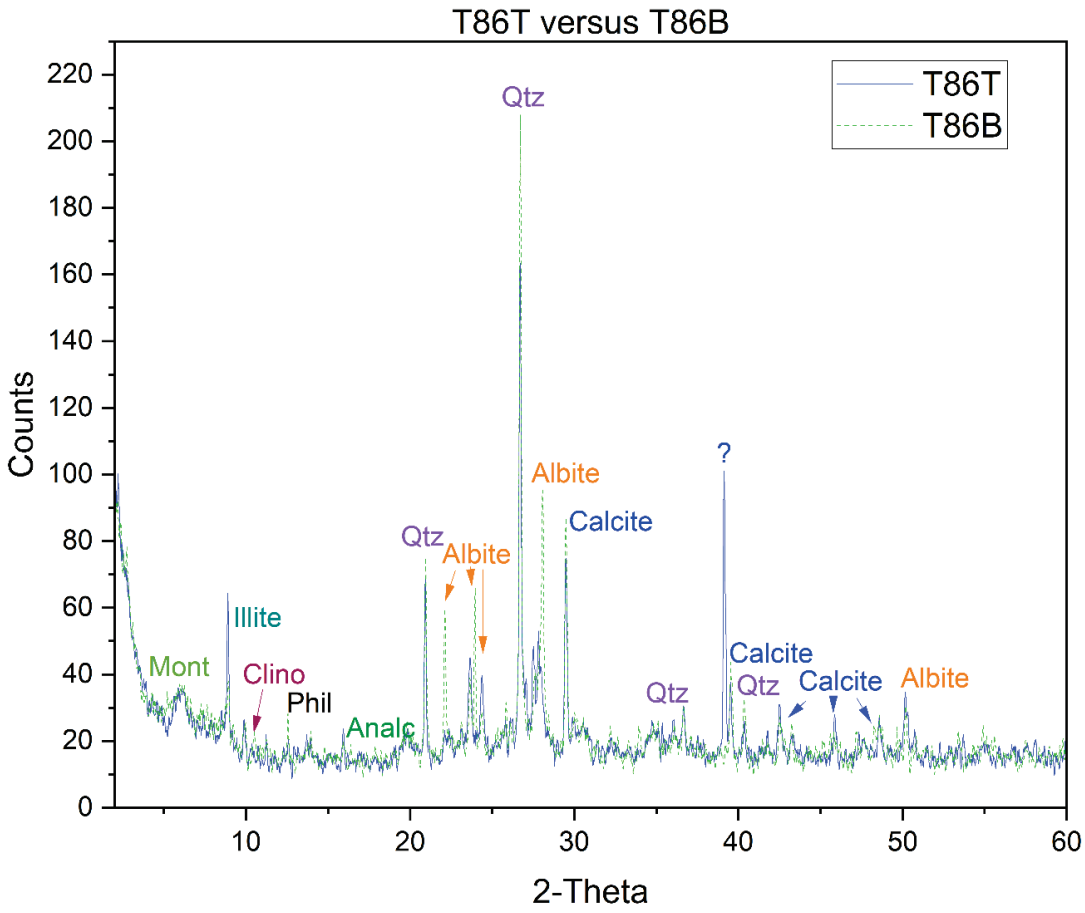

Figure 57: XRD patterns for the surface sample T86T (shown as a solid blue line) and subsurface sample T86B (shown as a dotted green line), near the bottom of Section 2. An unidentified peak near the 2-Theta of 40 degrees, appeared in T86T. The surface sample T86T lacks the zeolites clinoptilolite (Clino, dark red) and phillipsite (Phil, black) compared to the subsurface sample T86B. Both samples contain similar relative abundances of the zeolite analcime (Analc, green), smectite (Mont, yellow green), quartz (Qtz, purple), calcite (blue) and albite (orange). Surface sample T86T has a higher relative abundance of illite (turquoise) compared to subsurface sample T86B. It is likely that the whole section been overprinted by a mixture of sheet erosion, caliche from carbonate accumulation on the surface, and/or wind transport.

Appendix J: Bruker EVA XRD Plots

Section 1

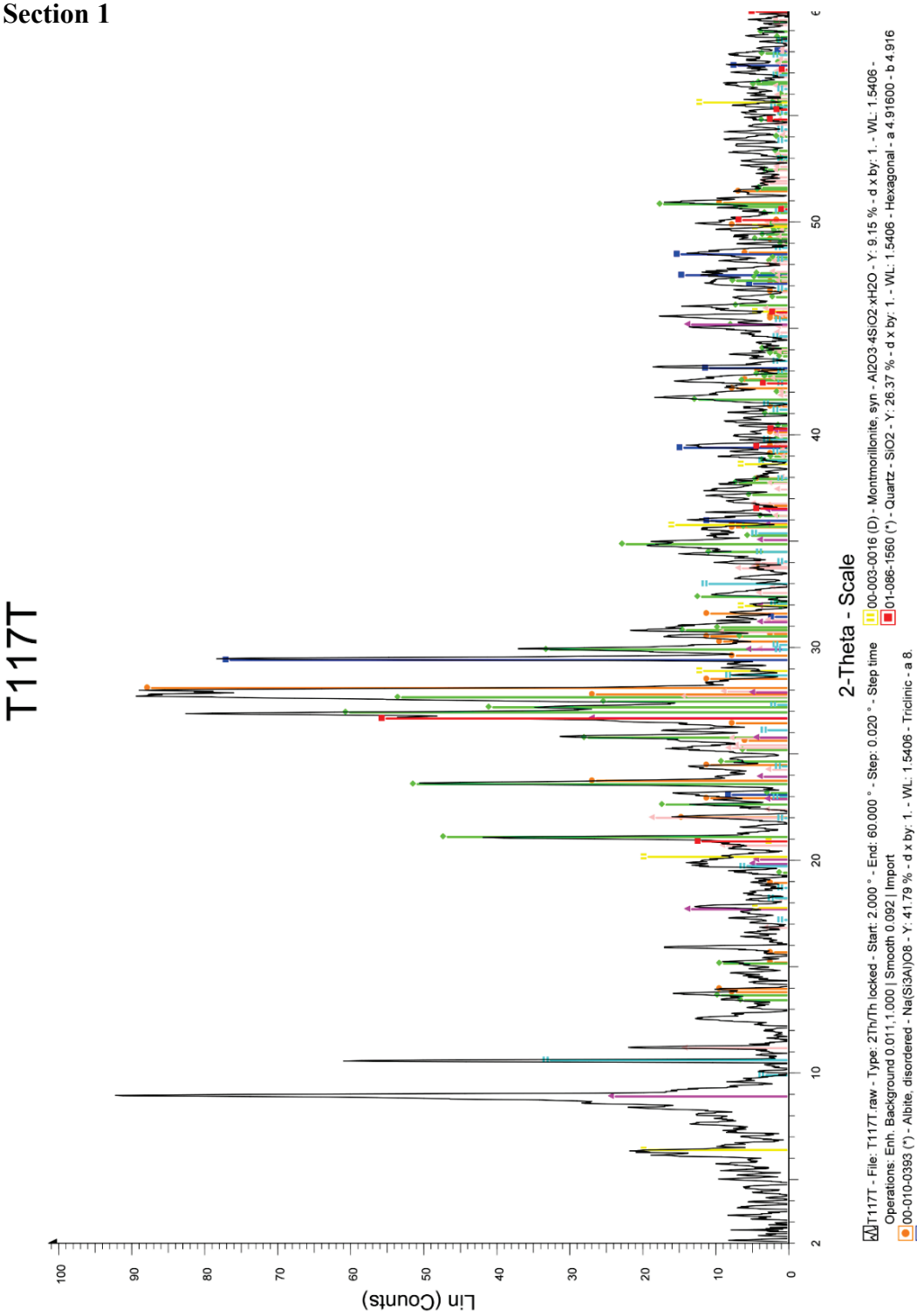

Figure 58: XRD pattern of T117T generated using the Bruker EVA software, showing albite (orange), calcite (blue), k-feldspar (green), searlesite (light pink), illite (pink), amphiboles (light blue), montmorillonite (yellow), and quartz (red).

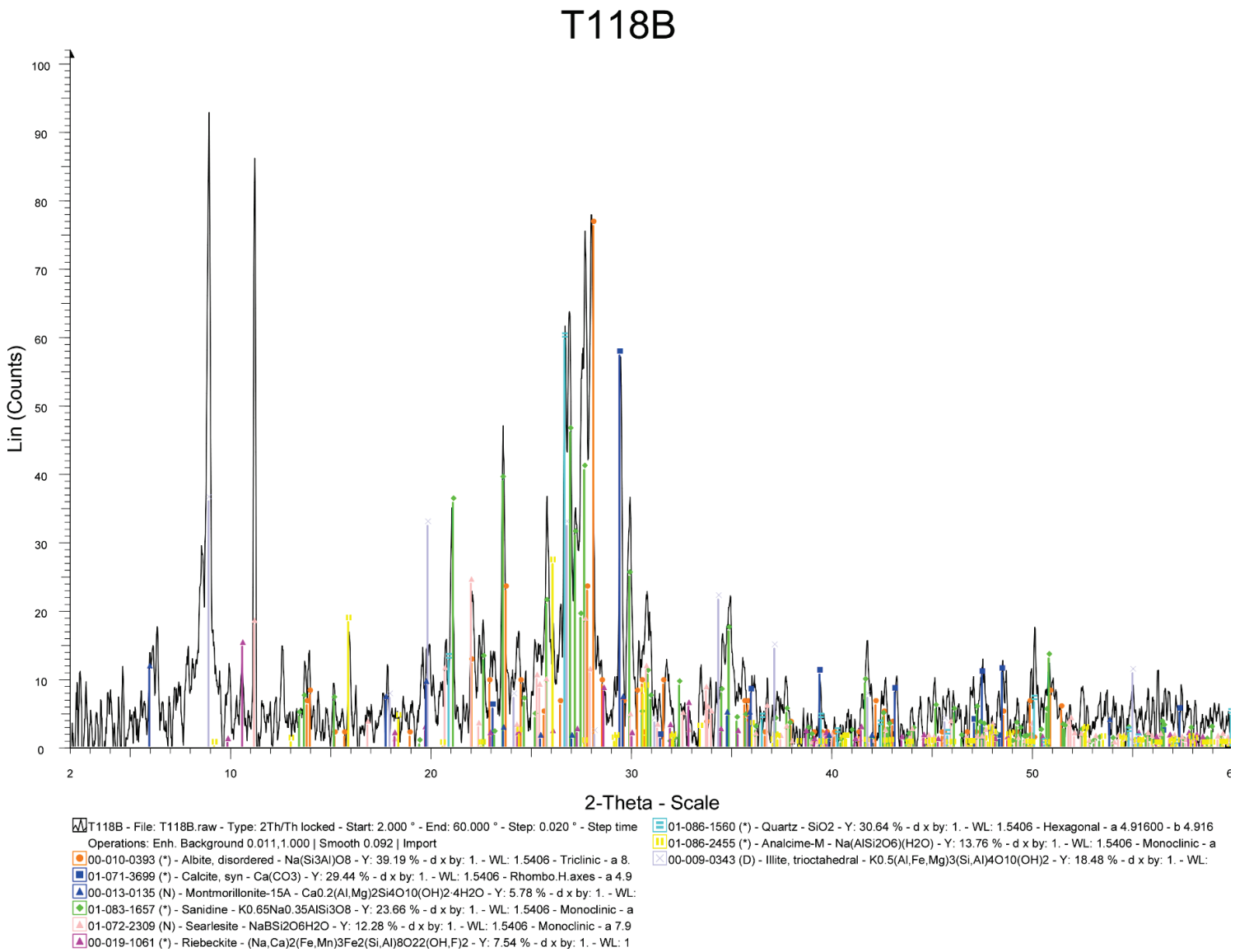

Figure 59: XRD pattern of T118B generated using the Bruker EVA software, showing albite (orange), analcime (yellow), calcite (blue), k-feldspar (green), searlesite (light pink), illite (lilac), amphiboles (pink), smectite (blue), and quartz (red).

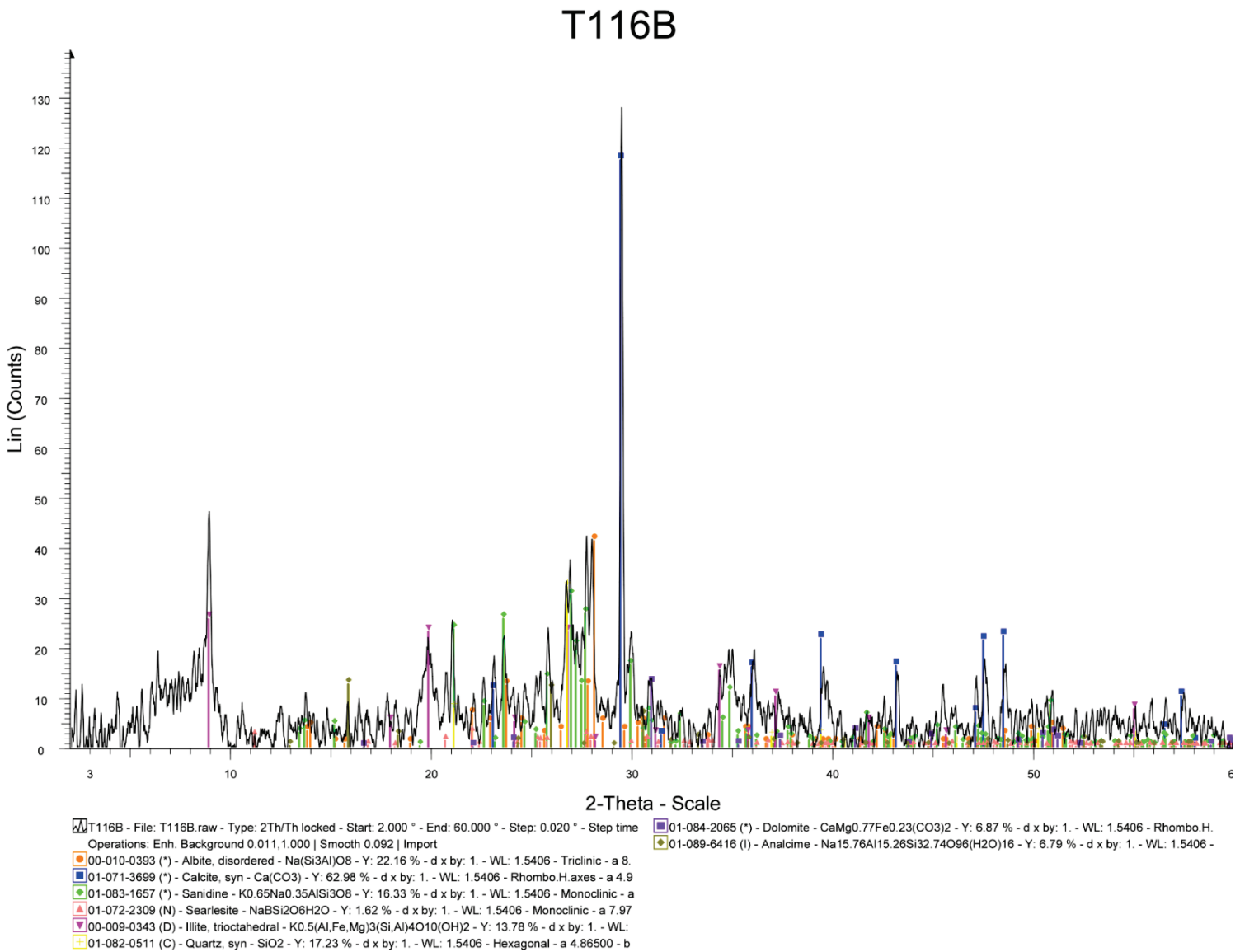

Figure 60: XRD pattern of T116B generated using the Bruker EVA software, showing albite (orange), analcime (dark yellow), calcite (blue), dolomite (purple), K-feldspar (green), searlesite (light pink), illite (pink), and quartz (red).

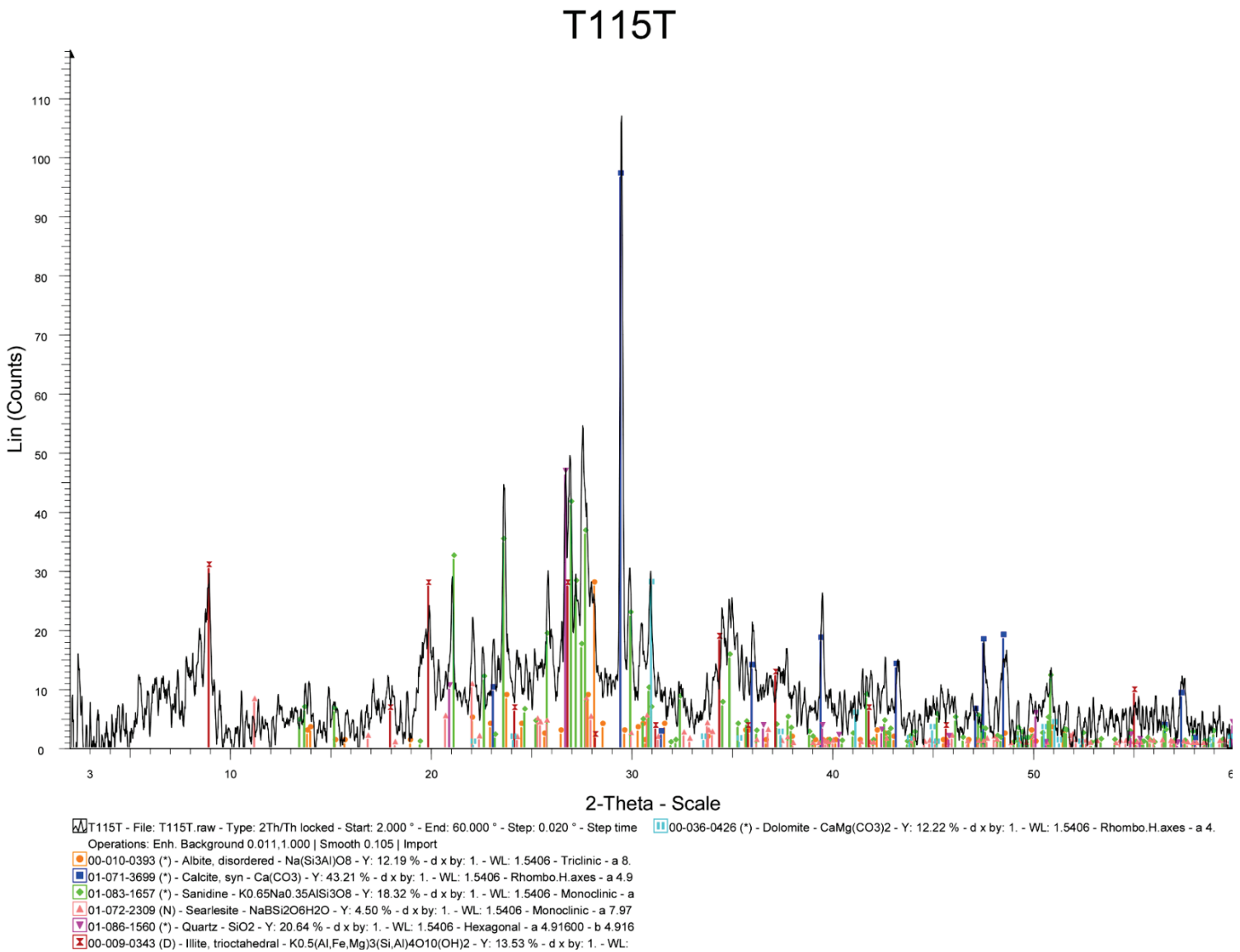

Figure 61: XRD pattern of T115T generated using the Bruker EVA software, showing albite (orange), calcite (blue), dolomite (light blue), K-feldspar (green), searlesite (light pink), illite (red), and quartz (pink).

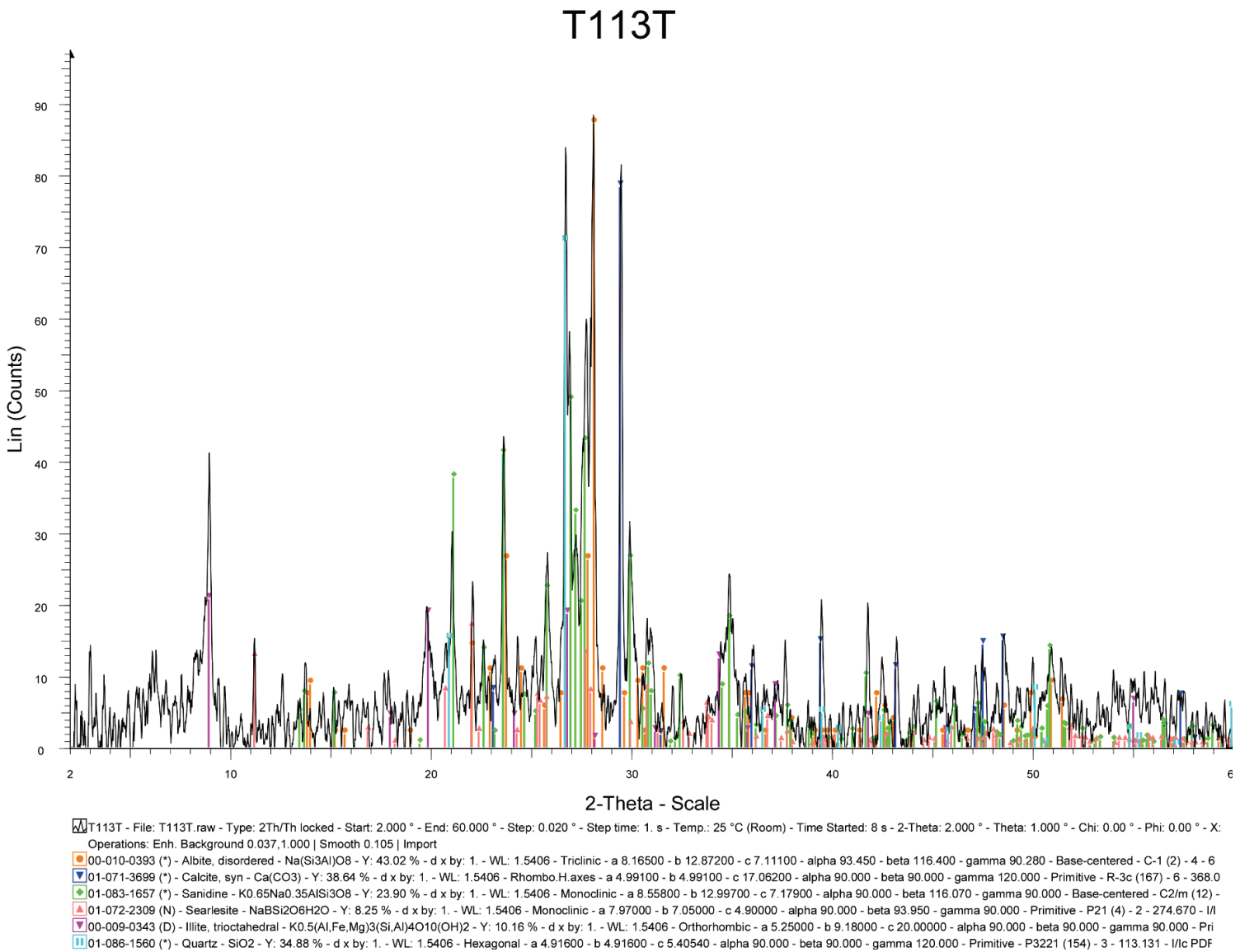

Figure 62: XRD pattern of T113T generated using the Bruker EVA software, showing albite (orange), calcite (blue), K-feldspar (green), searlesite (light pink), illite (pink), and quartz (light blue).

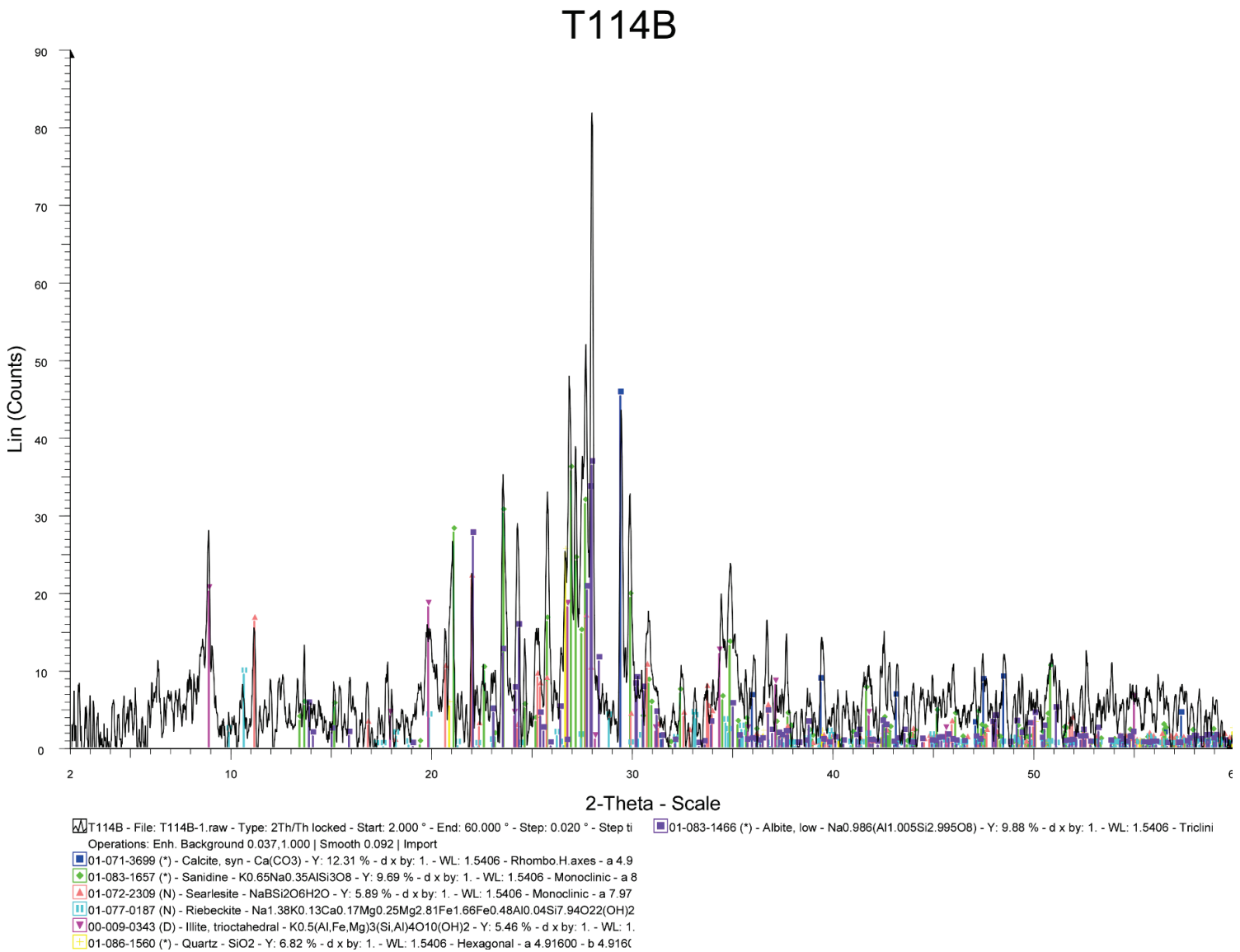

Figure 63: XRD pattern of T114B generated using the Bruker EVA software, showing albite (purple), amphibole (light blue), calcite (blue), K-feldspar (green), searlesite (orange), illite (pink), and quartz (yellow).

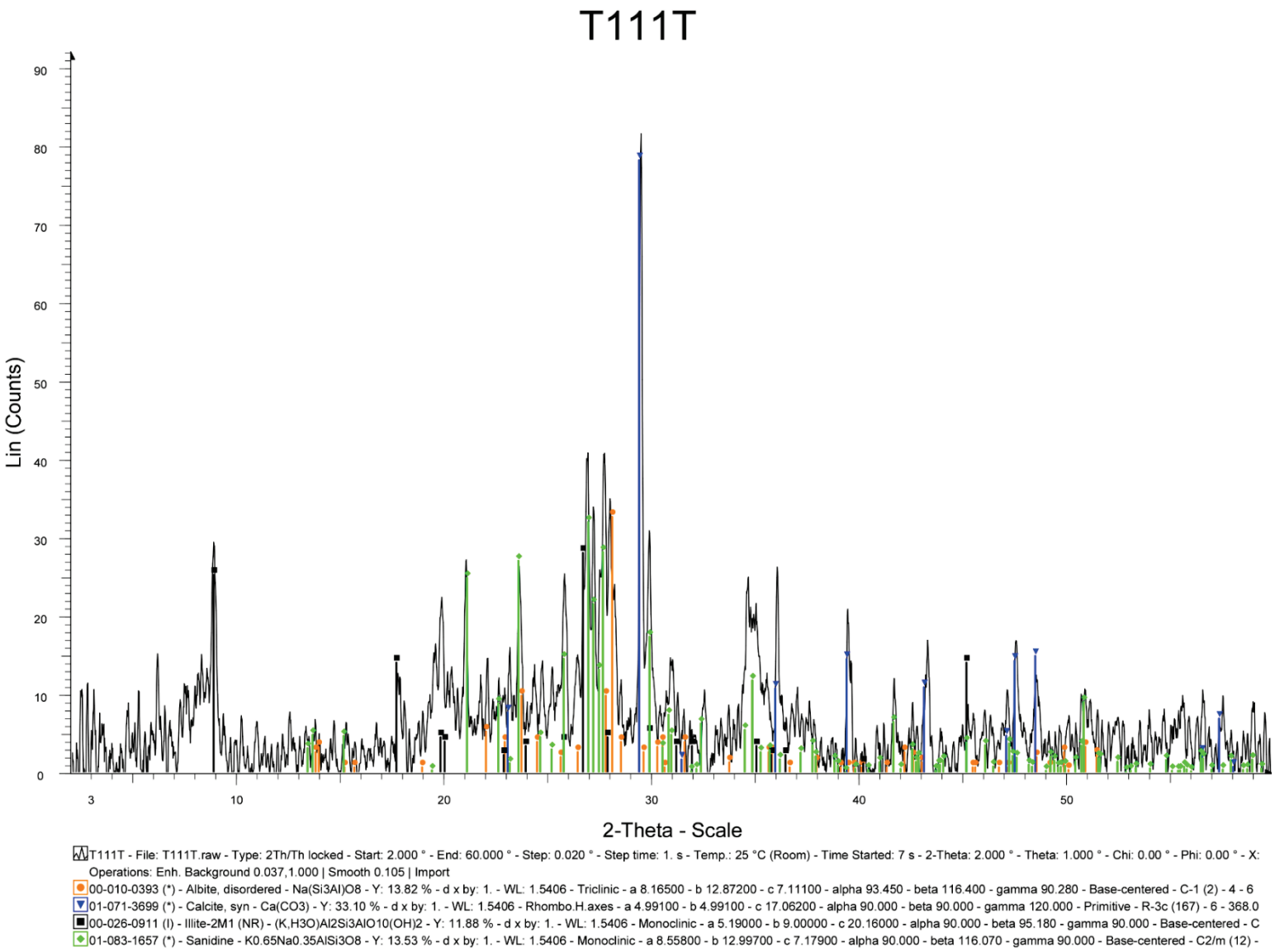

Figure 64: XRD pattern of T111T generated using the Bruker EVA software, showing albite (orange), calcite (blue), K-feldspar (green), and illite (blue).

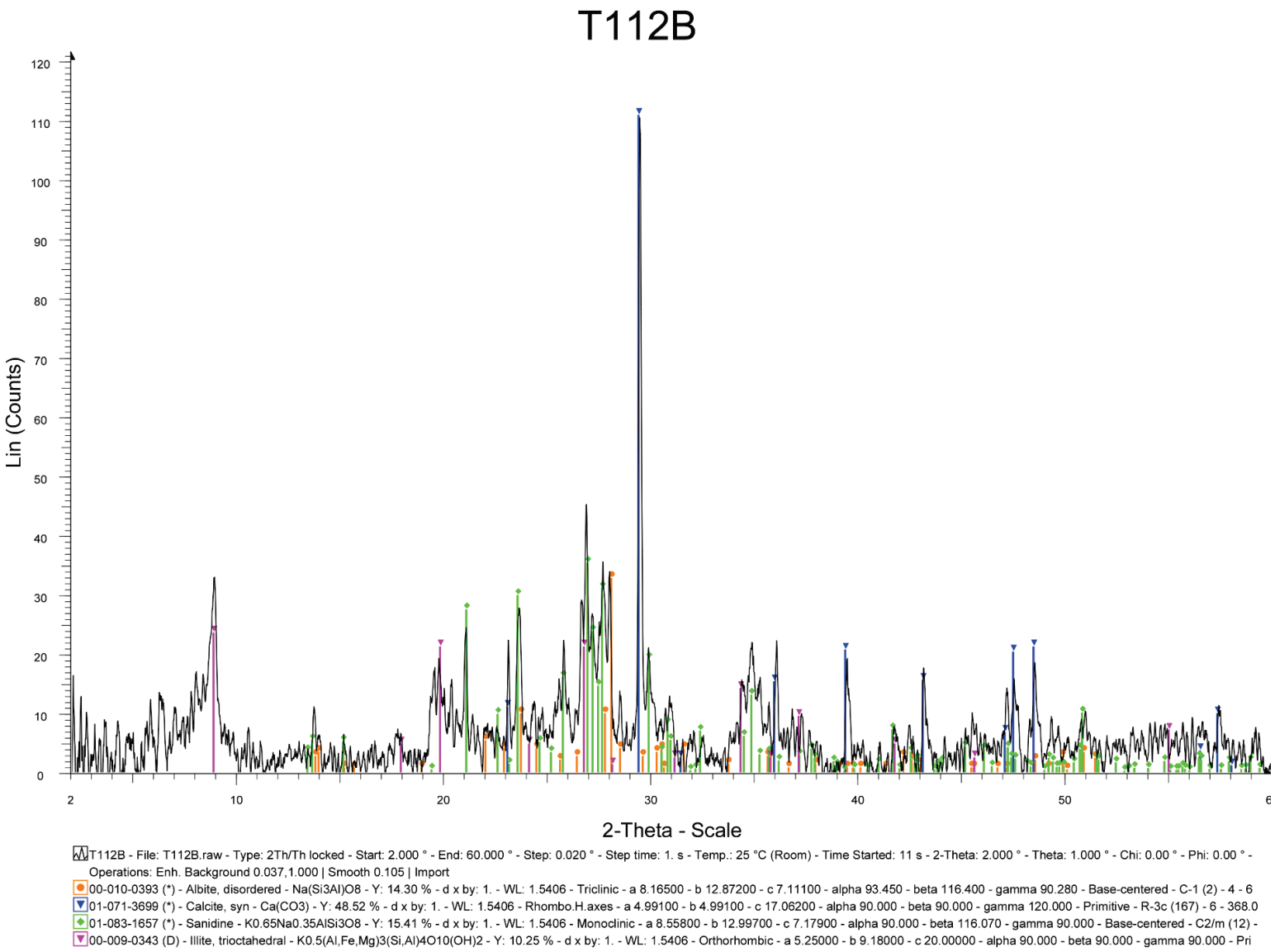

Figure 65: XRD pattern of T112B generated using the Bruker EVA software, showing albite (orange), calcite (blue), K-feldspar (green), and illite (pink).

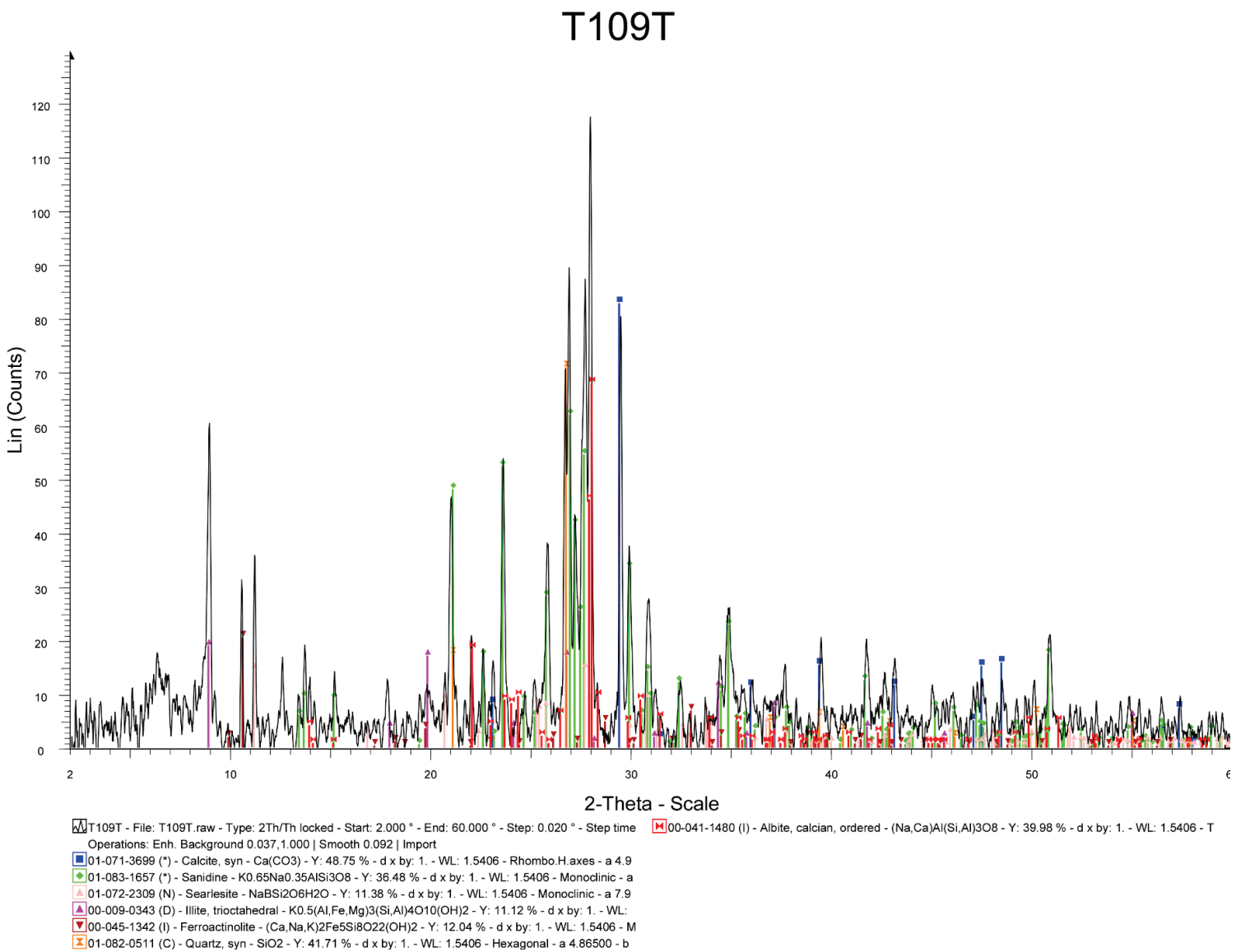

Figure 66: XRD pattern of T109T generated using the Bruker EVA software, showing albite (red), amphibole (dark red), calcite (blue), K-feldspar (green), searlesite (light pink), illite (pink), and quartz (orange).

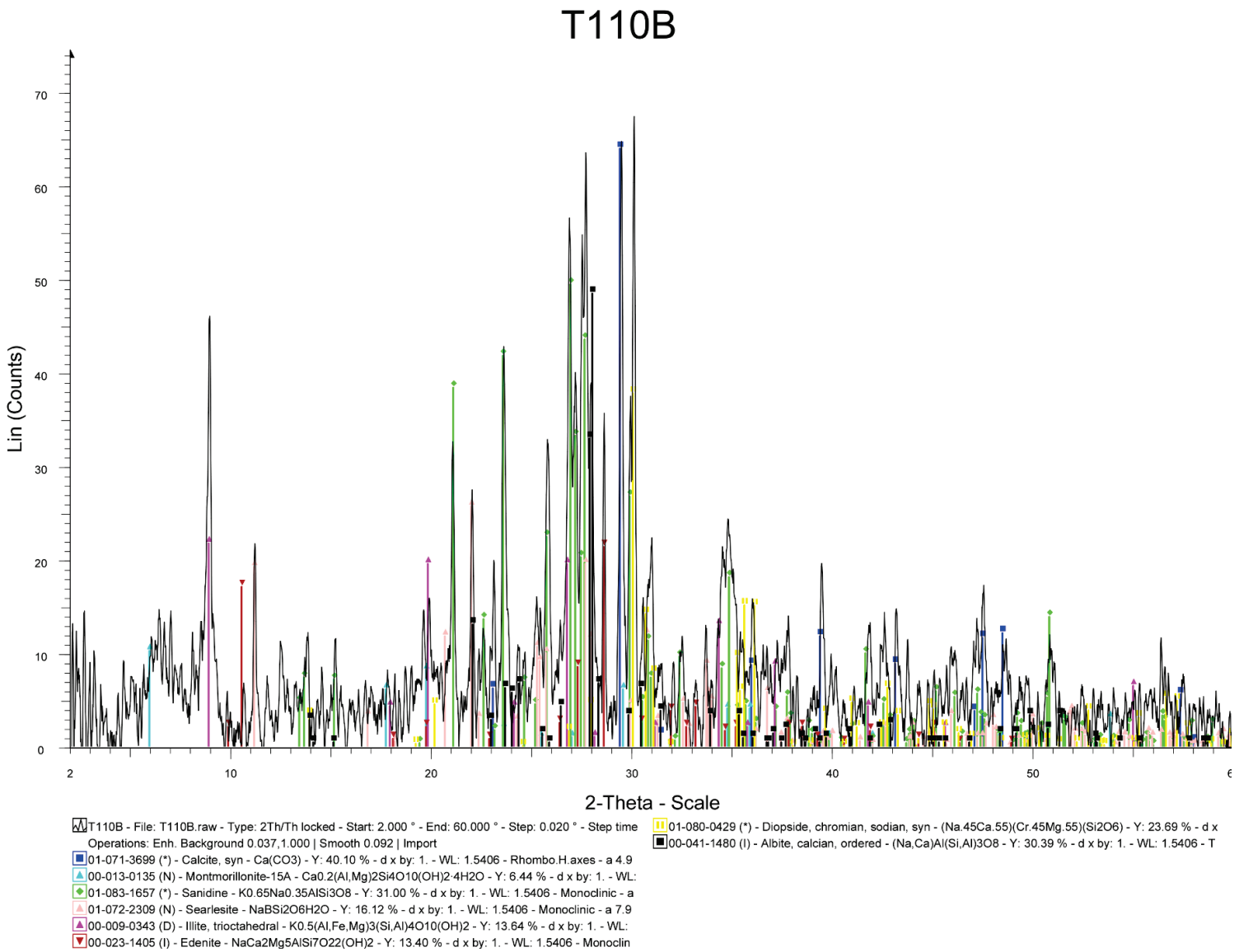

Figure 67: XRD pattern of T110B generated using the Bruker EVA software, showing albite (black), amphibole (dark red and yellow), calcite (blue), K-feldspar (green), searlesite (light pink), illite (pink), and smectite (light blue).

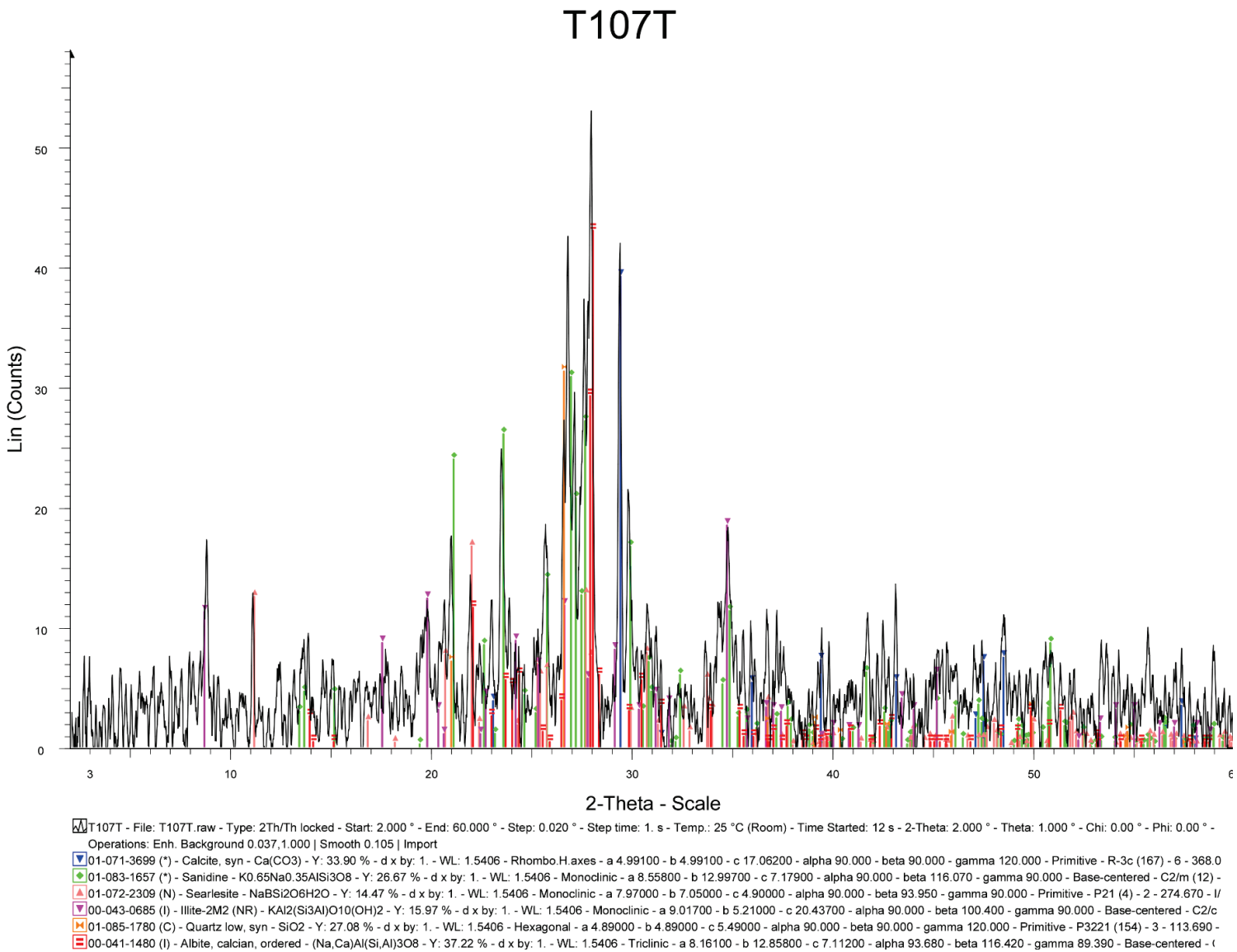

Figure 68: XRD pattern of T107T generated using the Bruker EVA software, showing albite (red), calcite (blue), K-feldspar (green), searlesite (light pink), illite (pink), and quartz (orange).

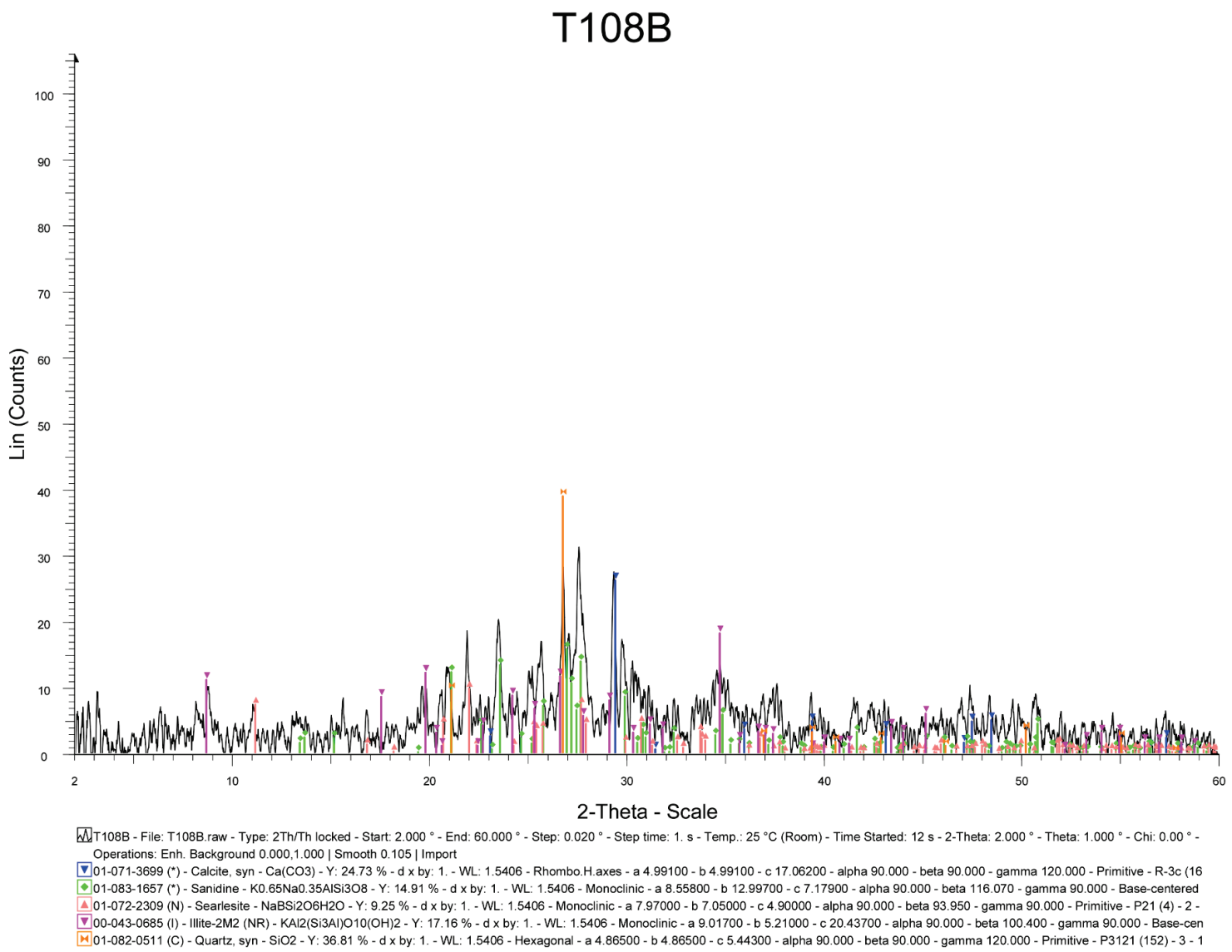

Figure 69: XRD pattern of T108B generated using the Bruker EVA software, showing albite (red), calcite (blue), K-feldspar (green), searlesite (light pink), illite (pink), and quartz (orange).

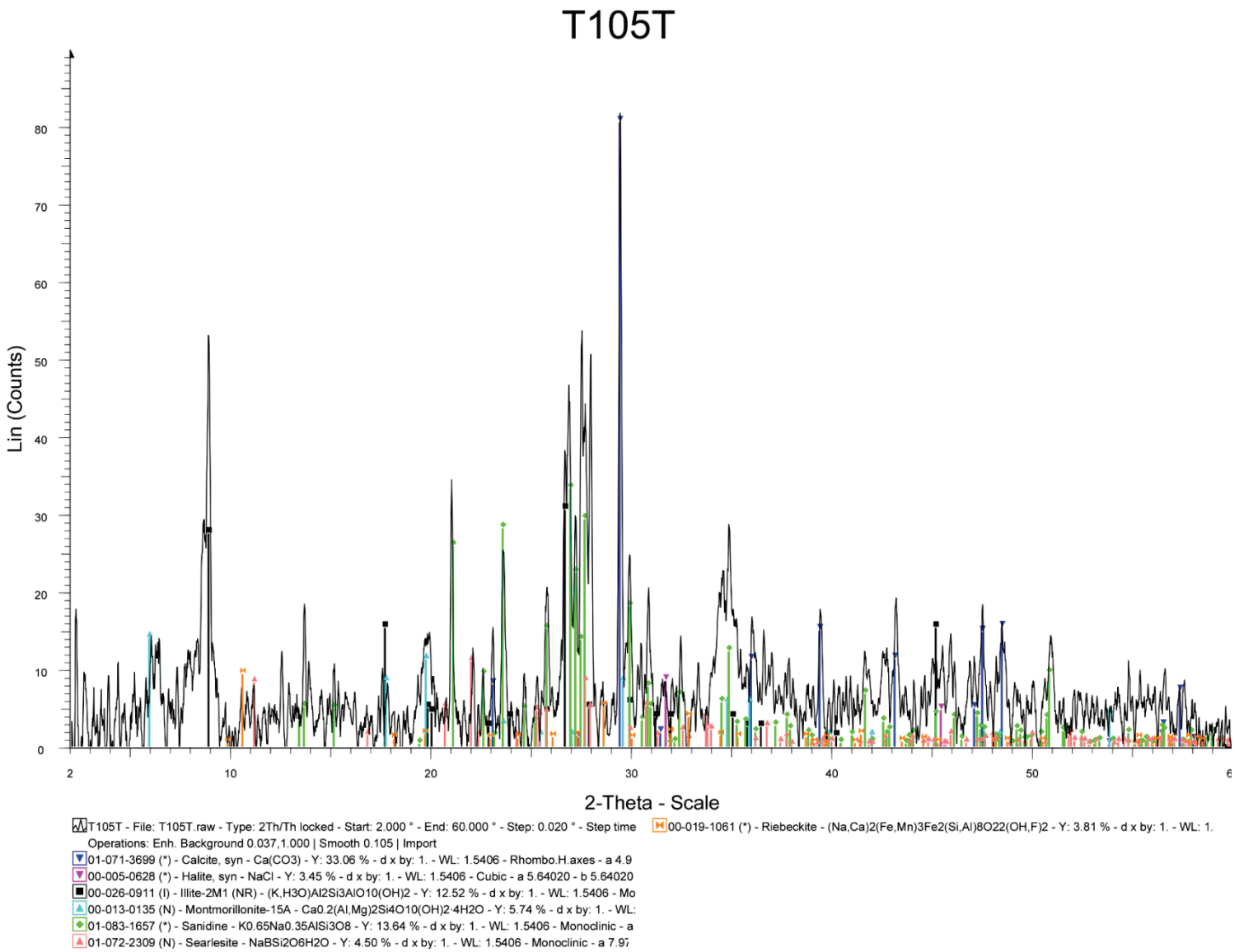

Figure 70: XRD pattern of T105T generated using the Bruker EVA software, showing amphibole (orange), calcite (blue), halite (pink), K-feldspar (green), searlesite (light pink), illite (black), and smectite (light blue).

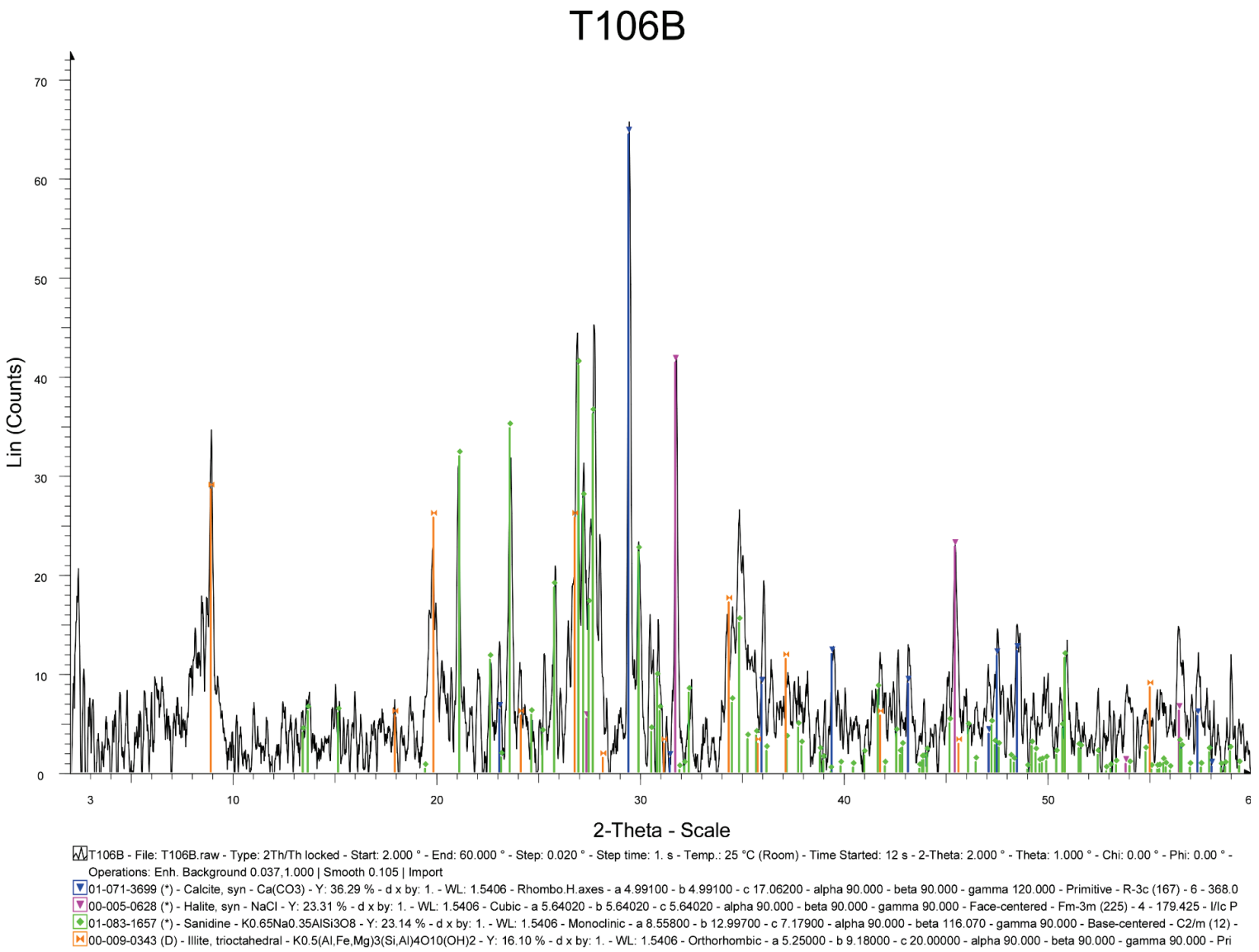

Figure 71: XRD pattern of T106B generated using the Bruker EVA software, showing calcite (blue), halite (pink), K-feldspar (green), and illite (orange).

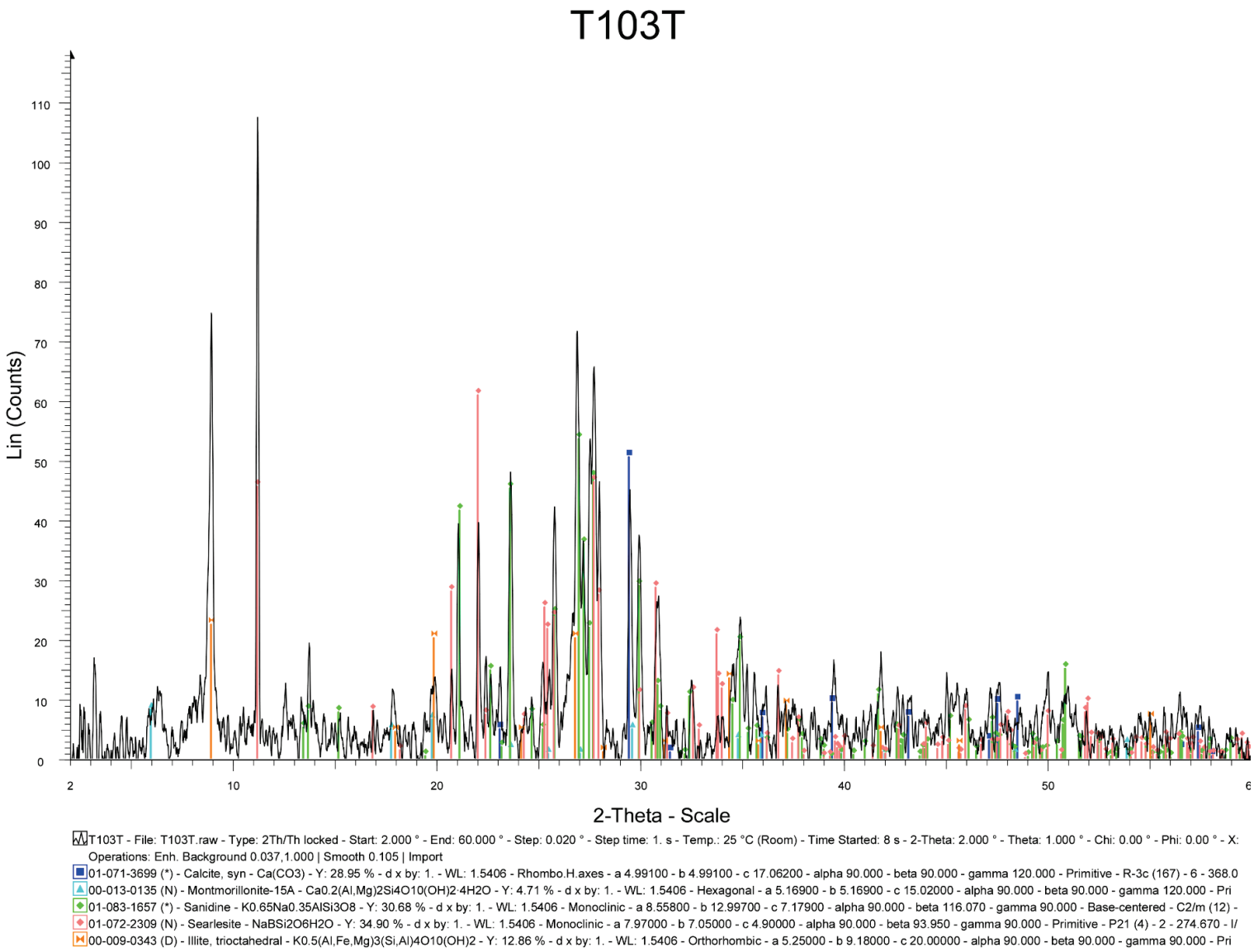

Figure 72: XRD pattern of T103T generated using the Bruker EVA software, showing calcite (blue), K-feldspar (green), searlesite (light pink), illite (orange), and smectite (light blue).

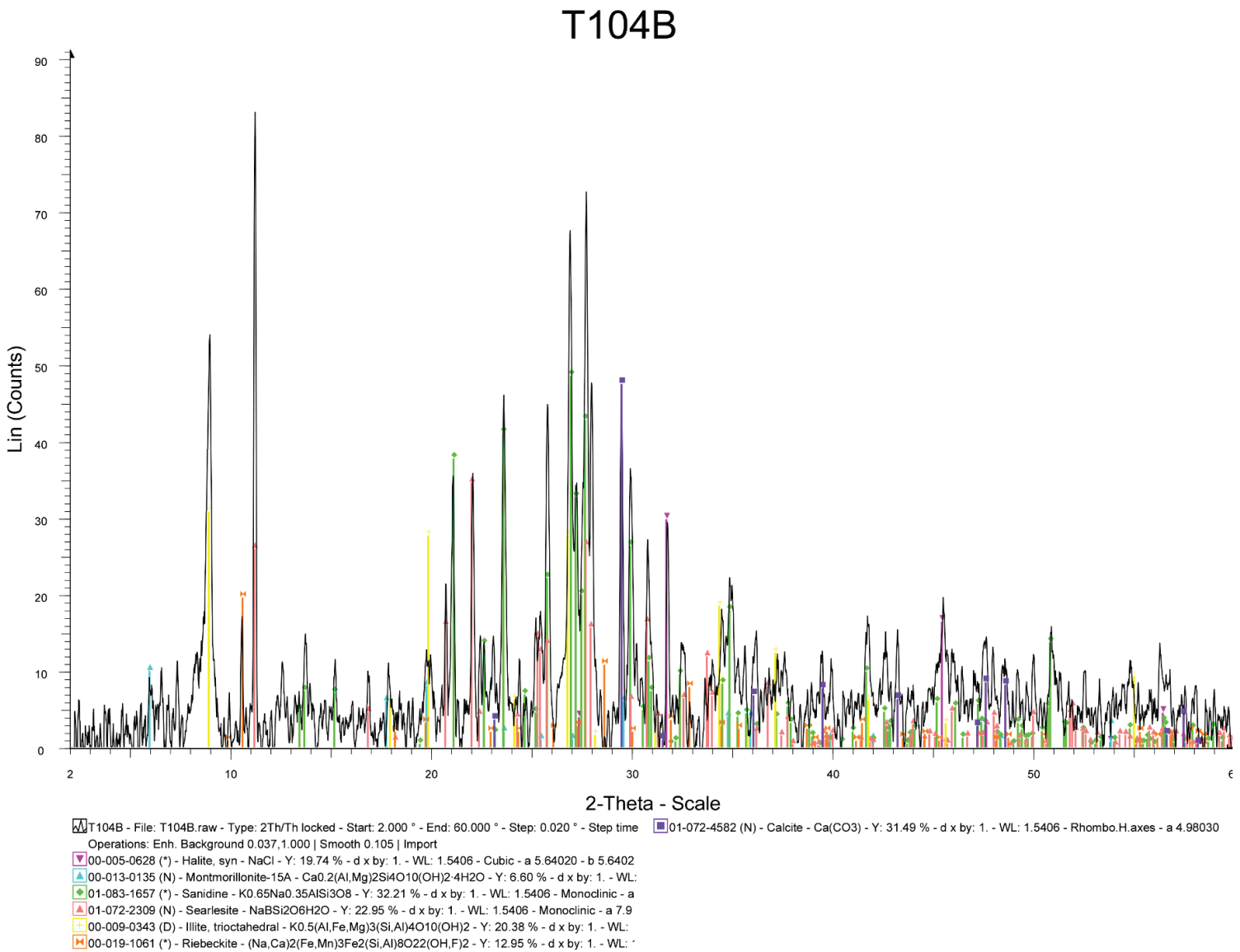

Figure 73: XRD pattern of T104B generated using the Bruker EVA software, showing amphibole (orange), calcite (purple), halite (pink), K-feldspar (green), searlesite (light pink), illite (yellow), and smectite (light blue).

Section 2

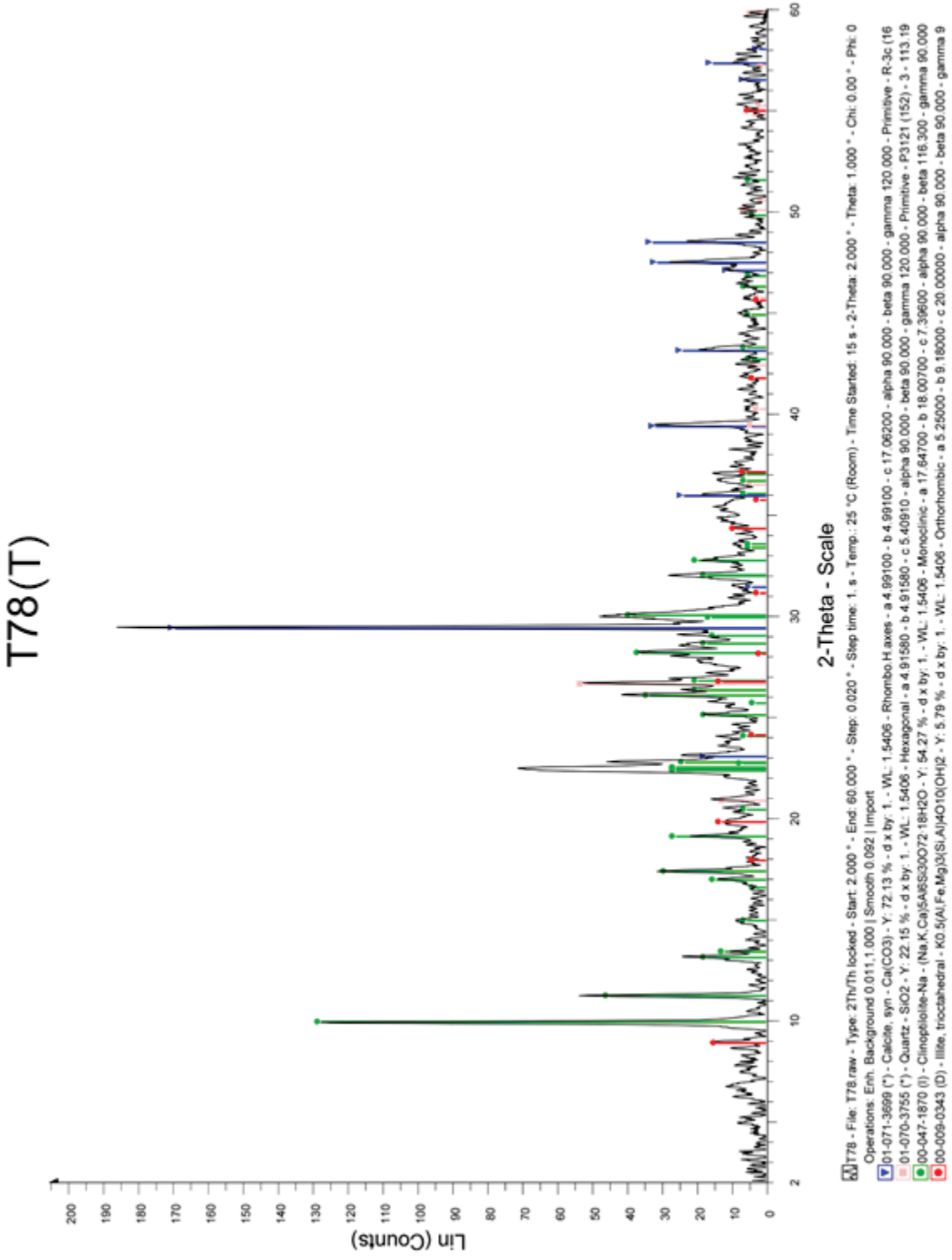

Figure 74: XRD pattern of T78(T) generated using the Bruker EVA software, showing calcite (blue), clinoptilolite (green), illite (red), and quartz (light pink).

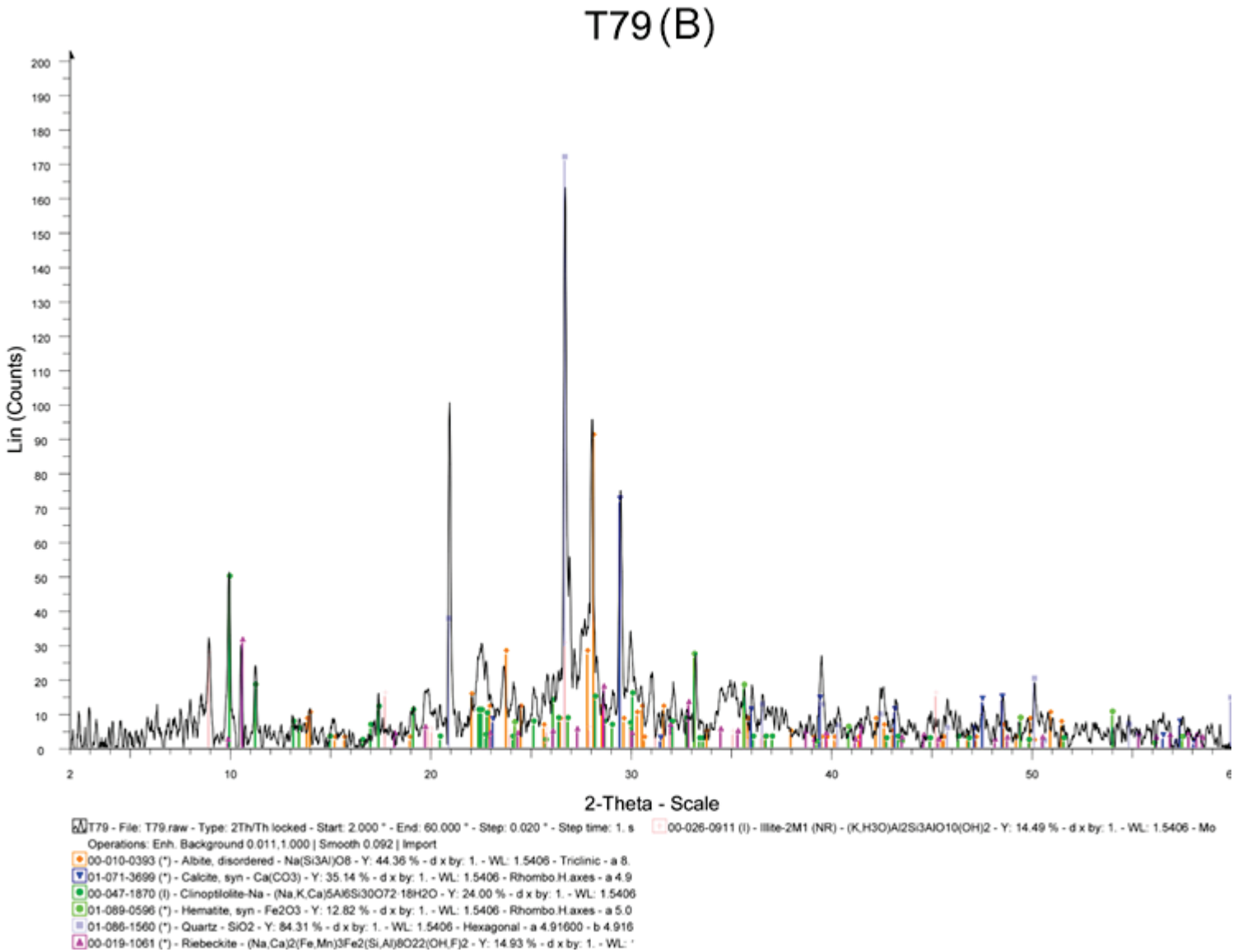

Figure 75: XRD pattern of T79(B) generated using the Bruker EVA software, showing albite (orange), amphibole (pink), calcite (blue), clinoptilolite (dark green), hematite (green), illite (light pink), and quartz (lilac).

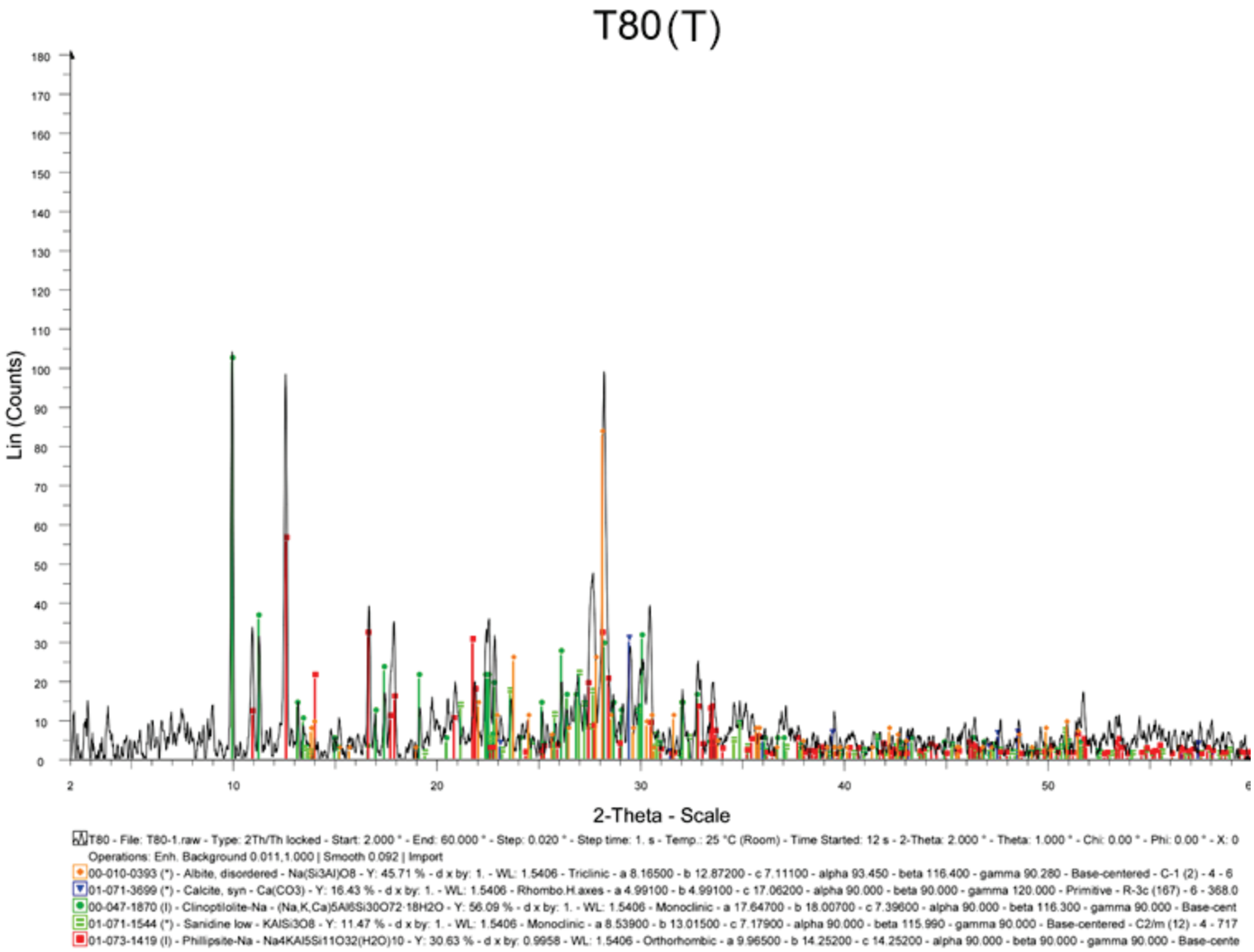

Figure 76: XRD pattern of T80(T) generated using the Bruker EVA software, showing albite (orange), calcite (blue), clinoptilolite (dark green), K-feldspar (green), and phillipsite (red).

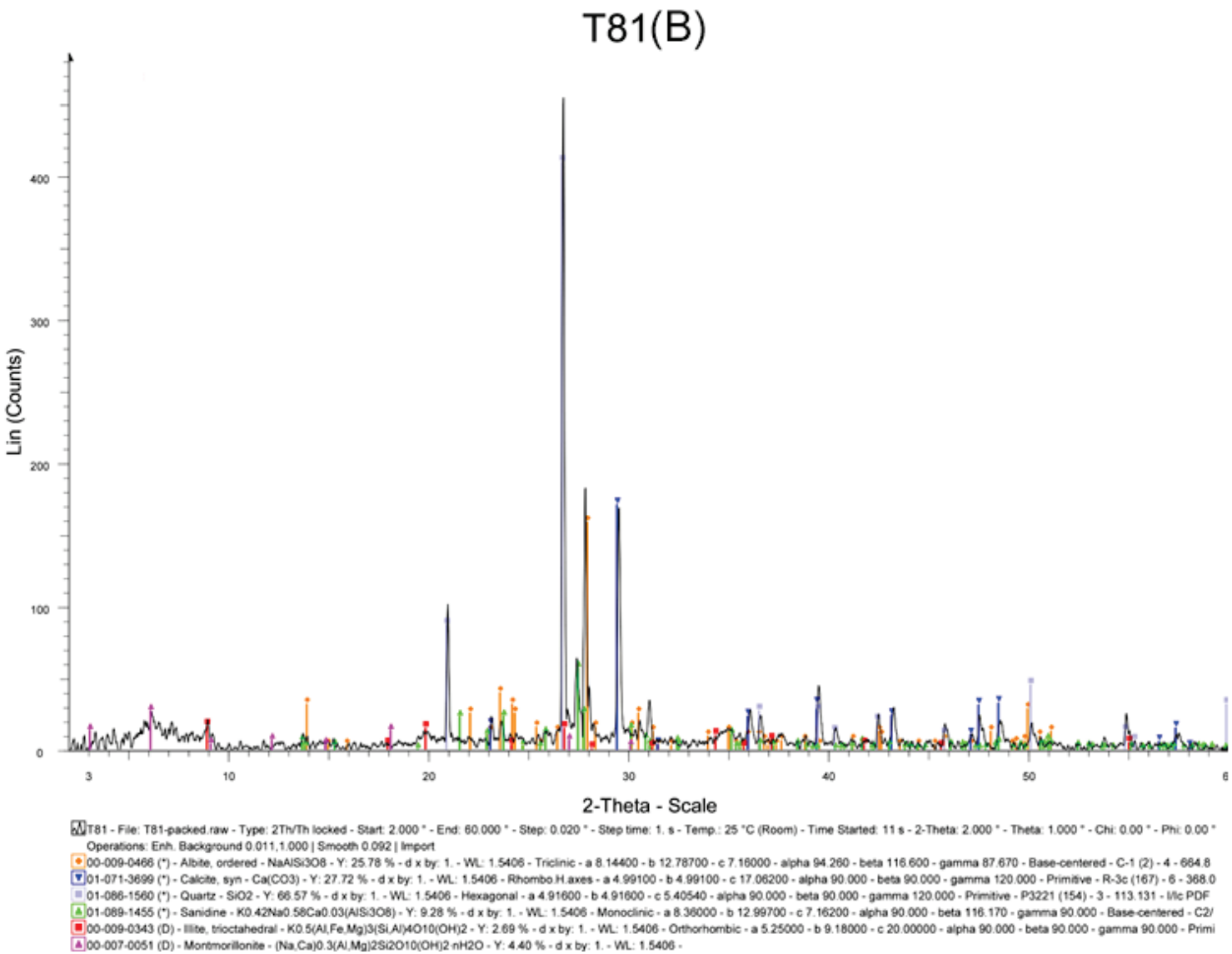

Figure 77: XRD pattern of T81(B) generated using the Bruker EVA software, showing albite (orange), calcite (blue), K-feldspar (green), illite (red), smectite (pink), and quartz (lilac).

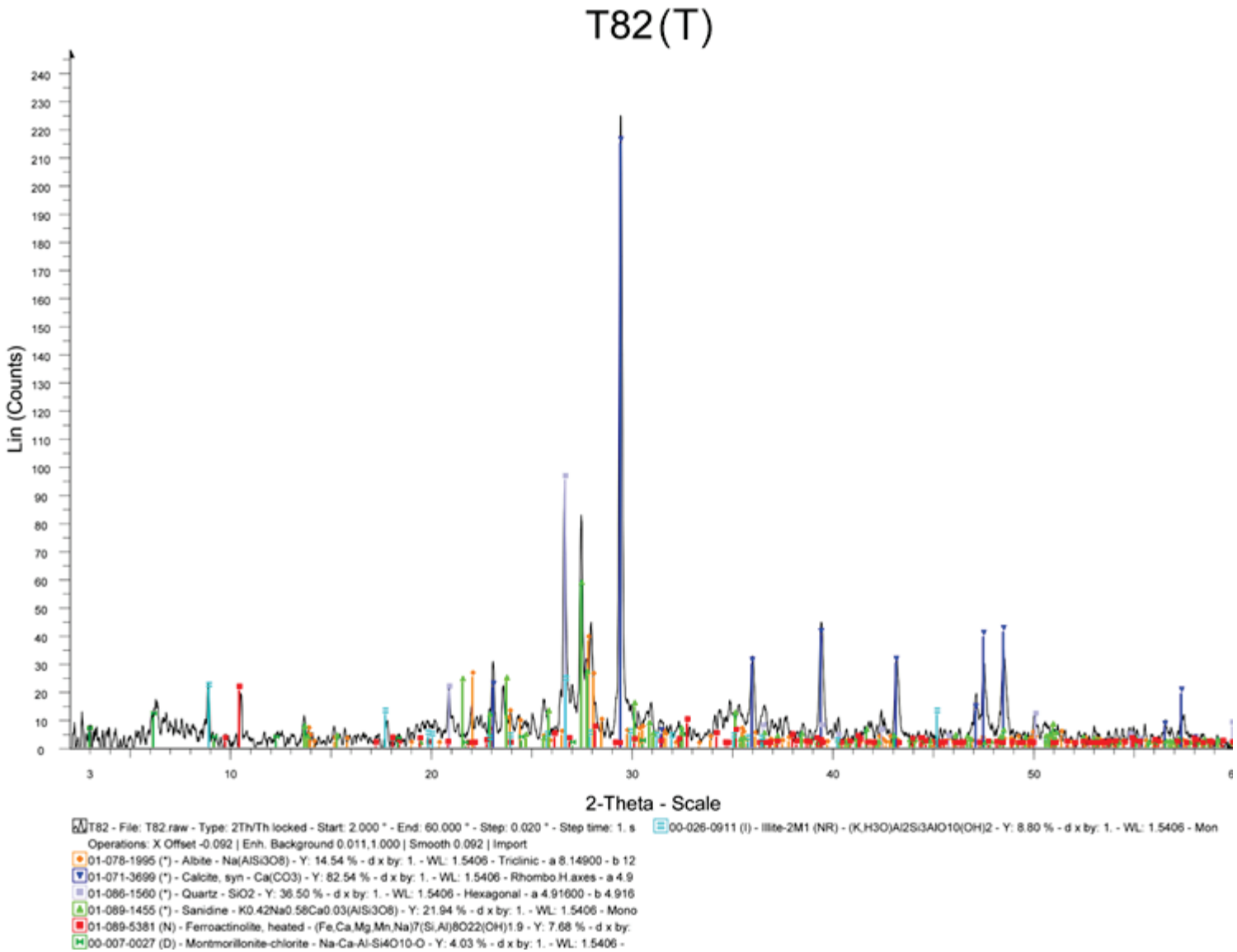

Figure 78: XRD pattern of T82(T) generated using the Bruker EVA software, showing albite (orange), amphibole (red), calcite (blue), K-feldspar (green), illite (light blue), smectite (dark green), and quartz (lilac).

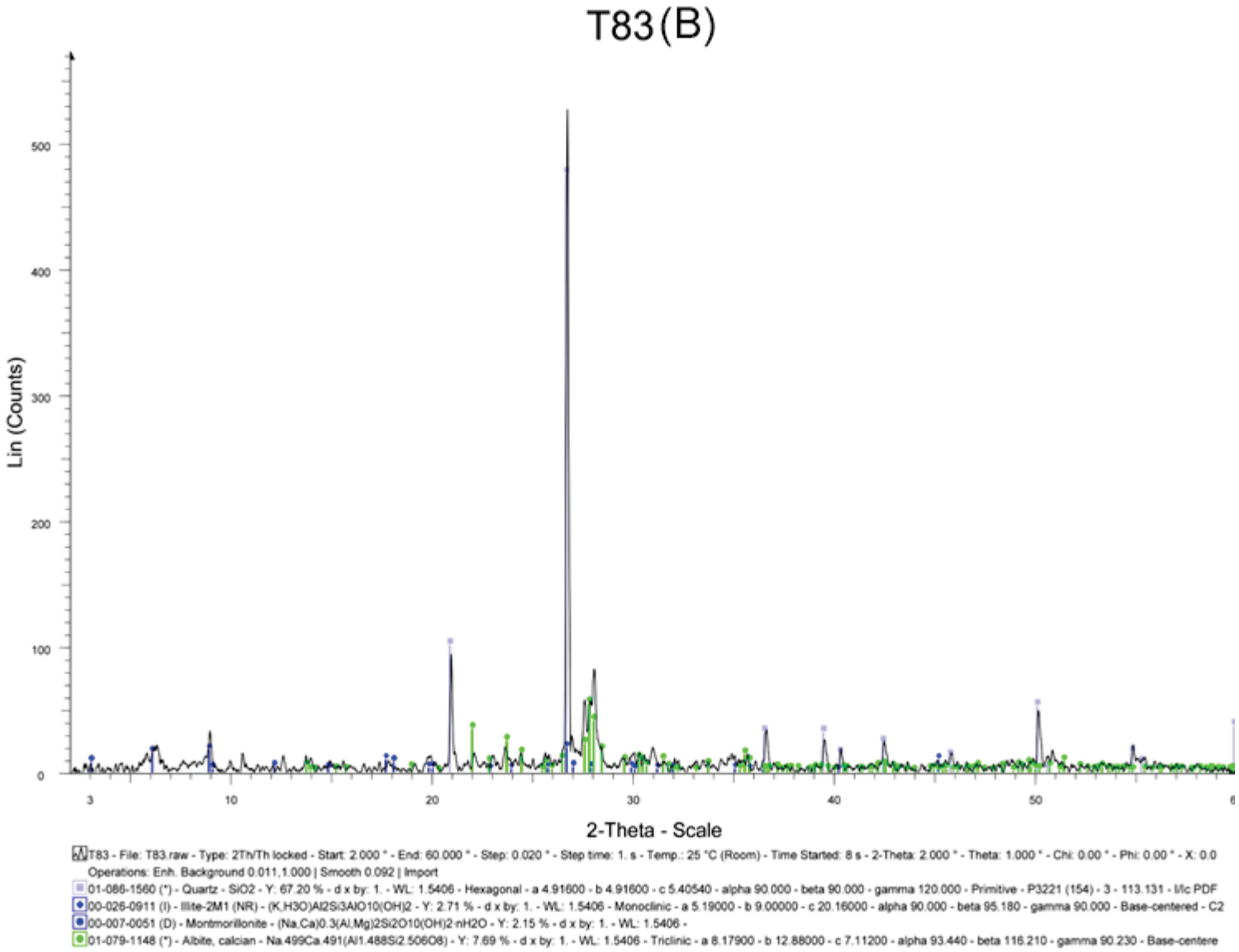

Figure 79: XRD pattern of T83(B) generated using the Bruker EVA software, showing albite (green), illite (blue 1), smectite (blue 2), and quartz (lilac).

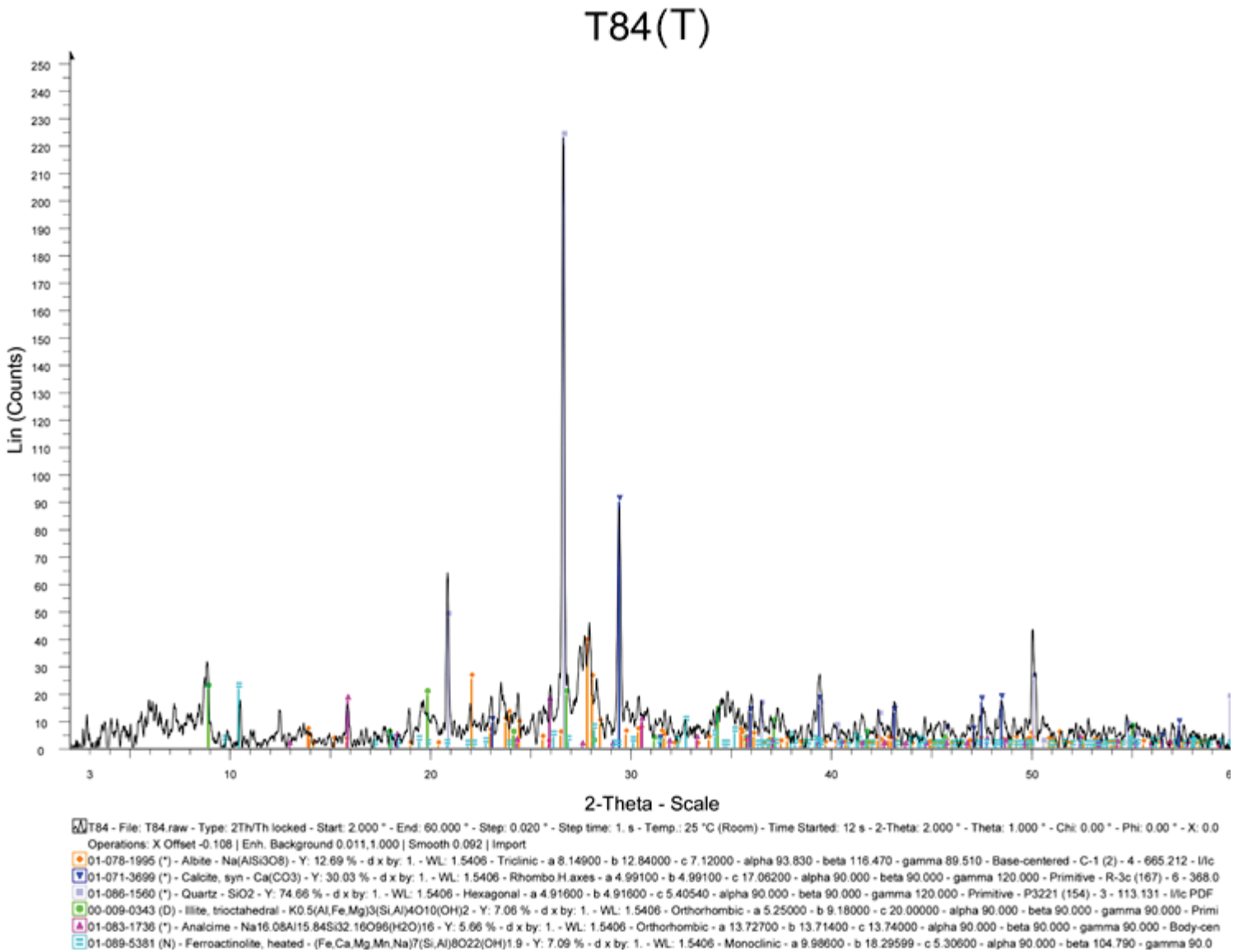

Figure 80: XRD pattern of T84(T) generated using the Bruker EVA software, showing albite (orange), amphibole (light blue), analcime (pink), calcite (blue), illite (green), and quartz (lilac).

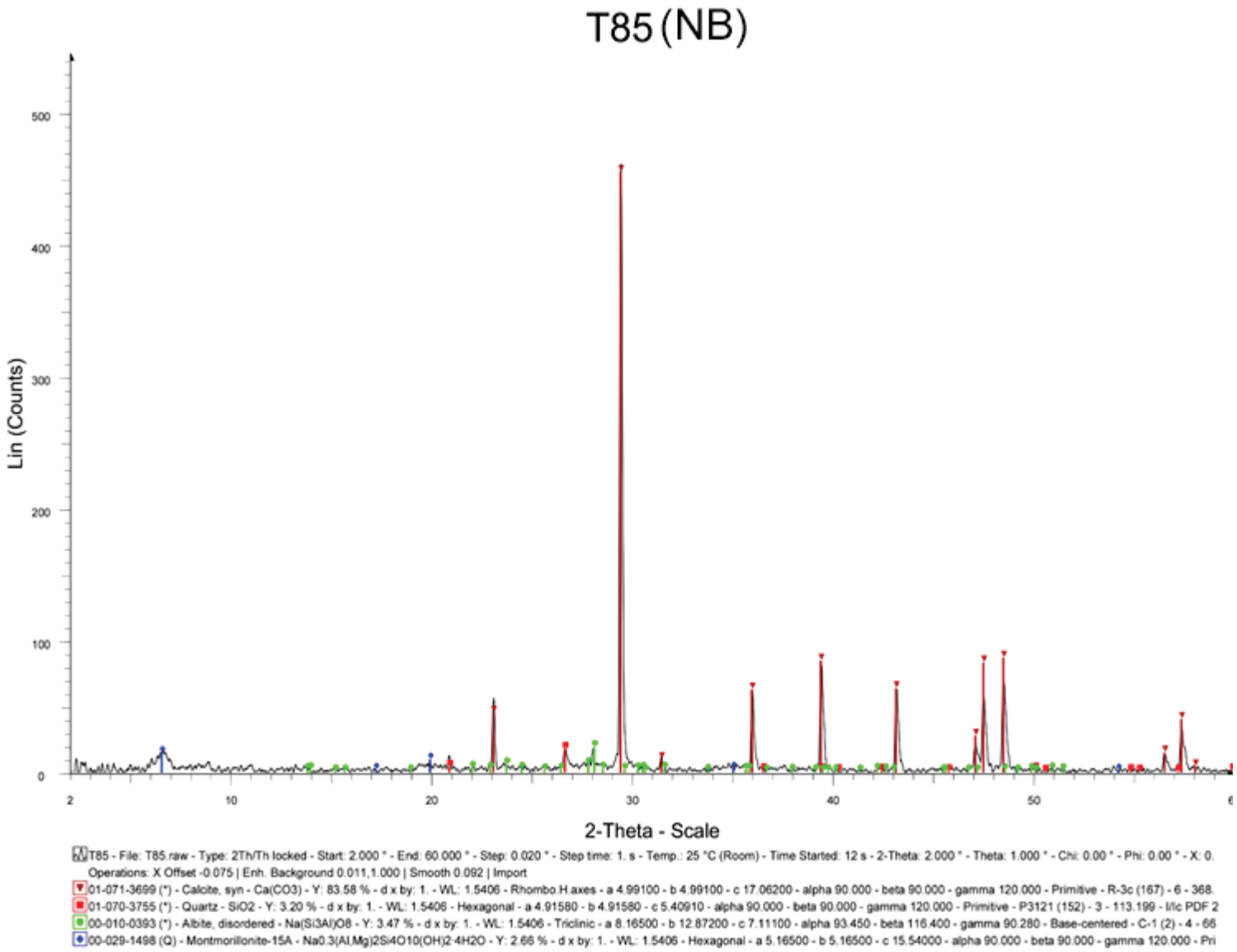

Figure 81: XRD pattern of T85(NB) generated using the Bruker EVA software, showing albite (green), calcite (dark red), smectite (blue), and quartz (red).

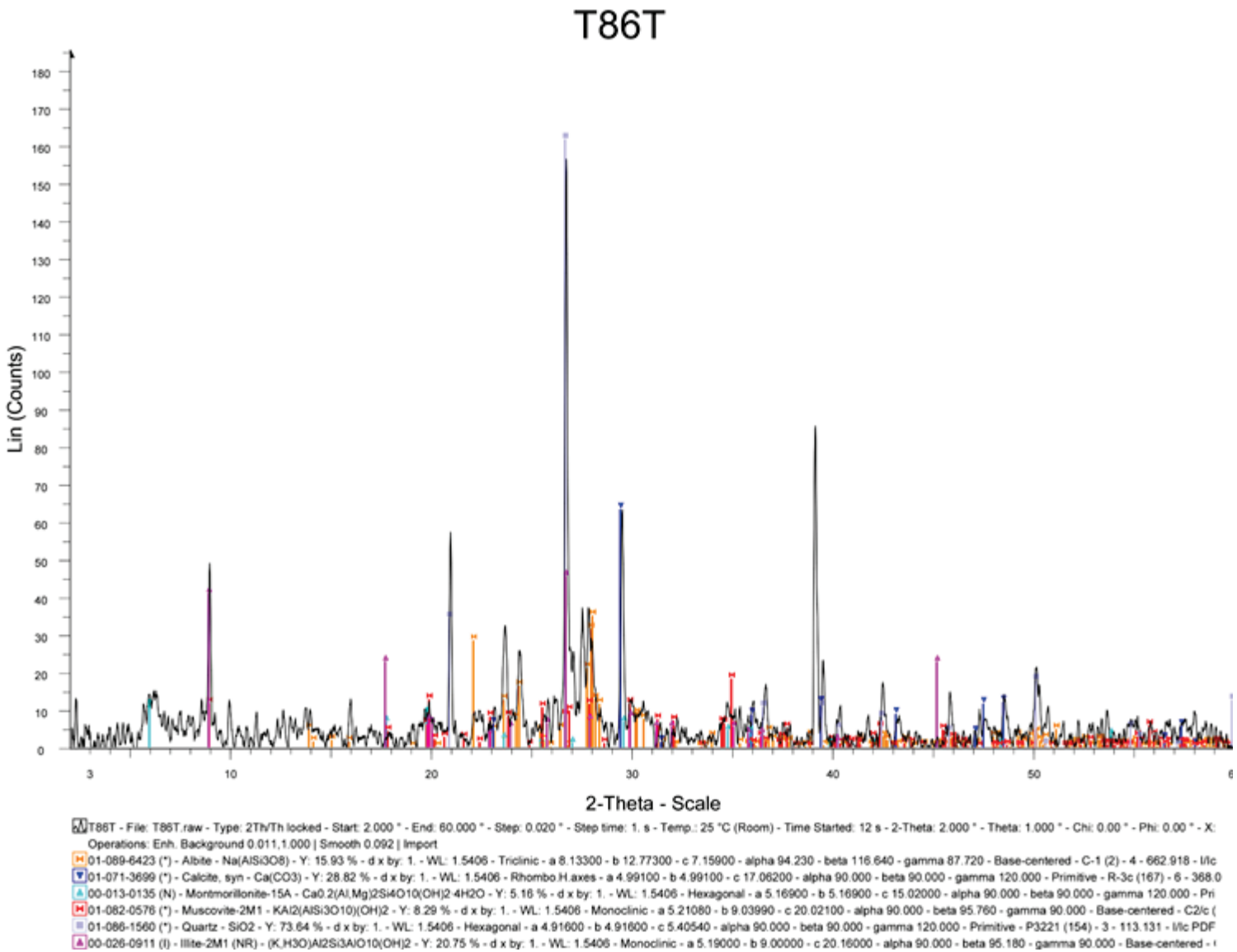

Figure 82: XRD pattern of T86T generated using the Bruker EVA software, showing albite (orange), calcite (blue), illite (pink), smectite (light blue), and quartz (lilac).

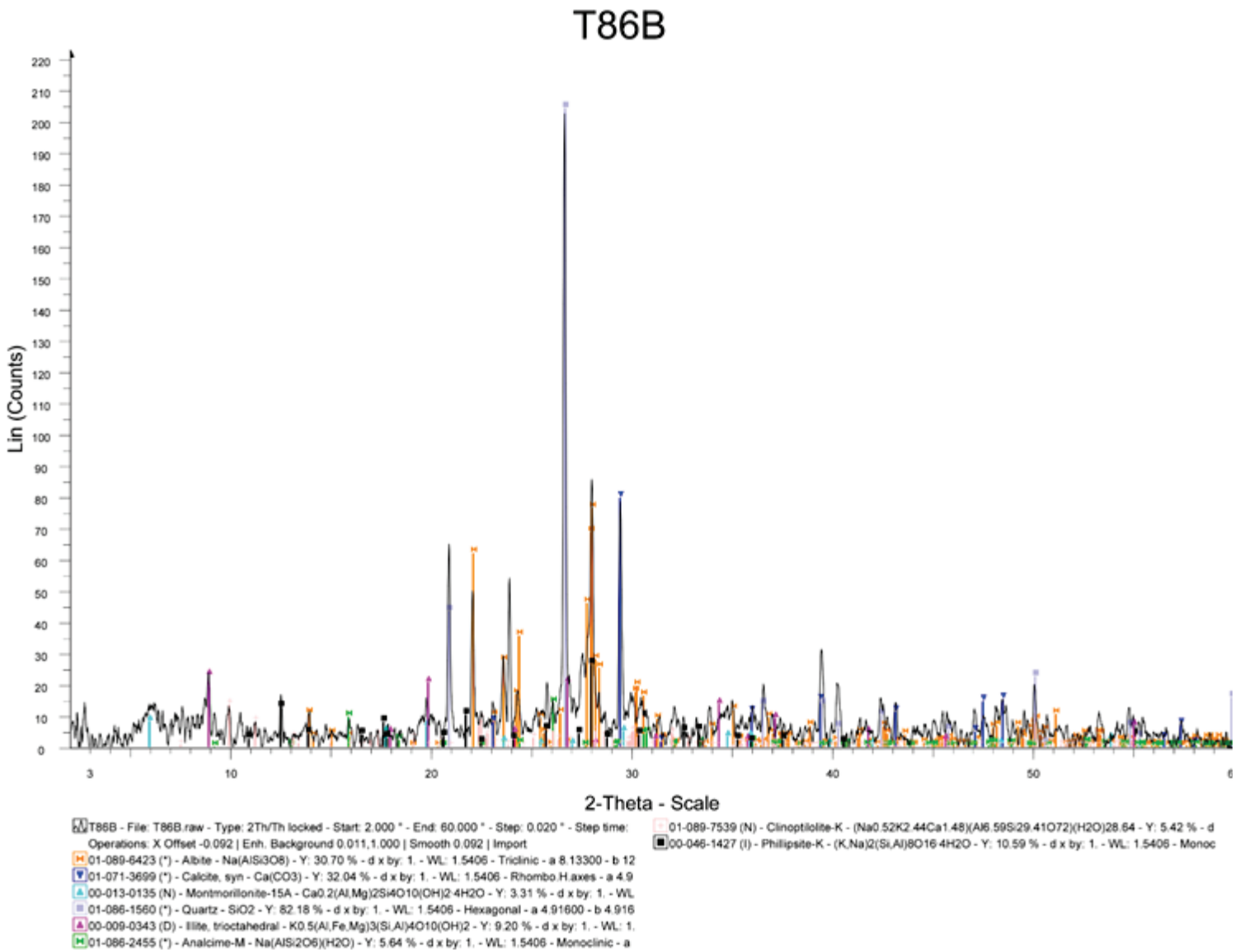

Figure 83: XRD pattern of T86B generated using the Bruker EVA software, showing albite (orange), analcime (green), calcite (blue), illite (pink), smectite (light blue), and quartz (lilac).

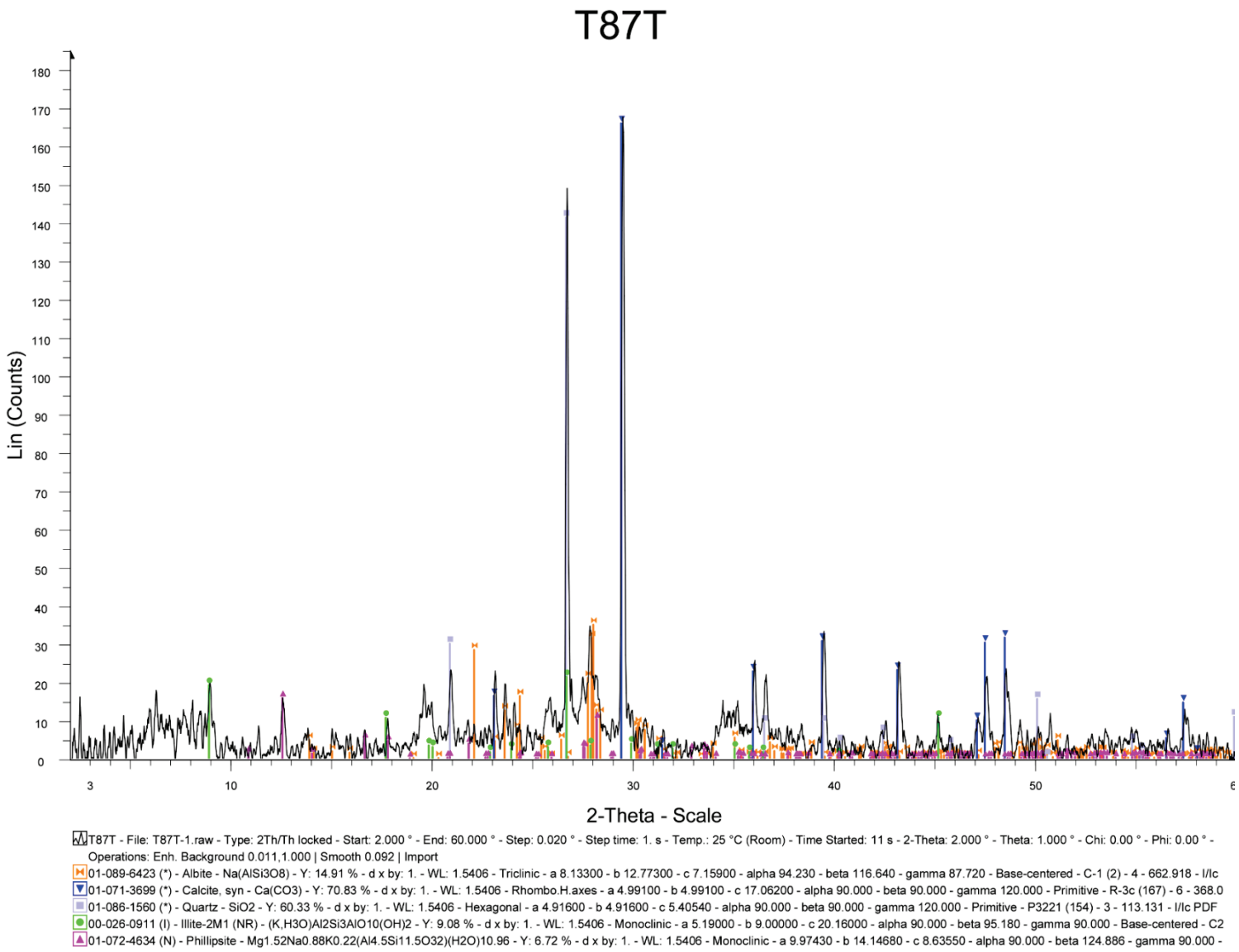

Figure 84: XRD pattern of T87T generated using the Bruker EVA software, showing albite (orange), calcite (blue), illite (green), smectite (light blue), phillipsite (pink), and quartz (lilac).

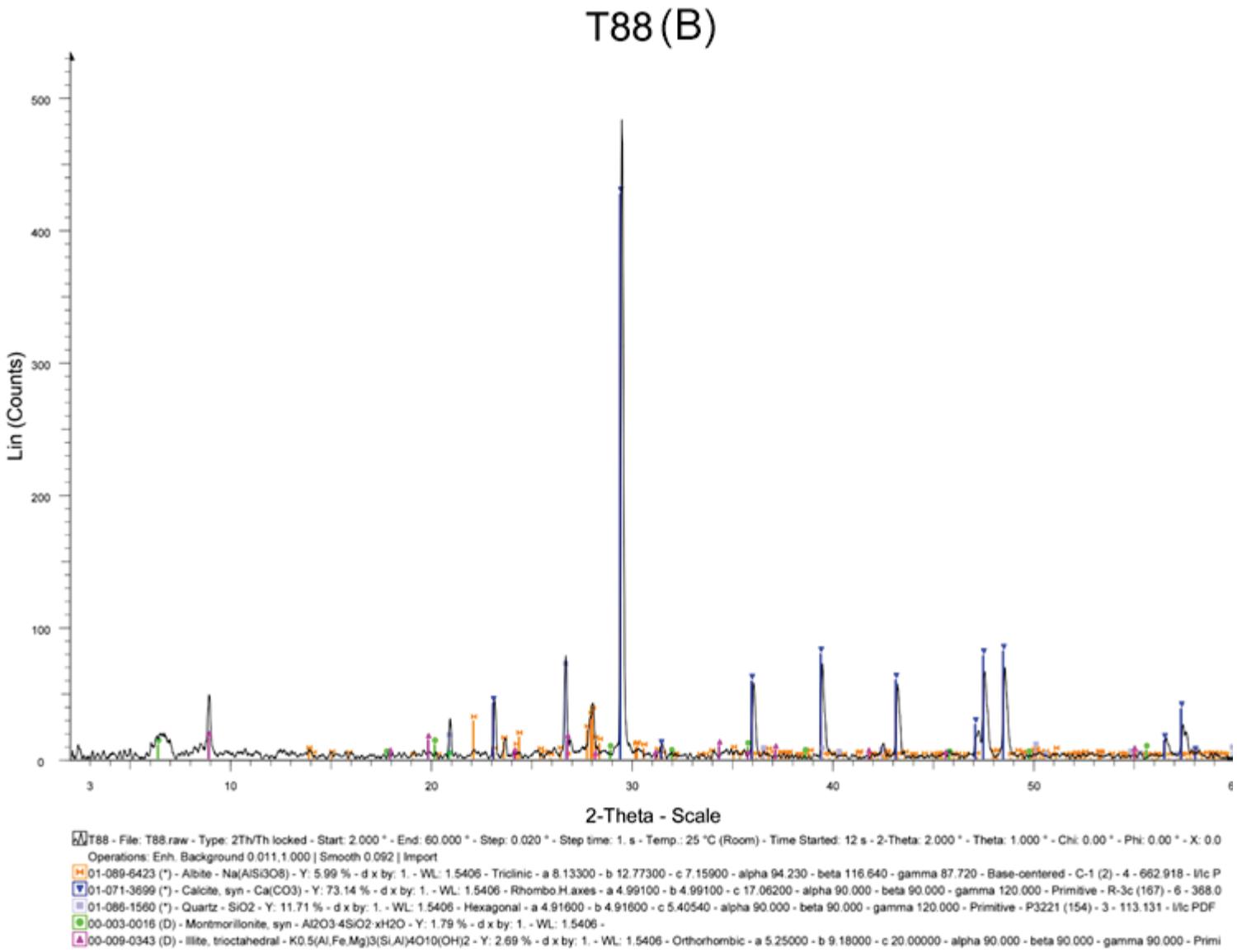

Figure 85: XRD pattern of T88(B) generated using the Bruker EVA software, showing albite (orange), calcite (blue), illite (pink), smectite (green), and quartz (lilac).

Additional Samples

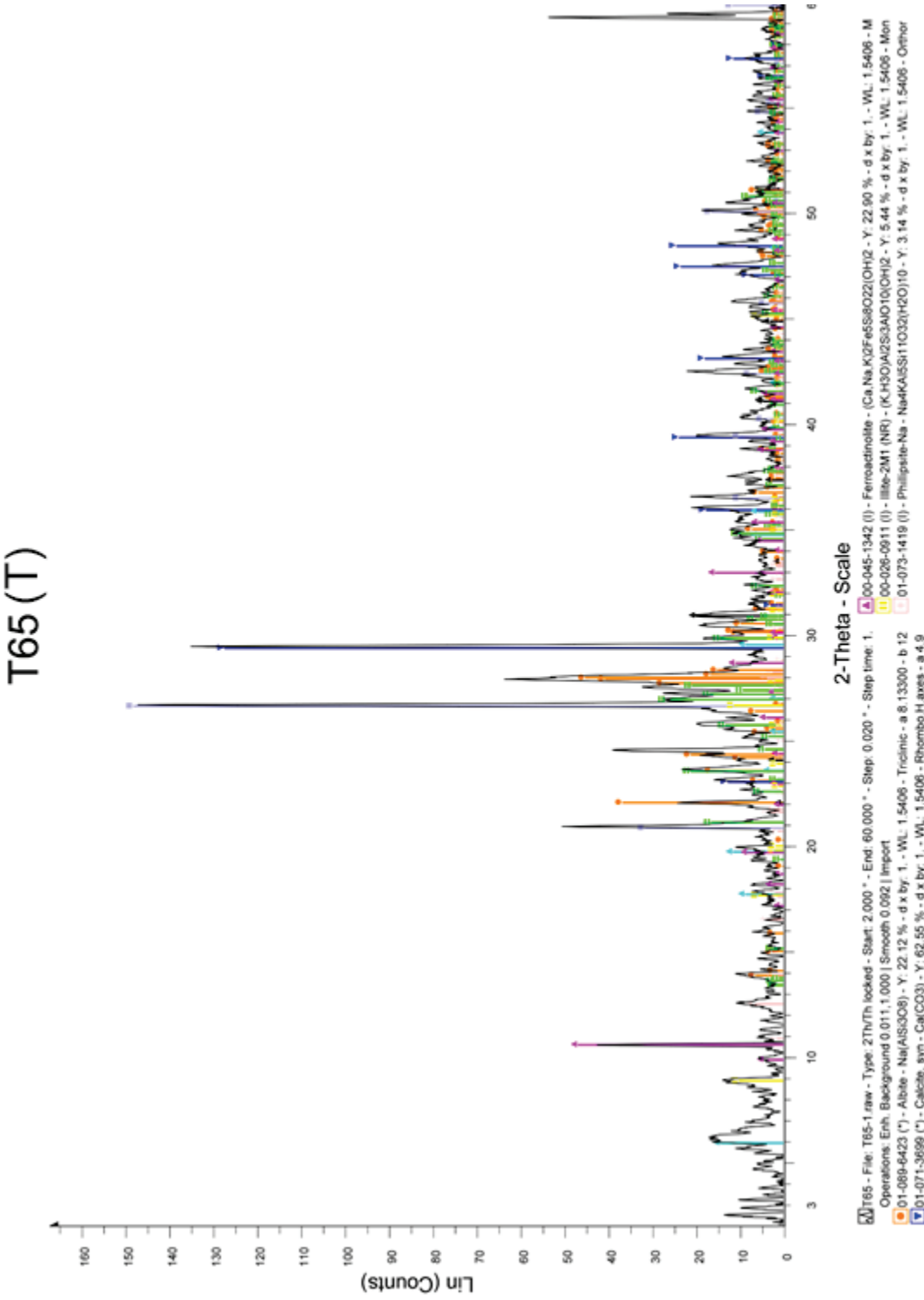

Figure 86: XRD pattern of T65(T) generated using the Bruker EVA software, showing albite (orange), amphibole (pink), calcite (blue), dolomite (black), k-feldspar (green), illite (yellow), smectite (light blue), phillipsite (light pink), and quartz (lilac).

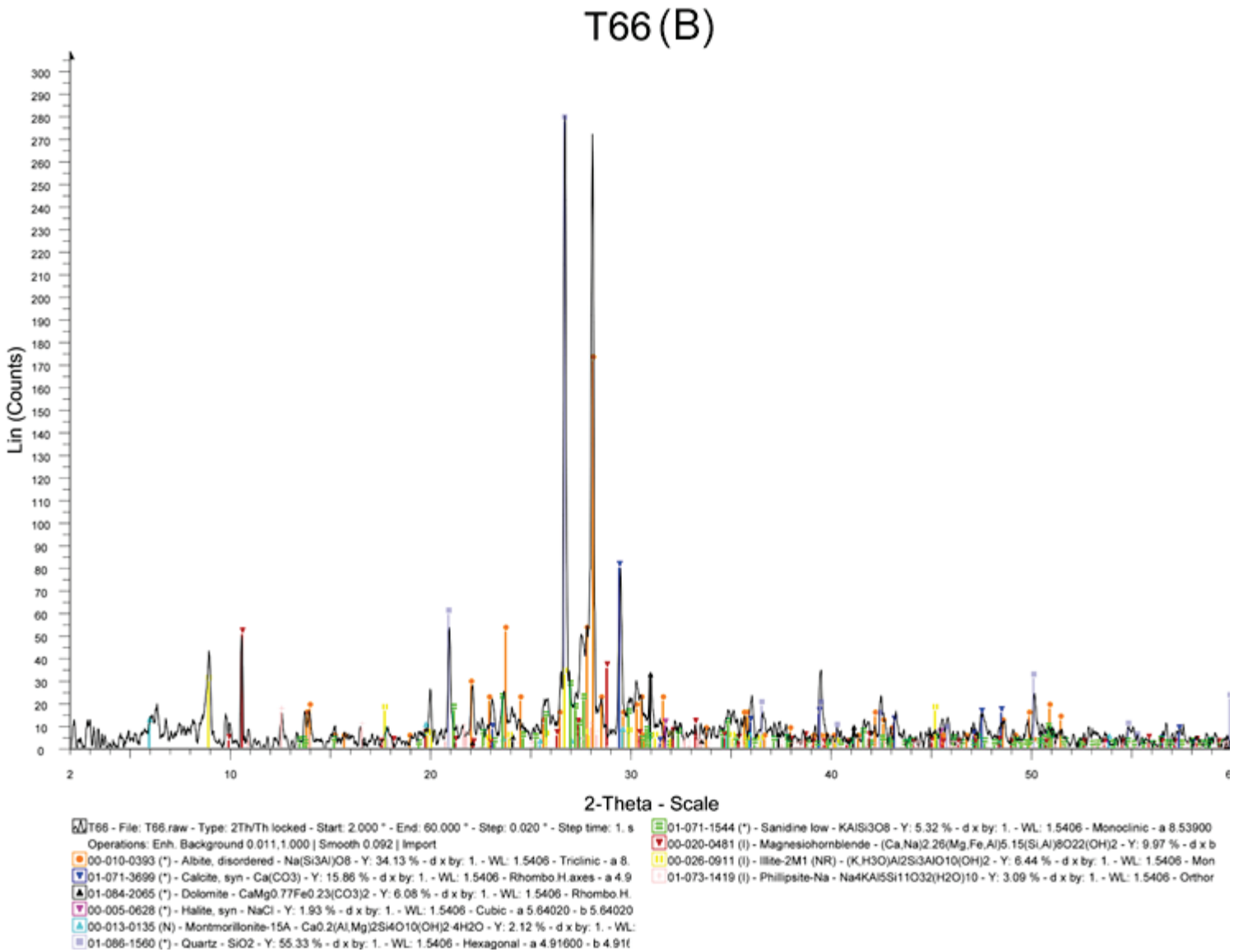

Figure 87: XRD pattern of T66(B) generated using the Bruker EVA software, showing albite (orange), amphibole (red), calcite (blue), dolomite (black), k-feldspar (green), halite (pink), illite (yellow), smectite (light blue), phillipsite (light pink), and quartz (lilac).

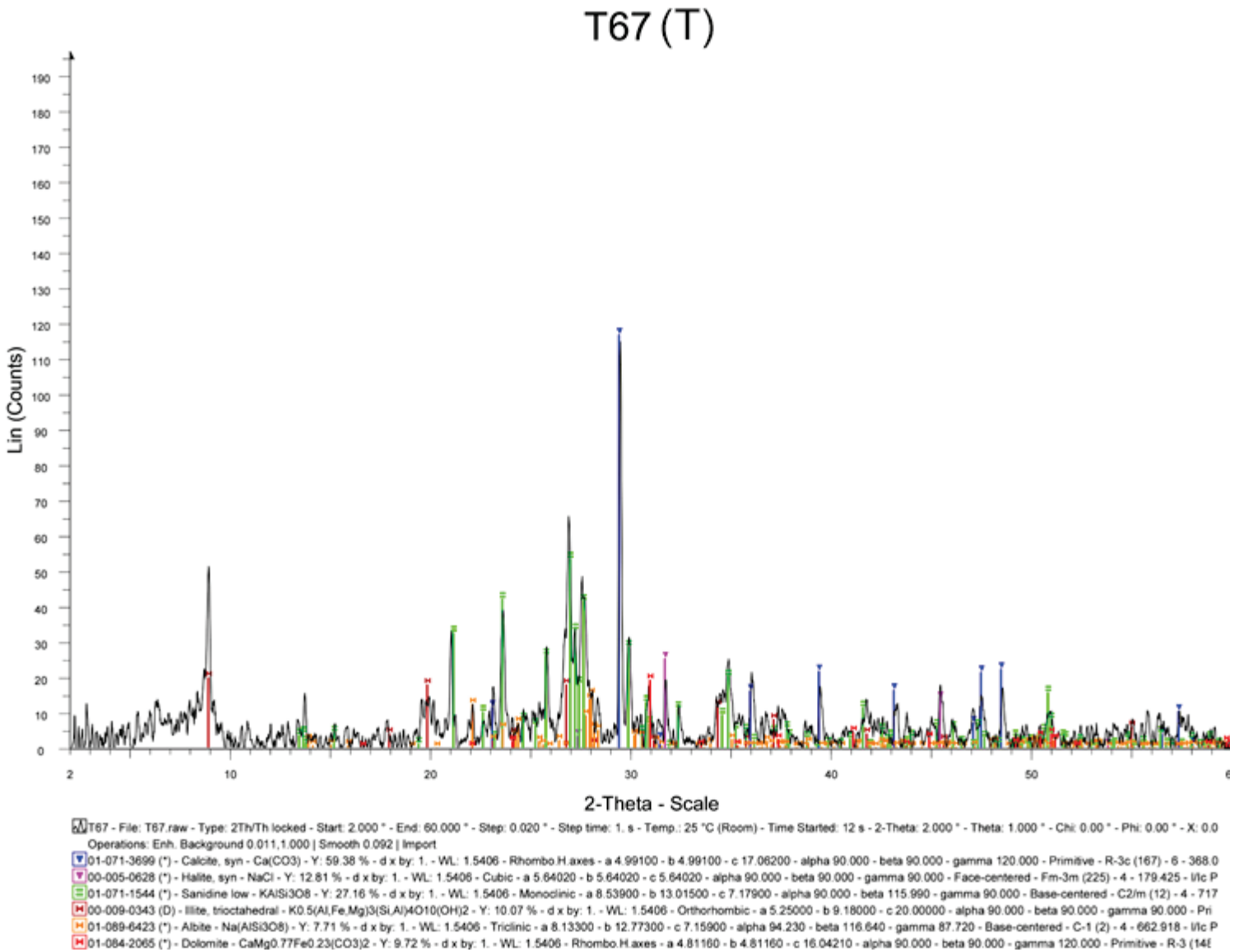

Figure 88: XRD pattern of T67(T) generated using the Bruker EVA software, showing albite (orange), calcite (blue), dolomite (red), k-feldspar (green), halite (pink), and illite (dark red).

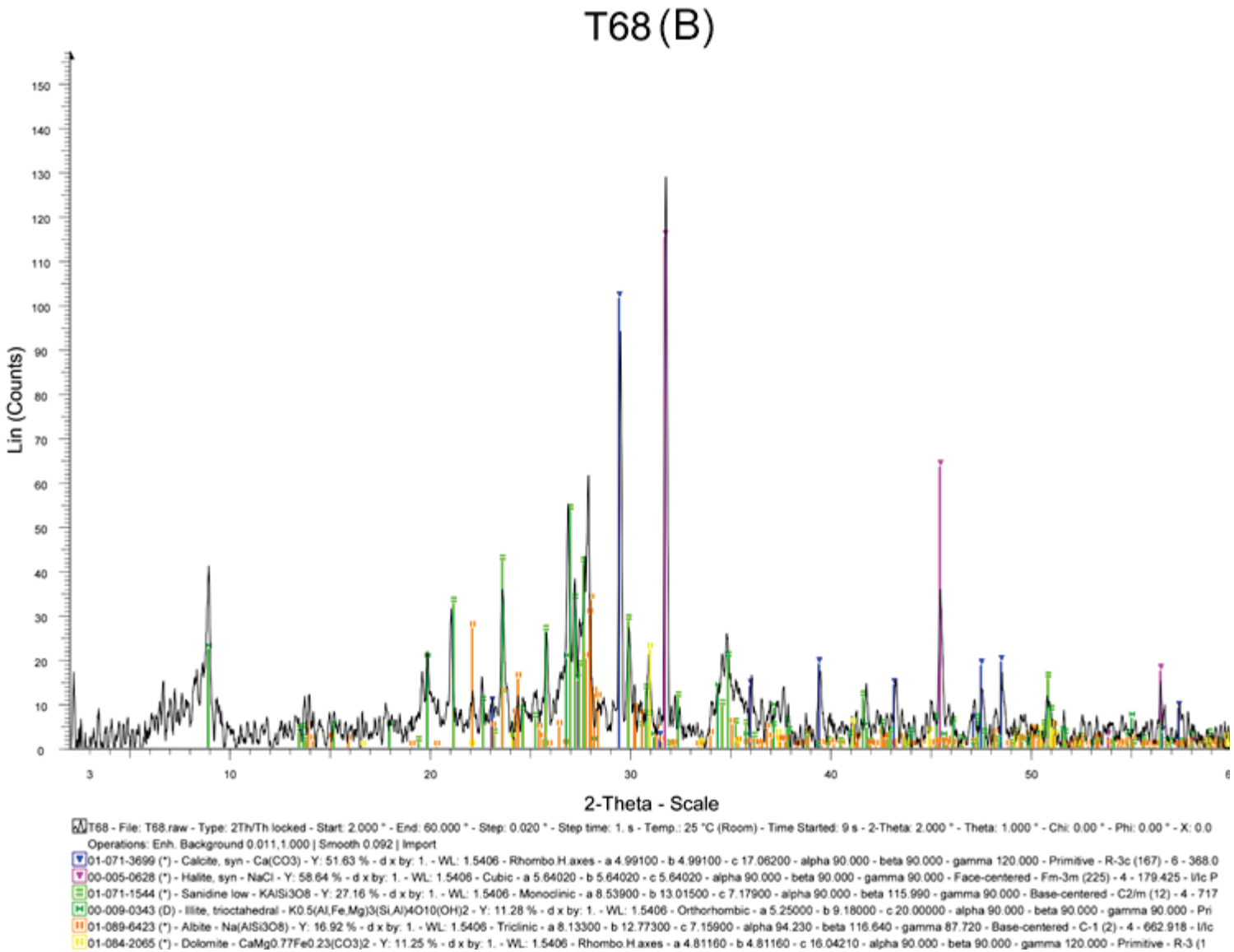

Figure 89: XRD pattern of T68(B) generated using the Bruker EVA software, showing albite (orange), calcite (blue), dolomite (yellow), k-feldspar (green), halite (pink), and illite (dark green).

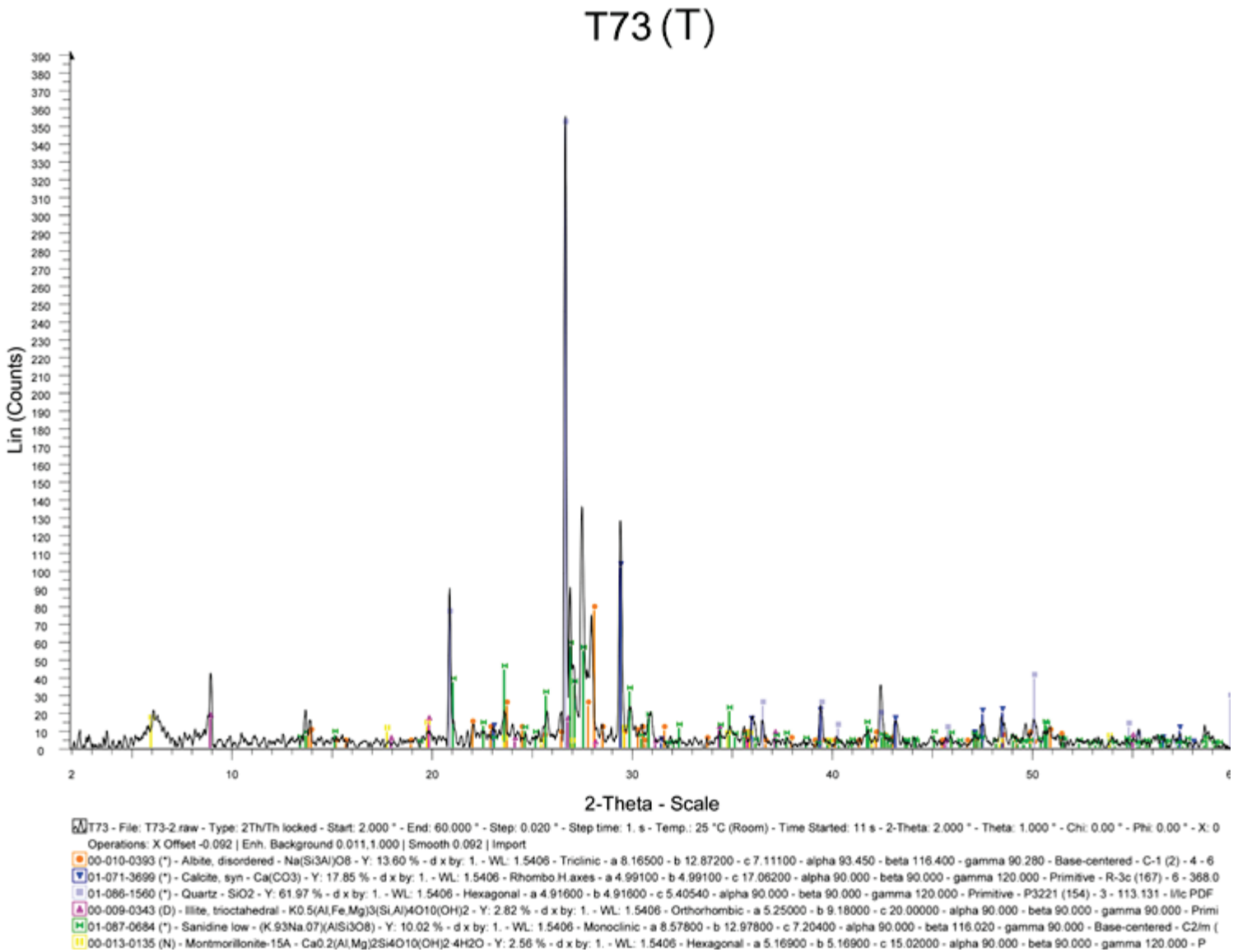

Figure 90: XRD pattern of T73(T) generated using the Bruker EVA software, showing albite (orange), calcite (blue), k-feldspar (green), illite (pink), smectite (yellow), and quartz (lilac).

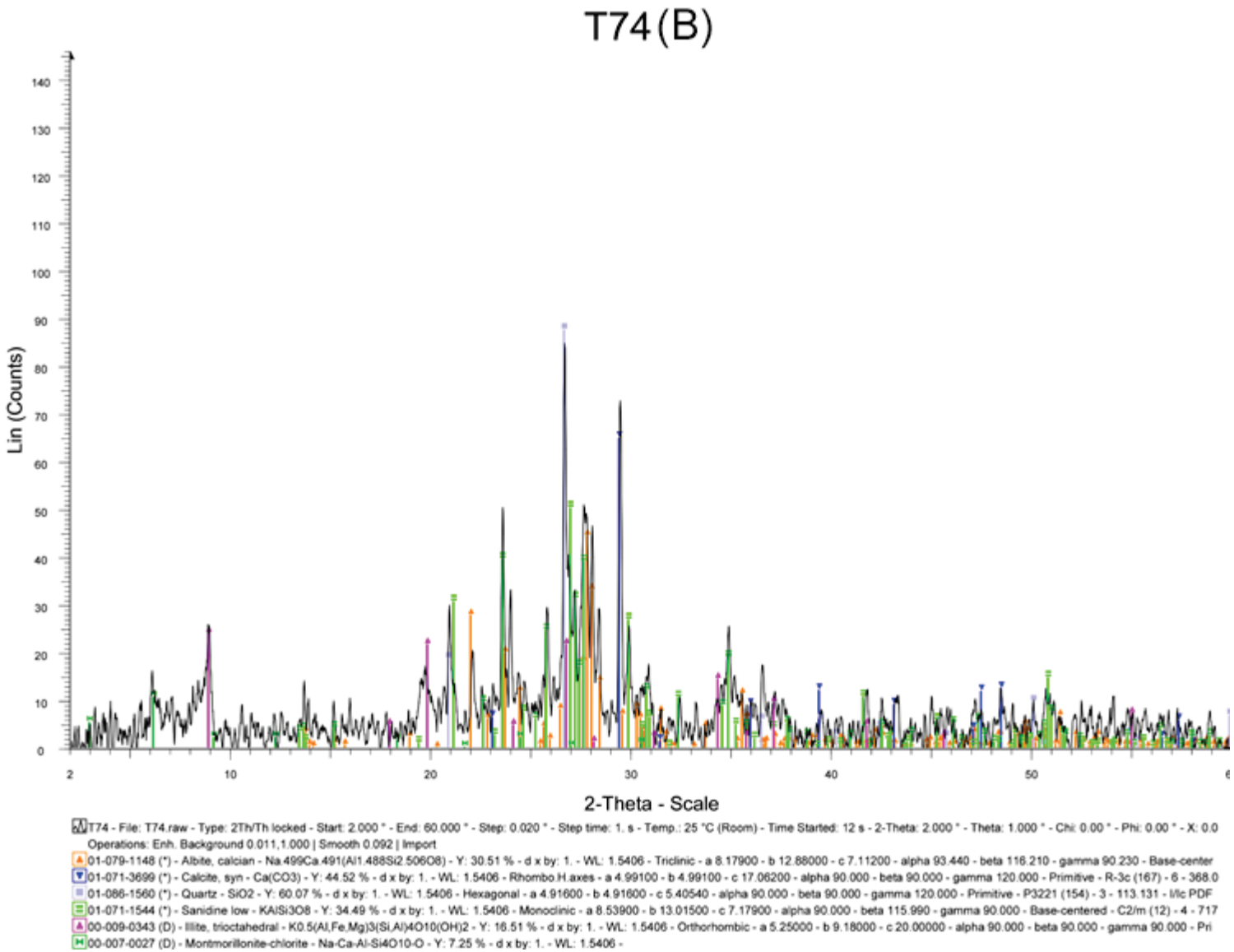

Figure 91: XRD pattern of T74(B) generated using the Bruker EVA software, showing albite (orange), calcite (blue), k-feldspar (green), illite (pink), smectite (dark green), and quartz (lilac).

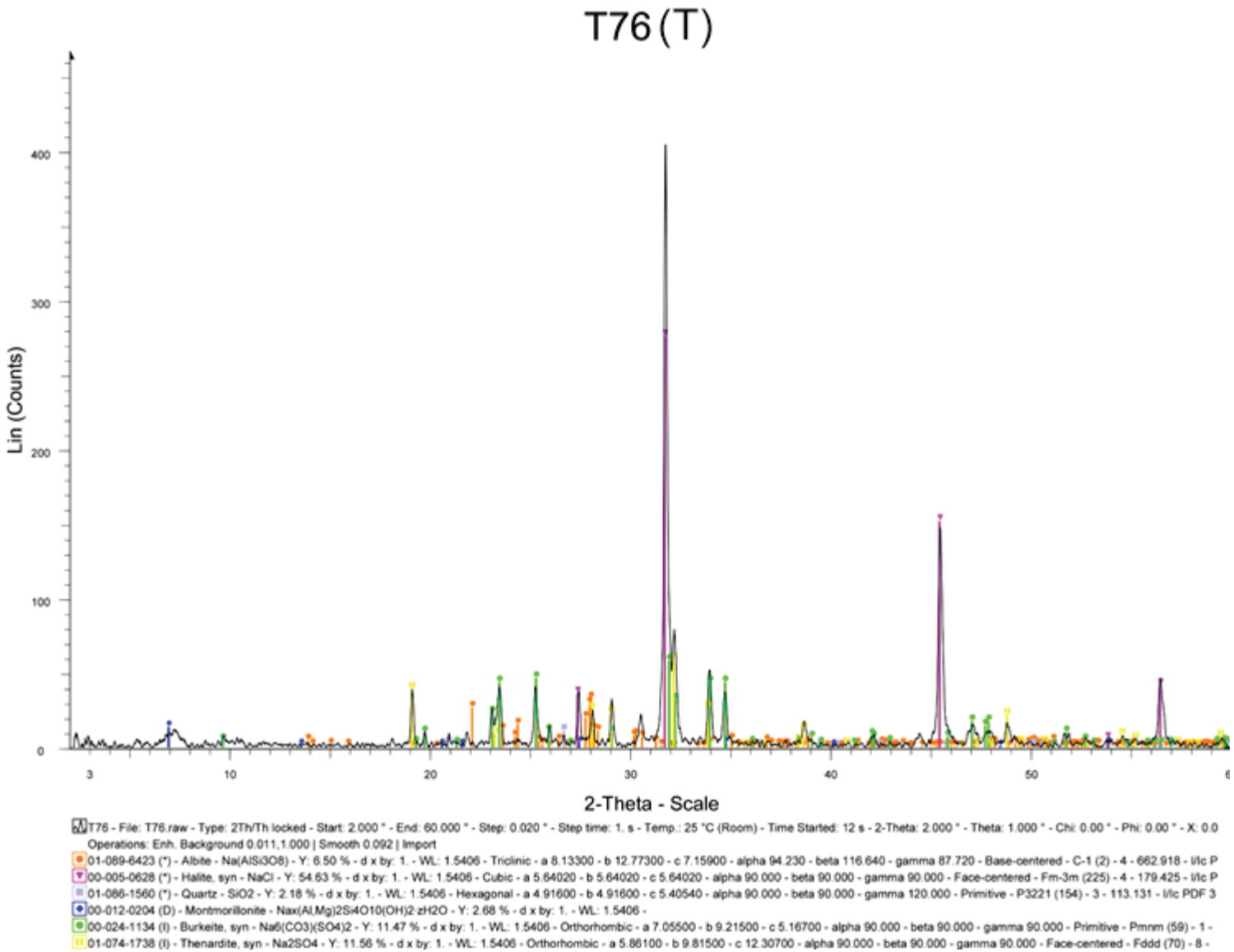

Figure 92: XRD pattern of T76(T) generated using the Bruker EVA software, showing albite (orange), burkeite (green), halite (pink), smectite (blue), thenardite (yellow), and quartz (lilac).

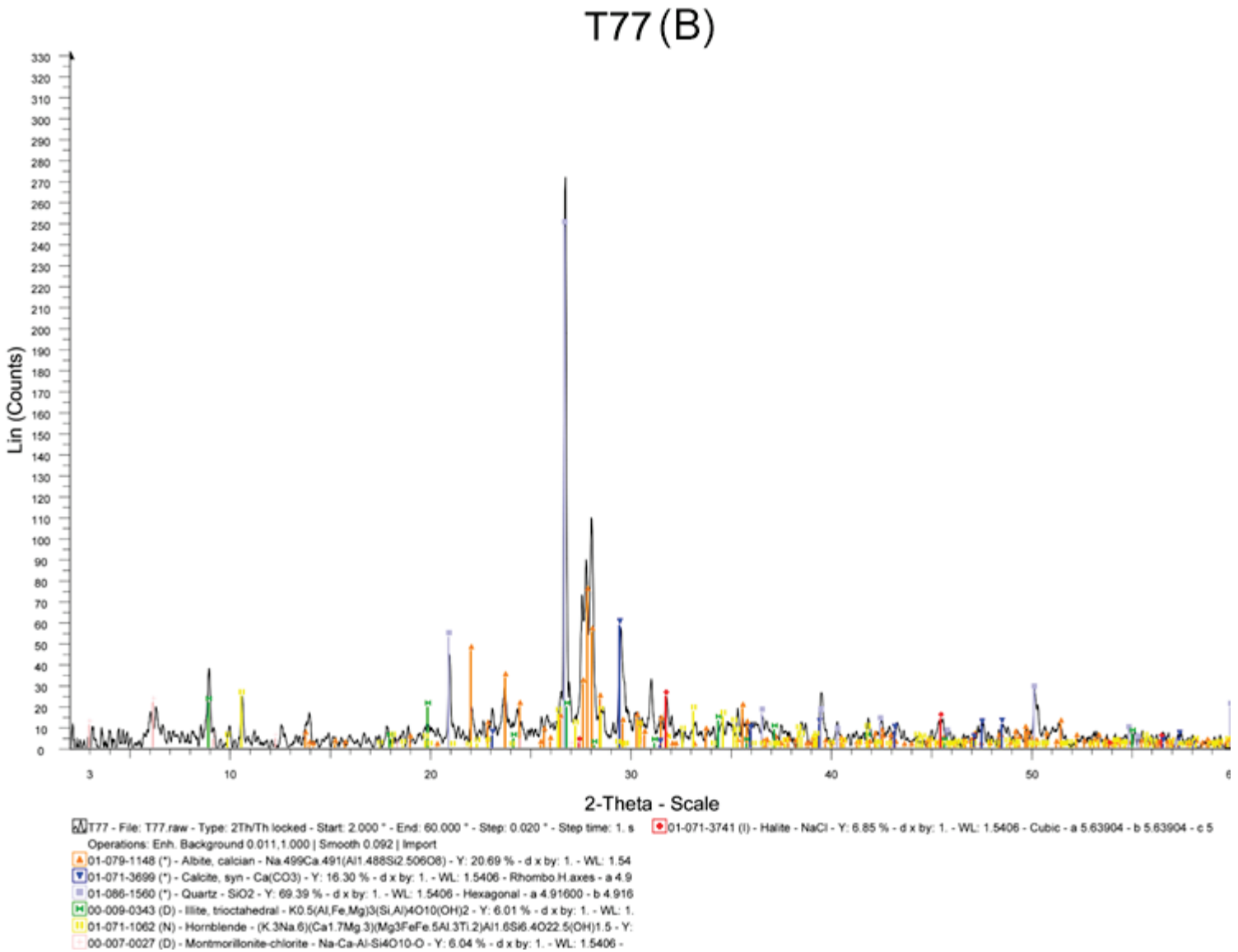

Figure 93: XRD pattern of T77(B) generated using the Bruker EVA software, showing albite (orange), amphibole (yellow), calcite (blue), halite (red), illite (green), smectite (light pink), and quartz (lilac).

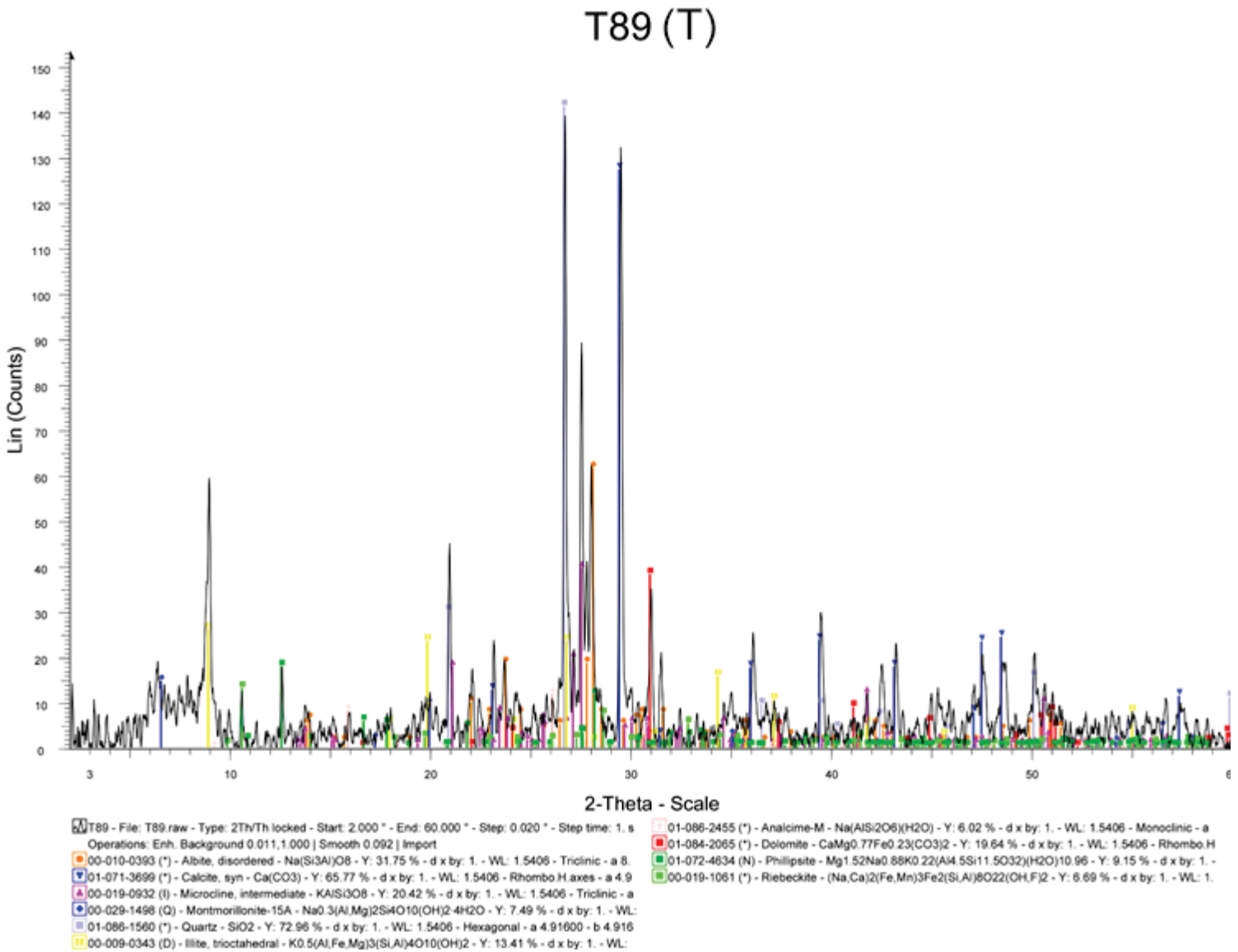

Figure 94: XRD pattern of T89(T) generated using the Bruker EVA software, showing albite (orange), amphibole (light green), analcime (light pink), calcite (blue), dolomite (red), k-feldspar (pink), illite (yellow), smectite (blue), phillipsite (green), and quartz (lilac).

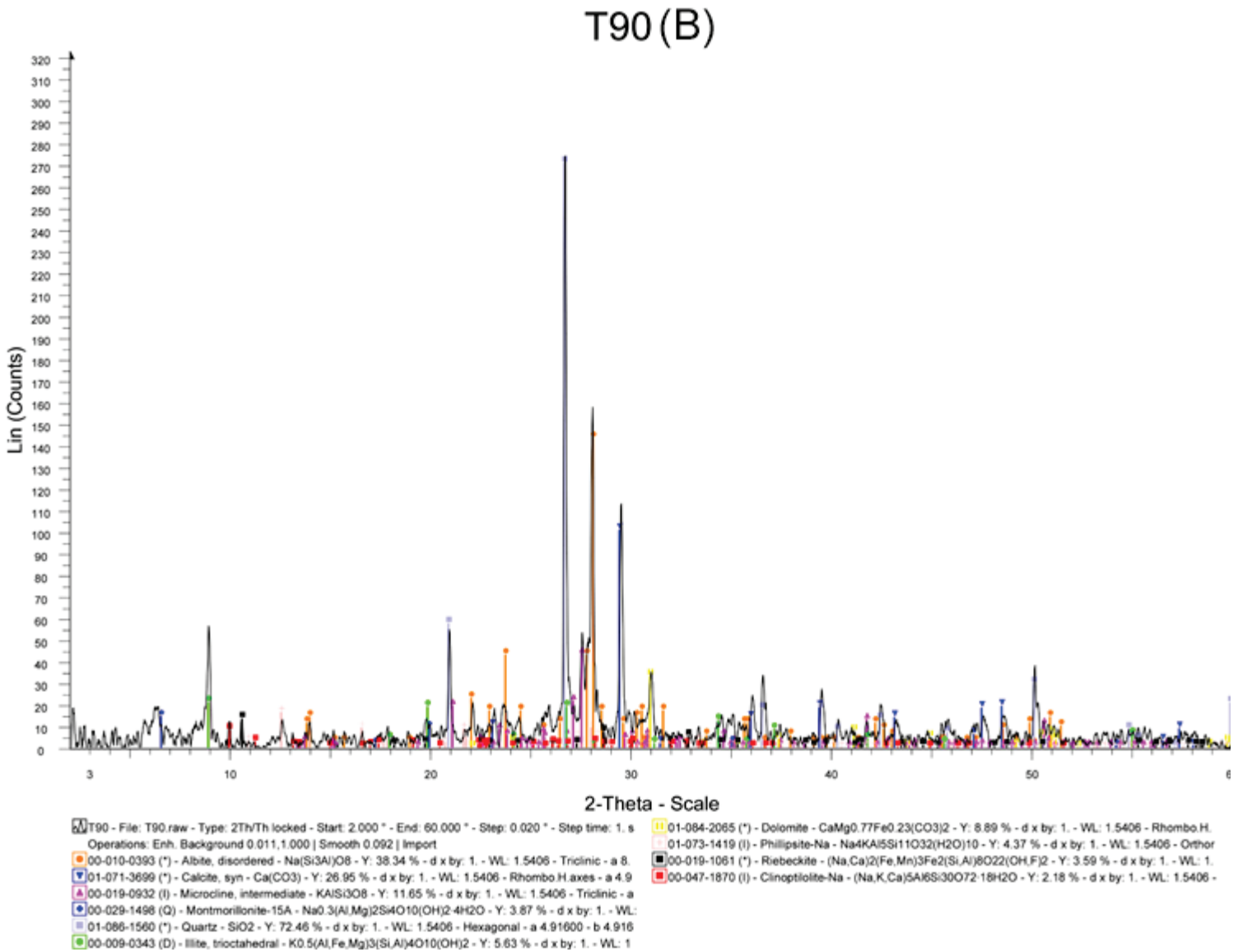

Figure 95: XRD pattern of T90(B) generated using the Bruker EVA software, showing albite (orange), amphibole (black), calcite (blue), clinoptilolite (red), dolomite (yellow), k-feldspar (pink), illite (green), smectite (blue), phillipsite (light pink), and quartz (lilac).

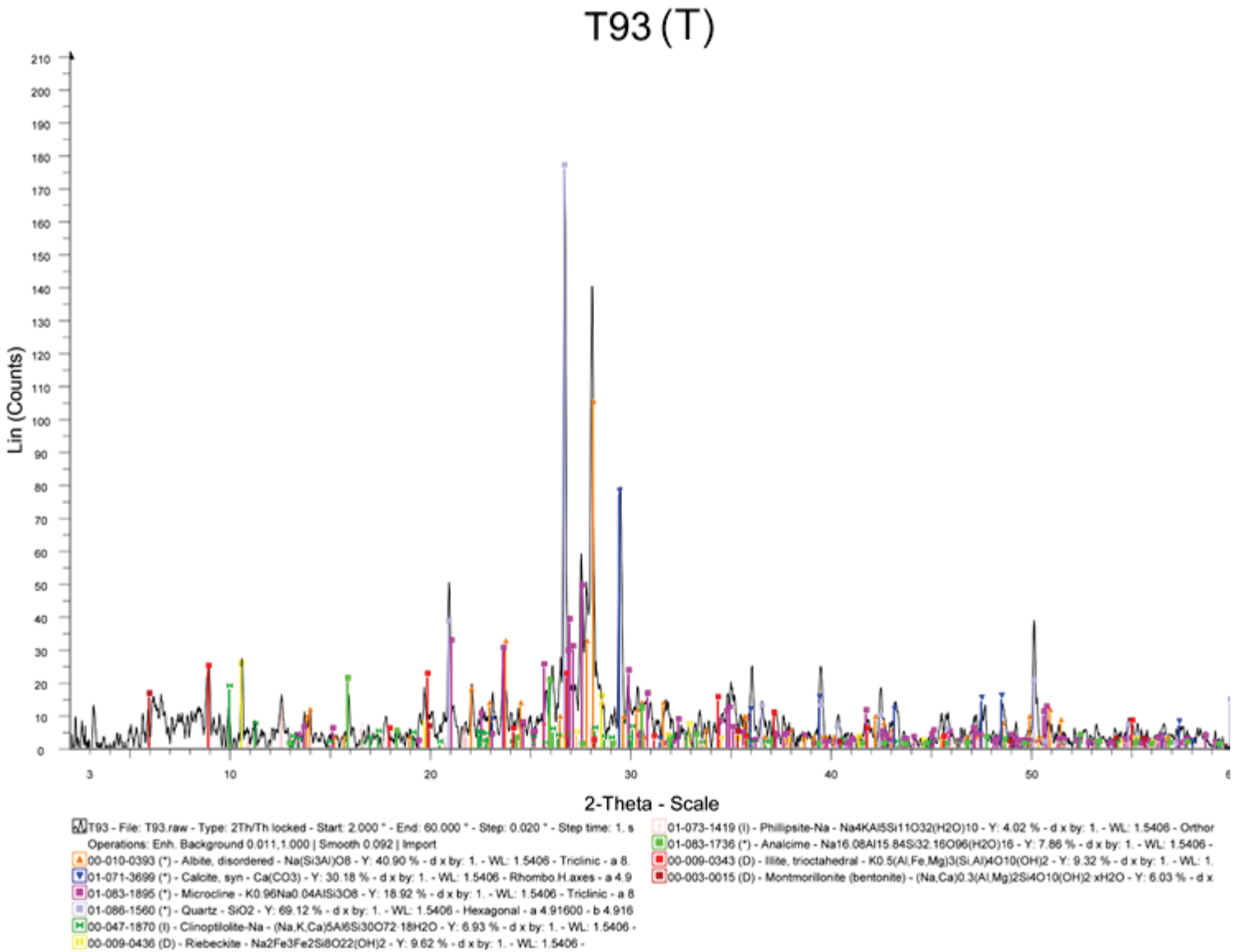

Figure 96: XRD pattern of T93(T) generated using the Bruker EVA software, showing albite (orange), amphibole (yellow), analcime (light green), calcite (blue), clinoptilolite (green), k-feldspar (pink), illite (red), smectite (dark red), phillipsite (light pink), and quartz (lilac).

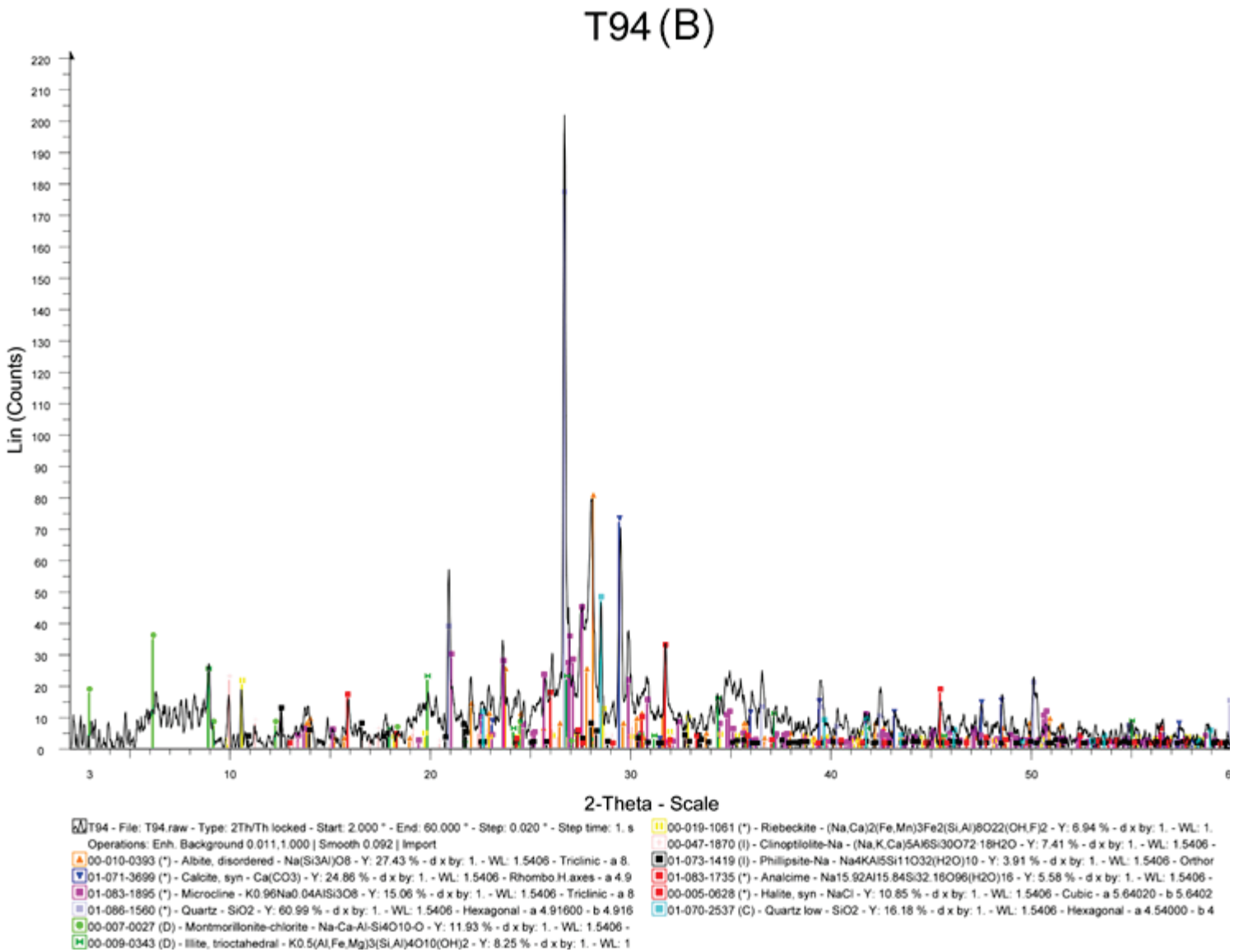

Figure 97: XRD pattern of T94(B) generated using the Bruker EVA software, showing albite (orange), amphibole (yellow), analcime (red 1), calcite (blue), clinoptilolite (light pink), k-feldspar (pink), illite (green), smectite (light green), phillipsite (black), halite (red 2), and quartz (lilac and light blue).

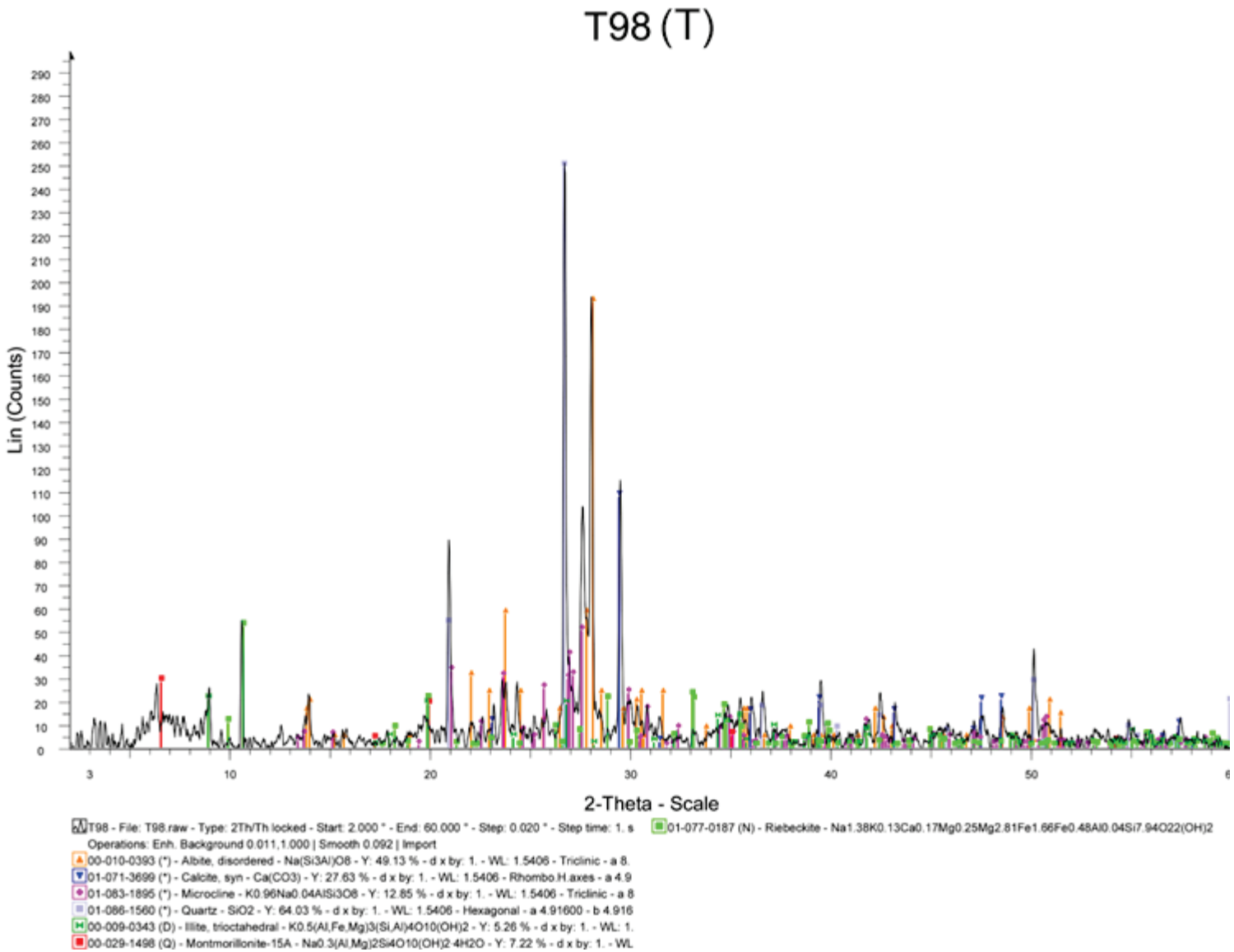

Figure 98: XRD pattern of T98(T) generated using the Bruker EVA software, showing albite (orange), amphibole (light green), calcite (blue), k-feldspar (pink), illite (green), smectite (red), and quartz (lilac).

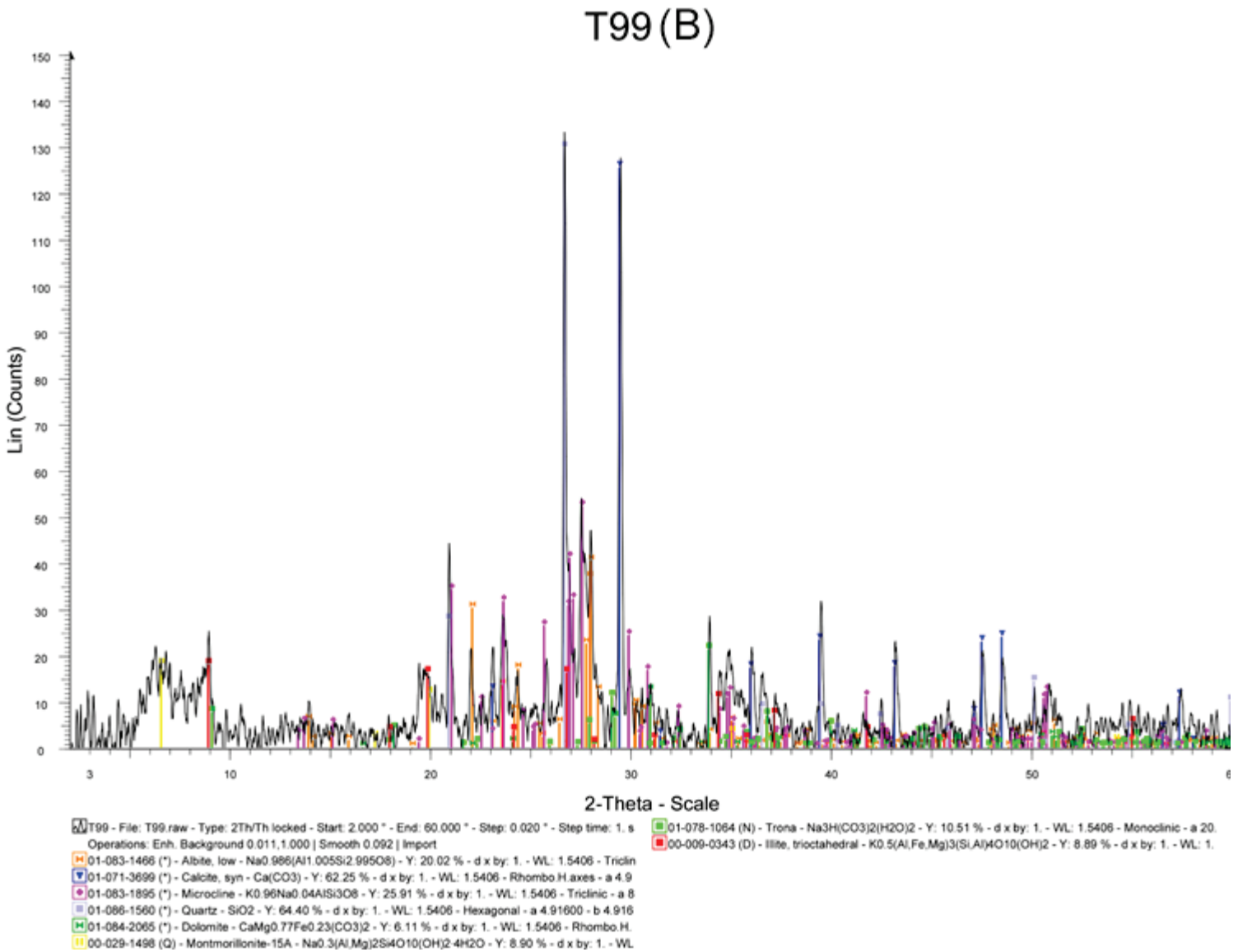

Figure 99: XRD pattern of T99(B) generated using the Bruker EVA software, showing albite (orange), calcite (blue), dolomite (green), k-feldspar (pink), illite (red), smectite (yellow), and quartz (lilac).

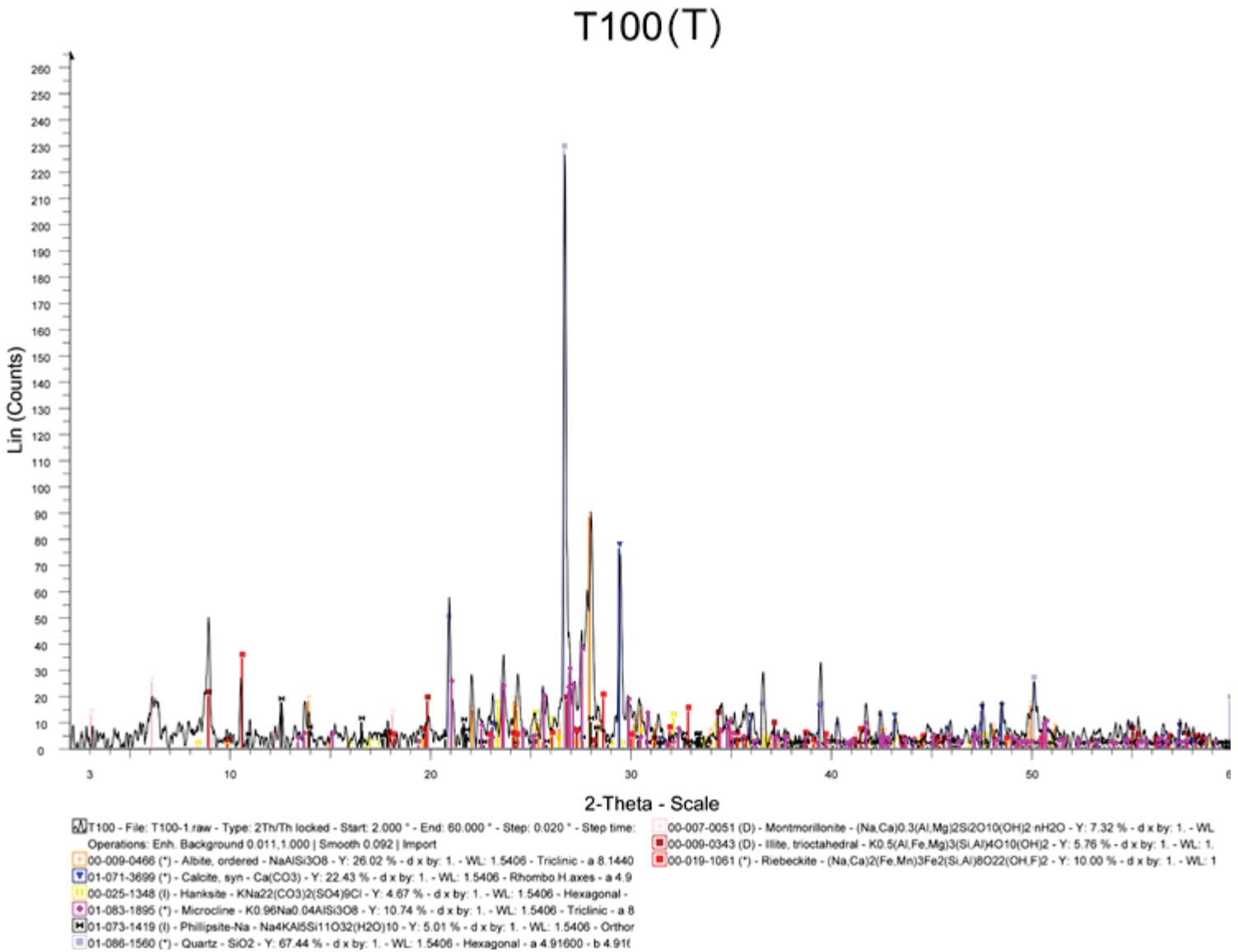

Figure 100: XRD pattern of T100(T) generated using the Bruker EVA software, showing albite (orange), amphibole (red), calcite (blue), k-feldspar (pink), illite (dark red), smectite (light pink), phillipsite (black), hanksite (yellow), and quartz (lilac).

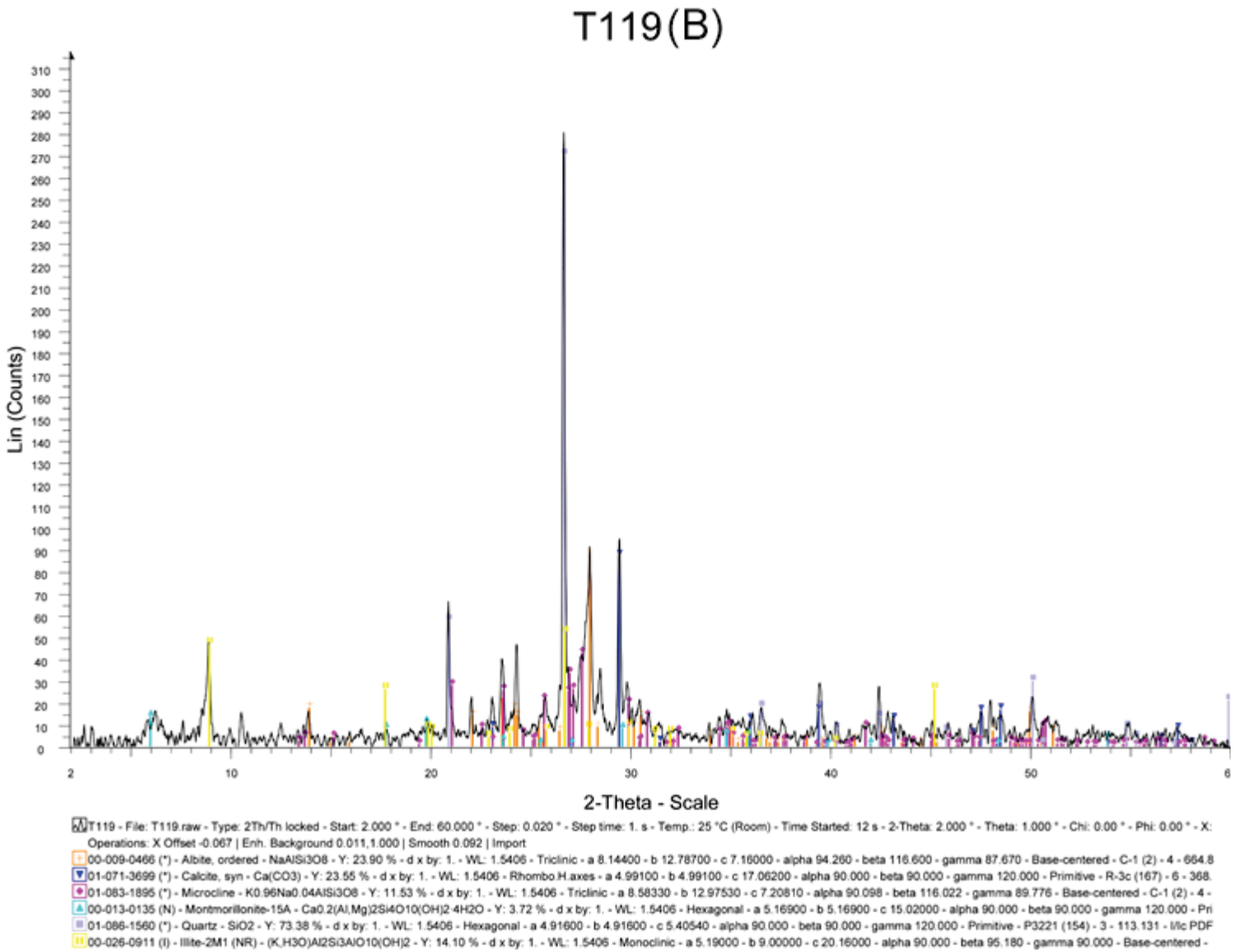

Figure 101: XRD pattern of T119(B) generated using the Bruker EVA software, showing albite (orange), calcite (blue), k-feldspar (pink), illite (yellow), smectite (light blue), and quartz (lilac).

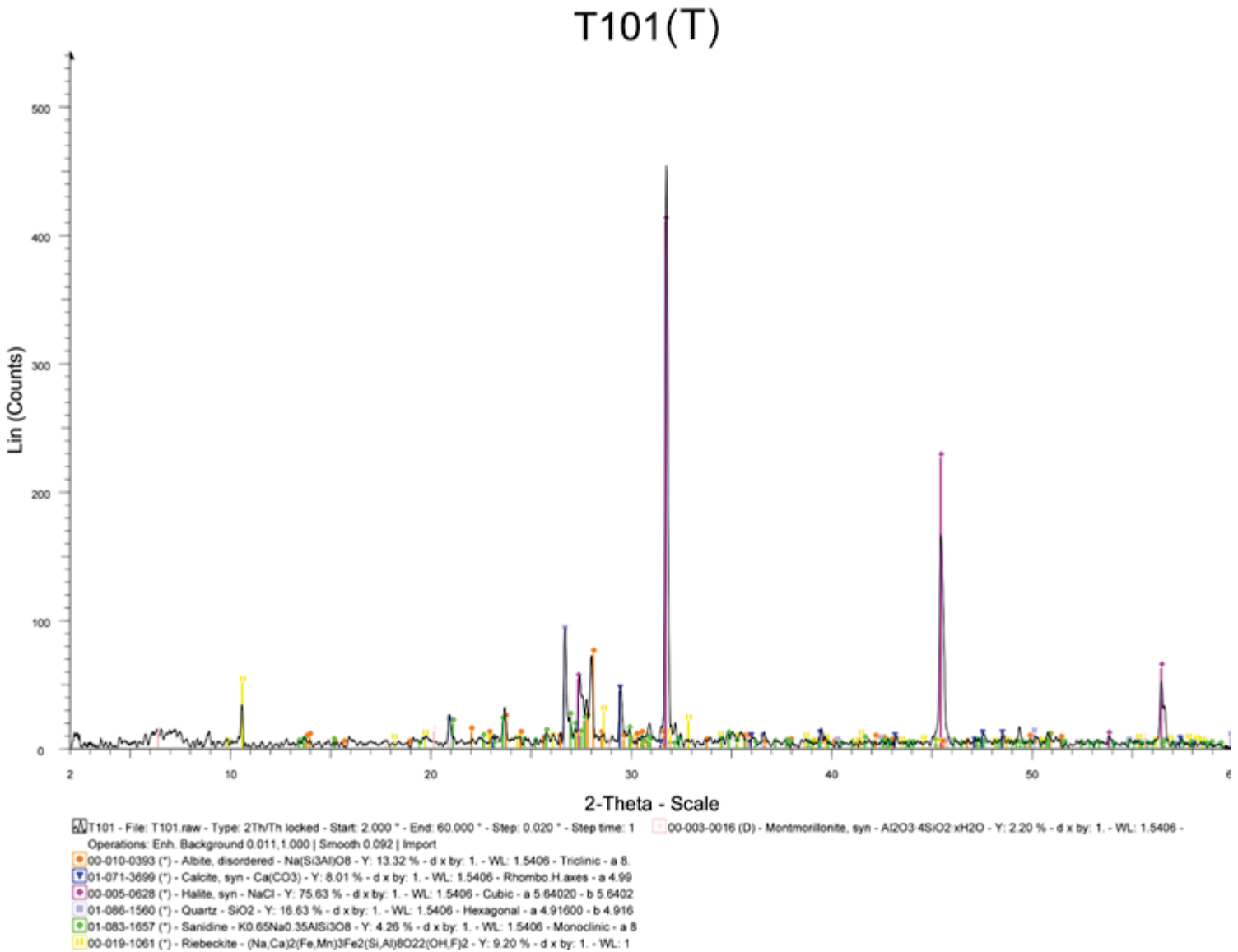

Figure 102: XRD pattern of T101(T) generated using the Bruker EVA software, showing albite (orange), amphibole (yellow), calcite (blue), k-feldspar (green), smectite (light pink), halite (pink), and quartz (lilac).

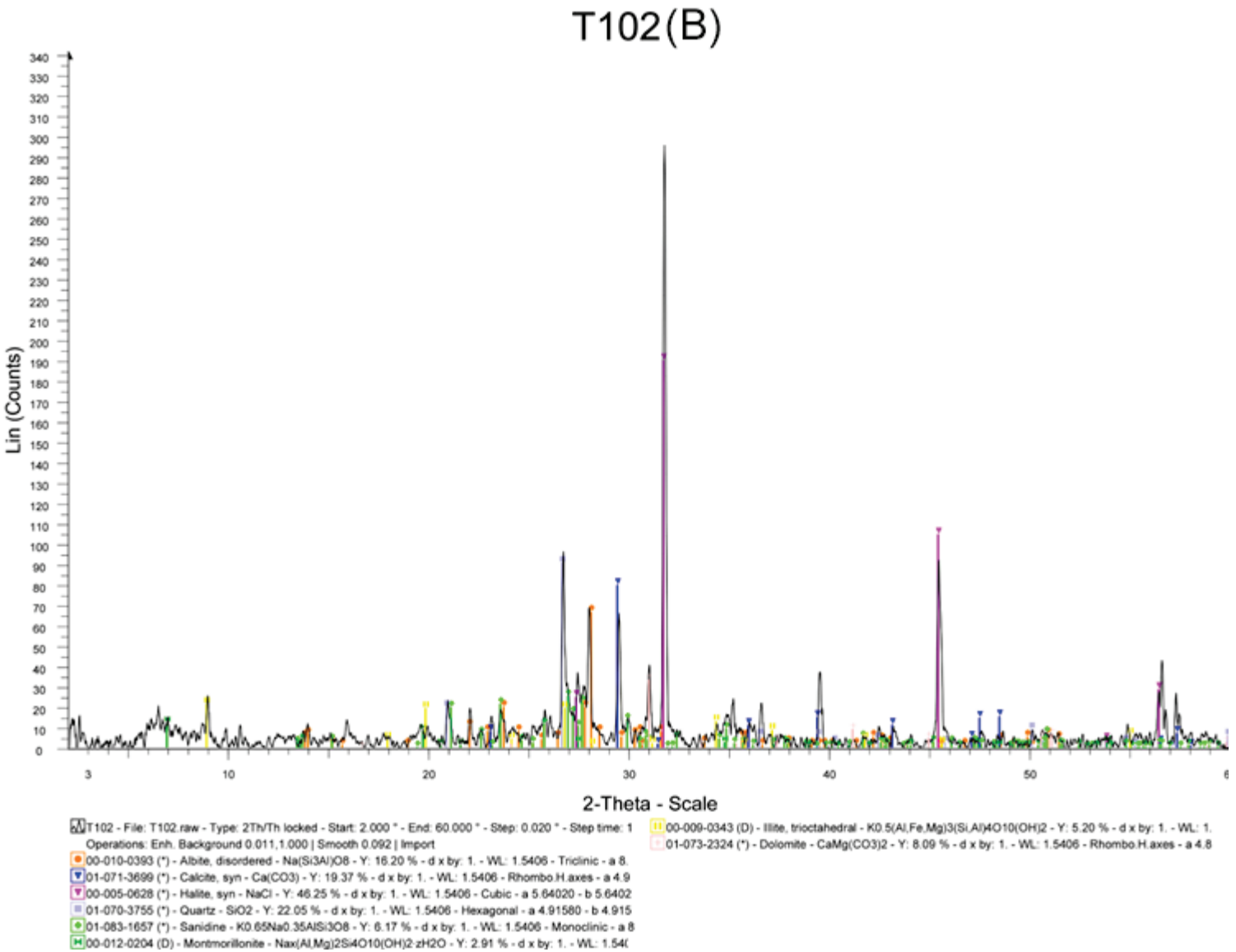

Figure 103: XRD pattern of T102(B) generated using the Bruker EVA software, showing albite (orange), calcite (blue), dolomite (light pink), k-feldspar (green), illite (yellow), smectite (dark green), halite (pink), and quartz (lilac).

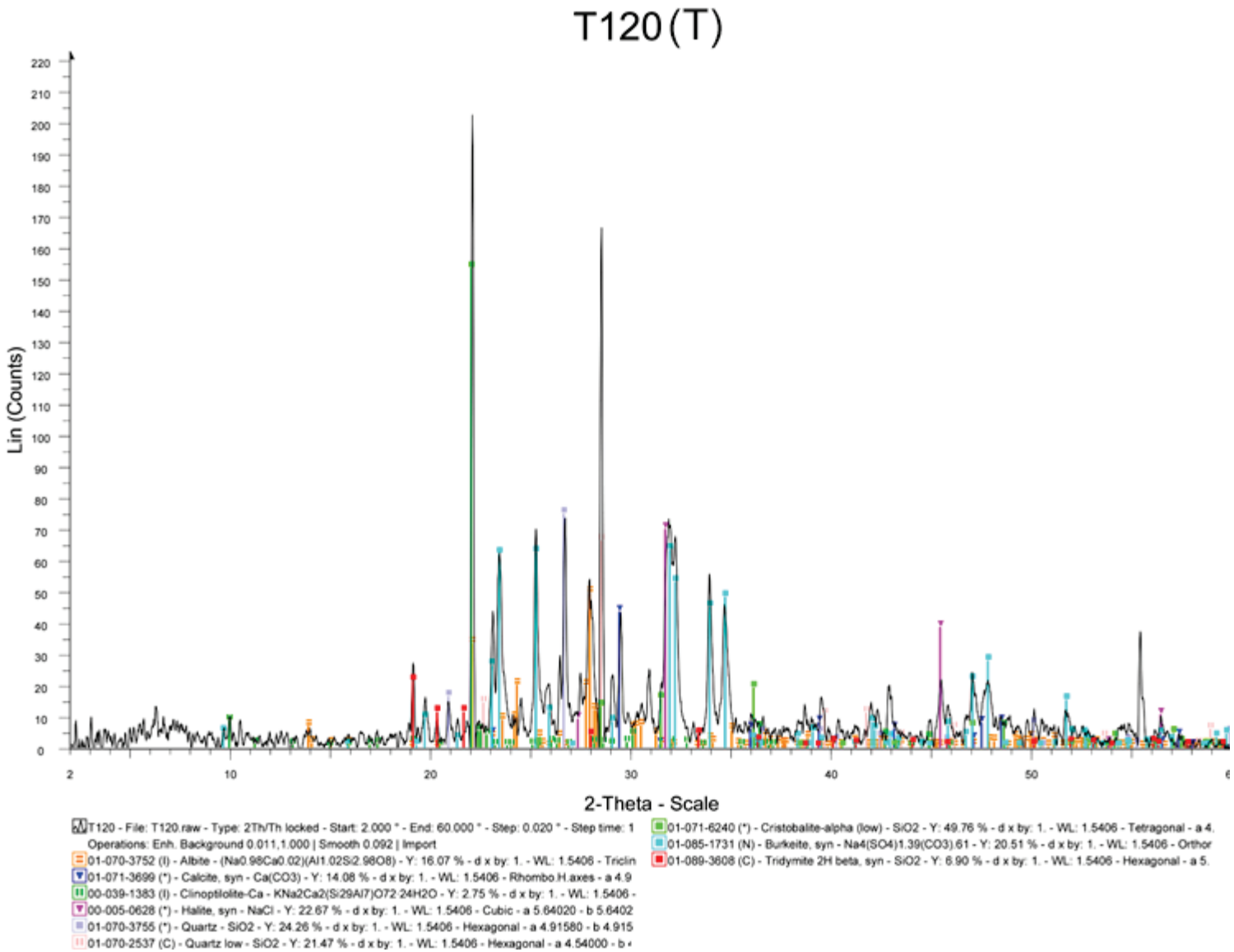

Figure 104: XRD pattern of T120(T) generated using the Bruker EVA software, showing albite (orange), burkeite (light blue), calcite (blue), clinoptilolite (green), low-cristobalite (light green), halite (pink), tridymite (red) and quartz (lilac and light pink).

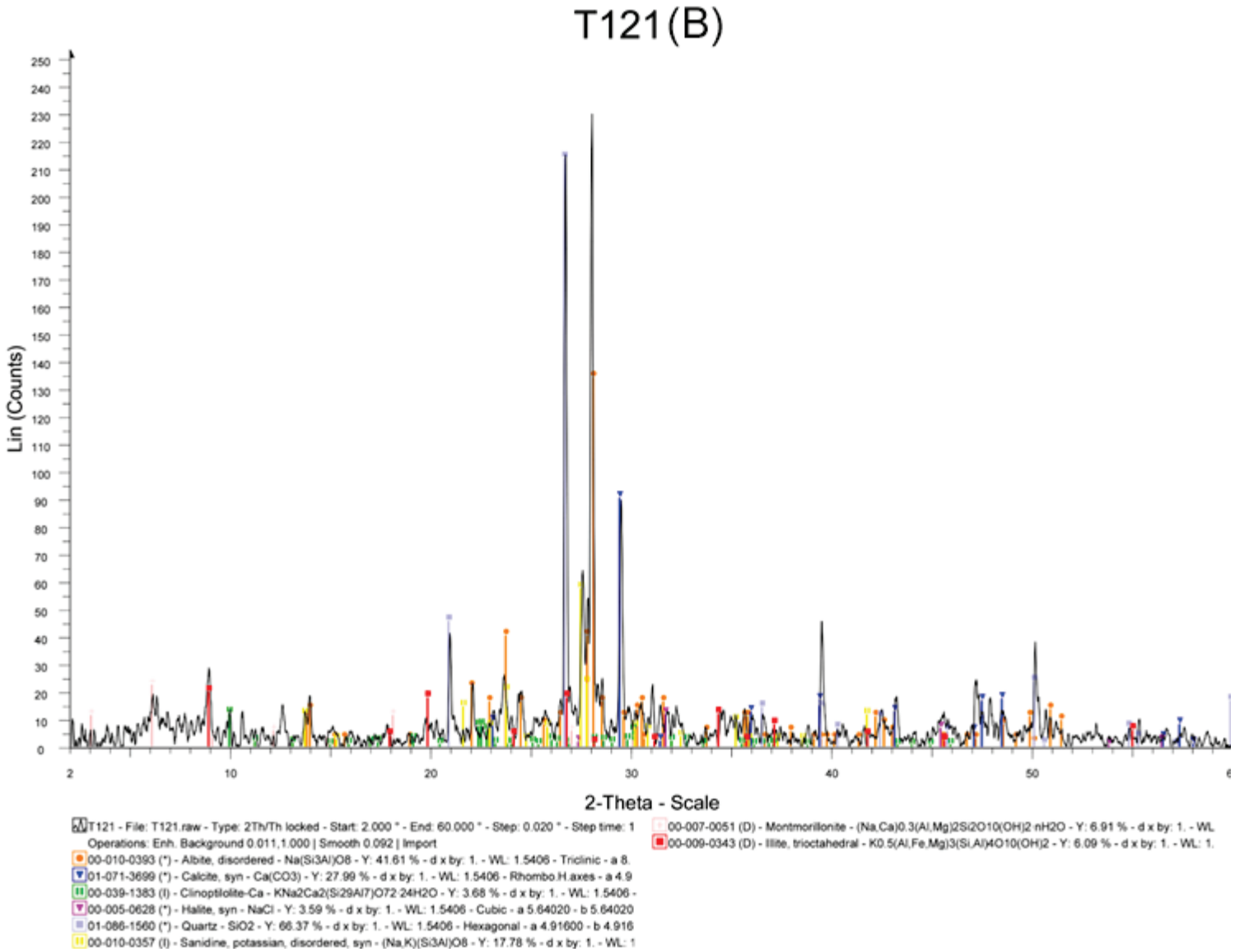

Figure 105: XRD pattern of T121(B) generated using the Bruker EVA software, showing albite (orange), calcite (blue), clinoptilolite (green), k-feldspar (yellow), illite (red), smectite (light pink), halite (pink), and quartz (lilac).

Appendix K: USGS v. 7 Spectral Plots, convolved to ASD (Analytical Spectral Devices) standard resolution and full range characteristics

I. Carbonates Group

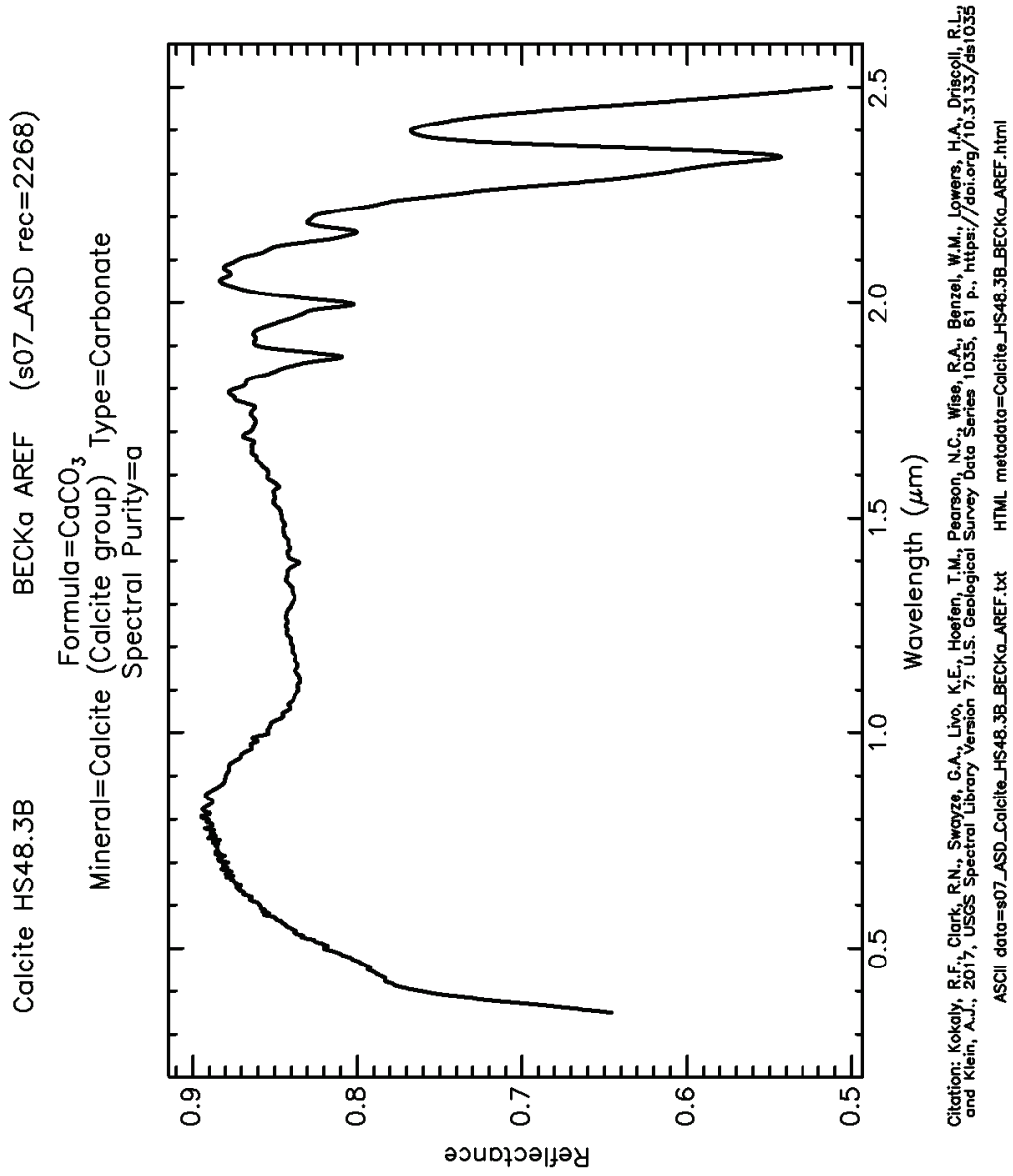

Figure 106: AREF of HS48.3B (74-250 μm), pure calcite with strong carbonate bands from 1.8 to 2.6μm and weak band near 1.1 μm (Hunt and Salisbury, 1971; Kokaly et al., 2017).

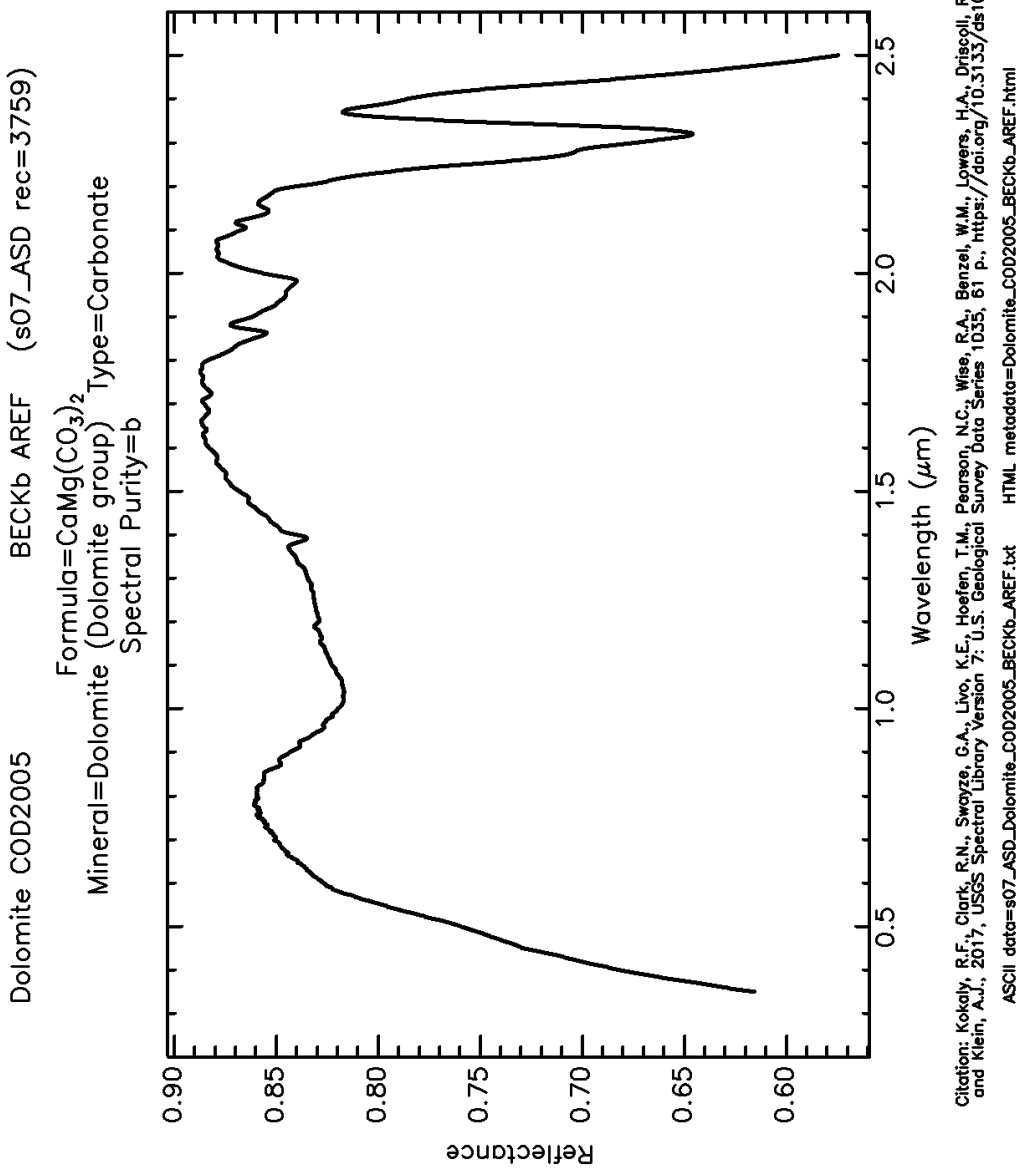

Figure 107: AREF of COD2005 (75 μm average grain size), dolomite with trace calcite (Kruse, F.A., 1992; Kokaly et al., 2017).

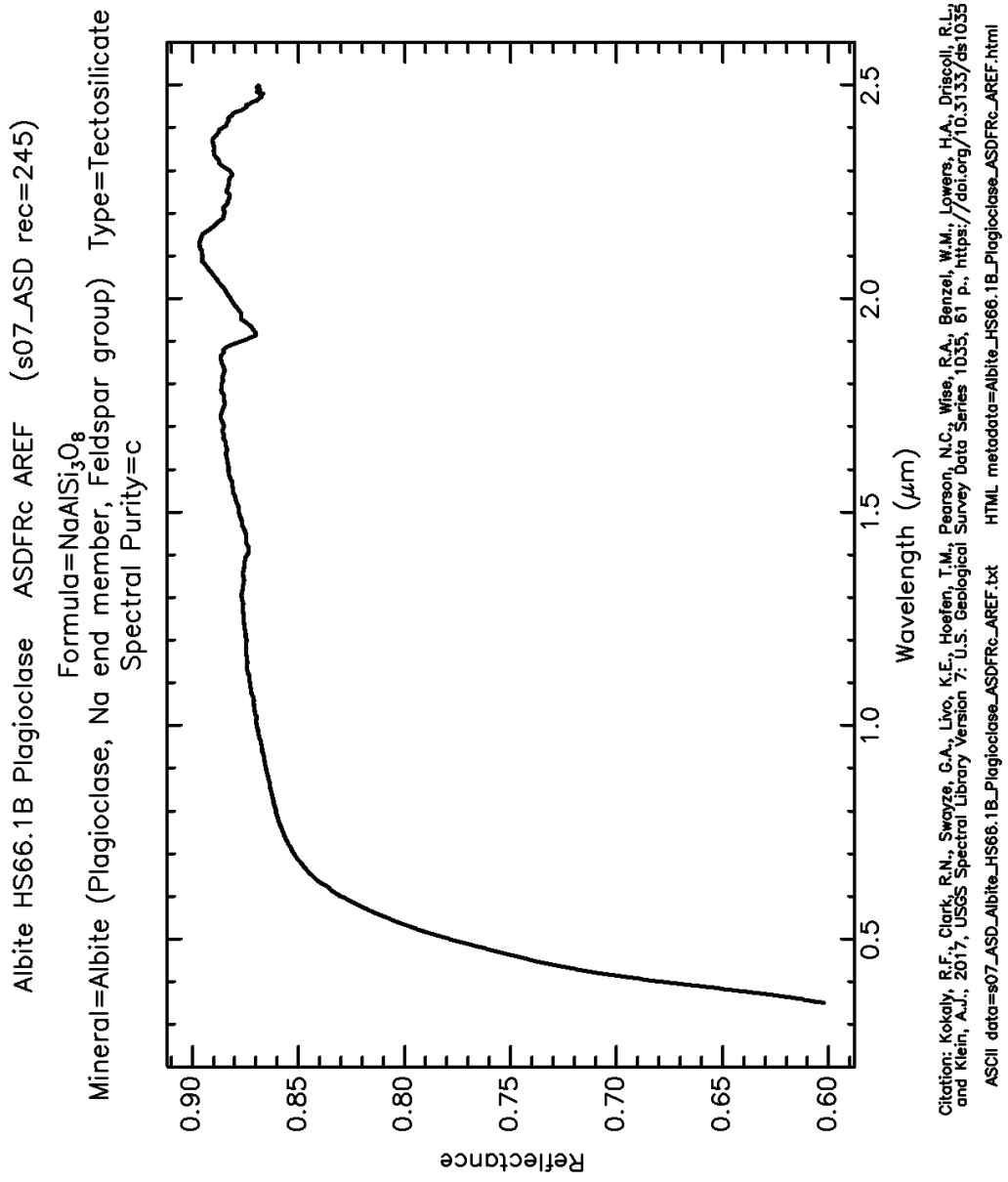

Figure 108: AREF of HS66.1B (<5 μm), albite with trace mica, and the two bands displayed (near 1.4 and 1.9 μm) are due to water in fluid inclusions (Hunt and Salisbury, 1970; Kokaly et al., 2017).

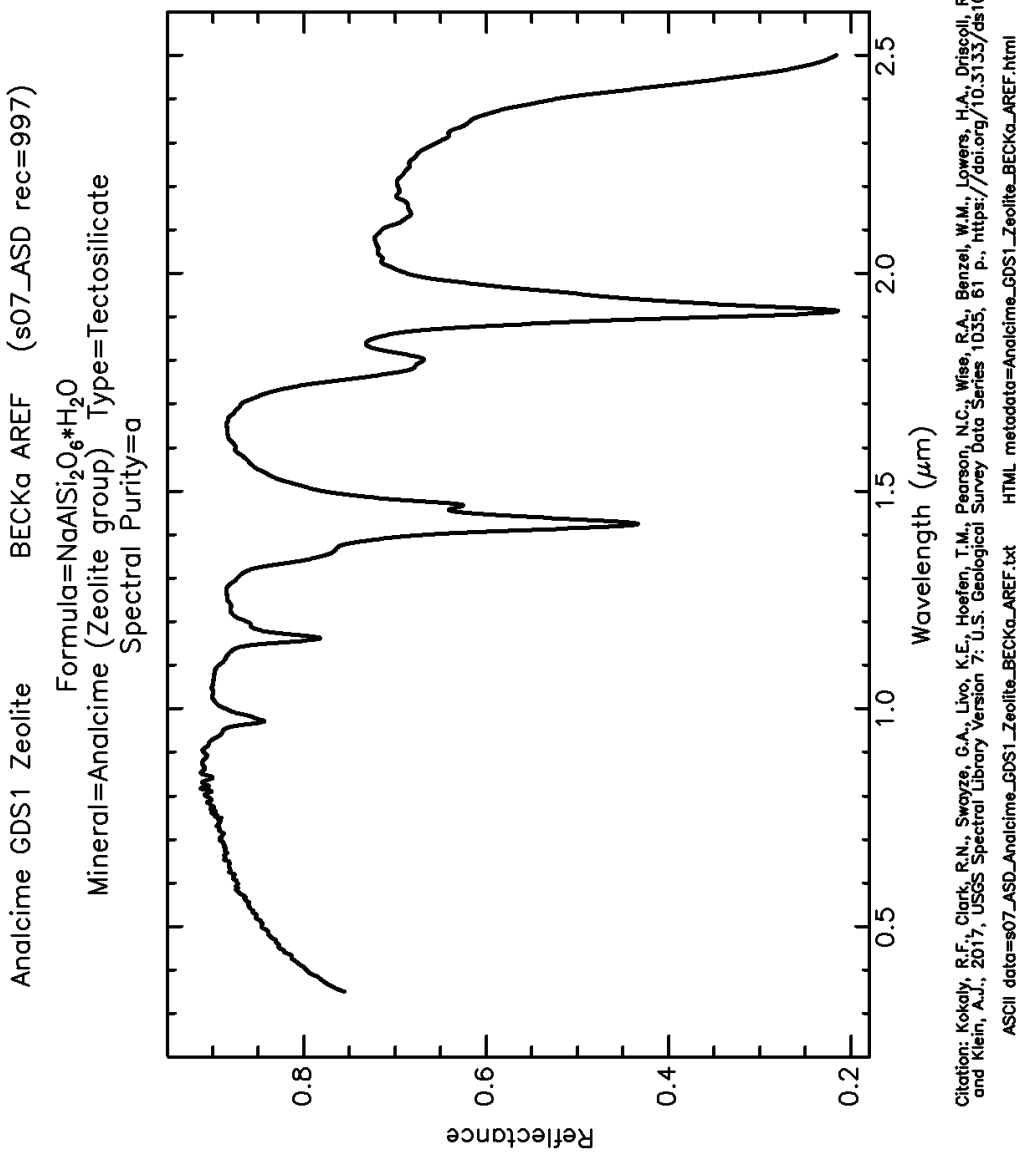

Figure 109: AREF of GDS1 (120 µm), pure Analcime and appears to be spectrally pure (Clark et al., 1990; Kokaly et al., 2017)

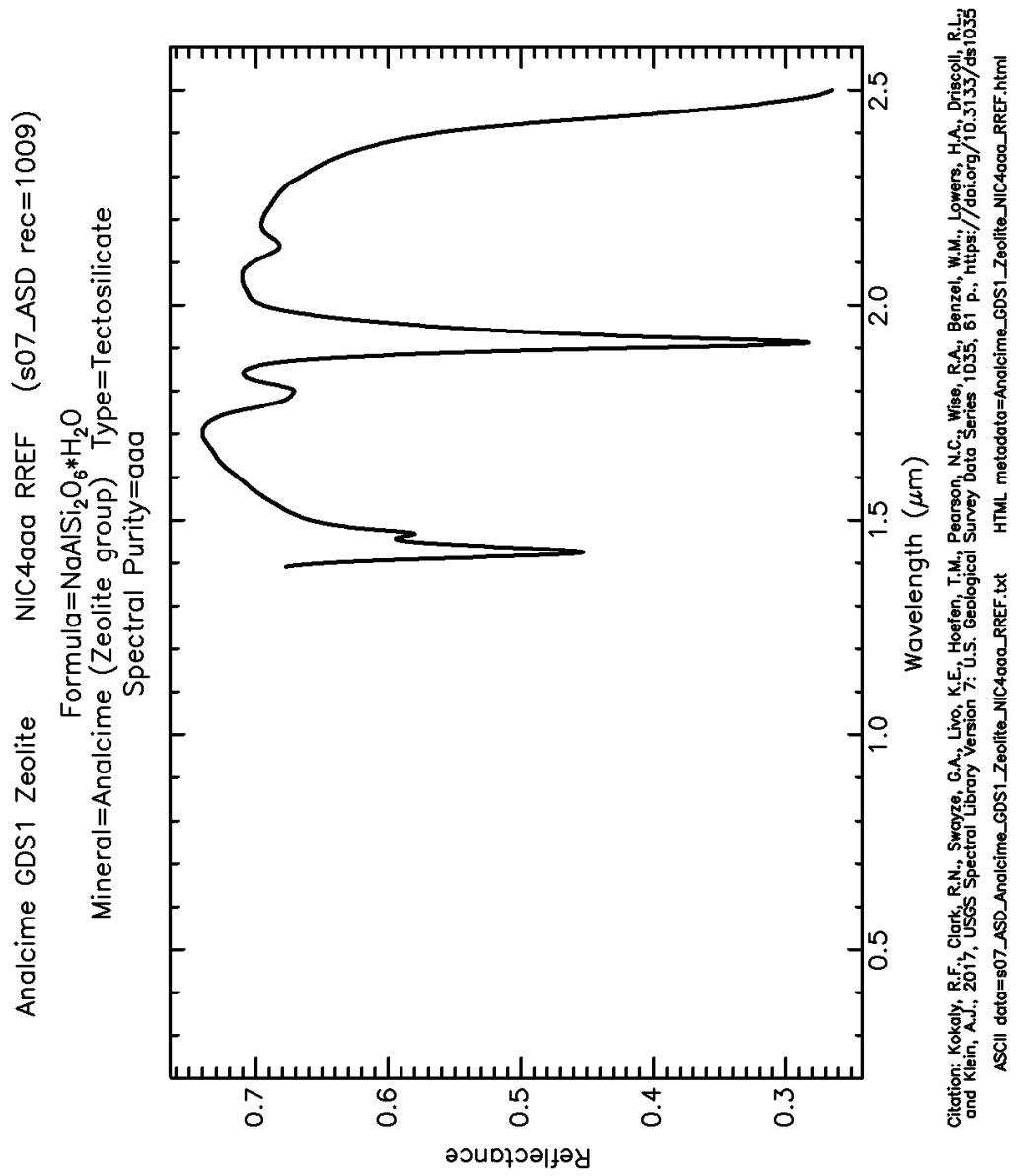

Figure 110: RREF of GDS1 (120 µm), pure Analcime and appears to be spectrally pure (Clark et al., 1990; Kokaly et al., 2017)

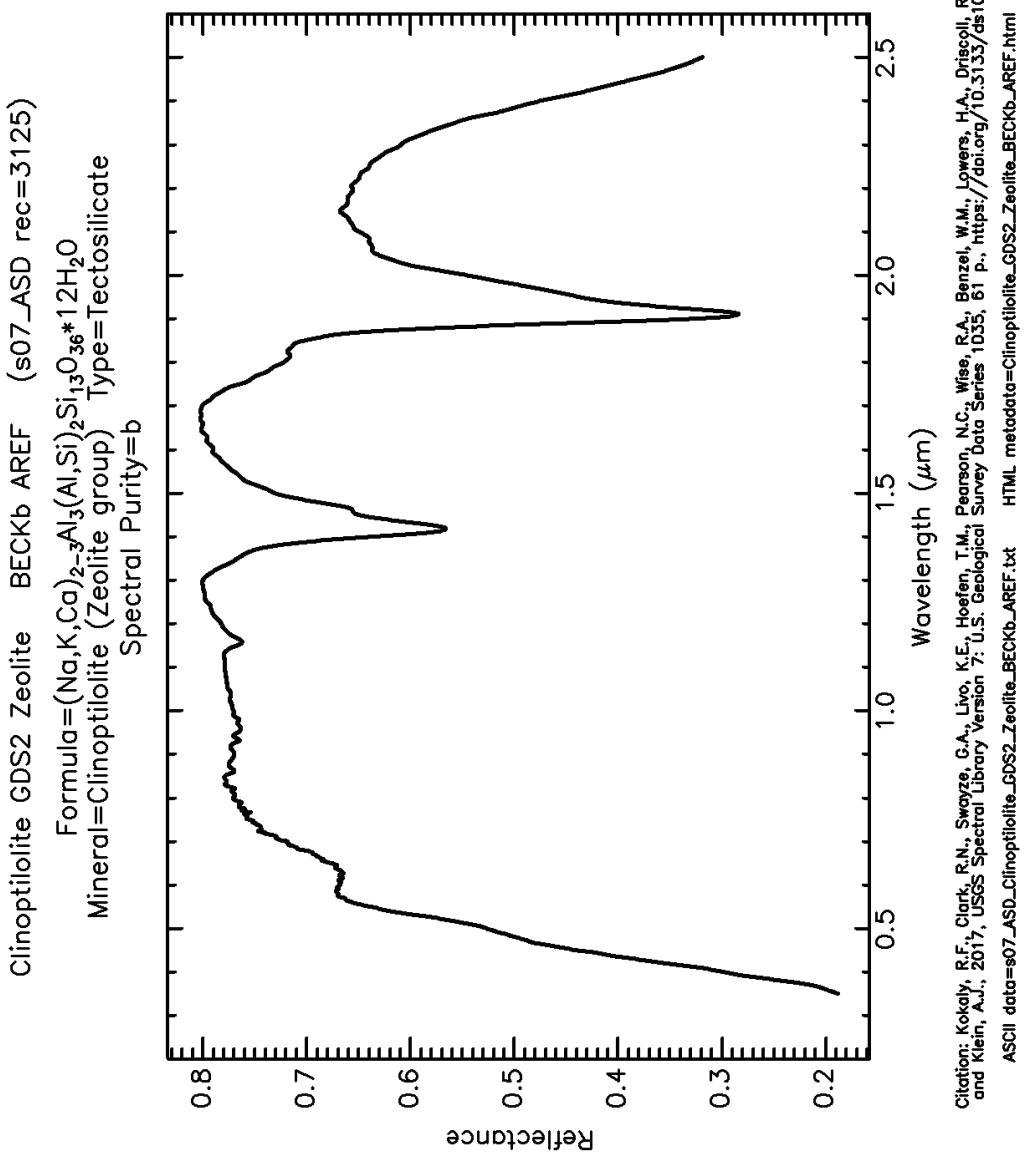

Figure 111: AREF of GDS2, 97-98 vol% clinoptilolite with 2- 3 vol% quartz or feldspar and trace opaques (Clark et al., 1990; Kokaly et al., 2017).

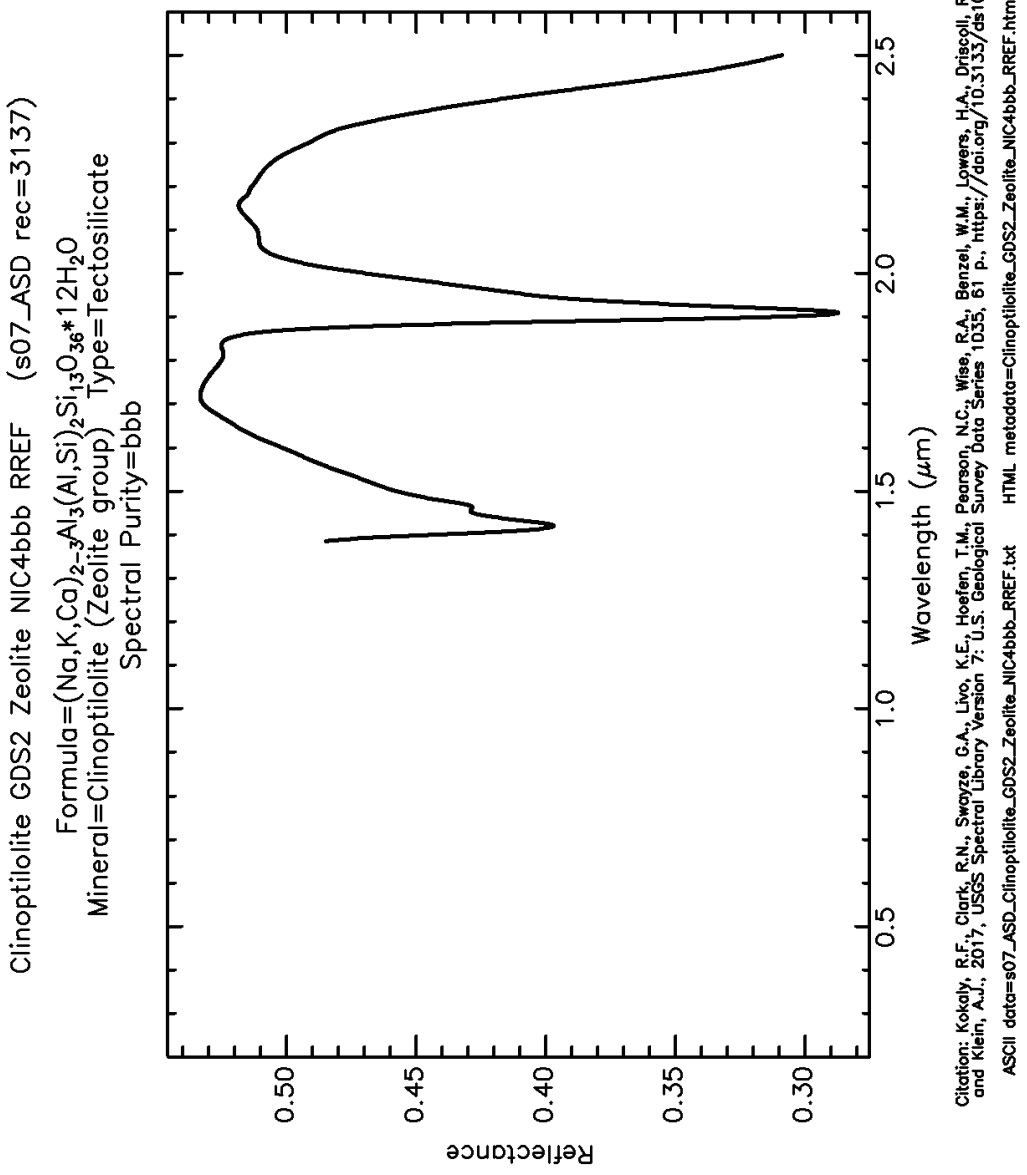

Figure 112: RREF of GDS2, 97-98 vol% clinoptilolite with 2- 3 vol% quartz or feldspar and trace opaques (Clark et al., 1990; Kokaly et al., 2017).

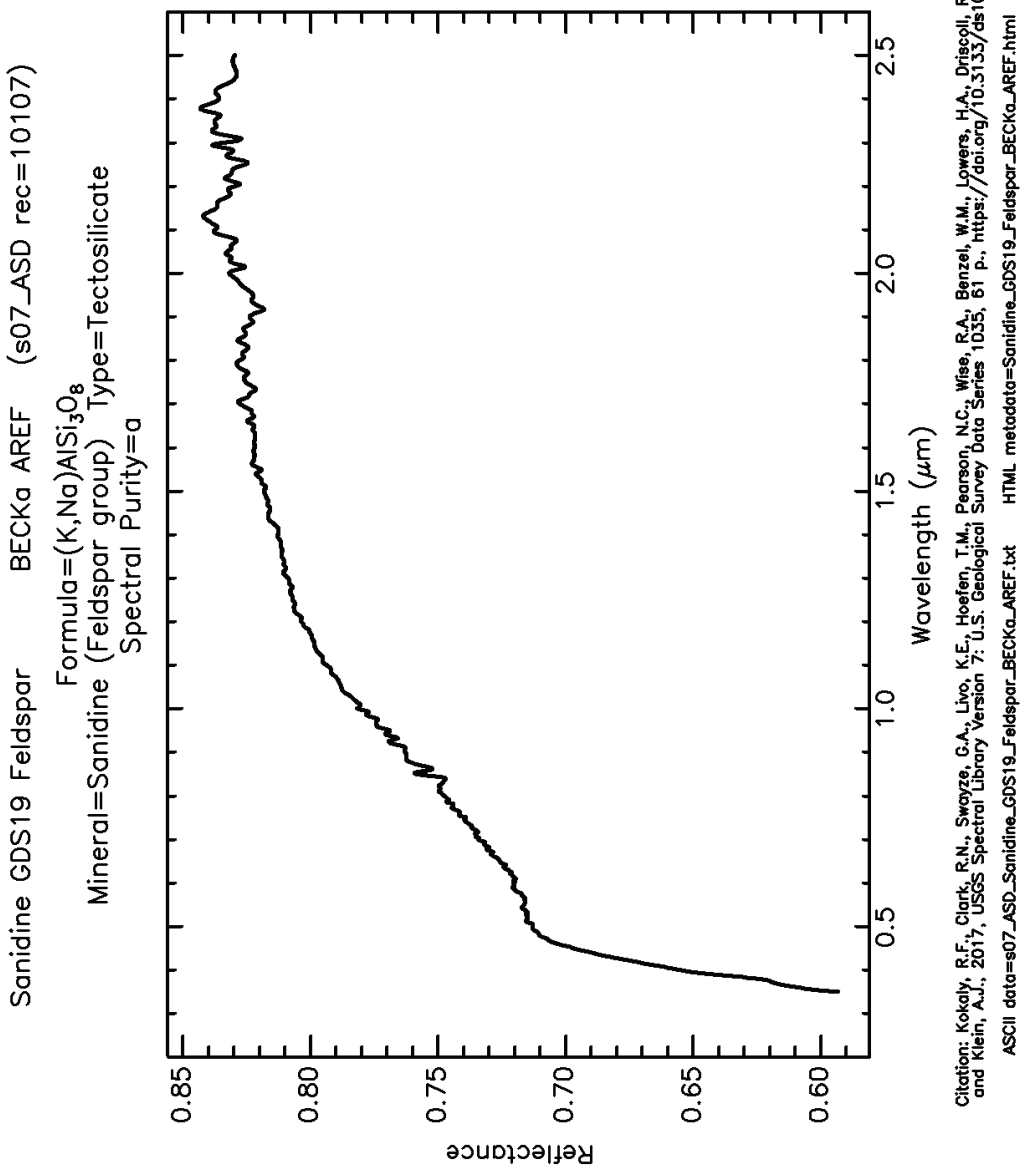

Figure 113: AREF of GDS19, pure sanidine grains with unusually low albite content (Salisbury and Walter, 1987; Kokaly et al., 2017).

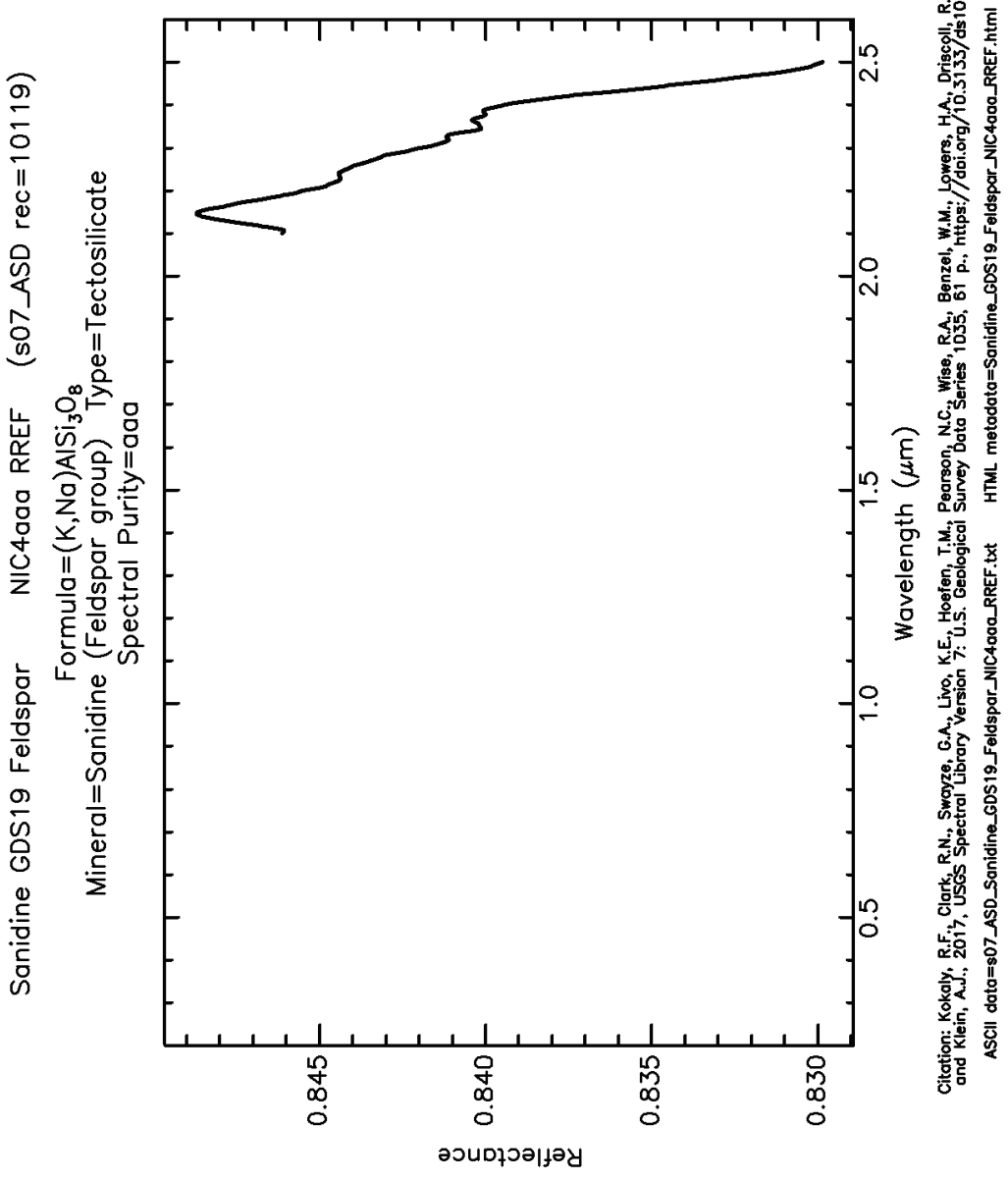

Figure 114: RREF of GDS19, pure sanidine grains with unusually low albite content (Salisbury et al., 1987; Kokaly et al., 2017).

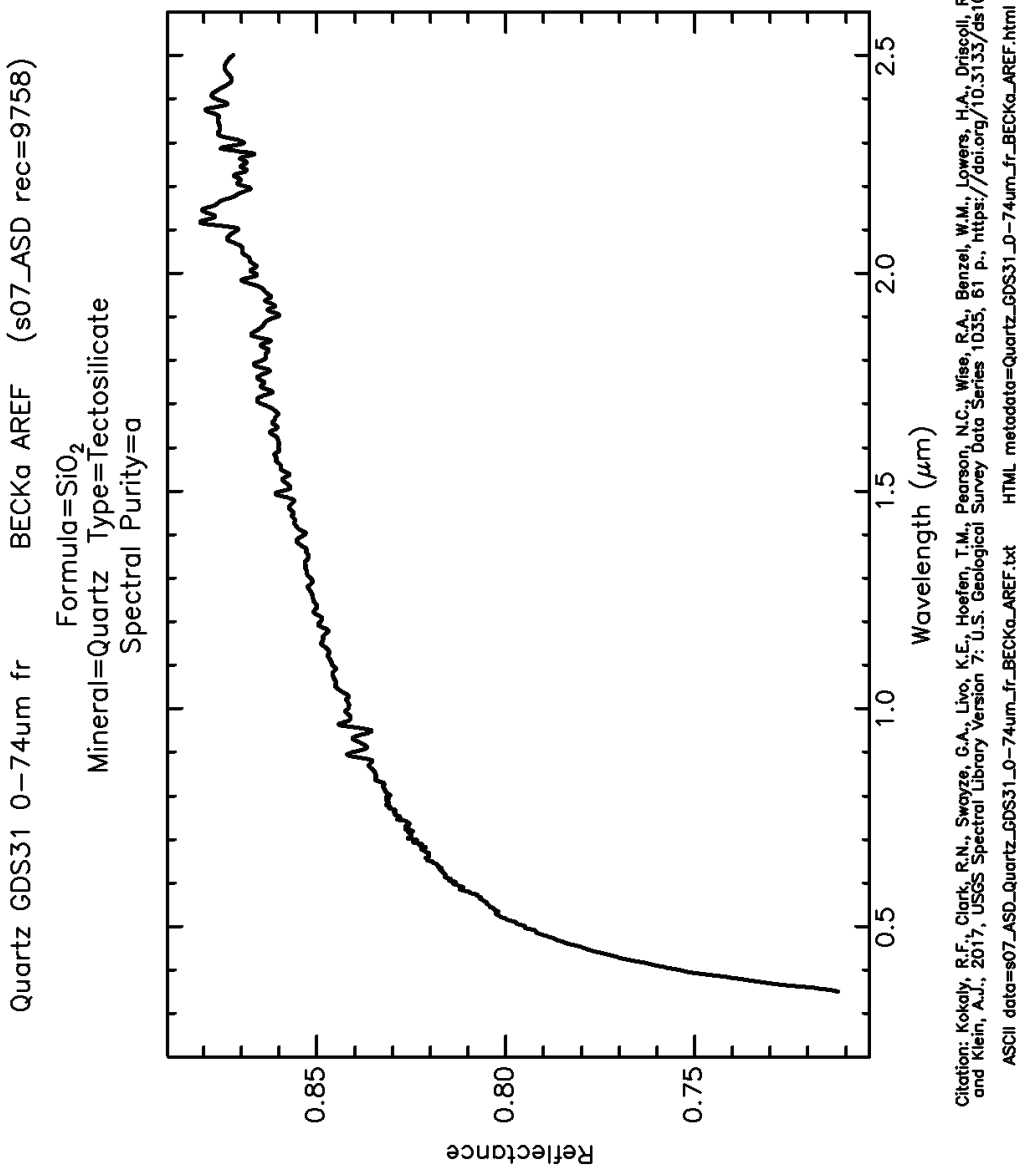

Figure 115: AREF of GDS31 0-74um for pure quartz from a single crystal (Salisbury and Walter, 1987; Kokaly et al., 2017) Weak spectral features.

III. Phyllosilicates Group

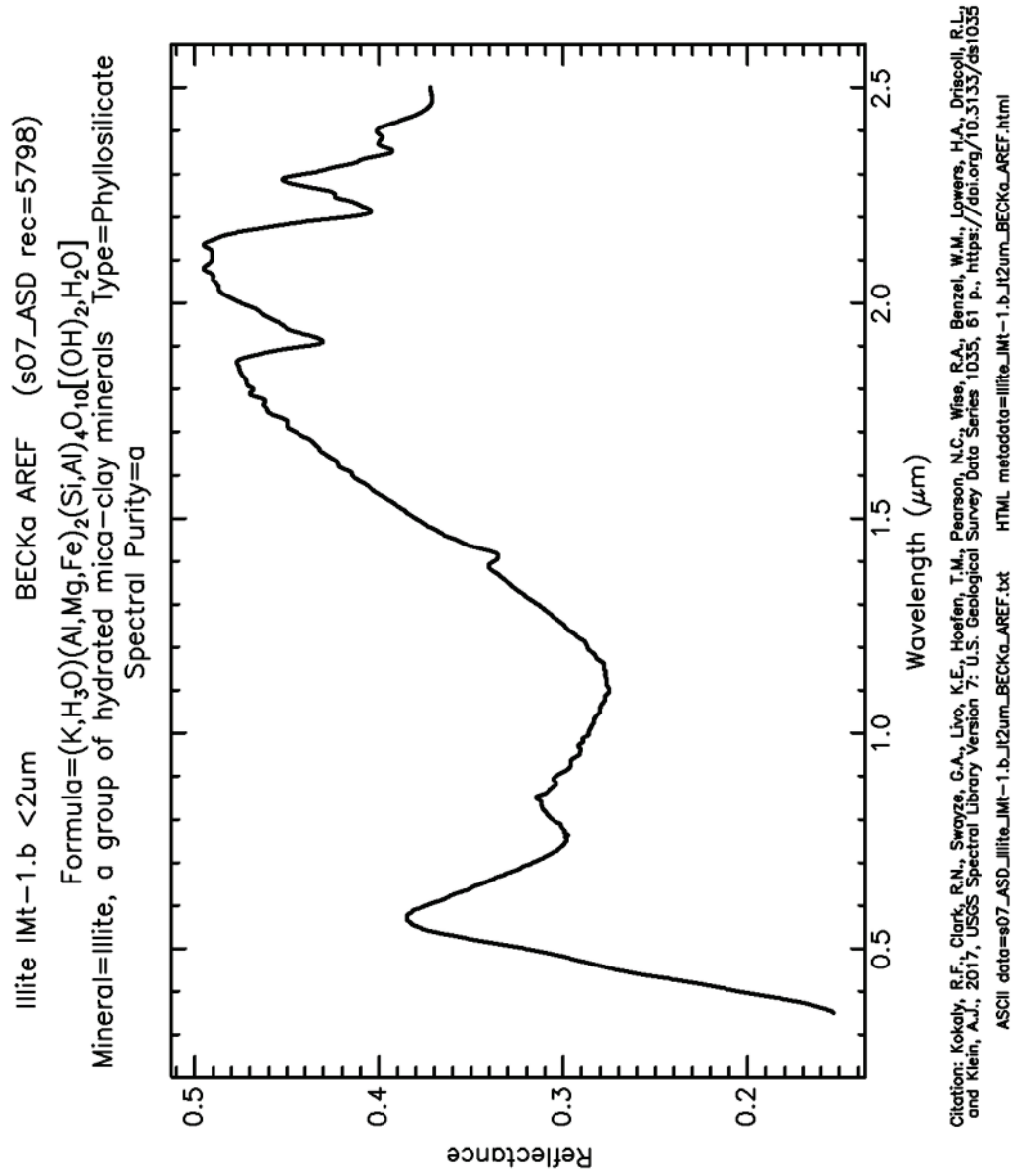

Figure 116: AREF of IMt-1.b (<2µm fraction), pure illite/smectite with 95% illite layers (Salisbury and Walter, 1987; Clark et al., 1990; Kokaly et al., 2017).

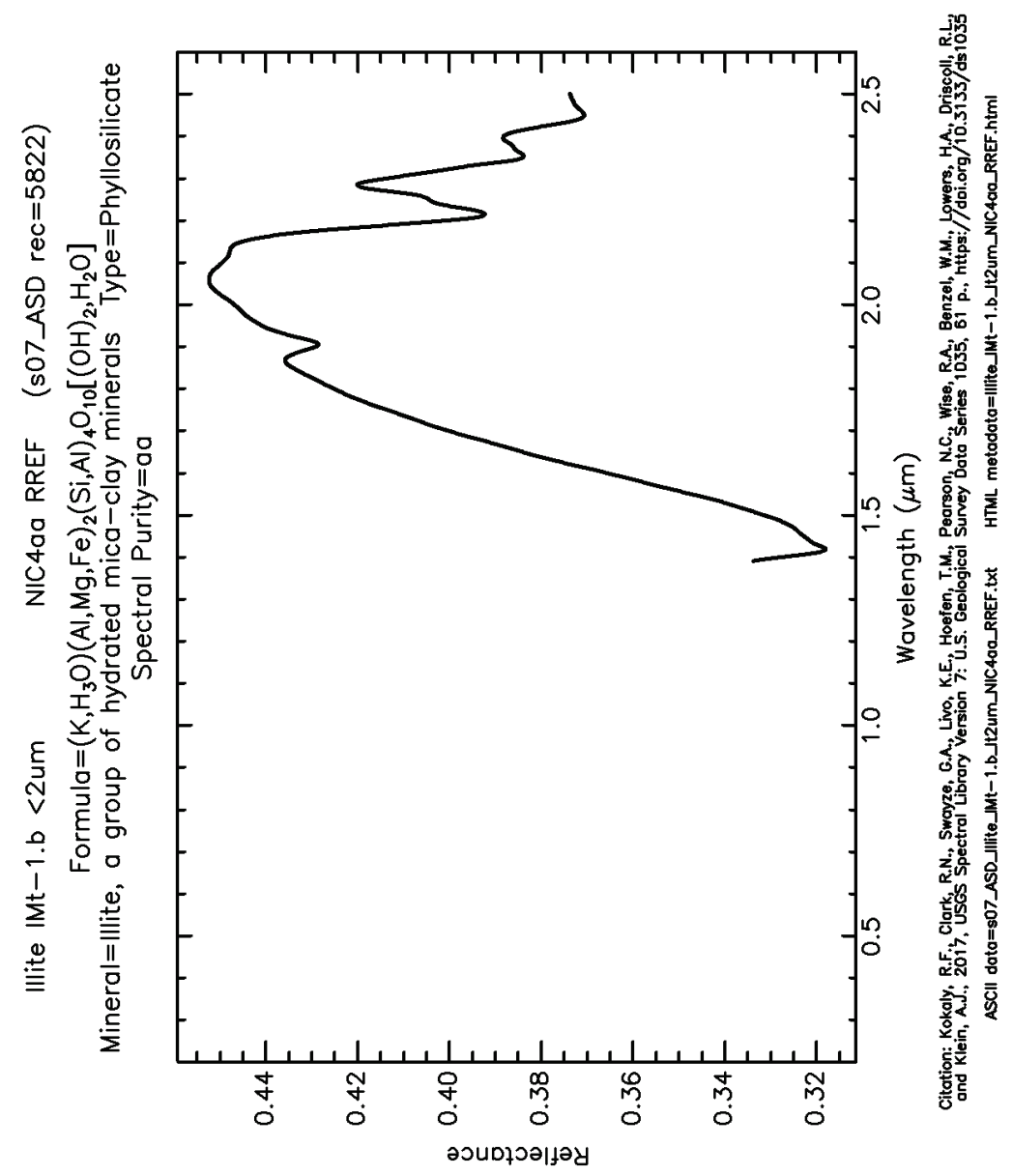

Figure 117: RREF of IMt-1.b (<2µm fraction), pure illite/smectite with 95% illite layers (Salisbury and Walter, 1987; Clark et al., 1990; Kokaly et al., 2017).

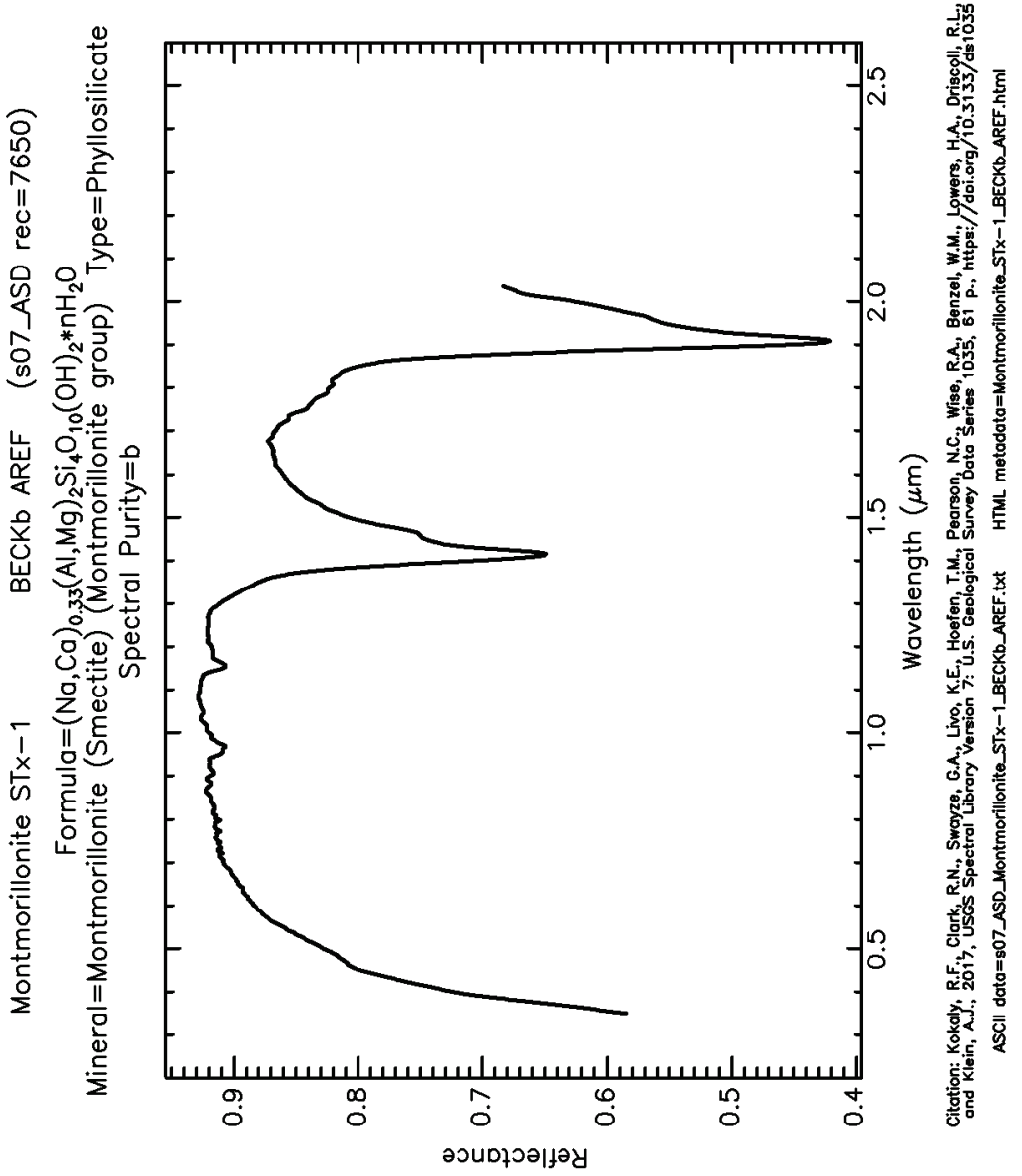

Figure 118: AREF of STx-1, smectite (montmorillonite) with trace quartz (Kokaly et al., 2017).

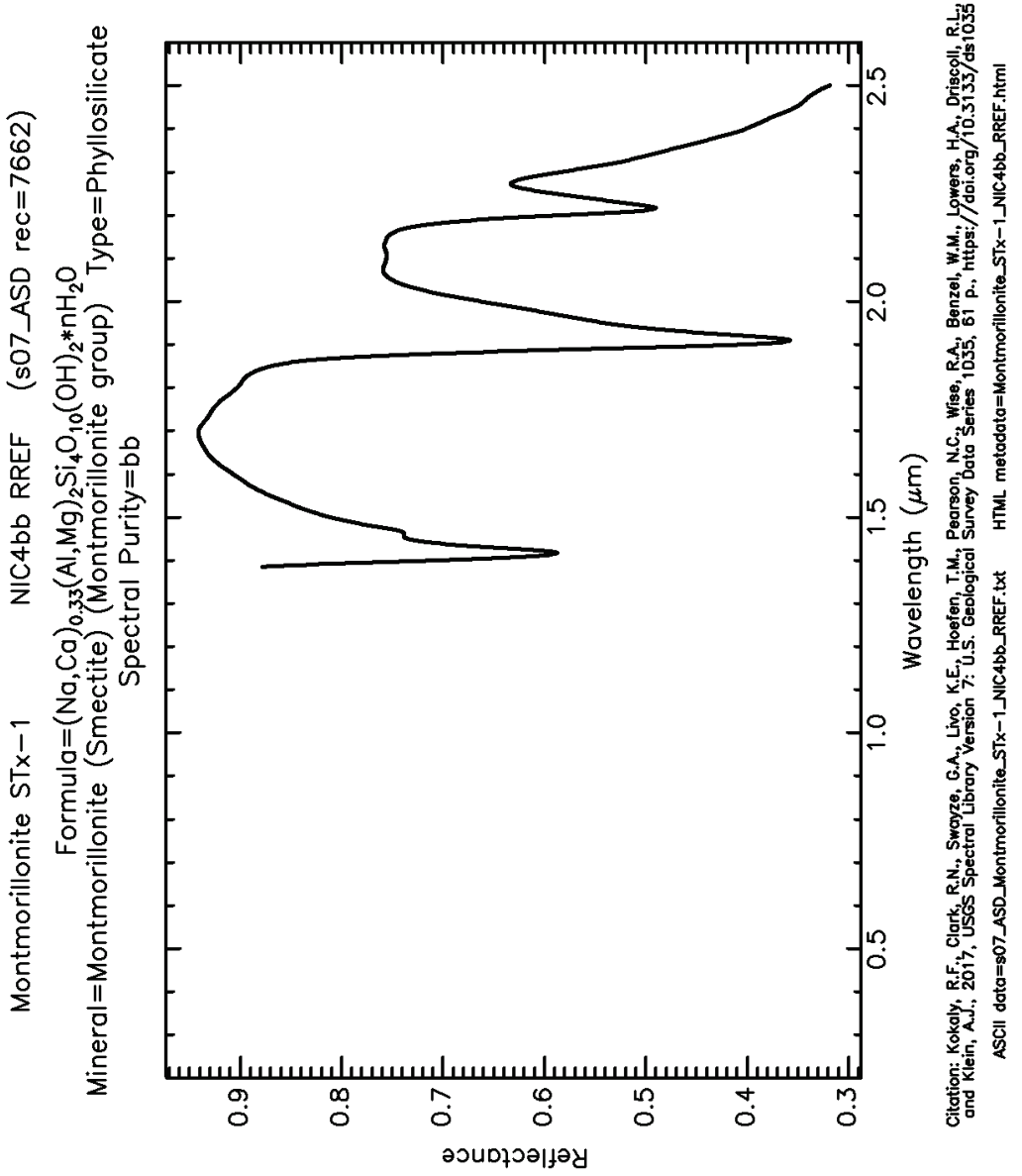

Figure 119: RREF of STx-1, smectite (montmorillonite) with trace quartz (Kokaly et al., 2017).

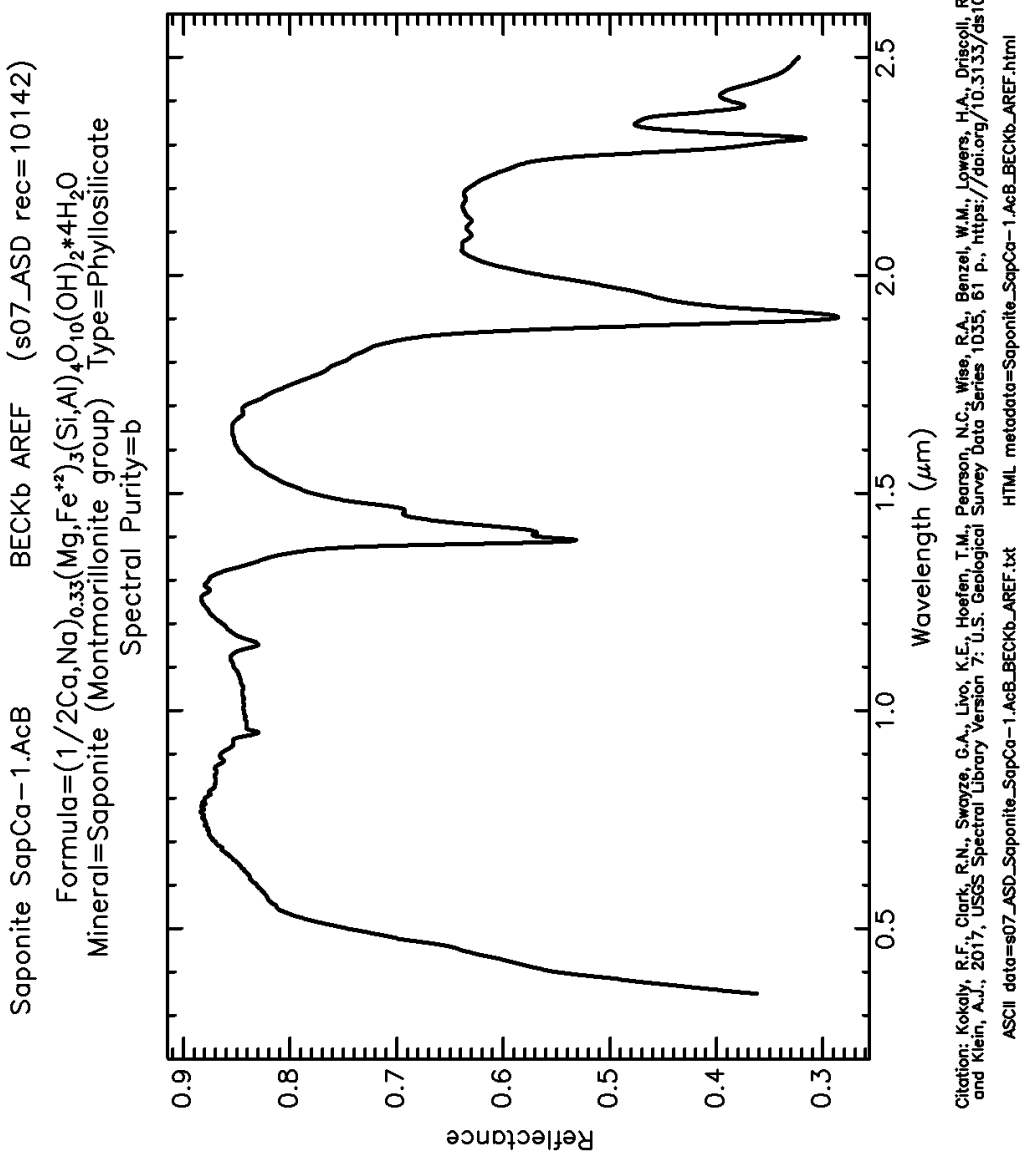

Figure 120: AREF of SapCa-1.AcB, Saponite (montmorillonite group) with trace material (Salisbury and Walter, 1987).

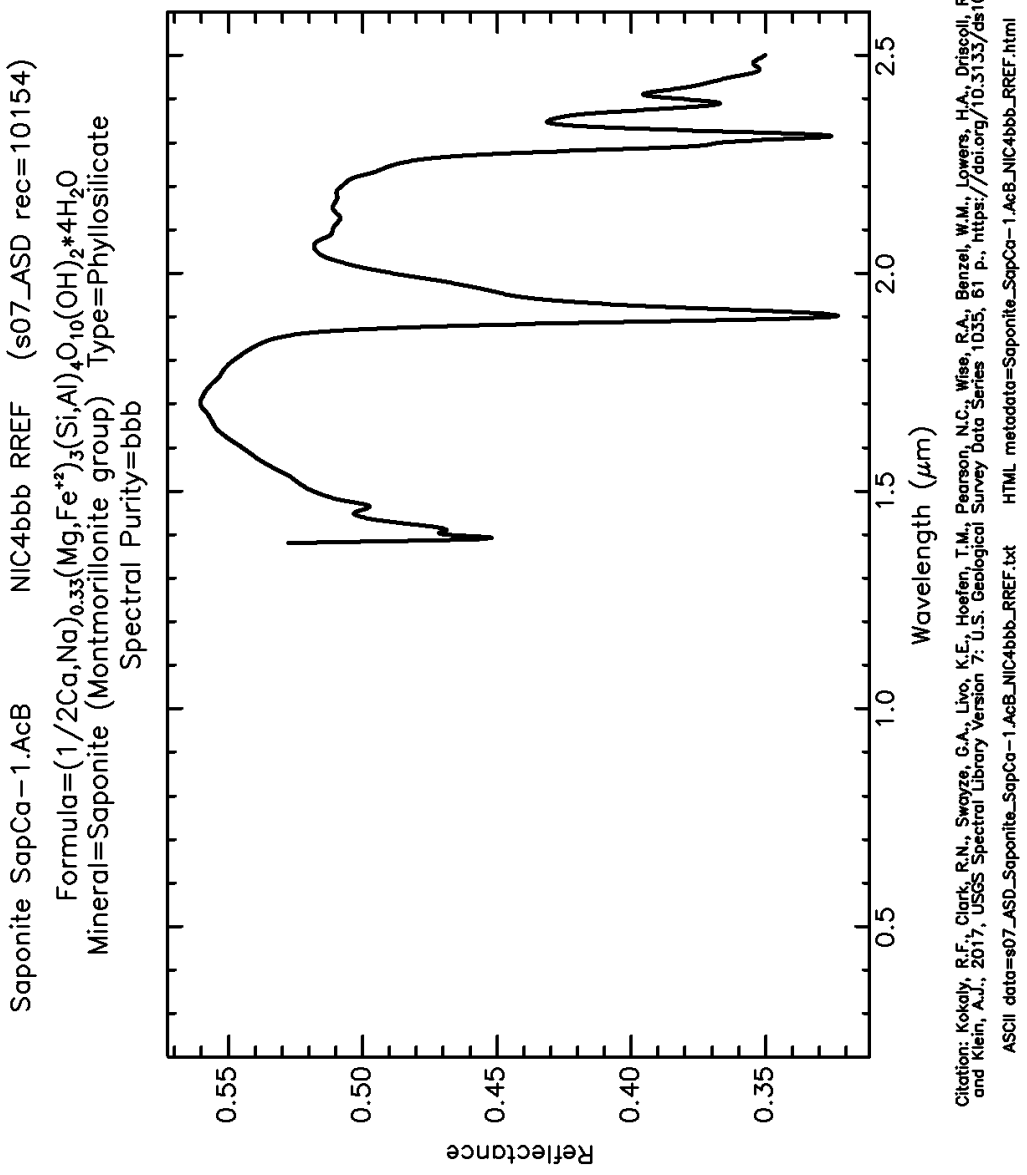

Figure 121: RREF of SapCa-1.AcB, Saponite (montmorillonite group) with trace material (Salisbury and Walter, 1987).

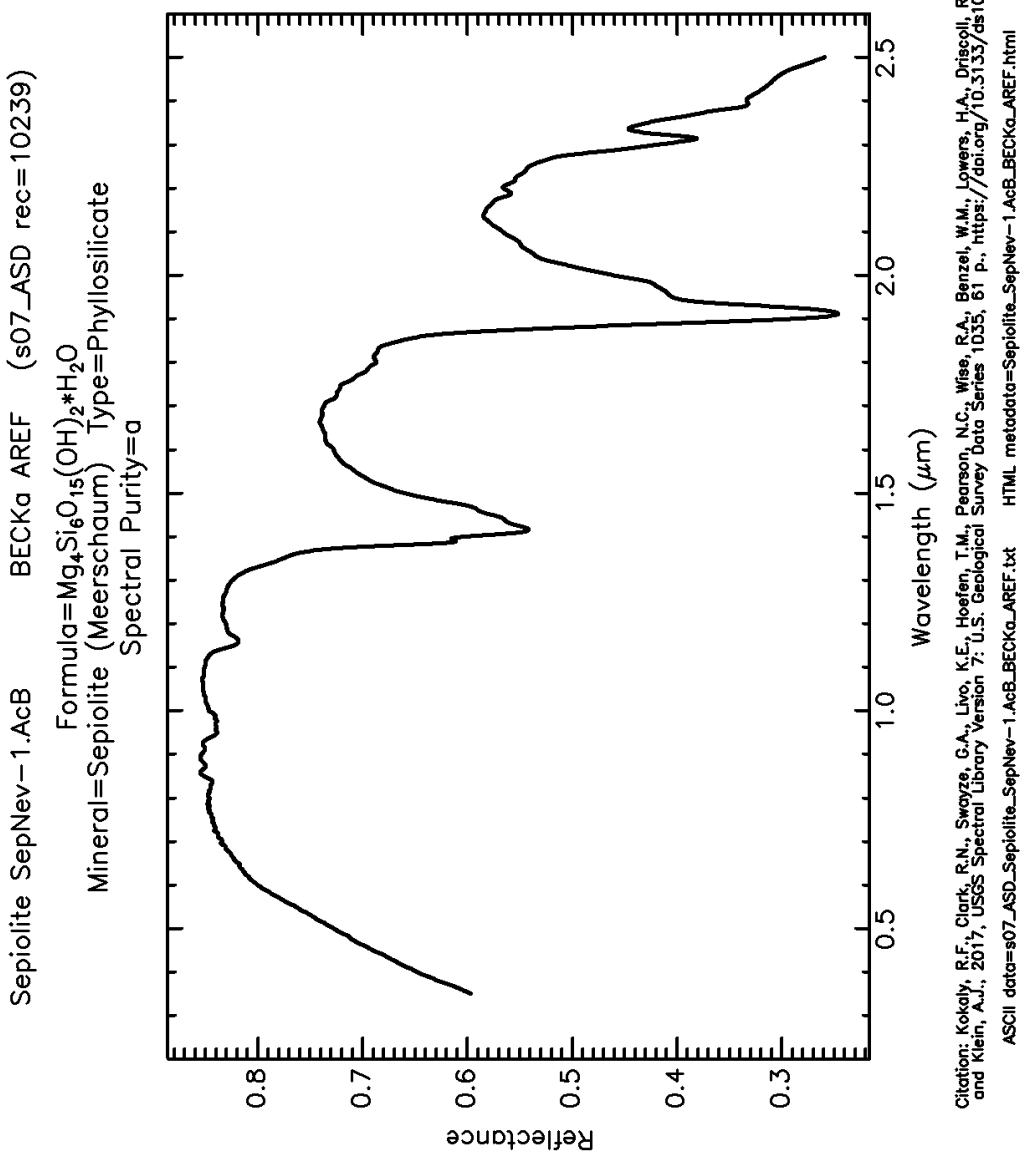

Figure 122: AREF of SepNev-1.AcB, pure Sepiolite (Salisbury and Walter, 1987).

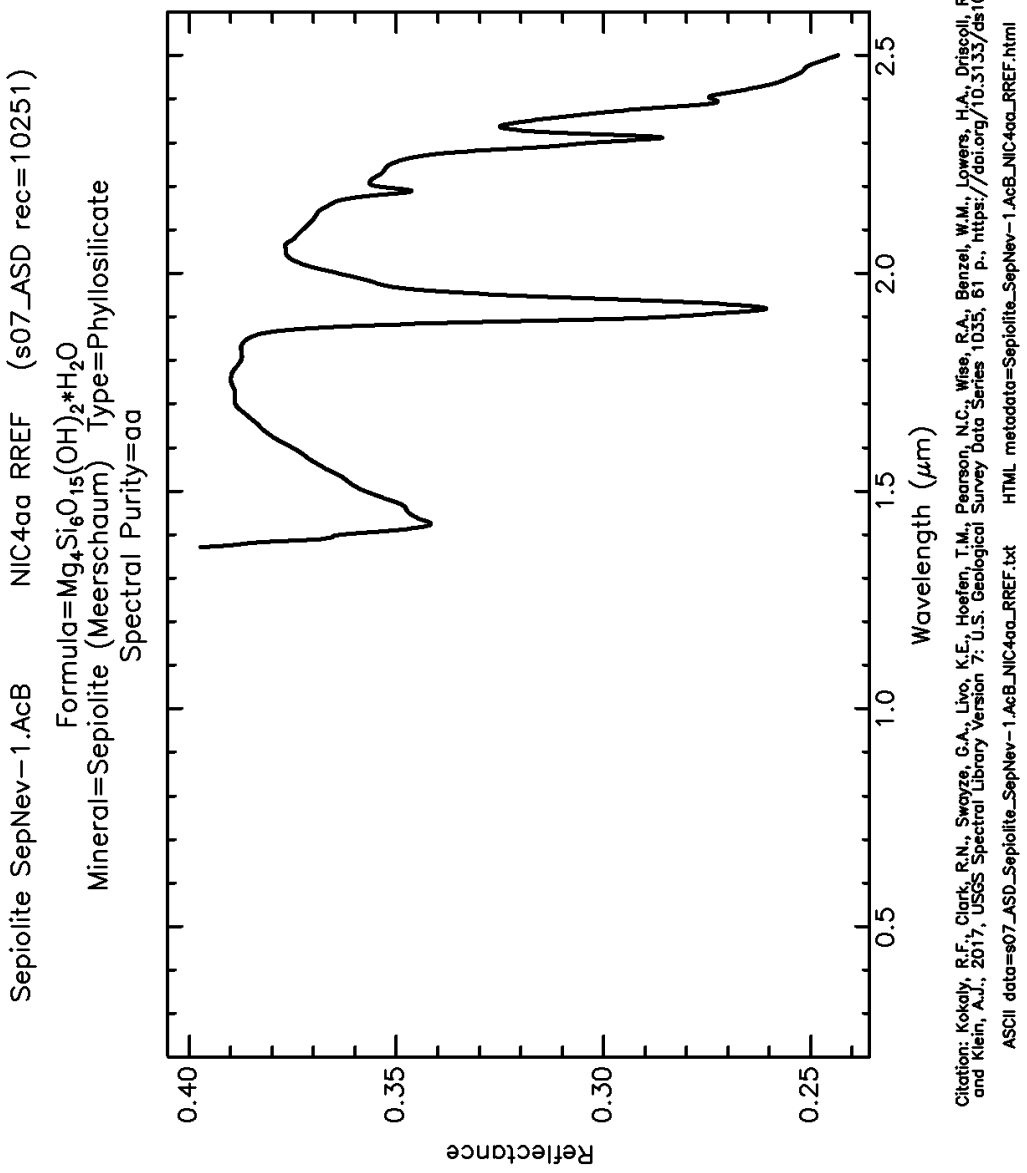

Figure 123: RREF of SepNev-1.AcB, pure Sepiolite (Salisbury and Walter, 1987).

IV. Inosilicates Group

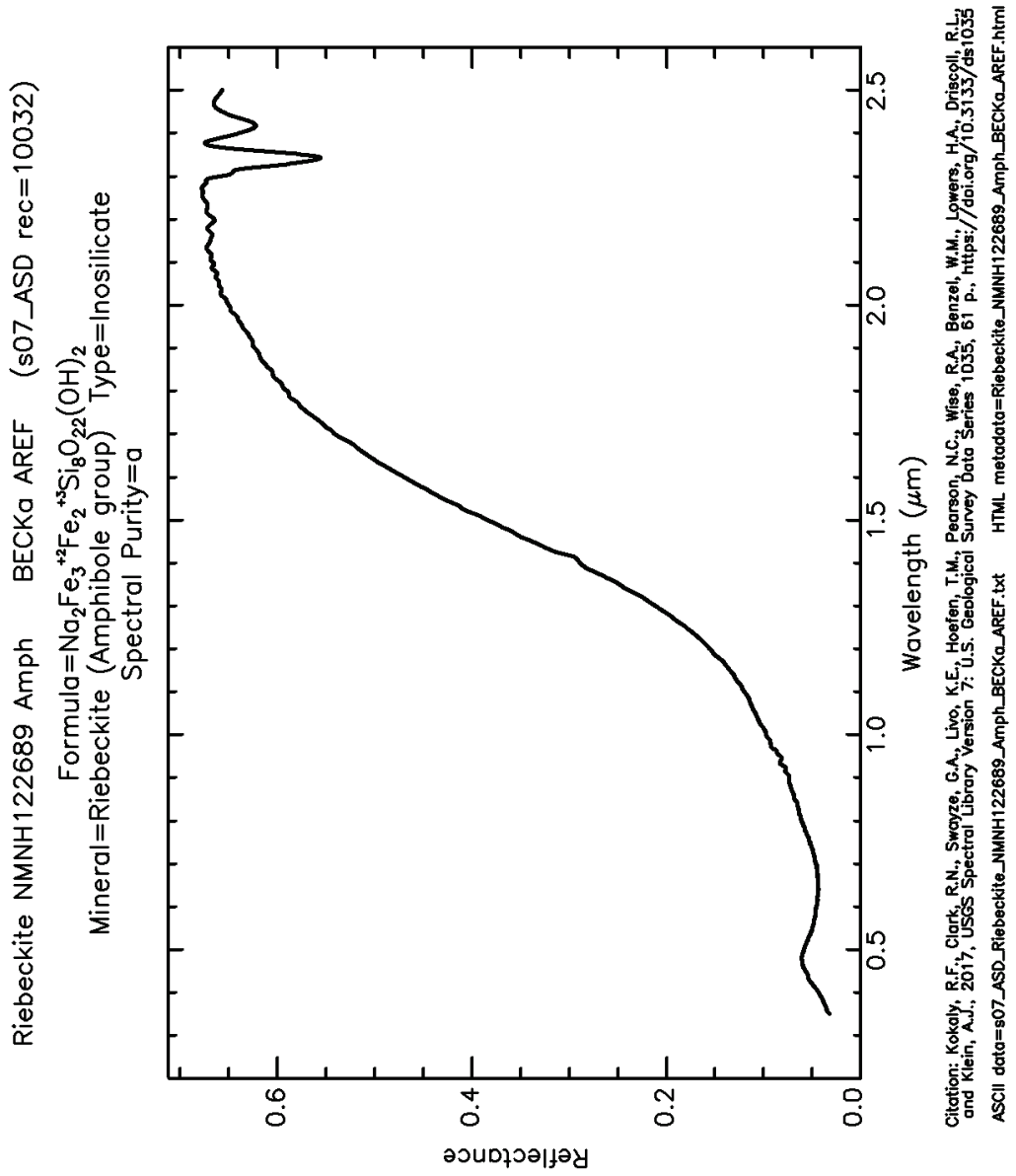

Figure 124: AREF of NMNH122689, individual pure riebeckite grains with less than 1% impurities (Kokaly et al., 2017).

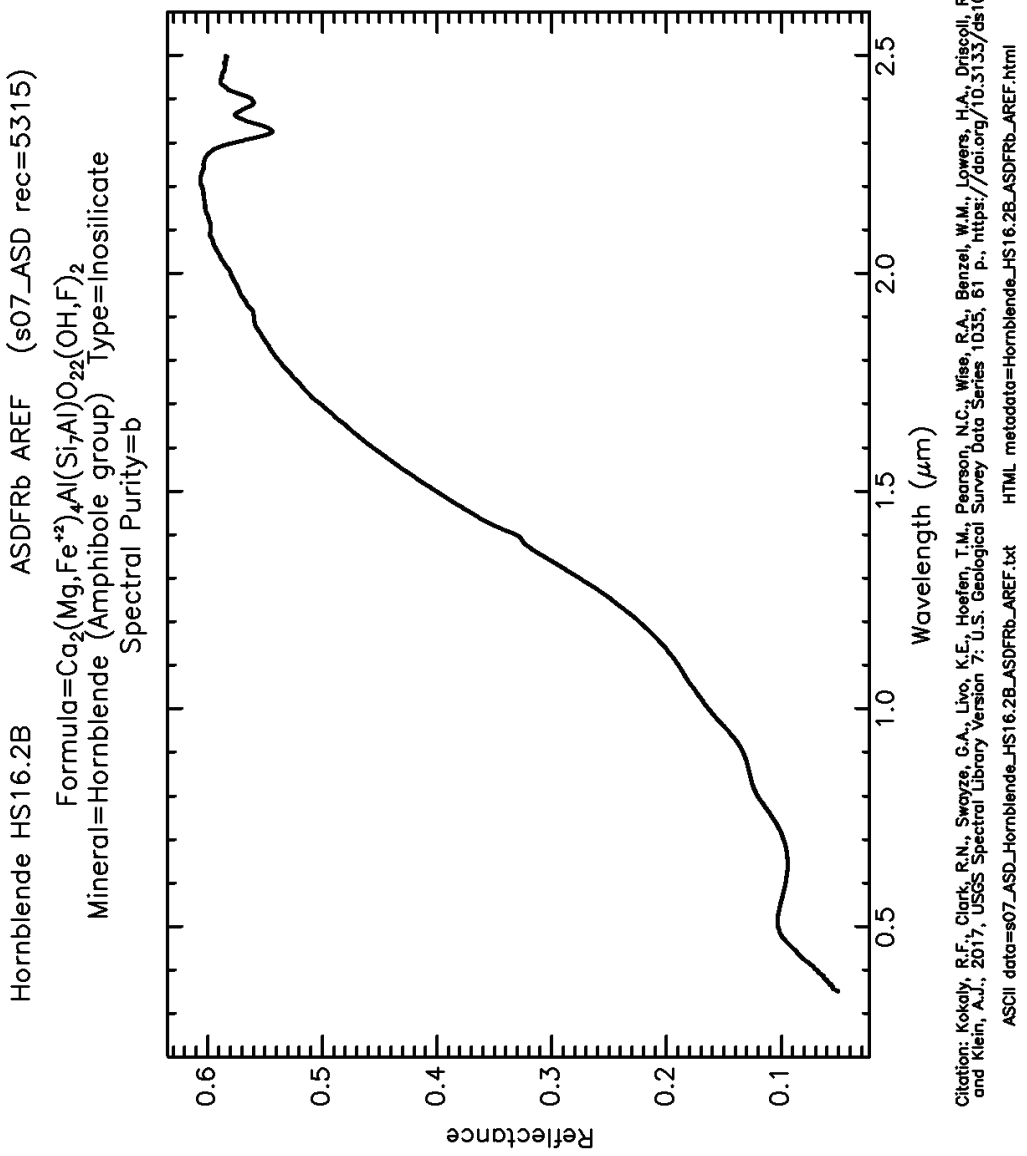

Figure 125: AREF of HS16.2B, clinoamphibole sample (contaminated with multiple phases). Broad Fe^{2+} and Fe^{3+} absorption near 0.7 and 1.0 µm. Reduced hydroxyl band at 1.4 µm, with only OH features at 2.33 and 2.4 µm (Hunt et al., 1973; Kokaly et al., 2017).

V. Halides Group

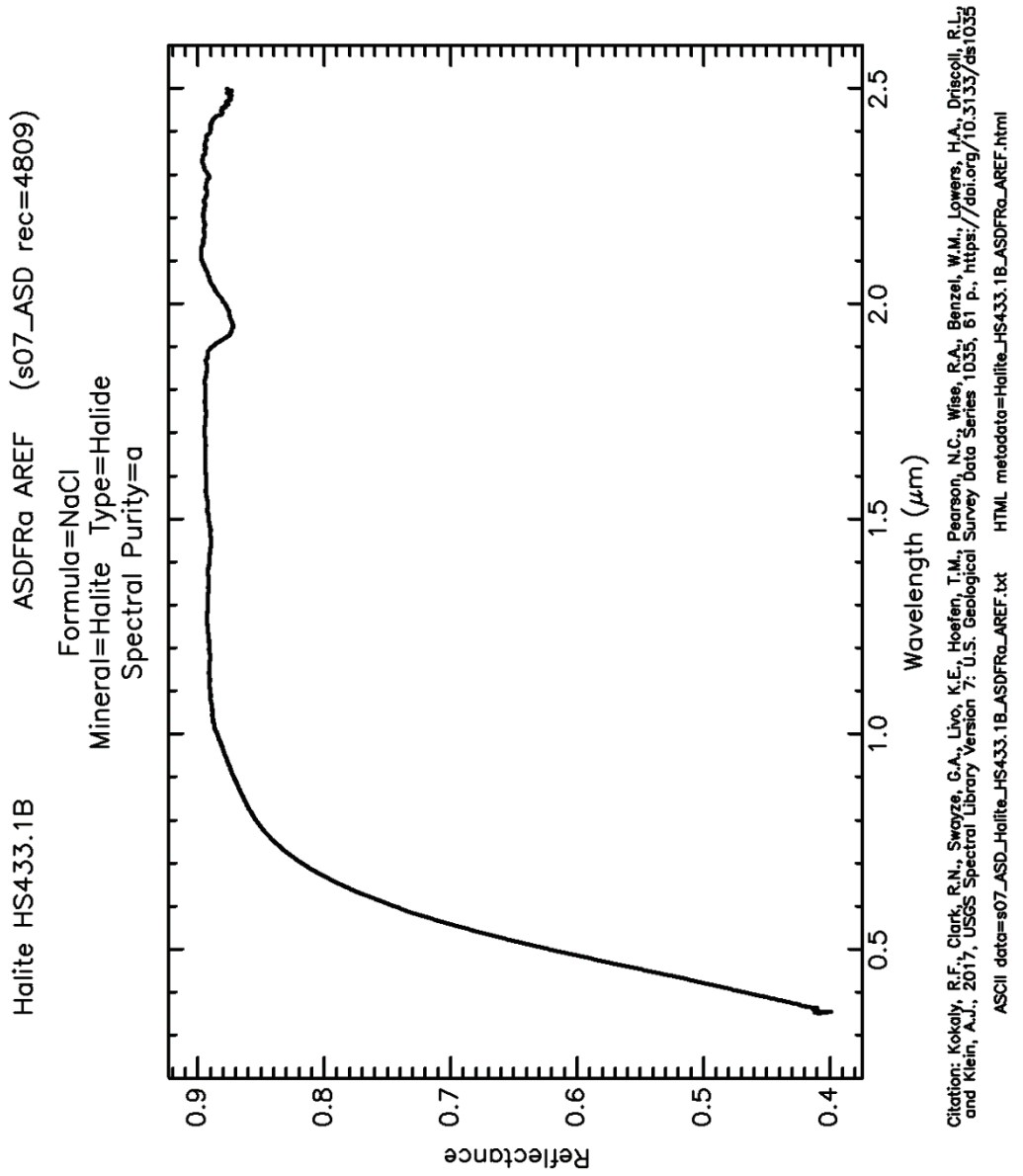

Figure 126: AREF of HS433.1B (<5 μm), pure halite with weak water bands from water in fluid inclusions near 1.95 and 2.25 μm (Hunt et al., 1972; Kokaly et al., 2017).

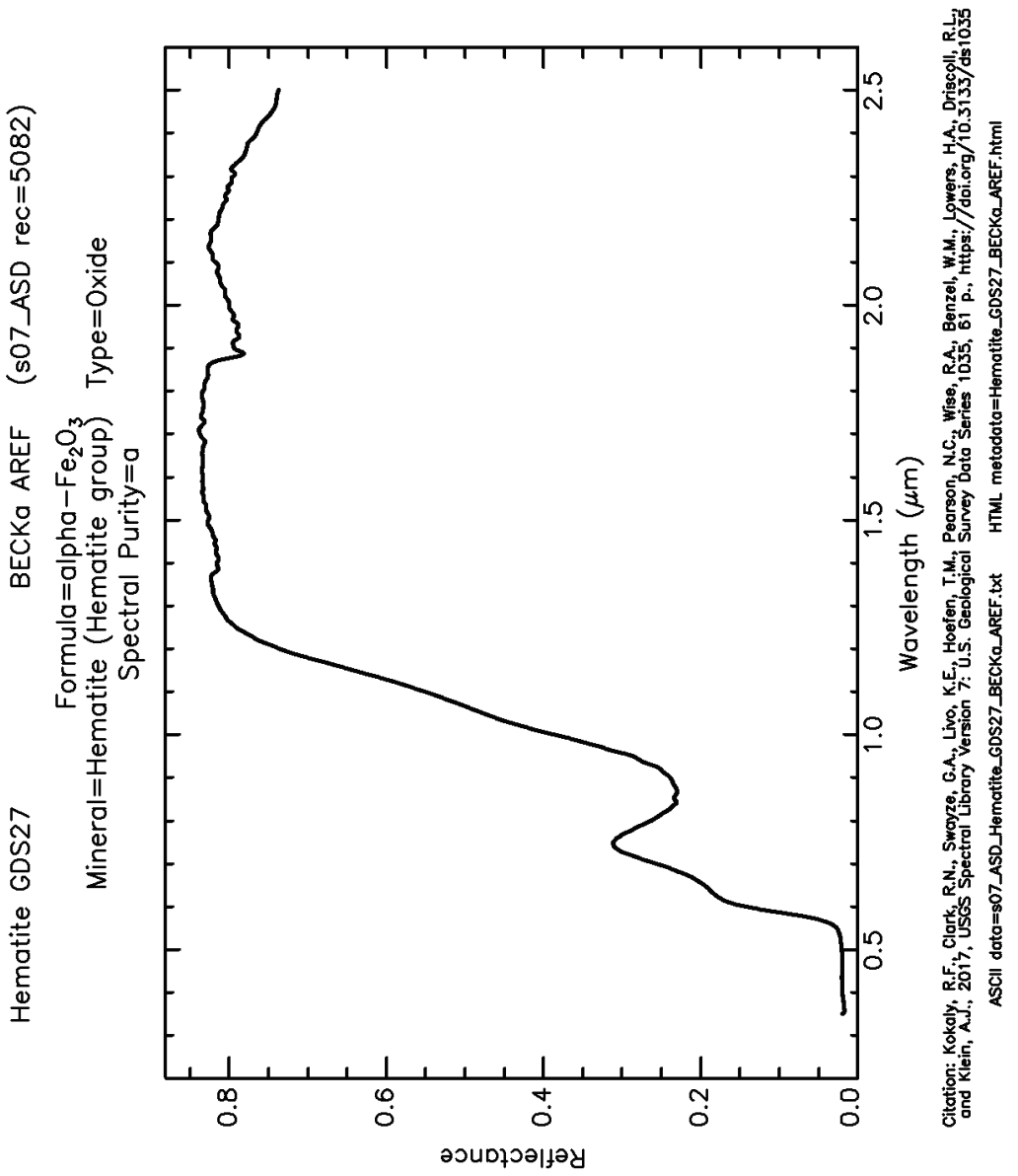

Figure 127: AREF of GDS27 (2-3 μm grains), pure hematite (Kokaly et al., 2017).

Appendix L: Process of running samples through the Malvern Mastersizer 2000

Note: Samples used for the Malvern are sieved using a #10 2mm sieve. 1 bag for samples <2mm and a second sample bag for samples >2mm if you have a gravel sample.

Equipment:

- 4 1000 mL Beakers
- 1 Sample beaker: filled with 600mL of DI water
- 3 flushing beakers: filled with 800mL of DI water
- The prepped sample (<2mm)
- DI water in a squeeze bottle

Sodium Meta-phosphate solution:

1. Place 1000ml (filled with 1000ml DI water) beaker on a magnetic mixer.
2. Make sure the magnetic stir bar is in the beaker.
3. Set speed to 3.
4. Add 50 grams Sodium Metaphosphate to the 1000 ml DI water. **The Sodium Metaphosphate should be added slowly to the DI water. If added to quickly, a gel-like material will form.**
5. Cover with parafilm.
6. Allow 4 hours for mixing.

How to prep samples:

I. Using a 125 mL Erlenmeyer flask, place on scale, zero out, then add sample.
   - For clay: measure out 0.10 grams of sample
   - For silt: measure out 0.25 grams of sample
   - For fine-medium sand: measure out 0.50 grams of sample
   - For coarse sand: measure out 1.0 grams of sample

   IT IS VERY IMPORTANT THAT YOU DO NOT USE MORE THAT 1 GRAM OF SEDIMENT IN A SAMPLE! 1 gram is the most sample you can use in the Malvern.

II. Label flask with Sample#, using sharpie marker on the clear glass part of flask.

III. Fill flask with 20 mL of Sodium Meta-phosphate solution.

IV. Cover with parafilm and let sit for 24 hours. If you have clay samples, you may have to let them sit for longer than 24 hours to allow solution to break up clay particles.

To start analysis:

I. There are 2 power switches, one on each piece of equipment (Hydro and Mastersizer).
II. Set the Pump Speed to 1400, the UltraSonic Displacement to 10.00 and UltraSonic timer to 60 seconds.
III. Lift the arm on the Hydro machine with one hand while holding down on the metal plate with the other.

IV. Place sampling beaker in the circular spot under fan. Lower the fan into the beaker.
V. Press green button and select ON button on the pump speed. This should turn the Malvern on.
VI. Open Mastersizer 2000 from desktop
    a. Select: OK
    b. Close out all open files. It is common to accidently start adding samples to the wrong folder.
    c. File → Close
    d. Go to File → Open → Measurement Data → "Site Folder" → Open
    e. To create a new folder:
        i. Select: Create New Folder
        ii. Assign a folder name (e.g. Tecopa 2019)

To start measuring:

I. Click Measure → Start SOP → Quartz.sop → Open
II. Enter sample# and grams of sample into info → OK
III. In the yellow box, it will inform you of the next steps. With clean DI water in sample beaker, Press Start.
IV. You will hear 2 lenses dropping inside the Malvern. Once it is done measuring the DI water (background), it will ask you to add your sample.
V. Add sample to sample beaker.
VI. Using distilled water squeeze bottle, flush all the sediment out of the Erlenmeyer flask into the l000mL sample beaker.

- Laser obscuration must be between 2% and 20% (2% < obscuration > 20%).
- If obscuration is too low:
  • Not enough measured sediment in the sample.
  • Redo sample with larger measure of sediment.
  • Label flask "REDO → "Sample#"
- If obscuration is too high:
  • Try adding more DI water to lower the %
  • Redo sample with smaller measure of sediment. Label flask "REDO → "Sample#"

VII. Push START on the UltraSonic timer. This will start a 60 count down. You need to allow this to complete. You will hear a loud noise, which will continue throughout the 60 seconds. Once the timer is finished, the noise will stop.
VIII. Once finished, select START on the desktop screen. There will be 3 (three) measurements taken. These 3 measurements, along with the average, are viewable under the Result Analysis tab. (More about the Result Analysis in "to check sample data" section)
IX. When measurements are completed, a box will pop up with "Post-Measurement Instructions entered into SOP"
X. Select: OK

- If you wish to continue running samples, click the YES button
- By selecting YES, you will start the process over.

- Enter (new) sample # and information. Press the OK button.

XI. If you are done running samples, select: NO

To set up for next sample run:

I. You will flush the system after every sample. By using the 3 (three) flushing beakers, filed with 1000mL DI, this will flush any residual sediment out of the system.
II. Press the green button to turn the fan off (IMPORTANT).
III. Pull up the arm.
IV. Rinse wand and fan with DI water squeeze bottle to remove any residual sediment.
V. Remove sample beaker.
VI. Place flushing beaker under the fan (same place the sampling beaker was placed) and lower the arm.
VII. Press the green button and allow fan to spin for "'15 seconds. Press the button to stop the fan.
VIII. Repeat with 2nd and 3rd flushing beaker.
IX. Rinse beakers and refill with DI water. Erlenmeyer flask should be rinsed and remove the sharpie writing with rubbing alcohol.

To check sample data:

I. Highlight and select the 3 (three) measured samples plus the average.
II. Select Result Analysis tab.
III. Make sure the curves match up.
IV. Select Records tab to return to the sample page.